ATMOSPHERIC COMPENSATION EXPERIMENTS ON FREE-SPACE OPTICAL COHERENT COMMUNICATION SYSTEMS

By

Esdras Anzuola Valencia

M.Sc., Polytechnic University of Barcelona, 2012

B.Sc., Polytechnic University of Zaragoza, 2007

A Thesis Submitted in Partial Fulfillment of the
Requirements for the Degree of
Doctor of Philosophy

in the
Doctorate Program on Signal Theory and Communications
Polytechnical University of Barcelona (*BarcelonaTech*)

Thesis Advisor

Aniceto Belmonte

Polytechnical University of Barcelona

March, 2015

Abstract

New, affordable adaptive compensation methods and technologies can help to improve substantially the performance and reliability of coherent optical systems in the atmosphere. The use of adaptive optics to mitigate turbulence-induced phase fluctuations in receivers employing coherent detection is poised to reduce performance penalties enabling a more sensitive generation of coherent instruments and applications.

In this work, we describe the implementation of a free space optical coherent communication system using QPSK modulation and heterodyne downconvertion that uses adaptive optics techniques and digital signal processing to mitigate turbulence-induced phase fluctuations and channel impairments in coherent receivers. A new method for generating atmospheric turbulence based on binary computer generated holography (BCGH) using binary arrays is presented and its performance is evaluated. The feasibility of FSO coherent systems working with adaptive optics is demonstrated and the system performance in terms of the BER is experimentally evaluated under the influence of atmospheric turbulence. The resulting system performance is compared against the theoretical models. The viability of the approach to improve the system efficiency and sensitivity of coherent receivers is experimentally demonstrated.

Keywords: Free space optics, Optical coherent communications, Adaptive optics, Atmospheric turbulence, Phase shift keying (PSK).

Prologue

In the last years free-space optical communications systems for wireless links have been proposed, studied, and implemented mainly due to the higher bandwidth that this technology is able to provide. Still, radio frequency (RF) systems have been maintained in practical wireless communications systems due to the improvement of the microwave sources and the development of high speed electronics. Nowadays the circumstances are changing as a consequence of the increasing data-rate needed in terrestrial and outer space communications. The shift from RF systems to optical communication systems in the free space applications provide a wide set of advantageous characteristics that are motivating the use of these optical technologies in detriment of the RF systems. One of the key reasons is the advantage of working with optical wavelengths in compare to the RF spectral band. As well as the already mentioned increase in the available bandwidth due to the fact that higher optical frequencies directly mean wider bandwidths, the use of optical frequencies lead to a better performance in terms of the received power: for equal antenna sizes the received signal goes inversely as the square of the wavelength. Also, significant advances in the technology for fiber-optic communication components at 1.5-micron wavelength, that may be applicable to free-space optical communications systems, are motivating a transitioning to optical communications for wireless applications. Of the most interest, recent coherent optical communication systems address modulation and detection techniques for high spectral efficiency and robustness against transmission impairments.

Coherent detection is an advanced detection technique for achieving high spectral efficiency and maximizing power or signal-to-noise (SNR) efficiency, as symbol decisions are made using the in-phase and quadrature signals, allowing information to be encoded in all the available degrees of freedom. As a consequence of this technical reality and its potential achievements, the first proposed objective of this project is to develop and demonstrate the coherent optical infrastructure necessary to produce robust high-capacity free-space optical communication links over the 1.5-micron wavelength spectral band.

In this context, the effects of Earth's atmosphere must be taken into account. As the interaction of electromagnetic waves with the atmosphere at optical frequencies is stronger in optical frequencies than at RF frequencies, it is important to show how the atmosphere influences the performance of laser communication systems. Turbulence-induced wavefront distortions that affect the transmitted beam responsible for deterioration of the link bit error rate (BER) can be mitigated with adaptive optics. The use of adaptive optics to mitigate turbulence-induced phase fluctuations in links employing coherent (synchronous) detection is poised to reduce performance penalties enabling a more capable next generation of free-space

optical communications. In this work we describe the implementation of an optical coherent receiver that uses phase compensation with adaptive optics techniques, as well as digital architectures for signal processing and control. The experimental set-up proposed reduces the complexity and the cost of the adaptive optic system while it provides effective wave-front correction, which could potentially benefit many applications through turbulence optical channels.

In order to evaluate the performance of adaptive optical systems in a laboratory a method for generating wavefront aberrations is required. For that, the use of a real atmospheric link or the implementation of a specific source that generates a distorted wavefront, which has characteristics close to those produced by real atmospheric turbulence, becomes mandatory. In our project one of the objectives is to study how to produce deterministic aberrations in order to have a complete knowledge of the aberration introduced. For that, binary computer-generated holograms (BCGH) using micro-electrical-mechanical system (MEMS) is proposed, studied and implemented. The fact that we can introduce deterministic aberrations allows us to perform a comparison between wavefront sensor and wavefront sensor-less architectures.

Finally, the feasibility of FSO coherent systems working with adaptive optics is demonstrated and the system performance in terms of the BER is experimentally evaluated under the influence of atmospheric turbulence. The experimental results are compared to the theoretical models for the performance of synchronous receivers under atmospheric turbulence. The viability of the approach to improve the system efficiency and sensitivity of coherent receivers is experimentally demonstrated.

Summarizing, the purpose of the project is to evaluate the performance and assess the feasibility of using adaptive optics to mitigate deleterious atmospheric effects and hence to improve the reliability of high data-rate FSO optical communications systems. Key in this project is to advance coherent optical communications in terms of its use of phase information for providing scalable channel capacity, increasing link availability, and providing for complex modulation formats.

Acknowledgements

The work presented in this thesis was carried out in the Optical Communications Research Group within the Signal Theory and Communications department at the Polytechnic University of Barcelona. The work was funded by the Spanish Department of Science and Innovation MICINN Grant No. TEC 2009-10025 and the Spanish MEC Secretary of State for Universities and Research Grant Fellowship, both which are gratefully acknowledged.

I would like to thank my thesis supervisor, Professor A. Belmonte, for his advice, guidance and support, and for giving me the opportunity to undertake my studies within his research group in the first place.

I thank my family, especially my parents for their constant support over all these years and to all my friends, which have been the best possible amusement during this period.

Declaration

I declare that this thesis is based on the results found by myself. Materials of work found by other researcher are mentioned by reference.

Esdras Anzuola Valencia

March 2015

Table of Contents

List of figures

List of Tables

Glossary of Abbreviations

ADC	Analog- to-Digital Converter
AO	Adaptive Optics
ASK	Amplitude Shift Keying
AWG	Arbitrary Waveform Generator
AWGN	Additive Gaussian Noise
BD	Balanced detection
BER	Bit Error Rate
BPF	Band-Pass Filter
BPSK	Binary Phase-Shift Keying
BS	Beam Splitter
BW	Bandwidth
CCD	Charge-coupled Device
CDF	Cumulative Distribution Function
CMRR	Common Mode Rejection Ratio
CohD	Coherent Detection
CW	Continuous Wave
DAC	Digital-to-Analog Converter
DD	Direct Detection
DM	Deformable Mirror
DMD	Digital Micro-mirror Device
DPSK	Differential Phase-Shift Keying
DSP	Digital Signal Processing
DWS	Direct Wavefront Sensing
FF	Feed Forward
FPGA	Field Programmable Gate Array
FSM	Fast Steering Mirror
FSK	Frequency Shift Keying
FSO	Free Space Optical
Gbit/s	Gigabit Per Second
GSa/s	GigaSample Per Second
ISI	Inter Symbol Interference

IM/DD	Intensity Modulation with Direct Detection
LC	Liquid Crystal
LMS	Least-Mean-Square
LO	Local Oscillator
MEM	Micro Electrical Mirror
ML	Maximum Likelihood
MOEM	Micro Optical Electrical Mirror
MZ	Mach-Zehnder
OPLL	Optical Phase-Locked Loop
OTG	Optical Turbulence Generator
PBS	Polarization Beam Splitter
PDF	Probability Density Function
PLL	Phase-Locked Loop
PM	Phase Modulator
PolPSK	Polarization Phase Shift Keying
PSD	Power Spectral Density
QAM	Quadrature Amplitude Modulation
QPSK	Quadrature Phase-Shift Keying
RF	Radio Frequency
SER	Symbol Error Rate
SM	Single Mode
SNR	Signal-to-Noise Ratio
SLM	Spatial Light Modulator
SPGD	Stochastic Parallel Gradient Descendent
TI	Texas Instruments
VCO	Voltage Controlled Oscillator

Glossary of Symbols

A_d	Differential Gain
A_s	Common Gain
E_S	Transmitted Optical Field
P_S	Transmitted Optical Power
w_S	Transmitted Optical Frequency
$\emptyset_S$	Transmitted Optical Phase
E_{LO}	Local Oscillator Optical Field
P_{LO}	Local Oscillator Optical Power
w_{LO}	Local Oscillator Optical Frequency
$\emptyset_{LO}$	Local Oscillator Optical Phase
I_{het}	Heterodyne Intensity
w_{IF}	Intermediate RF frequency
$I_{het,I}$	In-Phase Heterodyne Intensity
$I_{het,Q}$	Quadrature Heterodyne Intensity
$I_{hom,I}$	In-Phase Homodyne Intensity
$I_{hom,Q}$	Quadrature Homodyne Intensity
I_{sh}	Shot Noise Intensity
S_{sh}	Shot Noise Power Spectral Density
R	Responsivity
$\emptyset_{RF}$	Radio Frequency Signal Phase
$\overline{n_r}$	Number of detected photons per symbol
BW	Bandwidth
M	Modulation Order
f_{BP}	Band-pass central frequncy
$Z(t)$	Complex reconstructed signal
$\emptyset_{est,LO}$	Estimated low-pass filtered phase
τ	Coherence time
$\Delta\vartheta$	Laser Linewidth
σ_φ	Phase variance
f_S	Symbol frequency
Z_n^m	Zernike Polynomial for n and m (azimuthal and radial orders)
N_n^m	Normalization Zernike Factor

$R_n^{\|m\|}$	Radial Polynomial
W	Aberrated wavefront
a_i	Zernike i mode weight
A	Wavefront amplitude
$\boldsymbol{\lambda}$	Wavelength
C_n^2	Turbulence structure parameter
T	Temperature
C_T	Temperature structure constant
h	Observation height
V_{RMS}	RMS Wind velocity
H_{GS}	Ground station height
r_0	Fried Parameter
D	Telescope diameter
d_{airy}	Airy pattern diameter
f	Focal Length
X_i	Noise for the i^{th} Zernike mode
Δ_j	Kolgomorov residual errors
$D/r0$	Normalized turbulence strength
$r0$	Coherence length
α	Angular modulation angle
G	Interference pattern recorded on a hologram
K	Wave number
T_0	Amplitude transmittance of a hologram
T	Transmittance modulation parameter
$\emptyset$	Wavefront phase
q	Parametric hardclipping function for binary holography
T	Period
δ	Relative fringe location
dx_p	Pixel size
B	Incident angle
U_i	Difracted order i
S_i	Symbol i
N_x	Number of pixels in x axis
N_y	Number of pixels in y axis
$\bar{e}$	Mean error

σ_{tilt}	Atmospheric tilt standard deviation
M_{tilt}	Maximum atmospheric tilt
σ_{DM}	Tilt corrected standard deviation
f_{TG}	G-tilt frequency
f_{DM}	Deformable mirror frequency rate
J	Signal metric
G	Perturbation Gain
dQ	Perturbation size
η	Quantum efficiency
e	Electron charge
h	Planck constant
σ_{noise}^2	Noise power
γ_{het}	Heterodyne efficiency
$\Delta\varphi$	Corrected wavefront residual phase
erfc	Complementary error function

Dedication

To Elena and Esdras,

1 Introduction

This chapter describes the background, main motivations and objectives of this thesis work. First, a description of the background and challenges on free-space optical (FSO) systems is presented. Then, the main advantages of coherent detection are introduced and a brief summary of the specific issues related to coherent FSO is presented. The motivation for using adaptive optics (AO) in these systems is also addressed. Finally, the objectives and thesis outline are described.

1.1 Introduction to Free Space Optical Coherent Communications Systems

1.1.1 Motivation for Free-Space Optical Systems

Free-space optics (FSO), sometimes called optical wireless, refers to the transmission of light through the atmosphere for at least some part of the communications channel. This can include terrestrial, terrestrial-satellite, terrestrial-aircraft, aircraft-aircraft, and outer space communications. FSO communications systems for atmospheric links have been proposed, studied, and implemented for many years. The breakthrough of optical sources in the early 1960s motivated the growth of practical FSO systems [1]. The first study on FSO systems was performed in 1968 by Dr. Kube "Information transmission by light beams through the atmosphere," [2]. Also in 1968, the first FSO system was implemented by using frequency modulation and optical heterodyne downconvertion [3], which showed the receiver sensitivity improvement of coherent detection. In 1970, the first commercial FSO communication system was developed [4]. Since then, FSO has been continuously studied and used mainly in military and deep-space communications [5], [6]. Even though most of the technical problems associated with optical communication systems have been solved, advances in microwave sources and high-speed electronics have maintained traditional RF systems as the technology of choice for wireless communications systems designers. This situation is now changing motivated by the significant advantages of FSO systems over traditional RF and microwave systems. The main advantage of

FSO systems is that they can provide high data-rates due to the use of optical frequencies, implying higher carrier frequencies, which allow higher modulation bandwidths and increased information capacity of the system [7]. Moreover, the use of communications at the wavelength of light also provides a set of advantages in compare to the use of RF bands, which can be demonstrated by using basic antenna theory. First, the antenna gain is inversely proportional to the square of the wavelength, so for an antenna with an aperture diameter *D*, the approximation of the gain is given by [8]

$$G \cong \left(\frac{4D}{\lambda}\right)^2 \tag{1.1}$$

So the use of higher frequencies (smaller wavelengths) results into larger antenna gain. In the same way, the transmitted beam width θ_b is proportional to the wavelength by using a first order approximation [8] given by

$$\theta_b \cong \frac{\lambda}{D} \tag{1.2}$$

which implies a lower beam spread, leading to an increase of the power density in the receiver in compare to RF bands. Furthermore, at optical frequencies, these performance gains are obtained with much smaller component sizes, which is a very important consideration in space technologies. Other essential benefits are larger license-free bandwidths, better information security and greater link flexibility [9][10][11]. Also, significant advances in the technology for fiber-optic communication components at 1.5-micron wavelength, that may be applicable to free-space optical communications systems, are motivating a transitioning to optical communications for wireless applications. In Table 1-1 a comparison between FSO and RF communication systems is shown.

In the other hand, the interaction of electromagnetic waves with the atmosphere at optical frequencies is stronger than that at RF frequencies, so the effects of Earth's atmosphere must be taken into account in FSO systems. There are several phenomena that affect the light propagation through the atmosphere. First, a laser beam propagating through the atmosphere may lose its energy due to molecular scattering, molecular absorption, and particulate scattering. As it is widely known, the choice of the transmitting laser wavelength will be generally needed to be restricted to spectral regions of very low atmospheric absorption. These spectral regions, which

are defined by the absence of absorption caused by air molecules and aerosols, are known as optical transmission windows (see Fig. 1-1) [12]. For FSO systems, the main wavelength used are 808 nm (*Si* detectors), 1064 nm (Nd-YAG lasers) and 1550 nm (InGaAs detectors and erbium-doped fiber amplifiers) [13].

Table 1-1. Comparison between FSO and RF communication systems

	FSO	RF
Typical Data Rate	$\sim Gbps$	$\sim Mbps$
Antenna Gain	$\sim f_{opt}^2$	$\sim f_{RF}^2$
Beam Width	$\sim \lambda_{opt}$	$\sim \lambda_{RF}$
Channel Security	High	Low
Networking Architecture	Scalable	Non-scalable
Component Dimension	Small	Large
Degradation Sources	Atmospheric Turbulence	Multipath fading, interferences

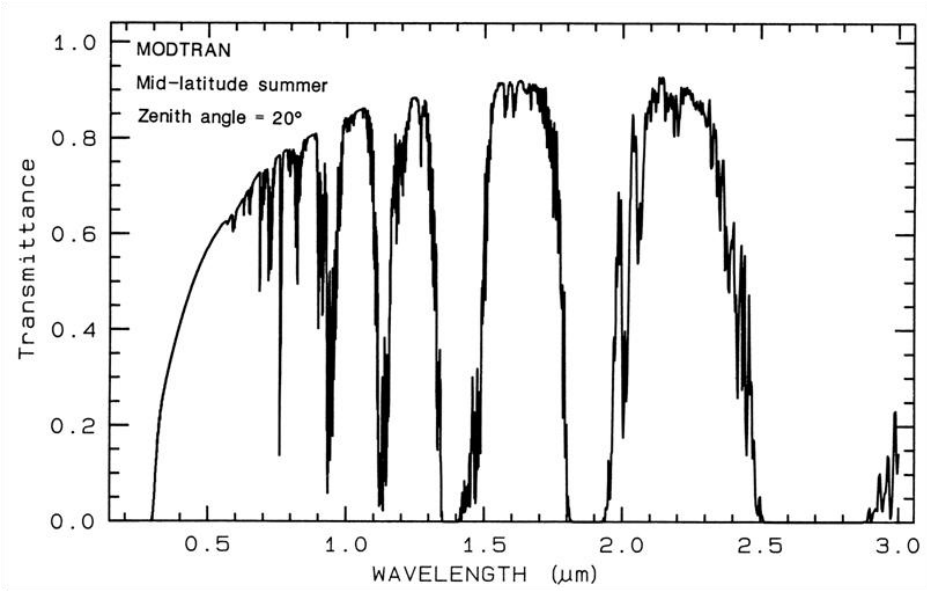

Fig. 1-1. Modeled atmospheric transmittance from visible to near-infrared spectral bands [12][14].

Also, and more importantly, random temperature fluctuations in the air cause variations on the refractive index of the earth's atmosphere [15]. Although the resulting refractive index fluctuations are only a few parts per million, their effect on optical wave propagation in the atmosphere is intense. Even under clear-weather conditions, the turbulence-induced optical phase perturbations are able to devastate the spatial coherence of a laser beam as it propagates through

the atmosphere by distorting the phase front (phase aberration) [16] as well as introducing random perturbation on the signal power (scintillation) [17]. Interestingly, the scintillation strength decreases as the inverse of the wavelength, so these effects can be diminished by operating at longer wavelengths. In this respect, using 1.5-micron wavelength technologies has clear advantages over other lower wavelengths in the visible and infrared bands. The loss of spatial coherence restricts the distance where the laser beam is collimated diminishing the received power levels at the receiver [18]. This fact motivates the detailed study of how the atmospheric effects limit the performance of free space optical systems. One of the main objectives of this thesis is to quantify its effects on FSO systems and develop system configurations and methods that are able to correct, or at least mitigate, the effect of atmospheric fluctuations.

1.1.2 Coherent Detection versus Direct Detection methods in FSO

The first generation of optical communications systems was developed around the early 1970's by the introduction of new technologies related with optical fibers and digital communications [19][20]. This technology rapidly became one of the preferred solutions for point-to-point communications due to its large bandwidth, low attenuation, immunity to interference and high security. For the next 30 years optical fiber systems were put into practice and a series of improvements appeared as a consequence of the severe limitations that these systems suffered in terms of chromatic and modal dispersion. The modulation scheme used during these years was called *intensity-modulation/direct-detection* (IM/DD). The intensity modulation term implies that the information is present only on the intensity or power of the transmitted electrical field. The direct detection term means that the received signal is applied directly to a photodetector. Practical IM/DD systems were widely used between the 1970's and early1990's mainly due to their easy implementation and at the cost of a very poor sensitivity.

Coherent optical communication attracted considerable attentions in the early 1990's, since it can approach the theoretical limit of the receiver sensitivity [21][22]. There were two fundamental advantages of coherent receivers over direct detection receivers; first, they are more sensitive, with the capability of maintaining an specific BER with less photons per bit in compare to the IM/DD systems [23][24]. And second, coherent receivers are more efficient in differentiating adjacent channels from a frequency-division multiplexed signal [25], which is the

key to exploit the large available bandwidth in optical communications. In coherent detection, the received optical signal is added to a local oscillator (LO) signal [26] and the resulting lightwave is translated into an electrical current by using a photodetector, which presents different characteristics depending on the amplitude and phase of both signals [27], opening the door to much more sophisticated schemes. In the other hand, knowledge of the LO phase is required in order to extract information on a coherent system [26]. In those days, experiments on phase-locked loop (PLL) were performed to control the phase of the LO in homodyne systems. However, it was complicated and unstable to use these PLLs in practice [28][29]. As a result, heterodyne detection was introduced to simplify the receiver design and relax the feedback delay of optical PLLs. In heterodyne systems the optical signal is first downconverted into an intermediate frequency (IF), and then an electrical PLL is used to track the phase of the IF signals at microwave frequency [30][31][32]. It can be found that most works were focused on simple modulation formats, such as binary phase shift keying (BPSK), differential phase-shift-keying (DPSK) and amplitude-shift keying, due to the wide laser linewidth and stringent requirement on the loop delay of PLLs [33]. Around the year 2000, the DPSK format was firstly demonstrated in experiments in junction with self-homodyne detection [34]. The self-homodyne receiver consists on Mach-Zehnder delay interferometers (MZDIs), which convert the phase difference between the current optical signal and its one-symbol delayed version into optical intensity, and a pair of balanced photodiodes [35]. The scheme removes the receiver LO laser, which is always present in a typical coherent receiver and, consequently, relaxes the laser linewidth tolerance as the transmitter and receiver sources are the same. Nowadays, recent advances in high-speed electronics and optical devices [36][37] have encouraged extensive researches on coherent optical communication once again. Compared to the early coherent receivers, there are several remarkable differences in current ones. First, high-speed *analog-to-digital converters* ADCs employed in current phase-diversity coherent receivers sample the photocurrents, corresponding to the received optical signals, at the Nyquist rate or above so as to retain full information of the electric field. Since the amplitude and phase information of the received optical signals are preserved, both of them can be modulated simultaneously to increase the system sensitivity and can be further utilized for compensation of linear and even nonlinear channel impairments [38]. Also, with the aid of high-speed electronics in a digital coherent receiver, the carrier estimation can be done applying high-speed digital signal processing (DSP) rather than using optical PLLs allowing for a free-running LO laser. Recent experiments have demonstrated that DSP-based frequency and phase estimation techniques are very effective to recover carrier phase [39].

Table 1-2. Comparison between direct detection and coherent detection methods.

	Direct Detection	Coherent detection
Complexity	Low	High
Degrees of Freedom (per polarization)	1	2
Receiver Sensitivity (Binary)	38 phot/bit (2-PAM)	18 phot/bit (2-PSK)
Receiver Sensitivity (Quaternary)	134 phot/bit	18 phot/bit (4-PSK)
Receiver LO source required	No	Yes
Noise limited	Background/Thermal	Shot noise
Polarization control at the receiver	No	Yes
Synchronization required	No	Yes

In Table 1-2 a comparison between those two detection methods is provided. Most of the actual direct detection (non-coherent) methods implemented use some kind of binary modulation format, which encodes one bit per symbol (on-off, DPSK). These schemes are often preferred in order to minimize the system complexity, especially at the receiver, as they do not require polarization control or synchronization. In the other hand, these architectures require much more photons per bit in compare to the synchronous (coherent) architecture, about one order of magnitude, when they are not background noise limited in order to provide an adequate BER [26]. On the other hand, an important goal of an optical link is to transmit the highest data throughput over the atmospheric channel. Given constraints on the system bandwidth it is important to maximize spectral efficiency. Direct-detection techniques provide good power efficiency at the cost of low spectral efficiencies [26]. This is due to the fact that these systems present a lack of degrees of freedom available to encode the information. In the other hand, coherent detection techniques achieve high spectral efficiency while maximizing power efficiency. In these systems, symbol decisions are made using the in-phase and quadrature signals, allowing information to be encoded in one additional degree of freedom as the receiver estimates the decisions based on the recovery of the complete electric field, containing amplitude and phase information. More importantly, coherent systems provide improved background noise rejection compared to direct detection. One of the main features of coherent detectors is that the receiver is limited only by LO induced shot noise when the power of the LO is sufficiently high. This is a significant difference from the intensity modulation based systems, in which background and/or thermal noise are the dominant noise factors.

The same comparison can be extrapolated to evaluate the performance of these detection methods in FSO systems, with the significant difference that atmospheric effects have to be taken into account. The evaluation of a coherent FSO system performance under the presence of atmospheric turbulence becomes a hard task due to the complexity of the effects that the atmosphere introduces in the transmitted wavefront and the consequences that arise when it is mixed with a local oscillator laser source. In order to maximize the coherent power at the receiver after the mixing stage, the spatial field of the received signal has to match the one of the local oscillator [26]. In the case of atmospheric turbulence, the communication channel introduces variations on the phase and the amplitude of the transmitted signal. The resulting signal after the mixing stage might be severely degraded in case that the atmosphere corrupts the phase and amplitude of the transmitted signal. In this case, so much of the advantage of using a coherent system is eliminated [38]. When no compensation techniques are introduced to balance the effects of the atmosphere, direct detection techniques are more appropriated as a useful matter to minimize system complexity and sensitivity [38], leading to low data-rate communications. Theoretically, adaptive compensation of atmospheric wavefront phase distortions improves the performance of atmospheric communication systems and it can mitigate very efficiently the impact of atmospheric-induced fluctuations on FSO links using coherent detection. The performance improvement when applying wavefront correction at the receiver may lead to consider coherent systems a viable alternative to incoherent modulations. The performance improvement of FSO coherent communications using atmospheric compensation has been widely studied in the literature. Lee and Chan [40] showed the performance improvement of coherent detection over IM/DD detection in lognormal environments by comparing the IM/DD PPM and coherent BPSK FSO systems and demonstrated theoretically that coherent FSO systems can lead to lower error rates. It was also found that coherent detection can provide additional outage probability improvement over direct detection [40]. In [18], Belmonte and Kahn proposed a statistical model considering spatial phase noise with lognormal turbulence and performed a capacity evaluation [41]. In this study, the intention is to elucidate how the addition of optical compensation techniques on the receiver side can reduce the effects of atmospheric propagation and, in so doing, to quantify experimentally the improvement on the performance of optical communications systems regarding coherent detection.

1.1.3 Motivation for Adaptive Optic Systems in FSO

As it has been stated, to maximize the coherent power at the receiver after the mixing stage, the spatial field of the received signal has to match the one of the local oscillator [26]. In the case of atmospheric turbulence, the communication channel introduces variations on the phase and the amplitude of the transmitted signal. The resulting signal after the mixing stage might be severely degraded in case that the atmosphere corrupts the phase and amplitude of the transmitted signal, so, much of the advantage of using a coherent system is eliminated [27]. Turbulence-induced wavefront distortions, responsible for severe wavefront aberrations on the received signal can be mitigated with adaptive optics. The use of adaptive optics to mitigate turbulence-induced phase fluctuations in links employing coherent detection is intended to reduce performance penalties, enabling a more capable next generation of coherent FSO communications by applying phase modulation in order to maximize the downconverted power at the receiver. These active compensation techniques allow increasing the performance of coherent atmospheric communications systems [17].

Table 1-3. Comparison between direct wavefront sensor and wavefront sensorless architectures.

	Wavefront Sensor	Wavefront Sensorless
Cost	High	Low
Requires wavefront sensor	Yes	No
Correction of receiver optic aberrations	No	Yes
Power Efficiency	Low	High
Iterations per correction	1	>>1
SNR dependent	Receiver Plane	Detector plane
Correction under fading channels	No	Yes
Pointing error compensation	No	Yes

An adaptive optic system is composed by optical elements, classically mirrors, which can customize their optical surface in order to compensate the wavefront phase aberrations present on the received signal [42]. Still, the use of adaptive optics has been limited by their considerable complexity and high cost, even if deformable mirrors have been present for many years. These facts limited their application to large and expensive imaging systems, usually used on astronomy. Now, new manufacturing technologies which provide reasonable cost and acceptable efficiencies are appearing [43]. This implies that the use of MOEMS (Micro-Opto-Electro-Mechanical Systems) deformable mirrors is broadening through a wide set of applications that

were intended to be improved by the use of adaptive optics. These devices provide a time-varying surface that modifies the characteristics of the reflected light, being able to eliminate the undesired aberrations associated with atmospheric turbulence.

Typical adaptive optical systems are based on two main architectures depending on the receiver design: direct [44] and indirect wavefront sensing [45]. Before the development of modern wavefront sensors, Muller and Buffington [44], in 1974, proposed image sharpening as a method to correct for aberrated wavefronts. The principle was to maximize a performance metric, in this case the image sharpening, which is directly related to the wavefront aberrations. Still, this method was limited by the low loop rate of the control hardware that drives the active optical elements. In those days, this limitation made it useless for compensating dynamic atmospheric wavefronts. With the arrival of Shack-Hartmann and curvature wavefront sensors, which could achieve higher loop rates, the indirect compensation approaches were neglected. In wavefront sensor architectures, the phase map of the incoming beam is directly measured, so direct commands can be applied to the AO to perform wavefront conjugation. Even if the calculations involved in these architectures are complex, the bandwidth efficiency achieved was high in compare to indirect methods, as the aberrations are almost completely compensated in each loop iteration. Still, several crucial disadvantages make this architecture suboptimal. First, part of the received power has to be re-directed to the wavefront sensor in order to measure the phase wavefront. As these devices typically present low power efficiencies, a significant part of the received power does not arrive to the coherent detector, so the performance of the communication is severely degraded in terms of the SNR after the mixing stage. The situation becomes more intricate in the case where intensity scintillation in the receiver aperture make wavefront measurements difficult and wavefront sensing cannot be used in a direct way for wavefront control. These are situations that easily could be encountered in free-space optical communication links in near-terrestrial environments [26]. Also, these devices present typical frames rates in the order of the tens of Hz, which limits the temporal response of the AO system.

Nowadays, the development of new technologies, which improve the computational time thanks to high speed electronics, are re-emerging the indirect methods as interesting solutions for FSO systems. Here, instead of implementing a phase conjugation by measuring the residual phase error, the phase correction strategy is based on the direct optimization of the system performance metric (received power, image sharpening, etc.) by introducing random fluctuations on the

wavefront and analyzing the resulting output. This approach, known as wavefront sensorless architecture, is determined by two central ideas that define the performance of indirect AO: the high-speed electronics, which define the loop rate of the AO system, and the blind search algorithm selected to perform the maximization process, which defines the number of iterations needed to converge. Problems related with the use of the wavefront sensing technique have encouraged this adaptive system architecture for a wide set of optical applications. Also, the emergence of affordable wavefront correctors based on MOEMS technology and liquid-crystal (LC) phase modulators provide the potential to define fast, small, and inexpensive adaptive systems which can eliminate the problems associated with the wavefront sensor architecture. Moreover, the development of capable blind search algorithms offers efficient signal processing architectures for adaptive optics applications.

For FSO communications applications there can be additional advantages of using wavefront sensorless architectures. The most intuitive one is that a wavefront sensor is not required, so the complexity and cost of the system is reduced. Then, information about the received power is available at the coherent detector and can be used as performance metric for the blind search algorithms. Also, this technique can be very useful to provide fine pointing and tracking procedures due to the fact that any failure of these stages is translated into a decrease of the receiver power used as performance metric [26]. Also, the wavefront sensorless technique can be used for compensate optical aberrations in the optical receiver system. In the other hand, the wavefront sensor architecture only considers the wavefront in the aperture plane, so any aberration introduced by the optics behind cannot be corrected. It is important to note that, in a wavefront sensorless architecture, the quality (or SNR) of the performance metric might affect the convergence of the optimization algorithm, leading to an efficiency loss.

New advances in technology are moving forward the implementation and generalization of wavefront sensorless architectures: improved and new efficient control algorithms, implementation using parallel processing hardware based on field programmable gate arrays (FPGAs), and the emergence of high-bandwidth wave-front phase controllers. All these new techniques allow considering this architecture as a promising technique for adaptive optic systems.

1.2 Thesis Objectives

FSO communications are emerging as a key technology to provide high data-rate links in the free-space data networks. Recent theoretical studies and experimental results [18][16] successfully showed that FSO technologies are close to be prepared to be implemented in practical systems. FSO networks will support the multi-gigabit data rates required by future optical networks only through coherent systems, which are able to modulate both the I and Q channels of a carrier, increasing the spectral efficiency of the communication system. Still, as the communication is performed through the atmospheric turbulent channel, serious distortions degrade the amplitude and phase of the received wavefront, leading to a performance loss on FSO systems. Fortunately, fading effects can be significantly reduced by the use of coherent systems, which present significant advantages in terms of power efficiency by mixing the incoming wavefront with a LO source at the receiver. In the other hand, coherent systems are much more susceptible to phase wavefront distortions as they degrade the mixing efficiency of the coherent receiver [18]. The use of affordable AO techniques has been proposed as an effective method to mitigate turbulence-induced signal fluctuations on coherent systems. These compensation techniques based on AO are being contemplated from a theoretical and experimental perspective as an attractive approach to mitigate atmospheric effects. The immense challenge now is to engineer the coherent FSO wireless networks in the presence of atmospheric turbulence and weather so it will behave properly. The aim of this project is to address experimentally this two related research problems, coherent communications and adaptive optics, as they have became essential for the development of the next generation of advanced FSO communication systems.

The central theme of this thesis is to advance the understanding and experimental demonstration of atmospheric coherent FSO systems. In general terms, this involves: (1) developing system-analytic models for propagation, detection, and communication scenarios; (2) using these models to derive the fundamental limits on FSO coherent system performance; and (3) identifying, and establishing through experimentation the feasibility of the techniques and devices which can be used to approach these performance limits. The objectives are based on the project funded by the Spanish Department of Science and Innovation MICINN Grant No. TEC 2009-10025, whose proposal is described in [46] and they can be summarized as follows:

1. Develop theoretical and experimental understanding of the performance of optical coherent transceivers using complex modulation and detection techniques for high spectral

efficiency and robustness against transmission impairments in optical coherent systems. Crucial advances in the technology for fiber-optic communication components at 1.5-micron wavelength, that can be applicable to free-space optical communications systems, are motivating a transitioning from direct detection methods to coherent optical communication systems in FSO systems. Therefore, it is essential to develop and demonstrate the coherent optical infrastructure necessary to produce robust high-capacity optical communication links over the 1.5-micron wavelength spectral band. Moreover, new digital processing (DSP) techniques and high-speed electronics have encouraged the development coherent receivers based on digital compensation methods that mitigate transmission impairments and perform new carrier phase-synchronization methods applicable to optical systems. As a result, a first engineering prototype for a fully functional optical coherent transceiver must be designed and implemented using commercially available devices. This task will describe and develop the optical terminals, electronic systems and digital signal processing techniques that define our coherent system, characterizing the different key parameters involved in the system performance: transceivers design, modulation and coding techniques, impairment compensation and system performance. Through this process, we will refine component and subsystem-level specifications in order to meet the system performance requirements.

2. Provide the theoretical background to quantify the loss of performance of simple, coherent diffraction-limited systems in the presence of atmospheric turbulence and elucidate those implications of the propagation that bear on the design and performance of coherent FSO systems. For that, the atmospheric turbulent channel basics are described and the work performed by the Free-Space Optical Communication Group at the UPC providing analytical models for the performance of coherent FSO under atmospheric turbulence is presented [18].

3. Investigate methods for introducing key atmospheric impairments to evaluate coherent FSO under atmospheric turbulence. In order to characterize different types of adaptive optical systems and analyze the performance of FSO coherent systems under atmospheric turbulence, an optical turbulence generator (OTG) that introduces optical aberrations which presents characteristics close to the atmospheric turbulence becomes suitable in the laboratory. The main advantages of using an OTG is that they allow us to carry out a performance analysis of AO and coherent FSO systems without the necessity of a real atmospheric link, saving telescope time and not being limited by the specific atmospheric condition at a certain time. Also, the capability of

introducing deterministic aberrations leads to essential advantages when evaluating these systems. In this work we perform a comparative between the different existing methods to generate atmospheric wavefronts, including wind chambers, phase screens, moving plates and spatial light modulators (SLMs). In this project we present a novel technique based on the use of binary digital micro-mirror devices (DMD), a recently developed technology based on binary amplitude modulation, which, in junction with binary computer-generated holography (BCGH), is demonstrated to provide wavefront phase modulation by just modifying the amplitude of the incoming light. The main advantage of this technique is that DMDs are commercially available for a fraction of the cost of a phase-only SLM. In this study we also analyze the limits and performance of this novel technique on emulating atmospheric wavefront aberrations. The proposed method and results were submitted to be published in [47].

4. Establish, through analysis and active experimentation, how the addition of AO architectures on the receiver can reduce the effects of atmospheric propagation. First, we will present the basics of AO systems and perform a comparison between two different adaptive optics methods: direct wavefront sensing and wavefront sensorless architectures. The fact that we are able to introduce deterministic aberrations through an OTG implies that the receiver has a complete knowledge of the aberrated wavefront phase, allowing us to perform conjugated compensation, emulating the performance of an ideal wavefront sensor. Also, we will investigate a non-conventional adaptive optics approach, know as wavefront sensorless architecture, which has certain advantages with respect to its incorporation into FSO communication terminals. This technique does not required wave-front measurements, which are difficult to achieve under the strong scintillation conditions, typical for communications scenarios. Instead, it is based on the direct optimization of a performance metric, such as the signal strength, together with an appropriate optimization algorithm. Then, we plan to define, implement and test a working AO to mitigate turbulence-induced phase fluctuations. A first integration of the phase wavefront compensation system, control algorithms, and its interface with the coherent optical receiver will be performed. Then, we will define the proper experimental system arrangement and components to evaluate the performance of the AO system by introducing aberrations by means of the OTG implemented. Both AO techniques will be experimentally evaluated, describing the advantages and disadvantages of each compensation scheme.

5. In the last step, the objective is to integrate the coherent transceiver, the FSO stage and the OTG stage to evaluate and quantify experimentally the performance achievable in FSO coherent optical systems using atmospheric compensation techniques and describe the performance limitations, with regard to atmospheric conditions. Very importantly, our experiments will entail to compare the experimental performance of coherent FSO systems against the theoretical models recently developed in the literature, where extensive research on fundamentals of the performance of synchronous receivers using atmospheric compensation techniques have been provided [18]. The method and experimental results related to the performance of coherent FSO achieved were submitted in [49].

1.3 Thesis Outline

This thesis is divided in six chapters, including this introduction chapter. In chapter two the design and implementation of an optical coherent communications system is presented. This chapter is based on the experimental set up developed to obtain my Masters degree. First, a brief theoretical introduction is intended to show the basics of optical coherent communications. Then, the main detection methods (coherent and non-coherent) used in optical communication systems are presented, as well as a description of the modulation formats used and the bit-error-rate associated to each one under AWGN. A coherent communication set-up on fiber is designed, involving hardware specifications and compensation stages. Then, a QPSK heterodyne system is implemented and its performance evaluated and compared against the theoretical models.

In chapter three we describe the fundamentals of atmospheric turbulence and its effects on laser beam propagation. The Kolmogorov theory of turbulence, as well as the Zernike polynomials and Noll's phase fluctuation model are presented. Then, the effects of phase fluctuations over FSO systems are addressed by modelling the resulting mixing efficiency under atmospheric turbulence. For simulating in the laboratory the influence that the turbulent atmosphere has on light beams, we introduce a practical method for generating atmospheric wavefront distortions that considers digital holographic reconstruction using a programmable micromirror array. We present the theoretical background of the method and we analyze the limits of the approach for different configurations of the micromirror array. An experimental set-up is then implemented in order to demonstrate the benchtop technique experimentally.

In chapter four we present the principles of AO systems, the main architectures used and the spatial and temporal requirements for its application on real systems. Then we perform an experimental implementation of a wavefront sensor-less optical system driven by a blind search algorithm, the parallel gradient descendent algorithm (SPGD), and we study its performance under different SNR scenarios and system parameters. Then, the AO is used to compensate phase wavefront distortions introduced by the OTG implemented in the previous chapter and its performance is evaluated under different turbulent strength scenarios.

In chapter five the objective is to develop theoretical understanding and experimental demonstration of the coherent communication performance achievable by using AO under atmospheric turbulence as well as validate the theoretical models with experimental results. We first introduce the model developed in [18], which describe the performance of synchronous receivers under atmospheric turbulence. Then, we develop an experimental set-up that involves the fiber coherent system, the OTG and the AO system, which have been described in previous chapter. The coherent FSO system performance is then experimentally evaluated using two different techniques: the full optimal compensation and the wavefront sensorles architecture using the SPGD algorithm. The resulting SERs are obtained and the experimental results are compared against the theoretical model.

Finally, in chapter six the main results and conclusions are summarized, including comments and recommendations for future research projects.

2 Optical Coherent Communication Systems

In this chapter the design and implementation of an optical coherent communications system is presented. This chapter is based on the experimental set up developed to obtain my Masters degree [48]. First, a brief theoretical introduction is intended to show the basics of optical coherent communications. Then, the main detection methods (coherent and non-coherent) used in optical communication systems are presented, as well as a description of the modulation formats used and the bit-error-rate associated to each one under AWGN. A coherent communication set-up on fiber is designed, involving hardware specifications and compensation stages. Then, a QPSK heterodyne system is implemented and its performance evaluated and compared with theoretical models.

2.1 Principles of Optical Coherent Systems

In order to fully understand the principles of coherent detection we cover some of the main ideas related to optical communications. These basic concepts allow us to further describe in detail the different optical detection architectures by describing the theoretical limits of direct and coherent detection methods, the noises involved in optical communications and the main mixing structures for coherent detection methods.

2.1.1 Quantum Limit and Super Quantum limit

In order to study the maximum achievable performance of optical systems we introduce the concept of *quantum limit* and *super quantum limit*. These boundaries provide a theoretical limit and reference to evaluate the performance of non-coherent and coherent communications systems. A beam light is an electromagnetic radiation that can be represented by either its electric or magnetic field. In [19] it was shown that the power of a wave is proportional to the product of the amplitudes of these fields, which imply that the amplitude is proportional to the square root of the power. Considering a monochromatic lightwave as:

$$E_S = \sqrt{P_{in}} \cdot exp(jw_o t) \tag{2.1}$$

where $|E_S|^2 = P_{in}$ is the average power and w_o is the frequency. At optical frequencies quantum-mechanical effects cannot be considered negligible and the fact that the light is actually a stream of particles called photons becomes important. Considering a light whose output is given by Eq. 2.1, the average number of photons emitted per second is:

$$N_p = \frac{2\pi P_{in}}{h\, w_o} \tag{2.2}$$

The precise moment that a photon is emitted from the light source cannot be exactly predicted. In fact, the emission times of the photons are randomly distributed according to a Poisson process. Let's consider a direct detection communication system where we count the number of photons in an interval of T seconds and decide that we have received a '1' when the number of counted photons is above zero. In this case, when a '0' is transmitted, the probability of receiving any photon is exactly zero. In the other hand, if a '1' is transmitted, the photons arrive according to the Eq. 2.2. So, the probability of receiving N photons in T second is given by the Poisson distribution [19]:

$$P(N|'1') = \frac{(N_p T)^2 exp\ (-N_p T)}{N!} \tag{2.3}$$

Therefore, there might be no received photons when a '1' is transmitted. This effect leads to a bit error ratio (BER) of [19]

$$BER = \frac{1}{2} exp\ (-N_p T) \tag{2.4}$$

where $N_p T$ is the expected number of received photons when transmitting a '1' bit ($\overline{N}$). The resulting BER in Eq. 2.4 is an important lower bound called the *quantum limit*. This limit indicates a minimum signal power required by a communication system to achieve a certain BER and represents a fundamental limit on the performance of optical detectors. It is also regularly used as an indicator to compare the sensitivity of any receiver architecture.

For coherent systems, it has been demonstrated that, in theory, the best performance that can be achieved is by defining a local oscillator that exactly matches the received signal field in every way [19]. The incoming lightwave and the LO have the same amplitude, polarization, frequency and the LO is exactly in phase with the received signal during a '1' and exactly out of phase during a '0'.

The resulting effect is that the optical fields are combined destructively in the photodetector when the received symbol is out of phase with the LO, so no photons arrive at the photodetector. When the received symbol is in-phase with the LO they combine constructively at the photodetector producing twice as photons. The BER performance for this quantum-optimum receiver for binary signaling can is given by [27]

$$BER = \frac{1}{2}\left\{1 - \sqrt{1 - exp\,(-4N_pT)}\right\} \tag{2.5}$$

which is asymptotically equal to

$$BER = \frac{1}{2} exp\,(-4N_pT) \tag{2.6}$$

The resulting number of photons required to achieve a BER equal to 10^{-9} is only 5 photons and is known as *super quantum limit* [27]. This implies a 3 dB better BER performance than an ideal optical homodyne receiver for binary PSK based on maximum-likelihood detectrion, expressed as [19]

$$BER = Q\,(\sqrt{4N_pT}) \tag{2.7}$$

where $Q(x)$ is the is the tail probability of the standard normal distribution [27]. These quantum optimum receivers are not realizable, but they are important theoretical constructions that provide a boundary on the receiver performance of coherent systems.

2.1.2 Noise in Optical Communications

In any optical receiver the incident optical power, P_{in} in Eq. 2.1, must be translated into an electrical current by means of a photodiode. Unfortunately, an ideal photon counter, like the one described in the previous section, cannot be constructed as real photodetectors introduce additional noise. The objective of this section is to describe the noise factors that affect the receiver performance for, then, discuss the signal-to-noise ratio (SNR) in optical receiver.

In optical communications systems the electrical current at the output of a photodetector in the absence of optical amplification is composed by [50]:

$$I(t) = I_s(t) + i_b(t) + i_d(t) + i_{sh}(t) + i_T(t) + n_e(t) \quad 2.8$$

where the photocurrent $I_s(t) = RP_{in}$ represents the electrical current converted from the incoming lightwave E_S and $R = \eta q/(hv)$ is the responsivity defined in [21], h is the Planck constant, v the frequency, η the quantum efficiency of the photodetector, $i_b(t)$ is the undesired background noise, $i_d(t)$ is the dark current, $i_{sh}(t)$ is the shot noise current, $i_T(t)$ is the intensity associated to thermal noise, and $n_e(t)$ is the total noise in the receiver circuit. The general case in communication systems is that the background noise and dark current can be considered negligible in compare to the thermal noise, dominant in most of practical IM/DD systems [21], and shot noise, made dominant in coherent systems by the use of a sufficiently large local oscillator [21].

The shot noise is an effect of the fact that an electric current consist of a stream of electron that are generated at random times. Firstly studied by Schottky [51] in 1918 it has been widely studied since then [52][53]. Mathematically, the current fluctuation related to shot noise $i_{sh}(t)$ is a stationary random process with Poisson statistics and usually approximated by a Gaussian statistics. The autocorrelation function of $i_{sh}(t)$ is related to the spectral density $S_{sh}(f)$ by the Wiener-Khinchin theorem [53]

$$< i_{sh}(t) i_{sh}(t+\tau) >= \int_{-\infty}^{\infty} S_{sh}(f) exp\ (2\pi i f \tau) df \quad 2.9$$

where the angle brackets denote an average over fluctuations. The shot noise is a white noise, so its resulting two-sided spectral density is constant and is given by $S_{sh}(f) = qI_s$. When only positive frequencies are considered by changing the lower limit of integration to zero, the one sided spectral density becomes $2qI_s$. To obtain the noise variance we have to set $\tau = 0$ in Eq. 2.9:

$$\sigma_{sh}{}^2 =< i_{sh}{}^2(t) >= \int_{-\infty}^{\infty} S_{sh}(f) df = 2qI_s \Delta f \quad 2.10$$

where Δf is the effective noise bandwidth of the receiver and depends on the receiver design. Since the dark current $i_d(t)$ also generates shot noise, its contribution must be included in Eq. 2.10 by replacing I_s by $I_s + i_d$, so the total shot noise is given by:

$$\sigma_{sh}{}^2 = 2q(I_p + i_d)\Delta f \quad 2.11$$

The thermal noise is a fluctuating current effect due to the random movements of the electrons in any conductor at a finite temperature. Mathematically, the current produce by the thermal noise $i_T(t)$ is modeled as a stationary Gaussian random process with a spectral density that is frequency independent and is given by

$$S_T(f) = \frac{2k_B T}{R_L} \tag{2.12}$$

where k_B is the Boltzmann constant, T is the temperature in Kelvin and R_L is the load resistor in the front-end of an optical receiver. Similarly to the shot noise, the noise variance of $i_T(t)$ is given

$$\sigma_T{}^2 = < i_T{}^2(t) > = \int_{-\infty}^{\infty} S_T(f)df = \frac{4k_B T}{R_L}\Delta f \tag{2.13}$$

where Δf is the same effective noise bandwidth that appeared on the shot noise. It is important to note that $\sigma_T{}^2$ does not depends on the received signal. Since $\sigma_{sh}{}^2$ and σ_T^2 are independent we can consider them separately. The resulting total variance of current fluctuations can be then expressed as: $\sigma_{tot}^2 = \sigma_{sh}{}^2 + \sigma_T^2$, obtaining

$$\sigma_{tot}^2 = \sigma_{sh}{}^2 + \sigma_T^2 = 2q(I_p + i_d)\Delta f + \frac{4k_B T}{R_L}\Delta f \tag{2.14}$$

One of the main communication parameters to evaluate the performance of an optical receiver is the SNR and it is defined as the average signal power versus the noise power. The resulting SNR expression obtained by using Eq. 2.14 and Eq. 2.8 in the absence of background noise and dark current is

$$SNR = \frac{(RP_{in})^2}{2qRP_{in}\Delta f + \frac{4k_B T}{R_L}\Delta f} \tag{2.15}$$

The thermal noise limit is achieved when $\sigma_T^2 \gg \sigma_{sh}^2$, and SNR can then be expressed as

$$SNR_T = \frac{R_L(RP_{in})^2}{4k_B T\Delta f} \tag{2.16}$$

It can be seen in Eq. 2.16 that the SNR depends on $P_{in}{}^2$ in the thermal noise-limit. By increasing the load resistance we can also improve the SNR. This is why the use of high-trasimpedances is extended in most of optical receivers. If we consider that $\sigma_{sh}^2 \gg \sigma_T^2$ the resulting SNR is

$$SNR = \frac{RP_{in}}{2q\Delta f} \tag{2.17}$$

So, in the shot noise limit, the SNR increase with P_{in}. This expression can be written in terms of the number of photons per bit N_p by considering that

$$P_{in} = \frac{N_p}{h\nu B} \tag{2.18}$$

where B is the bit rate. If we take a typical value for the bandwidth ($\Delta f = B/2$) the SNR per bit in a shot noise limited scenario is given by

$$SNR_{b,sh} = \eta N_p \tag{2.19}$$

This means that, in order to achieve a SNR of 20 dB, around 100 are needed just for the shot-noise limit (Eq. 2.19) while several thousand photons would be required in the thermal-noise limit (Eq. 2.16).

2.2 Optical Detection Methods

As it has been previously stated, in optical communications there are two major kinds detection methods: direct detection (DD) and coherent detection (CohD) [55]. The direct detection is so named because the incoming signal is detected directly with the photodiode which is the element in charge of converting the optical power into a current. With the direct detection only the amplitude of the signal can be obtained, losing its phase. On other hand, for coherent detection the incoming light wave is mixed with other light beam coming from the local oscillator (LO) before being detected by the photodiode. The signal detected by the coherent detector preserves both the amplitude and the phase of the signal. For coherent detection there are two basic schemes depending on how the downconvertion from optical frequencies to baseband frequencies is performed [55]. These schemes are called heterodyne detection and homodyne detection. In homodyne detection the local oscillator is tuned so that the output of the optical mixer is at baseband frequencies. In heterodyne detection, a signal of interest at some frequency is non-linearly mixed with a reference LO source that is set at a close-by frequency. The outcome is centered at the difference frequency, which carries the information in amplitude, phase or frequency of the original higher frequency signal, but oscillating at intermediate carrier frequency

which can be handled easily. The translation to baseband frequencies can be performed then using electrical techniques or numerical methods after analog to digital conversion.

Coherent systems have several advantages over direct detection systems, but for many years it has not been developed or used due basically to two reasons: the complexity of the optical and digital systems used in coherent communications and the reasonable bandwidth provided by the direct detection, enough for the requirements of many applications. Coherent optical detection systems present important potential advantages over direct detection methods: a greater wavelength selectivity, increased sensitivity in the reception stage [55], greater distances in optical links [56], higher spectral efficiencies [57] and so on (see section 1.1.2).

During the mid-80's and 90's of last century there was a great activity on the research and development of optical coherent communications systems, which decreased gradually due mainly to the appearance of optical amplifiers and to the great technological limitations imposed by phase noise of optical sources [58]. Recently, however, has revived the interest in such systems [59], on a quest to increase the capacity and in view of new technological developments in the area of optical sources, balanced photoreceptors, digital processing of high-speed signals [60] and applying innovative techniques of coding and synchronization. The current trend in coherent optical communications is primarily oriented to the digital processing and compensation of phase perturbations in optical systems with phase modulation [61] [62]. In this section we describe the system model and equations that characterize each one of these systems.

2.2.1 Non-coherent detection

In non-coherent detection, or direct detection (DD), the information is extracted by the receiver based on the measurement of the signal energy. The simplest and widely used direct detection method is the on-off-keying (OOK) using a simple photodiode (Fig. 2-1). Here, the incoming optical signal $E_s(t)$ is directly detected with a photodiode, which converts the optical power into a current $I_p(t)$. Two zero-mean white Gaussian additive noises are then added, n_{sh} and n_T, representing the shot noise and thermal noise and respectively. For our purposes, it is enough to model the noises as it was explained in the previous section. The resulting current $I(t)$ is then integrated over an specific period of time and a symbol decision block generates the demodulated symbols S_i. Mathematically we can express $I(t)$ as

$$I(t) = R|E_S|^2 + n_{sh}(t) + n_T(t) \qquad 2.20$$

The zero-mean Gaussian processes are expressed using the Eq. 2.10 and Eq.2.13. To compute the signal produced by the integrator we first need to re-scale $I(t)$ by *1/q* to compute the means and variances of

$$y = \frac{1}{q}\int_0^T I(t)dt \qquad 2.21$$

Applying the *maximum likelihood* (ML) function [54] in the decision block, the receiver minimizes the BER by selecting the symbol S_i that maximizes the likelihood function. The resulting BER for a realistic IM/DD system can be expressed as [54]

$$BER = Q\left(\frac{M/\sigma_0}{1+\sqrt{1+M/{\sigma_0}^2}}\right) \qquad 2.22$$

Where $M = \eta|E_S|^2T/hv$ is the mean number of detected photons for the bit '1', ${\sigma_0}^2 = 4k_BT/R_Lq^2$ is the variance for y conditioned on sending a '0' [21] and Q is the Gaussian function defined in [63]

$$Q(\rho) = \int_\rho^\infty \frac{1}{\sqrt{2\pi}} exp\ (-x^2/2)dx \qquad 2.23$$

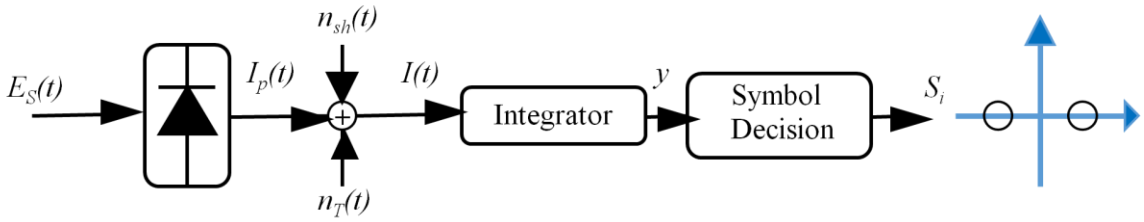

Fig. 2-1. Direct detection receiver scheme. The incoming optical signal $E_s(t)$ is directly detected with a photodiode, which converts the optical power into a current $I_p(t)$. Two zero-mean white Gaussian additive noises are then added, n_{sh} and n_T, representing the shot noise and thermal noise and respectively. The resulting current $I(t)$ is then integrated over an specific period of time and a symbol decision block generates the demodulated symbols S_i.

To encode more than one bit per symbol, other modulation formats are present: multi-level amplitude shift keying (ASK), frequency-shift keying (FSK) with wide frequency separation between carriers and so on. The main limitation of non-coherent detection is that the detection is only based on energy measurements, so the information can only be encoded on one degree of freedom. Also, the irremediable loss of information suffered in the detection process makes impossible the complete equalization of linear channel impairments by linear filters. Even if

maximum likelihood detection is used to estimate the demodulated symbols, the achievable performance is suboptimal compared with equalization using the full electric field [64].

2.2.2 Differentially coherent detection

In a differentially coherent detector the receiver estimates the decisions based on the measurement of the differential phase between the symbol to be demodulated and the reference symbols. The most commonly used modulation for this type of schemes is the differential phase-shift keying (DPSK), where the phase reference is provided by the previous. A binary DPSK receiver is shown in Fig. 2-2. The resulting output photocurrent can be expressed as

$$I_{DPSK}(t) = R \cdot Re\{E_S(t)E_S^*(t - T_S)\} \qquad 2.24$$

where $E_S(t)$ is the received optical field, R is the responsivity of each photodiode and T_S is the symbol period. Higher modulation orders can be also explored by increasing the complexity at the receiver [65]. The main incentive for using this type of systems is that binary DPSK presents a 2.8 dB higher sensitivity than IM/DD at a BER of 10^{-9} [66]. Nevertheless, most of the constraints associated with non-coherent detection methods are still present in these architectures as it exist only one degree of freedom for each polarization and carrier, meaning that linear impairments cannot be completely compensated after the photodetection.

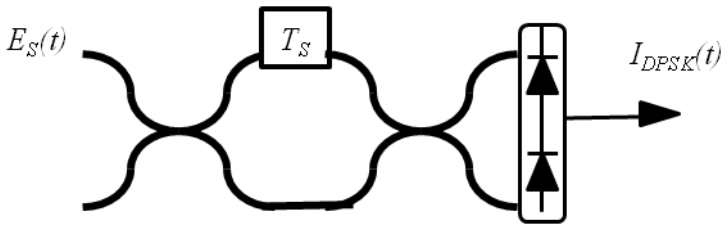

Fig. 2-2. Differentially coherent phase detector of a 2-DPSK coherent detection

A highly developed detector for M-ary DPSK is the multichip DPSK receiver, which provides a set of multiple DPSK receivers ordered in parallel presenting each one a different delay multiple of T_S [67][68]. The consequence is that extra information is available at the receiver as the receiver compares the phase to multiple previous symbols, increasing the sensitivity. In an ideal system where the number of parallel DPSK is infinite, the performance of these system approaches the coherent PSK [75]. In practice, even when the multi-chip DPSK does not call for a LO, the hardware complexity can be an important disadvantage.

Another coherent detection scheme related to this family is the hybrid of non-coherent and differentially coherent detection. The main format of this kind is the polarization-shift keying (PolSK), which encodes information in the Stokes parameter. The purpose of this project does not involve modulation on polarization, but further information can be found in [75]. This scheme presents a much better response against laser phase noise than QAM and PSK modulation formats, what made it very interesting in the early 1990s. Nowadays the advantages of these systems have reduced due to tunable laser with linewidths below 100 KHz, symbol rates of tens of GHz and the development of new synchronization methods [29]. A detailed study of these techniques is beyond the scope of this project and a complete description can be found in [67][68].

2.2.3 Coherent detection

Coherent systems are defined by the characteristic that the incoming light wave is mixed with other light beam coming from the LO source before being detected by a photodetector. This addition is clear in the mathematical domain as

$$E = E_{i1} + E_{i2} \tag{2.25}$$

Where E_{i1} and E_{i2} are the inputs of the mixer.In the other hand, its realization is not so evident. In fiber optical system this process is performed by using an optical coupler. This device is shown in Fig. 2-3 and the output electrical fields can be written as

$$E_{o1} = (E_{i1} + E_{i2})\sqrt{1-k} \tag{2.26}$$

$$E_{o2} = (E_{i1} + E_{i2} exp\ (j\Delta))\sqrt{1-k} \tag{2.27}$$

where E_{o1} and E_{o2} are the output ports of the coupler, k is the power splitting ratio and Δ is the phase shift introduced from the input port 1 to the output port 2. These equations can also be expressed in terms of the scattering matrix S as

$$\begin{bmatrix} E_{O1} \\ E_{O2} \end{bmatrix} = \begin{bmatrix} s_{11} & s_{12} \\ s_{21} & s_{22} \end{bmatrix} \begin{bmatrix} Ei_1 \\ E_{i2} \end{bmatrix} = \begin{bmatrix} \sqrt{1-k} & \sqrt{1-k} \\ \sqrt{k} & exp\ (j\Delta)\sqrt{k} \end{bmatrix} \begin{bmatrix} Ei_1 \\ E_{i2} \end{bmatrix} = \boldsymbol{S} \begin{bmatrix} Ei_1 \\ E_{i2} \end{bmatrix} \tag{2.28}$$

In these expressions we have assumed that the hybrid presents no losses.

One of the most popular hybrids for coherent communications is the 3 dB coupler or 180º hybrid, where k=1/2 and $\Delta = \pi$, so substituting in Eq. 2.26 and Eq. 2.27 we obtain that the output fields can be expressed as

$$E_{o1} = (E_{i1} + E_{i2})\sqrt{2} \quad 2.29$$

$$E_{o2} = (E_{i1} + E_{i2} exp\ (j\pi))\sqrt{2} \quad 2.30$$

Here, if we want to detect the sum of these fields the first option is to place a photodetector at any of its outputs. The photodiode current produced is the half of the total possible, as we are wasting one of the two branches. For a lossless network, $\boldsymbol{S}$ must be unitary [69], which excludes the possibility of finding a coupling system in which all the power is driven to one of the output ports.

An improved manner of adding two lightwaves is using *balanced photodetection*. Balanced photodetection has been used due to its high sensitivity in compare to simple detection. The reason is that it is able to detect low power signals where the dominant noise is additive and it is present in both branches [70]. The use of balanced photo detectors allows reducing or eliminating the noise from the electrical signal, as well as it enables to maximize the use of the optical power generated by the local oscillator. The balanced configuration consists on using two photodetectors with identical quantum efficiency in each one of the output coupler ports (Fig. 2-4). The resulting signals can be subtracted in order to eliminate the noise present in both branches. In this arrangement, the resulting currents from each photodiode can be written as

$$i_1(t) = R|E_{o1}|^2 + n_1(t) \quad 2.31$$

$$i_1(t) = R|E_{o2}|^2 + n_2(t) \quad 2.32$$

where R is the responsivity of each photodiode. By considering the shot noise limit scenario, $n_1(t)$ and $n_2(t)$ are the shot noise currents of each branch having a PSD of $S_{sh,1} = qR|E_{o1}|^2$ and $S_{sh,2} = qR|E_{o2}|^2$. The resulting output current of the balanced photodiode can be expressed as

$$I_{out}(t) = i_1(t) - i_2(t) = R(|E_{o1}|^2 + |E_{o2}|^2) + n(t) \quad 2.33$$

Where $n(t)$ is an approximated zero mean white Gaussian noise with PSD

$$S_{sh} = qR(|E_{o1}|^2 + |E_{o2}|^2) \quad 2.34$$

The PSD of the two different branches can be added because they have different origin, so they are independent.

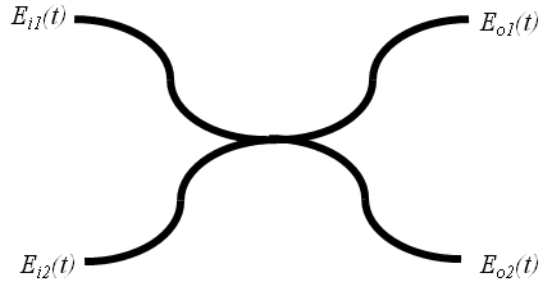

Fig. 2-3. Optical 180^0 hybrid. Each input field (Ei_1, Ei_2) is splitted into the two output ports (E_{o1}, E_{o1}). A phase shift of 180 degrees is introduced in one of the branches.

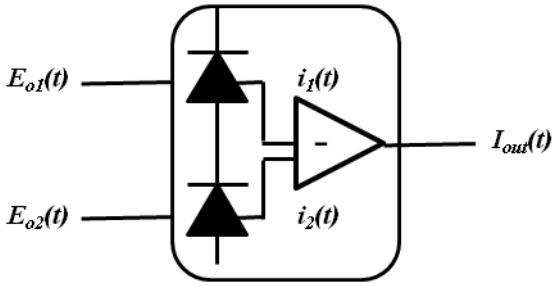

Fig. 2-4. Balanced photodetector model. Two photo detectors with identical quantum efficiency transform the input fields $E_{i1}(t)$, $E_{i2}(t)$ into electrical currents. The resulting signals are subtracted to eliminate the common noise present in both branches, obtaining $I_{out}(t)$.

In the balanced photo detector almost all the power is exploited, increasing the receptor sensitivity in compare to a simple detector [71]. Furthermore, the implementation of this type of front end improves the robustness against LO laser noise [72][73], diminishes the adjacent channel interference for multichannel systems [74] and ,when both photodiodes have matched frequency responses and optical paths, so the resulting dc currents are annulled, a high pass filter is not essential. In practice, the performance of a balanced photo detector is not perfect due to differences on the detectors responsitivities, electrical path length or other non-idealities [54].

In a coherent detector the receiver recovers information on both, the amplitude and phase of the electric field, allowing a wide set of modulation formats and making it one of the most attractive detection methods. In order to extract the information, the receiver necessitates to have

information about the carrier phase as the signal is demodulated by a LO source, which acts as phase reference. In order to circumvent this requirement, the carrier synchronization can be achieved by several techniques. First, an optical PLL (OPLL) can be implemented to perform the synchronization between the LO and the transmission laser. Another option is to divide the down-conversion process from optical frequencies to baseband signals into two stages: first the downconversion to an intermediate frequency (IF) is performed by a free-running LO laser followed by an analog or digital PLL who is in charge of the synchronization process. This process presents an important sensitivity to propagation delay in the feedback path of the *voltage-control oscillator* (VCO), which may degrade the synchronization process due to the rigorous requirements in this parameter [65]. In the other hand, Feedforward (FF) carrier synchronization overcomes this limitation by using both, past and future symbols, to estimate the carrier phase.

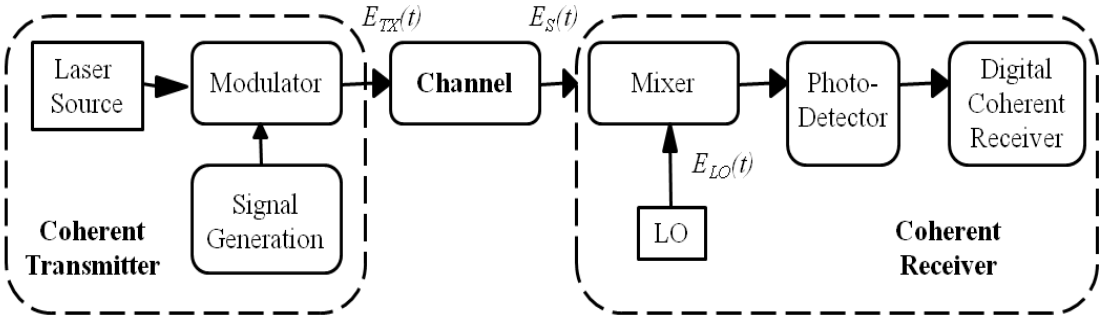

Fig. 2-5. Coherent System Scheme. In the transmitter side, the data bits are translated into electrical signals by a signal generator, which is also responsible for pulse shaping. The light coming from the laser source is shaped by the optical modulator, which translates the phase and amplitude information contained in the electrical domain onto the optical carrier producing $E_{TX}(t)$. This signal is sent through the channel and the received signal $E_S(t)$ is mixed with the LO signal $E_{LO}(t)$ using an optical mixer. The output of the mixer is translated into intensity currents and translated to symbols by the coherent receiver.

In Fig. 2-5 the basic block diagram of a coherent system is shown. In the transmitter side, the data bits are translated into electrical signals by a signal generator, which is also responsible for pulse shaping. The light coming from the laser source is shaped by the optical modulator, which translates the phase and amplitude information contained in the electrical domain onto the optical carrier producing $E_{TX}(t)$. We can express this signal as [65]

$$E_{TX}(t) = \sqrt{P_t} \sum_k x_k b(t - kT_S)\, exp\,[j(w_s t + \emptyset_s)] \qquad 2.35$$

where T_S is the symbol period, P_t is the average transmitter power, $b(t)$ is the pulse shape, w_s and $\emptyset_s$ are the frequency and phase of the TX laser, x_k is a vector cointaining the *k-th* transmitted

symbol. The resulting signal is sent through the channel, which in absence of nonlinear effects can be modelled as $h(t)$ and $H(w)$ in the time and frequency domain respectively. The channel in a fiber coherent system is degraded by several effects as chromatic dispersion, polarization-dependent loss, etc. These effects can be introduced in this model but, as this project is focused on free space optics, we assume that the optical system presents only AWGN in the absence of atmospheric turbulence, which will be later considered. This AWGN is composed by the receiver LO shot noise and the receiver thermal noise. As we saw in Eq. 2.14, these noises can be modelled as a unified noise source with cumulative variances. The resulting received signal $E_S(t)$ can be expressed as [65]

$$E_s(t) = \sqrt{P_r} \sum_k x_k c(t - kT_S)\, exp\,[j(w_s t + \emptyset_s)] \qquad 2.36$$

where $c(t) = b(t) \otimes h(t)$ is a normalized pulse shape.

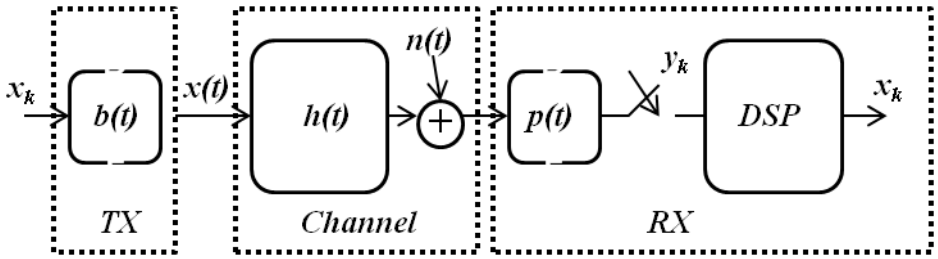

Fig. 2-6. Coherent system model.

The received signal $E_S(t)$ is mixed with the LO signal $E_{LO}(t)$ using an optical mixer. At this point we will also assume that the spatial phases and polarization of both signals are perfectly matched. The light generated by the local oscillator (LO) can be represented as:

$$E_{LO}(t) = \sqrt{P_{LO}} exp\,[j(w_{LO} * t + \emptyset_{LO})] \qquad 2.37$$

Here, $P_{LO}[W], w_{LO}[rad/s]$ and $\emptyset_{LO}[rad]$ are the power, frequency and phase of the local oscillator signal [58]. Both signals are combined in the optical mixer.

At this point, depending on the relationship between the optical frequencies of the signal and the local oscillator two different demodulation schemes arise. In heterodyne detection $w_{LO} \neq w_S$, so the downconvertion must be performed in two separated steps (Fig. 2-7). The coherent detector is a 3-dB fiber coupler (or 180º hybrid) whose outputs are converted into a

current $I_{het}(t)$ by one single balanced photodetector. The same scheme can be implemented in free space optics using a 50/50 beamsplitter [76], but since they present the same transfer function there is no difference in their performance. The output intensity is centered at an intermediate frequency $w_{IF} = w_S - w_{LO}$. This current is digitally processed and the baseband conversion is performed by a digital downconvertion. The resulting basebands currents are $I_{het,I}(t)$ and $I_{het,Q}(t)$, which correspond to the in-phase and quadrature branches of a complex demodulator (Fig. 2-8).

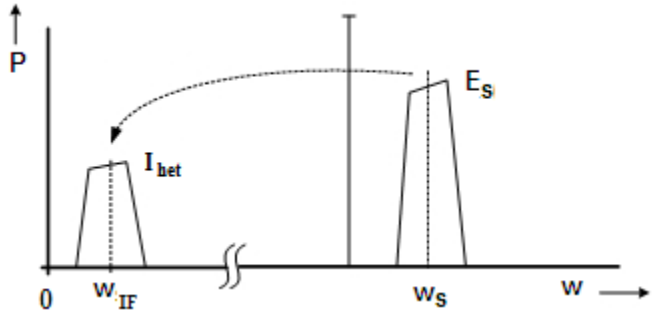

Fig. 2-7. Heterodyne signal frequency spectrum. The incoming signal $E_s(t)$ is mixed with a reference local oscillator source (LO) set at a close-by frequency. The outcome of the coherent receiver is the centered at the intermediate frequency, which carries the information in amplitude, phase or frequency of the original higher frequency signal.

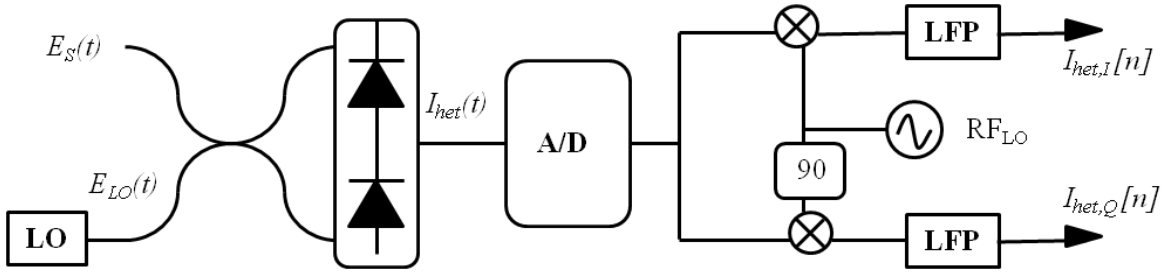

Fig. 2-8. Coherent Heterodyne demodulation scheme. The incoming optical signal $E_s(t)$ is mixed with the local oscillator light beam $E_{LO}(t)$ in a 180^0 Hybrid. The outputs of the coupler are connected to a balanced photo detector, which generates a current $I_{het}(t)$. An analog to digital converter transform $I_{het}(t)$ to baseband frequencies by multiplying it with a digital RF oscillator obtaining $I_{het,I}[t]$ and $I_{het,Q}[t]$, corresponding to the I and Q components, respectively.

In heterodyne detection the local oscillator frequency w_{LO} is not matched with the signal central frequency w_S so the detected signal is present around an intermediate frequency w_{IF}. The equation analysis is based on the demodulation scheme that uses an optical coupler, which mixes the incoming signal and the local oscillator generated field. Assuming that we are working in a shot noise limited scenario, so thermal noise sources can be neglected [77][54], and that we do

not consider ASE noise in our system because no optical amplification is used, the output heterodyne current can be expressed as:

$$I_{het}(t) = R(|E_s(t)|^2 + |E_{LO}(t)|^2) = 2RIm\{E_s(t)E_{LO}(t)^*\} + I_{sh}(t) \quad 2.38$$

where $I_{sh}(t)$ is the LO shot noise. Assuming that we are working on the shot noise limit scenario where $P_{LO} \gg P_S$, $I_{sh}(t)$ presents a two-sided PSD can be expressed as [21]:

$$S_{sh}(f) = qR(P_{LO} + P_S) \cong qRP_{LO} \quad 2.39$$

By replacing Eq. 2.39 in Eq. 2.36 the resulting heterodyne intensity is expressed as

$$I_{het}(t) = 2R\sqrt{P_{LO}}\left(\sqrt{P_s}\left[y_i(t)\,sin(w_{IF}t + \emptyset) + y_q(t)\,cos(w_{IF}t) + \emptyset\right]\right) + I_{sh}(t) \quad 2.40$$

where $y_i(t)$ and $y_q(t)$ are the real and imaginary parts of

$$y_0(t) = \sum_k x_k c(t - kT_S)\,exp\,[j\emptyset] \quad 2.41$$

and $\emptyset = \emptyset_S - \emptyset_{LO}$. After optical down-conversion to the intermediate frequency, an electrical demodulation must be performed to extract the I and *Q* components. For that purpose we use the scheme shown in Fig. 2-8. Here, the different intensities can be expressed as:

$$I_{RF}(t) = I_{RF}sin\,(w_{RF}t + \emptyset_{RF}) \quad 2.42$$

$$I_{het,I}(t) = I_{het}(t)I_{RF}(t) \quad 2.43$$

$$I_{het,Q}(t) = I_{het}(t)I_{RF}sin\,(w_{RF}t + \emptyset_{RF} - \frac{\pi}{2}) \quad 2.44$$

where w_{RF}, $\emptyset_{RF}$ and I_{RF} are the frequency, phase and amplitude of the radiofrequency oscillator. Assuming a perfect frequency match between w_{RF} and w_{IF} we can express the resulting baseband signals after low pass filtering as

$$I_{het,I}(t) = R\sqrt{P_S}\sqrt{P_{LO}}I_{RF} \cdot y_i cos[(\emptyset - \emptyset_{RF})] + I_{sh,I}(t) \quad 2.45$$

$$I_{het,Q}(t) = R\sqrt{P_S}\sqrt{P_{LO}}I_{RF} \cdot y_q sin[(\emptyset - \emptyset_{RF})] + I_{sh,Q}(t) \quad 2.46$$

where $I_{sh,I}(t)$ and $I_{sh,Q}(t)$ have a resulting PSD of $S_{sh}(f) = qR\frac{P_{LO}}{2}\ [\frac{A^2}{Hz}]$.

In homodyne detection the local oscillator is tuned so that it matches the optical frequency ($w_{LO} = w_S$) obtaining a baseband current at the output of the coherent receiver (Fig. 2-9). In this scheme the down-conversion is achieved in one single step. The coherent detector is a 90^0 hybrid, formed by four hybrids of 180^0 and a 90 degrees phase shifter, which output fields are converted into two currents, $I_{hom,I}(t)$ and $I_{hom,Q}(t)$, generated by two balanced photo detectors.

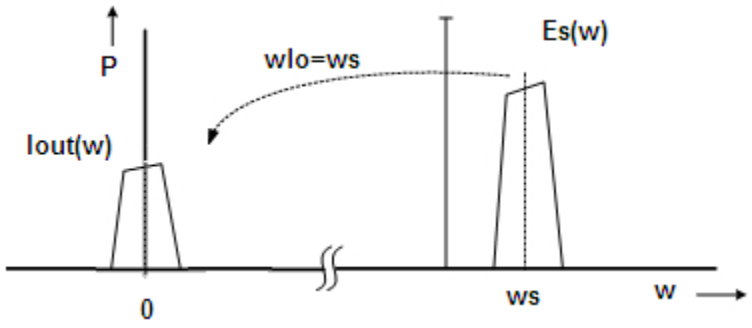

Fig. 2-9. Homodyne signal spectrum. The local oscillator is tuned so that it matches the optical frequency obtaining a baseband current at the output of the coherent receiver.

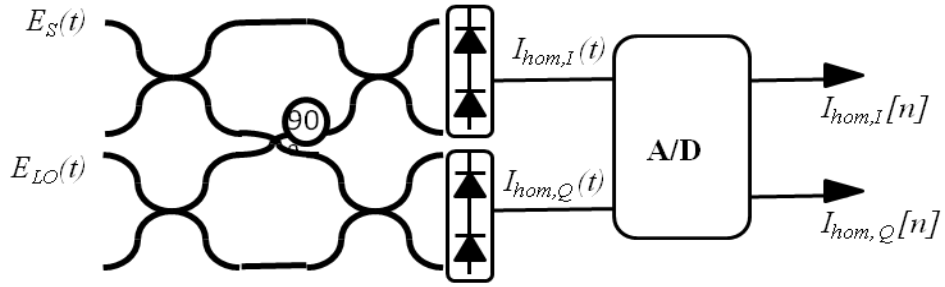

Fig. 2-10. Coherent Homodyne demodulation scheme. The incoming optical signal $E_S(t)$ is mixed with the local oscillator light beam $E_{LO}(t)$ in a 90^0 Hybrid, which is composed by four 180^0 hybrids and a 90^0 phase shifter. The outputs of the hybrid are connected to two balanced photo detectors, which generate two baseband currents $I_{hom,I}(t)$ and $I_{hom,Q}(t)$. An analog to digital converter transform both currents into a digital signal, which can be processed by the digital demodulator.

If we follow the same procedure as for the heterodyne case, we find that the expression for the $I_{hom,I}$ and $I_{hom,Q}$ signals are the equivalent to Eq. 2.45 and Eq. 2.46 respectively

$$I_{hom,I}(t) = R\sqrt{P_S}\sqrt{P_{LO}}I_{RF} \cdot y_i cos\,(\emptyset) + I_{sh,I}(t) \qquad 2.47$$

$$I_{hom,Q}(t) = R\sqrt{P_S}\sqrt{P_{LO}}I_{RF} \cdot y_q sin(\emptyset) + I_{sh,Q}(t) \qquad 2.48$$

This means that the resulting baseband signals for the heterodyne case have exactly the same expression that the homodyne case and that all the noises have the same PSD's. For this reason, the heterodyne and the two-quadrature homodyne schemes present the same performance [78]. The only difference between these two methods arises when the transmitted signal occupies only one quadrature (e.g. BPSK) and the system is working in a shot limited scenario. In this case the output photocurrent is equivalent to the $I_{het}(t)$ from Eq. 2.40, so the term is doubled in compare to Eq. 2.45 and Eq. 2.46, having

$$I_{BPSK}(t) = 2R\sqrt{P_{LO}}\left(\sqrt{P_s}y_q(t)\right) + I_{sh}(t) \qquad 2.49$$

implying that the signal term is doubled (four times the power), while the shot noise power is only increased by two [79], obtaining a sensitivity improvement of 3 dB compared to the heterodyne case.

Table 2-1. Comparison between homodyne and heterodyne downconversion. For the shot limited scenario $\overline{N_r} = \eta\overline{N_s}$ is the number of detected photons per symbols, η is the quantum efficiency and $\overline{N_s}$ is the average number of photons received per symbol.

	Homodyne	Heterodyne
Number of Balanced Photodetectors Required	2	1
Minimum Photodetector Bandwidth	BW	2BW
Hybrid at the Mixing Stage	90º	180º
Shot-noise-limited SNR	$\overline{N_r}$	$\overline{N_r}$

The main advantage of using a heterodyne optical system is that only one balanced photo detector is needed and that a simpler optical hybrid is used. The hybrid used in the heterodyne case is a 180º hybrid versus the 90º required for the homodyne case. In the other hand, the photocurrent in the heterodyne case has a larger bandwidth than the homodyne case due to the fact that the information signal is modulated in an intermediate frequency. Typically, this frequency w_{IF} is chosen to be close to the signal bandwidth (BW), which implies a total required bandwidth required for the heterodyne case doubles the one required in the homodyne case. In Table 2-1, a comparison between homodyne and heterodyne downconvertion is shown. As it was shown in Eq. 2.17, the resulting SNR for the shot noise limited scenario for both schemes is simply the number of detected photons per symbol, except for the one-quadrature homodyne case, where the SNR is doubled.

2.3 Modulation Formats and BER for Coherent System

As we saw in the previous section, coherent receivers maintain the phase of the received signal, so information can be sent in the phase, the frequency or in the amplitude of the signal. This feature allows a wide set of different options of sending information by modulating any of these electrical field components. Therefore, different modulation formats known, such us as amplitude-shift keying (ASK), phase-shift keying (PSK), frequency-shift keying (FSK) [65] or quadrature-amplitude modulation (QAM), can be considered for optical coherent communications. Also, the fact that synchronous detection is applied by using a sufficient large LO power allows us to consider the shot-noise limited scenario, where the shot noise is dominant. The problem has thus been reduced to the classical detection problem of a certain signal in AWGN. In this section we briefly describe each format separately for, later, discuss the performance of each format in terms of the BER.

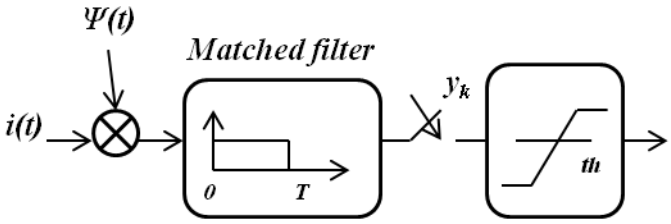

Fig. 2-11. ML receiver for signals under AWGN. The parameter *Ψ(t)* is $1/\sqrt{T}$ for the homodyne case and $\sqrt{2/T}$ for the heterodyne case. The matched filter the pulse shape used at the transmitter side.

The associated electric fields of a transmitted optical signal can be reduced from Eq. 2.36 to

$$E_{TX}(t) = A_S exp[w_0 t + \emptyset_S(t)] \qquad 2.50$$

where $A_S = \sqrt{P_S}$. In the case of PSK format, the information in transmitted in the phase of the optical carrier $\emptyset_S(t)$ while A_S and w_0 are kept constant. An attractive feature of the PSK format is that the optical intensity is constant and the signal presents the appearance of a continuous wave (CW). The use of PSK requires that the phase of the carrier remains stable in order to be able to extract the phase at the receiver. This implies a stringent condition on the laser linewidth on both, the transmitter laser and LO laser. The optimal receiver is formed by a matched filter followed by a threshold test (Fig. 2-11) [63][64]. In this model, *Ψ(t)* is a normalized unit energy signal that is constant and take values equal to $1/\sqrt{T}$ for the homodyne case and $\sqrt{2/T}\cos(w_{IF}t)$ for the heterodyne case. The output of the ML receiver can be expressed as

$$y(t) = \frac{1}{\sqrt{T}} \int_0^T (i(t) \cdot \Psi(t) + I_{sh}(t)) dt \qquad 2.51$$

If we consider the BPSK homodyne intensity expression from Eq. 2.49 and substitute $i(t)$ by $2R\sqrt{P_{LO}}\left(\sqrt{P_s} y_q(t)\right)$ in Eq. 2.51, the output $y(t)$ is a Gaussian random variable with mean $2R\sqrt{P_{LO} P_s T}$ and variance $\mathrm{q}RP_{LO}$. The probability density function of $y(t)$ can be seen in Fig. 2-12. The BER for this specific example is directly calculated as

$$BER = \frac{1}{2} P(y > 0 | '0') + \frac{1}{2} P(y < 0 | '1') = P(y > 0 | '0') \qquad 2.52$$

Considering that $\sqrt{E_b} = 2R\sqrt{P_{LO} P_s T}$, being E_b the bit energy and that $N_0 = \mathrm{q}RP_{LO}$ the noise variance in the shot limited scenario, we can express the error probability as

$$BER = \frac{1}{\sqrt{\pi N_0}} \int_0^\infty exp\left[-\frac{(\sqrt{E_b})^2}{N_0}\right] = \frac{1}{\sqrt{\pi}} \int_{\sqrt{\frac{E_b}{N_0}}}^\infty exp\left[-\frac{E_b}{N_0}\right] \qquad 2.53$$

By using the complementary error function *erfc(x)* function we can express the previous equation as

$$BER = \frac{1}{2} erfc\left(\sqrt{\frac{E_b}{N_0}}\right) = Q\left(\sqrt{\frac{2E_b}{N_0}}\right) \qquad 2.54$$

where E_b/N_0 is the SNR per bit γ_b. The BER obtained for the homodyne BPSK can be used to derive the PSK heterodyne BER by just modifying the γ_b associated to it. Using Eq. 2.46 and Eq. 2.47 we can similarly compute the output of the ML receiver. The probability density function of its output is equivalent to that of the homodyne BPSK case, with the only difference that the mean of $y(t)$ resulting from Eq. 2.51 is scaled by a factor of $1/\sqrt{2}$, so $\sqrt{E_b} = R\sqrt{P_{LO} P_s T}$ while the noise variance remains equal to $\mathrm{q}RP_{LO}$. So for the special cases of BPSK and QPSK we have the same exact expression for the system BER as a function of γ_b:

$$BER_{BPSK} = BER_{QPSK} = \frac{1}{2} erfc\left(\sqrt{\gamma_b}\right) \qquad 2.55$$

For higher modulation orders of M-ary PSK modulation the same procedure can be applied. The BER using coherent detection is given approximately by [81]

$$BER_{PSK}(M) = \frac{1}{b} erfc\left(\sqrt{b\gamma_b} sin\left(\frac{\pi}{M}\right)\right) \quad 2.56$$

Where M is the modulation order and b is the number of bits encoded per symbol $b = log_2(M)$.

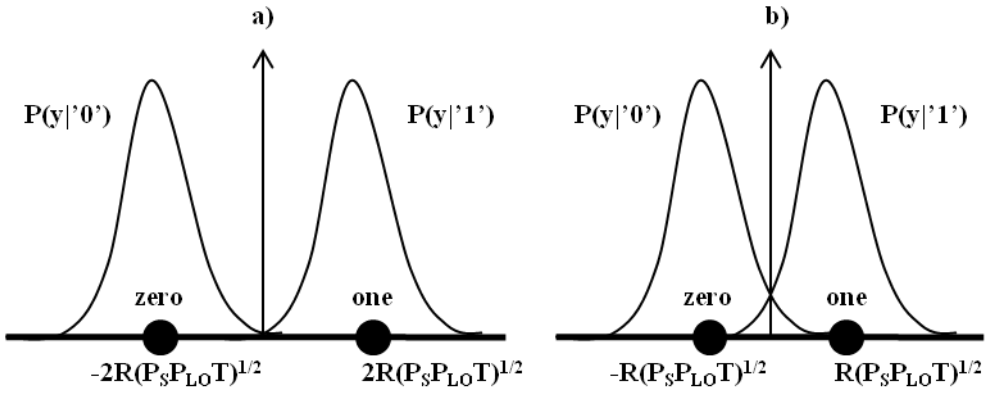

Fig. 2-12. Probability density functions for a) BPSK homodyne detection and b) QPSK heterodyne and homodyne detection.

The same performance evaluation can be developed for other modulation schemes, but, as it is not the purpose of this project a profound study on this subject, we will just the expressions of previous work [27][81][82] to provide the BER of each modulation technique.

For QAM modulation information is encoded in the phase and amplitude of the electrical field expresses in Eq. 2.50. For this modulation scheme $\sqrt{P_S}$ and $\emptyset_S(t)$ are the modulated amplitude and phase containing the information while $w_0(t)$ is kept constant. In this case $\sqrt{P_S}$ and $\emptyset_S(t)$ take one of M possible values during each bit period as a function of the data bit to be transmitted. The resulting BER for a M-QAM constellation is approximated by

Table 2-2. BER and sensitivities in shot-noise-limited receivers for coherent detection. The parameter γ_b is the SNR per bit and the sensitivity is measured by the number of photons required to obtain a BER of 10^{-9}.

	2-PSK homodyne	Sync-PSK heterodyne	Sync-ASK homodyne	Sync-ASK heterodyne	Sync-FSK	DPSK
BER	$Q(\sqrt{4\gamma_b})$	$Q(\sqrt{2\gamma_b})$	$Q(\sqrt{\gamma_b})$	$Q(\sqrt{\gamma_b/2})$	$Q(\sqrt{\gamma_b/2})$	$(1/2)\exp(-\gamma_b)$
Sensitivity	9	18	36	72	36	20

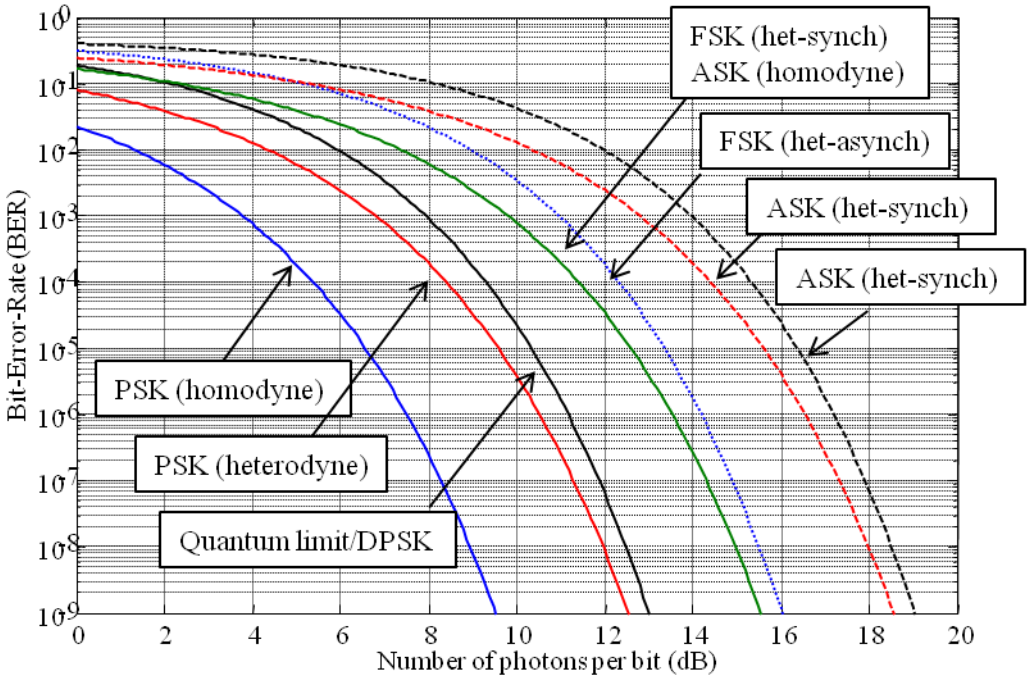

Fig. 2-13. BER curves for shot-noise limited scenario as a function of the number of detected photons per bit in dB for different modulation formats.

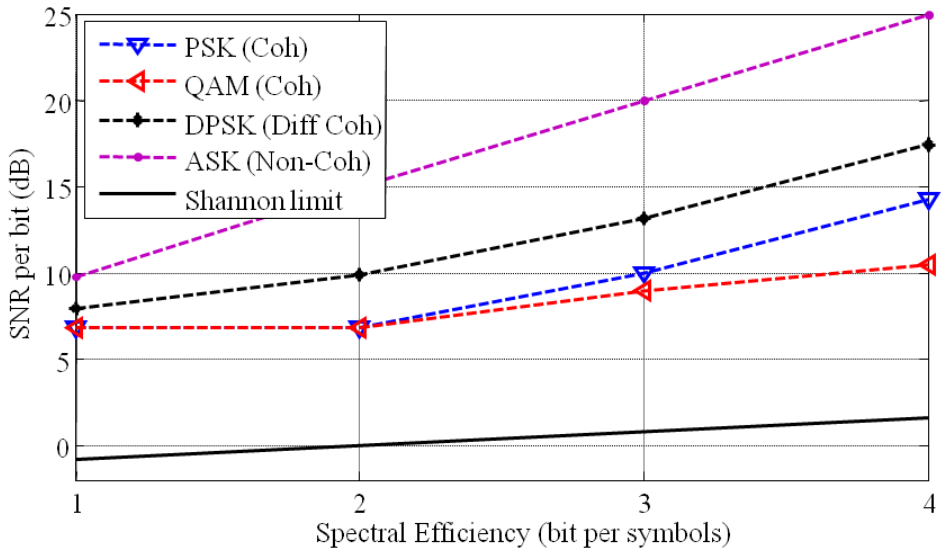

Fig. 2-14. Spectral efficiency versus the SNR required to achieve a BER of 10^{-3} is shown for different modulation formats and the Shannon capacity limit.

$$BER_{PSK}(M) = \frac{2}{b}\left(\frac{\sqrt{M}-1}{\sqrt{M}}\right) erfc\left(\sqrt{\frac{3b\gamma_b}{2(M-1)}}\right) \quad 2.57$$

Similarly, in synchronous ASK and FSK the modulation is introduced in $\sqrt{P_S}$ and $w_0(t)$ respectively. In Table 2-2 the BER and sensitivities in shot-noise-limited receivers are shown for different modulation techniques. The sensitivity is defined as the photons required to obtain a BER of 10^{-9}. In Fig. 2-13 the BER curves for shot-noise limited scenario as a function of the number of detected photons per bit in dB for different modulation formats can be seen. The binary PSK is the one that presents better performance in terms of sensitivity. In the other hand, its spectral efficiency is limited due to the fact that no higher order modulation formats can be used. To increase the spectral efficiency higher modulation orders are needed. Heterodyne PSK present a better performance than the IM/DD modulation working in the quantum limit. Other coherent techniques, such as ASK or FSK, present lower sensitivities and higher BER than the PSK modulation.

QAM modulation presents the same sensitivity as heterodyne PSK for low modulation orders (M= 4, 8) [21] but, because this modulation uses all available degrees of freedom for encoding information, it presents a better SNR for higher spectral efficiencies. This can be seen in Fig. 2-14, where the spectral efficiency versus the SNR required to achieve a BER of 10^{-3} is shown for different modulation formats and the Shannon capacity limit [68].

2.4 Design of a digital QPSK Coherent Optical Transceiver

Quadrature Phase Shift Keying or QPSK is a widely used modulation technique in fiber optical coherent communications. The QPSK modulation technique presents a good tradeoff between receiver complexity, bit error rate, data rate and bandwidth for free space links. It has twice the data rate for a given bandwidth comparing it to BPSK while maintaining the same bit error rate when using heterodyne detection, provides better performance in terms of sensitivity than other coherent systems (ASK, FSK) and it allows the implementation of higher modulation orders without increasing the system complexity. Comparing it to the QAM modulation it presents a slightly lower sensitivity for high modulation orders (*M>4*), however, the receiver design is less complex [81]. Also, recent advances in high-speed electronics and optical devices [65] have

encouraged the development of digital signal processing (DSP) that can provide remarkable advantages in compare to analog techniques. First, high-speed ADCs employed in current phase-diversity coherent receivers sample the photocurrents, corresponding to the received optical signals, at the Nyquist rate or above so as to retain full information of the electric field. Since the amplitude and phase information of the received optical signals are preserved, both of them can be modulated simultaneously to increase the system sensitivity and can be further utilized for compensation of linear and even nonlinear channel impairments. Also, with the aid of high-speed electronics in a digital coherent receiver, the carrier estimation can be done applying high-speed digital signal processing (DSP) rather than using optical PLLs allowing for a free-running LO laser. Recent experiments have demonstrated that DSP-based frequency and phase estimation techniques are very effective to recover carrier phase [39], which will be covered in this section.

In this project we are implementing a heterodyne QPSK modulation. As the heterodyne and the two-quadrature homodyne schemes present the same performance [78], the selection of this detection architecture is justified by the advantages it provides: first, only one balanced photo detector is needed, so the cost and complexity of the experimental set up is reduced. Also, a simpler optical hybrid, a 3 dB coupler instead of the 90º hybrid, is used. In the other hand, the photocurrent in the heterodyne case has a larger bandwidth than the homodyne case due to the fact that the information signal is modulated in an intermediate frequency. This reduces the spectral efficiency of the system, which leads to lower speeds in the communication rate.

To implement an optical coherent communication system, first, we need to study the transmitter and receiver architectures as well as the DSP involved in these modules. Based on this principle, a coherent optical transmitter, responsible for data and signal generation, and a coherent receiver, responsible for coherent detection, impairment compensation and data demodulation [81][83], are described and modeled in this section.

2.4.1 Design of a Optical Transmitter for Heterodyne QPSK

The basic function for a QPSK modulation scheme is given by

$$\emptyset_0(t) = \sqrt{2}p(t)cos[w_c t] \quad 2.58$$

$$\emptyset_1(t) = \sqrt{2}p(t)sin[w_c t] \quad 2.59$$

where $w_{if} = 2\pi f_c$, f_c is the carrier frequency and $p(t)$ is a unit energy pulse shape of *T* duration. This is an orthonormal basis of sinusoid and both channels are independent one from another. The resulting signal containing the information can be written as

$$s(t) = \sqrt{2}\sum_k x_0(k)\, p(t - kT_s)cos[w_c t] - x_1(k)p(t - kT_s)sin[w_c t] \quad 2.60$$

where $x_0(k)$ and $x_1(k)$ are the *k-th* transmitted symbol and T_s is the sampling time. This expression can be written as

$$s(t) = I(t)\sqrt{2}x_0(k)p(t - kT_s) + Q(t)\sqrt{2}x_1(k)p(t - kT_s) \quad 2.61$$

Where $I(t)$ stands for the *inphase* channel (*I*) and $Q(t)$ denotes the *quadrature* channel (*Q*) and are defined by

$$I(t) = \sum_k x_0(k)\, p(t - kT_s) \quad 2.62$$

$$Q(t) = \sum_k x_1(k)\, p(t - kT_s) \quad 2.63$$

The symbol constellation for QPSK modulation with Gray coding is shown in 2.20. The relationship between both signals, I and Q, define the demodulated data bits.

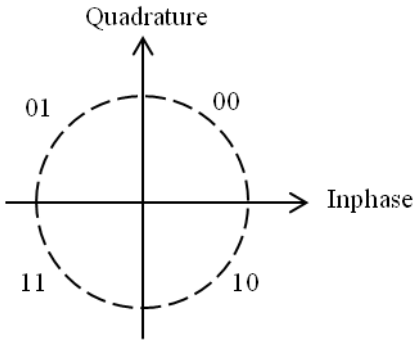

Fig. 2-15. QPSK Symbol constellation with Gray coding.

In order to create a QPSK communication system, first, a pseudo-random sequence of data bits $\boldsymbol{b}$ is generated. Note that it $\boldsymbol{b}$ is a bit array of length d_b and it acts as the information message to be transmitted. Then a unique word preamble $\boldsymbol{w}$ of length d_w is added before $\boldsymbol{b}$. The sum of both length are equal to *2k*. This preamble is needed in order to detect the beginning of the message and to design an ambiguity resolution circuitry at the receiver that will help us with the demodulation [81]. The data bits are transformed from serial to parallel to form pairs of bits. Each group of pair generates a pair of signals by using a lookup table containing the symbol constellation. In this block $x_0(k)$ and $x_1(k)$ are generated. The transmission filter is then applied by multiplying each signal by $p(t)$, generating $I(t)$ and $Q(t)$ from Eq. 2.62 and 2.63. The upconversion is then applied by multiplying both signals by the $cos[w_c t]$ and $sin[w_c t]$ respectively and the resulting signals are added to generate $s(t)$ (Fig. 2-16).

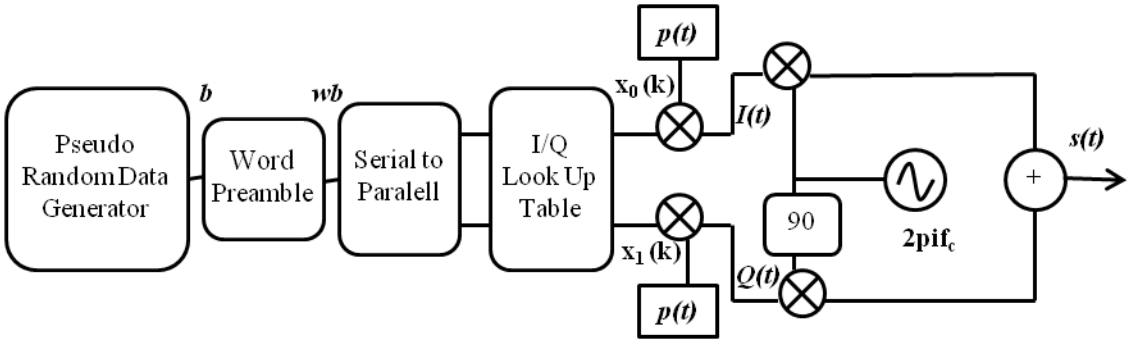

Fig. 2-16. Heterodyne transmitter block system. A pseudo-random sequence of data bits $\boldsymbol{b}$ is generated. Then a unique word preamble $\boldsymbol{w}$ of length $\boldsymbol{d_w}$ is added before $\boldsymbol{b}$. The data bits are transformed from serial to parallel to form pairs of bits. Each group of pair generates a pair of signals by using a lookup table containing the symbol constellation, where $\boldsymbol{x_0(k)}$ and $\boldsymbol{x_1(k)}$ are generated. The transmission filter is then applied by multiplying each signal by $\boldsymbol{p(t)}$, generating $\boldsymbol{I(t)}$ and $\boldsymbol{Q(t)}$. The upconversion is then applied by multiplying both signals by the $\boldsymbol{cos[w_c t]}$ and $\boldsymbol{sin[w_c t]}$ respectively. The resulting signals are added to generate $\boldsymbol{s(t)}$.

In practice, the modulation of lightwaves is achieved by using electro-optical components that introduces the phase, amplitude or frequency information on the optical electrical field. In our case, to develop a heterodyne optical system just a phase modulator is needed. These devices present a variable index of refraction that can be controlled by an external applied voltage. A model of a phase modulator is shown in Fig. 2-17. If the input of the phase modulator is given by $exp\ (jw_0 t)$ then the output of the phase modulator is written as

$$E_{o,pm}(t) = exp\left[j\left(w_0 t + \frac{\pi V(t)}{V_\pi}\right)\right] \quad 2.64$$

where V_π is the voltage necessary for a phase change of π radians. Notice that this voltage $V(t)$ is different from $s(t)$, so the previous general heterodyne system block from Fig. 2-16 must be modified to match to the phase modulator requirements. To implement a heterodyne PSK modulator we have to define

$$\frac{\pi V(t)}{V_\pi} = w_c t + \emptyset_{psk}(t) \quad 2.65$$

where $\emptyset_{psk}(t)$ is the symbol phase of a PSK constellation and w_c is the upconversion carrier frequency. In case of QPSK modulation, $\emptyset_{psk}$ can take values of $\pi/4, 3\pi/4, -3\pi/4, -\pi/4$. Therefore, $V(t)$ is a voltage ramp between $[-V_\pi, V_\pi]$ of frequency $2\pi w_c$ with a voltage offset of $V_\pi \emptyset_{psk}(t)/\pi$. At the same time, $\emptyset_{psk}(t)$ can be expressed in terms of $I(t)$ and $Q(t)$ from Eq. 2.62 and Eq. 2.63 as

$$\emptyset_{psk}(t) = phase\{exp(I(t) + jQ(t))\} \quad 2.66$$

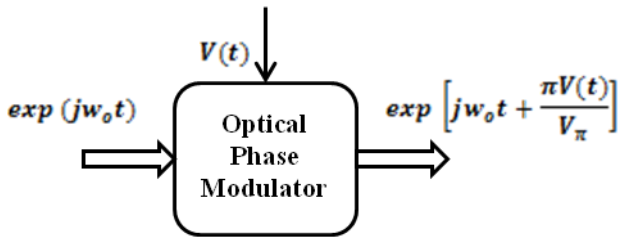

Fig. 2-17. Optical Phase Modulator model. The phase shift produced by a phase modulator is proportional to the modulating voltage $V(t)$.

The resulting design for the optical heterodyne transmitter for QPSK using a phase modulator (PM) is shown in Fig. 2-18. The resulting output signal is equivalent to the one expressed in Eq. 2.36for a coherent transmitter.

2.4.2 Design of a Optical Receiver for Heterodyne QPSK

The demodulation process of a coherent system can be divided into several major sections (Fig. 2-19). The incoming signal $E_S(t)$ from Eq. 2.36 is mixed with the LO signal $E_{LO}(t)$ (Eq. 2.37)

using a 3 dB optical coupler. After applying balanced photodetection, an electrical current $I_{het}(t)$ (Eq. 2.40) centered at an intermediate frequency w_c is translated into the discrete domain by an ADC. The resulting discrete signal is $I_{het}[x_n]$, where $x_n = nT_s$, n is the sample index and T_s is the sample period. The downconvertion to baseband signals is performed by multiplying this signal by a digital local oscillator working at a frequency of w_{if} (Eq. 2.42) and the resulting $\hat{I}[x_nT_s]$ and $\hat{Q}[x_nT_s]$ signals can be obtained by following the same procedure as for Eq. 2.45 and Eq. 2.46. Both signals can be expressed as

$$\hat{I}[x_n] = R\sqrt{P_S}\sqrt{P_{LO}}I_{RF} \cdot y_i cos\left[\Delta w[x_n]x_n + \emptyset_{psk}[x_n] + \Delta\emptyset[x_n])\right] + I_{sh,I}[x_n] \quad 2.67$$

$$\hat{Q}[x_n] = R\sqrt{P_S}\sqrt{P_{LO}}I_{RF} \cdot y_q sin\left[\Delta w[x_n]x_n + \emptyset_{psk}[x_nT_s] + \Delta\emptyset(t))\right] + I_{sh,Q}[x_n] \quad 2.68$$

where Δw and $\Delta\emptyset[x_n]$ are the residual frequency drift and phase offset due to the differences between the transmission laser, the modulation carrier, the LO optical and the digital downconverter. $I_{sh,I}[x_n]$ and $I_{sh,Q}[x_n]$ are the shot noise for each branch and $\Delta\emptyset[x_n]$ is the phase drift due to the phase difference of each and $\emptyset_{psk}[x_n]$ is the component carrying the data information.

$$\Delta w[x_n] = (w_0[x_n] - w_{LO}[x_n]) + (w_c - w_{if}) \quad 2.69$$

$$\Delta\emptyset = (\emptyset_0 - \emptyset_{LO}) + (\emptyset_c - \emptyset_{if}) \quad 2.70$$

Notice that the total phase offset is considered constant over the time. This can be assumed because any variation of the instantaneous phase is included in the frequency noise component. The $w_c - w_{if}$ term from Eq. 2.69 is constant, as both signals are generated by a digital oscillator. In the other hand, the frequency noise caused by the optical sources ($w_0[x_n] - w_{LO}[x_n]$) is time-variant due to spontaneous emission of the lasers [84]. Then, $\hat{\mathrm{I}}[x_n]$ and $\hat{\mathrm{Q}}[x_n]$ are combined into a complex variable expressed as

$$\begin{gathered} y[k] = \hat{I}[x_n] + j\hat{Q}[x_n] \\ y[k] = R\sqrt{P_S}\sqrt{P_{LO}}I_{RF} \cdot y_i exp\left[j(\Delta w[x_n]x_n + \emptyset_{psk}[x_n] + \Delta\emptyset))\right] + I_{sh,I}[x_nT_s] \end{gathered} \quad 2.71$$

To balance any frequency and phase offset impairments the implementation of compensation blocks is required. In the next sections we provide the description and analysis of these blocks.

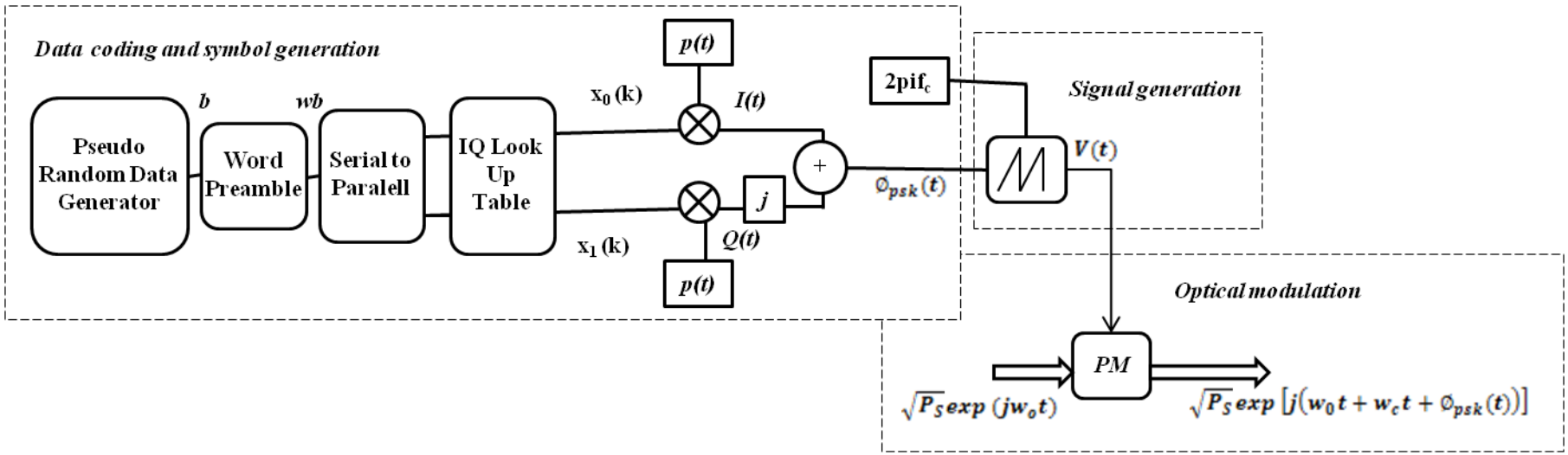

Fig. 2-18. Transmitter block design for heterodyne QPSK using a phase modulator (PM).

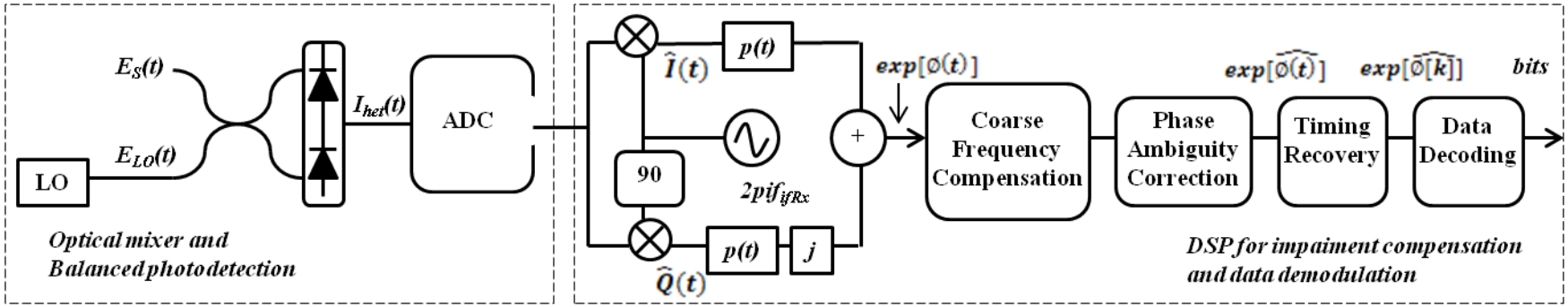

Fig. 2-19. Receiver block design for heterodyne QPSK using digital compensation algorithms.

2.4.2.1 Coarse frequency estimation

A frequency noise Δw produces a phase shift on the received constellation and diminishes the performance of a coherent detector, leading in most of the times to a complete loss of the data [21] (Fig. 2-20). This effect is the so called *laser phase noise* and it can be modelled as a Wiener process [85]:

$$\emptyset(t) = \int_{-\infty}^{t} \delta\omega(\tau) \qquad 2.72$$

where $\emptyset(t)$ is the instantaneous phase, $\delta\omega(t)$ is the frequency noise with zero mean and autocorrelation $R_{\delta\omega\delta\omega}(\tau) = 2\pi\Delta v\delta(\tau)$. The laser output presents a Lorentzian spectrum with a 3 dB linewidth Δv. It has been shown [86] that the laser linewidth is inversely proportional to output power, so lasers working at maximum are more desirable. The effect of the phase noise is a significant impairment in coherent systems as it influences the carrier synchronization process. Given that phase noise is a Wiener process with temporal correlation, the compensation can be applied by signal processing.

The conventional method for carrier synchronization is the PLL, in which the phase estimator output acts as a reference error signal that is processed by a loop filter and generates a control signal for the LO frequency [87][88]. Two main options exists for PLL in optical communications: first, an OPLL which synchronizes the frequency and phase of the LO laser with the TX laser, or, second, an electrical PLL where downconversion is performed by using a free-running LO laser followed by a second stage demodulation by an analog or digital electrical VCO whose frequency and phase are synchronized [87][88]. The main problem with it is that they are sensitive to propagation delay in the feedback path, and this requirement can be difficult to satisfy.

Feedforward (FF) carrier synchronization overcomes this problem. In addition, this synchronizer uses both past and future symbols to estimate the carrier phase. It can achieve better performance than a PLL which, as a feedback system, can only employ past symbols. Recently, DSP has enabled carrier synchronization to be performed in software by using high speed electronics [29]. For coherent communications it also provides lighter requirements in terms of

laser linewidth [89] FF recovery was demonstrated in real time for 4-QAM at 4.4 Gbit/s [82] and recent results have shown that FF synchronization performs coherent detection at data rates that are close to the limits of current technologies [29].

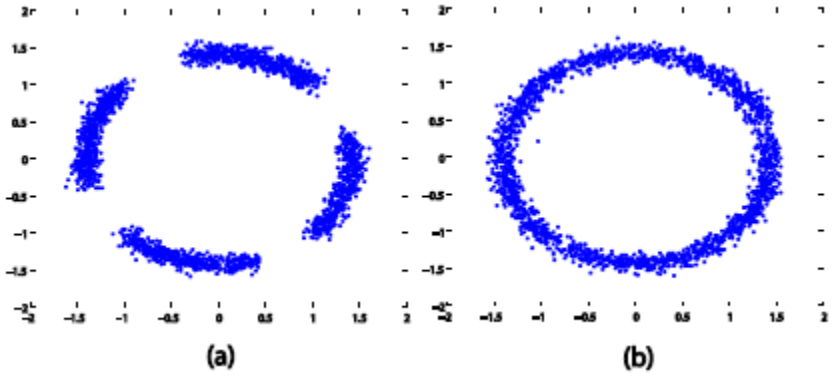

Fig. 2-20. Constellation rotation due to frequency noise. (a) Frequency noise leads to BER degradation or (b) a complete loss of the demodulated data.

We can calculate the frequency offset as an average of *K-1* data points containing the phase difference between samples. It has to be noticed that each symbol contains a phase jump inherent to the phase modulation, which will have to be discard in order to neglect the modulation effect. This estimator is based on the *multiply-filter-divide* concept [90], which takes advantage of the self-multiplication in order to remove the modulation components. It works following the scheme shown in Fig. 2-21: the input signal is powered to the M-order, which deletes the modulation phase $\emptyset_S = n\frac{2\pi}{M}\ [rad]$ by trigonometrical identity, turning the modulation phase into a 2π modulus phase. Then, a band pass filter is applied arround $f_{BP} = M * f_{IF}\ [Hz]$, which contains the pure carrier component multiplied by *M*. Then we have to divide the frequency in order to extract the exact carrier frequency and use it to demodulate the incoming signal.

From Eq. 2.71 we have that the sampled waveforms can be described as

$$y[x_n] = A_o exp\left[j(\Delta w[x_n] + \emptyset_{psk}[x_n])\right] + I_{sh,I}[x_n] \qquad 2.73$$

where $A_o = R\sqrt{P_S}\sqrt{P_{LO}}I_{RF} \cdot y_i$. To estimate the phase, the M-*th* power scheme proposed in [39], a nonlinear transformation is performed to extract the unknown carrier phase from the received M-PSK signals by rising $y[x_n]$ to the M-*th* power:

$$(y[x_n])^M = {A_o}^M exp\left[j\left(M\Delta w[x_n] + M\emptyset_{psk}[x_n]\right)\right] = {A_o}^M exp[jM\emptyset_n[x_n]] \qquad 2.74$$

where the noise term $I_{sh,I}[x_n]$ has been neglected for illustration purposes. By averaging over *2L+1* samples from $(x_n - L)T_s$ to $(x_n + L)T_s$, the estimated phase reference at $t = x_n T_s$ is

$$\emptyset'[x_n] = arctan\left[\sum_{(x_n-L)T}^{(x_n+L)T} (y[x_n])^M\right]/M \qquad 2.75$$

Unfortunately, there are two sources of error to consider here. The factor $1/M$ in this operation introduces an M-fold phase ambiguity [90]. The estimated phase reference $\emptyset'[x_n]$ resulting from the $arctan\,(\cdot)$ function results into an output between $-\pi/M$ and $-\pi/M$. consequently, if the laser drift exceeds the range between $\pm\pi/M$, an instantaneous phase jump of $\pm 2\pi/M$ occur, leading to symbol errors [91]. To circumvent theses phase jumps, the $\emptyset'[x_n]$ must be compared with $\emptyset'[x_n - 1]$. When the difference between this terms is between $-\pi/M$ and $-\pi/M$, the estimated phase is considered valid, if not it must be added or subtracted by multiple of $2\pi/M$. This process is known as *phase unwrapping*.

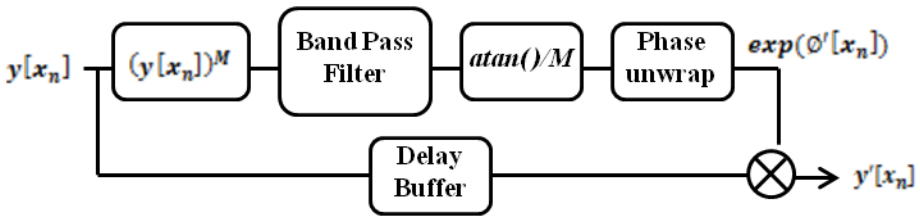

Fig. 2-21. Multiply-Filter-Divide estimator. The input signal phase $y[x_n]$ is multiplied by the modulation order (*M*) to remove the modulation factor. Then it is band-pass filtered and the frequency obtained is divided by the modulation order in order to obtain the carrier frequency. The phase ambiguity introduced by the *atan* function is removed by unwrapping the phase and the estimated phase $\emptyset'[x_n]$ is subtracted from $y[x_n]$ to obtain the baseband corrected signal $y'[x_n]$.

A second error source is the mentioned shot noise present in each sample, which distorts the phase estimation. This shot noise is reduced in Eq. 2.75 by averaging the data samples, but this estimation will inherently introduce some error on the phase estimation. It is obvious that the higher number of samples we consider, the better estimation we get. But in practical systems we cannot consider as many samples as we want due basically to two reasons. First, the linewidth laser limitations constraints the time while the phase offset can be considered constant. If the acquisition time is higher than the correlation time of the laser, the estimation will reduce the

phase accuracy of each sample instead of increasing it. Second, real-time systems have limited memory and calculation power, which impose a physical limitation to achieve the calculation rate needed.

2.4.2.2 Phase ambiguity resolution

M-PSK systems experience from a condition called phase ambiguity, which is due to the nonlinear operation performed on the synchronization process when using FF recovery. In this process, the signal is powered to the *M-th* order to remove the carrier component and then powered to the 1/M-th order to recover the phase offset. In this last step we obtain a set of *M* possible different solutions, but only one of them is the correct one. The FF methods may lock onto a wrong phase and this incorrect locking characteristic introduces a static phase rotation. In QPSK systems, phase ambiguity is given at any multiple of 90 degrees. The effect is that the symbol previously located in the first quadrant at the transmitter may now be located in a different quadrant at the receiver. The phase error exhibited in this symbol will also exist for every other symbol. To correct this effect we need to calculate the proper phase offset and shift the demodulation constellation by the estimated quantity (Fig. 2-22).

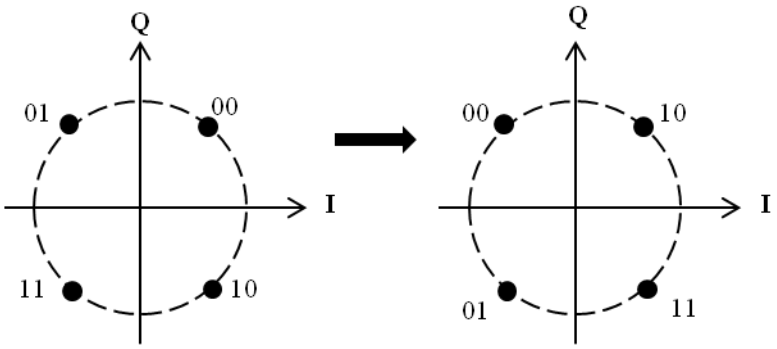

Fig. 2-22. Phase ambiguity correction example for a +90 degrees ambiguity. The demodulation constellation is shifted after estimating the correct phase offset.

Resolving this king of ambiguities is very significant since a failure in correctly detecting them usually leads to the loss of the entire data packet. Traditional methods dealing with ambiguity compensation operate in data aided mode by adding pilot symbols to make their decision using maximum- likelihood (ML) estimation. [93][94]. The appearance of turbo codes for ambiguity resolution [92] has become a quite challenging task: synchronizers have to face the low SNR at which these powerful codes run and the low BERs achieved by these codes implies the need of accurate estimates of the synchronization parameters. These characteristics imply that

this kind of ambiguity-resolution methods may need quite a few number of pilots to correctly synchronize the communication, leading to a loss of spectral and power efficiency. To overcome this difficulty, these ML estimators have been improved by modifying the characteristics of the estimation and several options have been proposed in the technical literature [26][55][96], still assuming a certain degree of non-optimal solution. In this project we implement the ML phase offset estimation using pilot symbols at the beginning of each transmission. However, a profound performance analysis of this block is not intended and the errors associated to this block can be removed by detecting the burst errors.

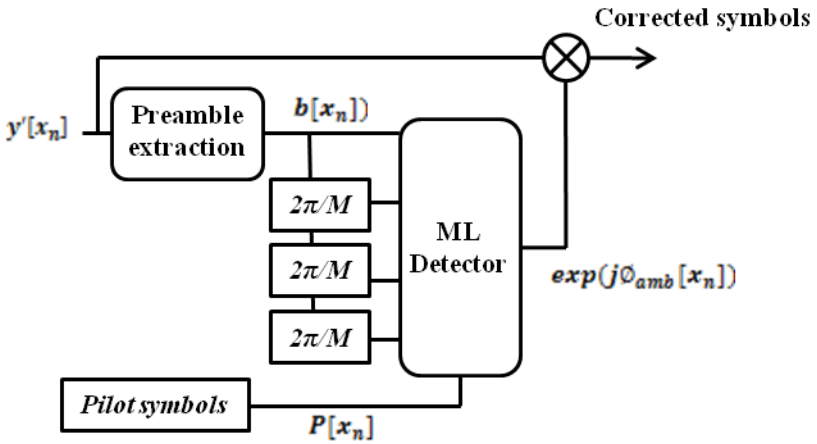

Fig. 2-23. Phase ambiguity corrector block. The preamble symbols $b[x_n]$ are extracted from the incoming signal and they are compared to a previously defined pilot symbols $P[x_n]$ by using a ML detector. The estimated phase ambiguity $\emptyset_{amb}[x_n]$ is applied to the incoming signal to obtain the corrected symbols.

In Fig. 2-23 the block squeme for the phase ambiguity corrector is shown. The preamble symbols $b[x_n]$ are extracted from the incoming signal and are compared to a previously defined pilot symbols by $P[x_n]$ using a ML detector. The estimated phase ambiguity $\emptyset[x_n]$ is applied to the incoming signal to obtain the corrected symbols. The ML detector computes the convolution of $P[x_n]$ with the four quadratural statues of $b[x_n]$ and the estimated ambiguity phase can be written as

$$\emptyset_{amb}[x_n] = jn \ni max = \sum_{length(b[x_n])} b[x_n]P[x_n]exp(jn) \qquad 2.76$$

where $n = 0, 1, 2, 3$ for a QPSK system. The output that maximizes Eq. 2.76 is chosen as the phase ambiguity correction, which is removed from the estimated phase $\emptyset'[x_n]$ from Eq. 2.75.

2.4.2.3 Clock Recovery using Fixed-Rate resampling

Reference clock differences between transmitter and receiver produce misalignments on the sampling time between the transmitter and the receiver. This effect diminishes the performance of any detector as the symbol detector does not sample the receiver signal at optimal times. Many solutions have been proposed and studied to overcome this deviation, many of them based on edge detectors that look for transitions between zero and one [97]. Generally, these methods are based on statistical parameters, which introduce some uncertainty, especially in noisy scenarios [97]. In our project we consider an easy and robust method, based on the previous characterization of the clock difference of transmitter and receiver [98]. This compensation is based on the direct measurements of the clock difference between transmitter and receiver which is used at the receiver to re-sample the incoming waveform after the ADC conversion. We can define the clock difference as

$$T_{s,RX} = K * T_{s,TX} \tag{2.77}$$

where $T_{s,TX}$ and $T_{s,RX}$ are the transmitter and receiver sampling times, respectively, and K is a parameter that relates both quantities. The re-sampling process at $1/K$ imply that the symbol durations in both places are matched and detection can be performed without losing information. In the other hand, there is no flexibility to change the transmitter or receiver without changing the system parameters. The noise added by the re-sampling process can be neglected if we consider that the sampling frequency is much higher than the data rate [98].

2.5 Experimental Set Up for a QPSK Coherent Communication System

2.5.1 Overview of the Experimental Setup

On the previous section we defined the necessary blocks for the transmitter and receiver of an optical coherent system. In this chapter we define the experimental set up, describe the different devices compounding the system and characterize several effects introduced by hardware limitations. The objective is to develop a coherent QPSK heterodyne system on fiber that acts as a free space optical communication front end to further analyze the atmospheric effects in this type of systems. The idea is to build a complete coherent system using the transmitter and receiver block system defined in Fig. 2-18 and Fig. 2-19 by using commercially available devices. This

implementation involves the use and of different devices and techniques, each one of them working in the optical, electrical or digital domain.

Several assumptions have to be taken into account to provide a general overview of how we deal with the key concepts of coherent communications. First, a heterodyne QPSK system architecture is implemented with the attribute that the transmitter and receiver beam lights are generated by splitting a single laser source. The technique of using the same laser for the transmitter and LO is widely known as self-coherent detection. Still, this project does not perform an implementation of self-coherent detection as the frequency carrier is not sent together with the signal and synchronization cannot be achieved without the carrier and phase estimation blocks. The reason for this is that a time delay is introduced between the signal and LO by adding fiber length in the LO path, which introduces a phase difference between both signals that, in junction with the variations of the instantaneous frequency of the laser, generates a mismatch between the received and LO signal frequencies. The frequency noise between the received and the LO signal can be modeled as

$$\Delta w(t) = (d_S - d_{LO}) * \frac{2\pi}{\lambda(t)} \qquad 2.78$$

Where d_S and d_{LO} are the signal and LO path, and $\lambda(t)$ is the instantaneous wavelength of the laser. The resulting effect is a time-varying frequency and phase drift between both signals when they arrive to the mixing stage. Actually, the self-heterodyne method [99] is a technique which can be used to measure the linewidth of a laser, particularly a single-frequency laser. For sufficiently long delays, the superimposed beams are essentially uncorrelated, and the output spectrum becomes a simple self-convolution of the laser output spectrum [99], from which the laser linewidth is easily retrieved. The main difference with a two laser system is that the frequency separation between both signals is lower. This is equivalent to assume that a real heterodyne receiver provides a sufficiently large electrical bandwidth enough to perfectly sample the intermediate electrical signal produced by the balanced photodetector to fulfill the Nyquist criteria.

Another characteristic of the implemented system is that we perform a burst mode communication. In this scheme a packet of data symbols of a certain size is transmitted to the receiver and the next data packet is not sent until the receiver has demodulated the previous one.

The compensation algorithms introduce a computation latency that is not enough to perform real time processing while implementing the DSP calculations previously explained in section 2.4.2. By measuring the computation latency, the transmitter is configured to send the packets at a frequency rate that the receiver is able to decode. This type of communication allows us to reduce the requirements on the computational speed needed to perform real time processing and circumvents the necessity of implementing digital signal processing in VLSI electronics, which is beyond the scope of this study.

The resulting implementation scheme can be seen in Fig. 2-24. The light beam coming from the laser is sent through an optical isolator and is divided by a 90/10 beam splitter. The high power signal is sent to a phase modulator where the modulated optical signal $E_S(t)$ is generated. The modulator is driven by the heterodyne current $V(t)$ from Eq. 2.65, which is generated by amplifying the output of a signal generator. The phase modulator (PM) is sensitive to polarization, so we have to adjust the polarization state at the entry by introducing a polarization controller in order to maximize the modulated power at the PM. The signal coming from the transmitter is mixed by the 3 dB coupler LO signal, which is passed through an attenuator that controls the LO power arriving to the receiver, and a polarization controller, that maximizes the mixing efficiency at the coupler. The 3 dB coupler outputs are connected to a balanced photo detector, which generates the intermediate frequency current. This current is then amplified and translated into the digital domain by an analog to digital converter in order to apply digital compensation algorithms and demodulation.

2.5.2 Implementation of an Optical Coherent Transmitter

The optical experimental setup is shown in Fig. 2-24(a-b). For the signal generation block, a N8241A Agilent arbitrary waveform generator (AWG) that present a 1.25 GS/s bandwidth is selected. The AWG is driven by control software developed using Labview, which is used to implement the digital blocks responsible for data and symbol generation from section 2.4.1. The arbitrary waveform generator presents several parameters providing different advantages or disadvantages with regards to the working and filtering regime at its output. There are three key tools that control our signal generator. The first tool is an integrated pre-distortion filter, which compensates for the variation in the magnitude response of the output response as a function of frequency. This process creates a linear phase response and attenuates the lower frequency

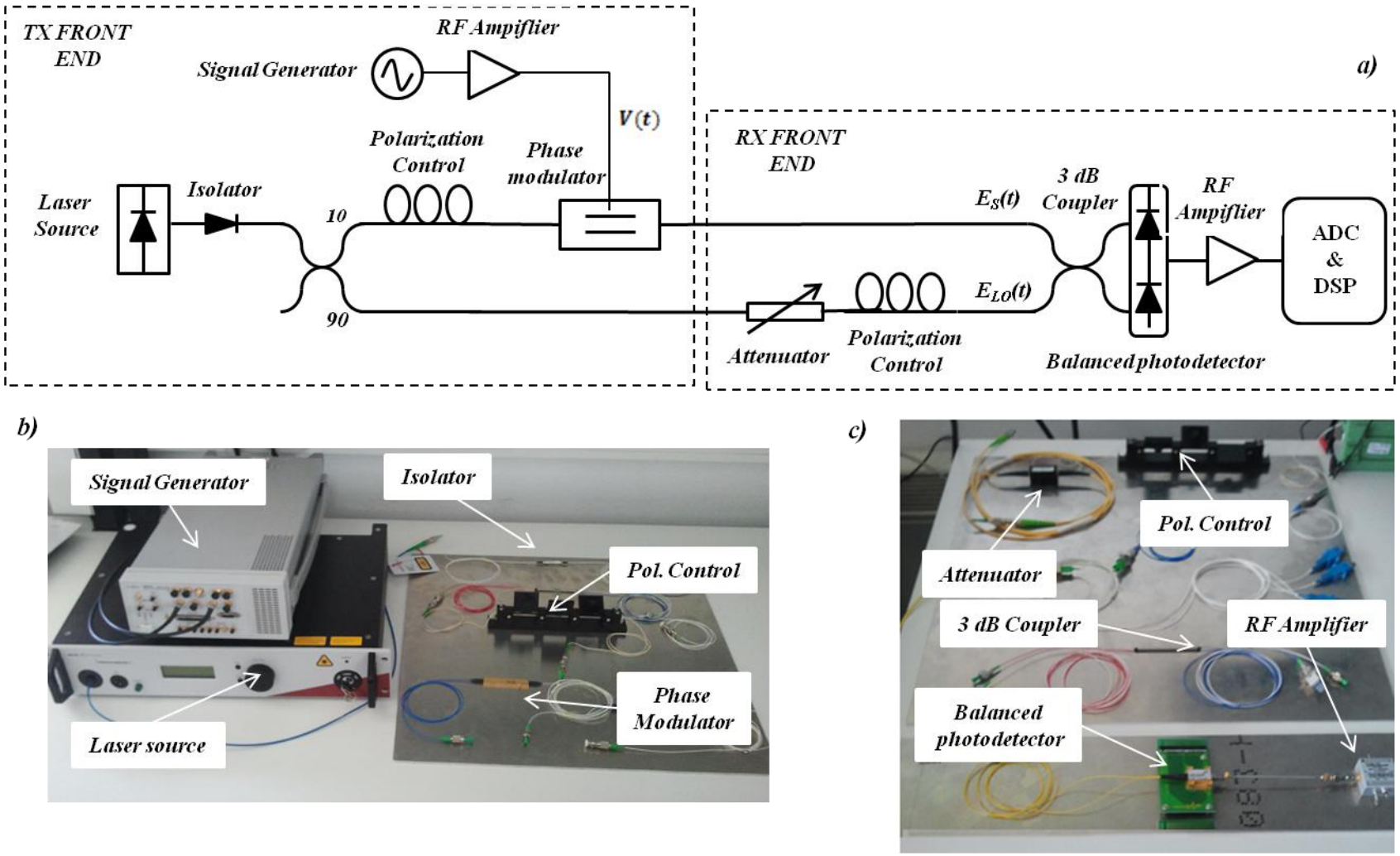

Fig. 2-24. a) Experimental setup for optical self-heterodyne QPSK communications front end. The light beam coming from the laser is sent through an optical isolator. The resulting signal in divided by a 90/10 beam splitter. The high power signal is sent to a phase modulator where the modulated optical signal $E_S(t)$ is generated. The modulator is driven by the heterodyne current V(t) from Eq. 2.65, which is generated by amplifying the output of a signal generator. The signal coming from the transmitter is mixed by the 3 dB coupler LO signal, which is passed through an attenuator that controls the LO power arriving to the receiver, and a polarization controller, that maximizes the mixing efficiency at the coupler. The 3 dB coupler outputs are connected to a balanced photo detector, which generates the intermediate frequency current $I_{het}(t)$. This current is then translated into the digital domain by an analog to digital converter in order to apply digital compensation algorithms and demodulation. b) Implementation of the transmitter front end. c) Implementation of the receiver front end.

Table 2-3. Description of the commercial devices used to implement the coherent transmitter.

Description	Brand & Model	Parameter	Typical Value	Units
Arbitrary Waveform Generator	Agilent N8241A	Sample Rate	1.25	GS/s
		Resolution	15	Bits
		Noise Floor	< 150	dBc/Hz
		Waveform Length	8	MS/Channel
		Analog Output Vp-p	1	V
RF TX Amplifier	Mini-Circuits TB-409-84+	Frequency Range	DC-6	GHz
		Gain	24.3	dB
		Max. Ouput Power @1dB Compression	20.8	dBm
		Noise Figure	4.4	dBm
Laser Source	Koheras Adjustik System Laser E15	Central wavelength	1550	nm
		Laser emission	CW	
		Ouput power	< 80	mW
		Linewidth (Lorentzian)	0.1	kHz
		Frequency noise	26@1kHz	$Hz/\sqrt{Hz}$
		Phase noise	0.8@1kHz	$\mu rad/\sqrt{Hz}$
		Optical SNR	>50	dB
		Operating Temperature Range	15-50	ºC
Fiber Isolator	Thorlabs IO-H-1550 APC	Insertion loss	<0.6	dB
		Extinction Ratio	>20	dB
		Return Loss	>55	dB
		Isolation	40	dB
90/10 Fiber Optical Coupler	Thorlabs 10202A-90-FC	Coupling ratio	90/10	
		Insertion Loss	12.7/0.8	dB
		Excess Loss	0.2	dB
		Directivity	>60	dB
Phase Modulator	Thorlabs LN53S-FC 10 GHz	E/O Bandwidth	10	GHz
		RF Drive π Voltage	4.5	V

		Optical Return Loss	40	dB
		Polarization Dependent	Yes	
		Insertion Loss	0.5	dB
Manual Polarization Controller	Thorlabs FPC032	Loop Diameter	27	mm
		Paddle Rotation	+117.5	º
		Bend Loss	< 0.1	dB

signals. The consequence is a small dynamic range and a reduced output voltage at all frequencies. A second integrated tool is the reconstruction filter at 500MHz realized as a 7-pole elliptical filter plus thru-line output. The filter purpose is to attenuate the harmonics generated by the DAC and reduce the noise floor. In the other hand, they cause a power loss around 2 dB and reduces the bandwidth to 500MHz. The last parameter we can configure in the signal generator is the amplification level. It consists on an analog amplifier, placed after the DAC, which amplifies the RF signal. Unfortunately, it diminishes the signal purity and increase the noise floor.

Table 2-4. N8241A Agilent AWG performance for different configuration parameters

Predistortion Filter	Amplification	Reconstruction Filter	Maximum Power (dBm)	Noise Floor (dB)	2^{nd} Harmonic
X	✓	X	0	-82	-53
X	✓	✓	-0.82	-80	-71
X	X	X	-5.84	-96	-75.19
X	X	✓	-6.11	-96	-75
✓	✓	X	-7.2	-100	-77
✓	✓	✓	-10.1	-100.1	-80.3
✓	X	X	-11.4	-100.1	-82.2
✓	X	✓	-16.27	-105	-87.11

In order to decide which parameters would provide us a better solution, we present the AWG results in Table 2-4. Here we can see that the best noise floor level and an acceptable harmonic generation are obtained with the pre-distortion filter active. In this scenario, introducing the reconstruction filter doesn't improve the performance of the noise floor, but it leads to a high power loss. The light coming from the laser at 1550nm is transmitted through an optical isolator, the Thorlabs IO-H-1550-APC, which presents isolations above 36 dB. This device protects the source of possible back reflections. The beam is then divided by a 90/10 optical beam splitter that

presents 0.81 dB losses. The function of the beam splitter is to divide the incoming signal on two: the optical signal that will be modulated and the optical signal that will act as local oscillator. Before the optical modulator, the beam is sent through a Thorlabs FPC032 polarization controller that allows us to modify the polarization state of the light coming from the laser.

The electrical signal generated on the AWG modulates the optical signal using a Thorlabs LN53S 10GHz integrated Mach-Zehnder optical phase modulator designed for high-speed data communications. It presents a typical working wavelength of 1525 nm and a RF π −drive voltage of 4.5 V. By default, this device has been bias trimmed so its zero-volt operating point is near the negative-slope quadrature. The implication of operating on the negative slope quadrature point is that the modulator will cause data inversion. This can be corrected by applying a bias voltage to achieve operation on the positive slope quadrature point, but this is not a preferred solution as the required bias voltage will be quite large. In our system we have the advantage that the phase offset can be corrected by software. This means that a sign inversion of the data will not affect our system performance and the optimal bias voltage can be used. To adapt the signal coming from the AWG (max. output 1 V) with the π −drive voltage (4.5 V) a RF amplifier is needed. For that purpose, the Mini-Circuits TB-409-84+ broadband amplifier with variable gain is used, which presents a variable gain from 0 to 24 dB up to 1 Ghz. The resulting signal coming out from the phase modulator acts as the transmitted signal of the system. The output power can be directly controlled from the laser source control panel.

As we saw previously in this section, there is a phase offset $\emptyset_S\,[rad]$ that must be calculated in order to demodulate any M-PSK signal. Since usually the line frequency width is much smaller than the symbol rate, it is reasonable to assume that $\emptyset_S\,[rad]$ is constant over each symbol duration. In real systems, we have to consider how this line width influences the bit error rate of the system. For that we use the expression obtained in [100]:

$$BER = \int \frac{1}{\sqrt{2\pi\sigma_\varphi}} e^{-\varphi^2/(2\sigma_\varphi^2)} d\varphi \qquad 2.79$$

where ${\sigma_\varphi}^2 = 2\pi\tau * \Delta\vartheta\,[W]$, $\tau\,[s]$ is the coherence time, and $\Delta\vartheta\,[Hz]$ is the laser linewidth. In Fig. 2-25 the influence of the variance on the bit error of an ideal PSK demodulator can be observed.

Our laser specifications indicate that its Lorentzian line width is less than 0.1 Khz. Also, if the laser variance ${\sigma_\varphi}^2$ is lower than 0.01 there is no effect on the system BER. This means that we can calculate the maximum coherence time so we can avoid this effect:

$$\tau_{max} = \frac{{\sigma_{\varphi,max}}^2}{2\pi\Delta\vartheta} = \frac{0.01}{2\pi * 100} = 1.59155 \times 10^{-5} \qquad 2.80$$

This time corresponds to a symbol frequency of 62.831 Khz. The maximum bandwidth in our system is 625 MHz, which means that the phase offset can be calculated calculated over a maximum number of symbols N_{max} calculated as:

$$N_{max} = \frac{BW}{f_S} = \frac{625\ x10^6}{62.831\ x10^3} \cong 10^4 \qquad 2.81$$

where BW is our system bandwidth [Hz] and f_S is the symbol frequency [Hz]. So by using a maximum of 10^4 symbols we will avoid the laser phase noise influence over the phase offset estimation.

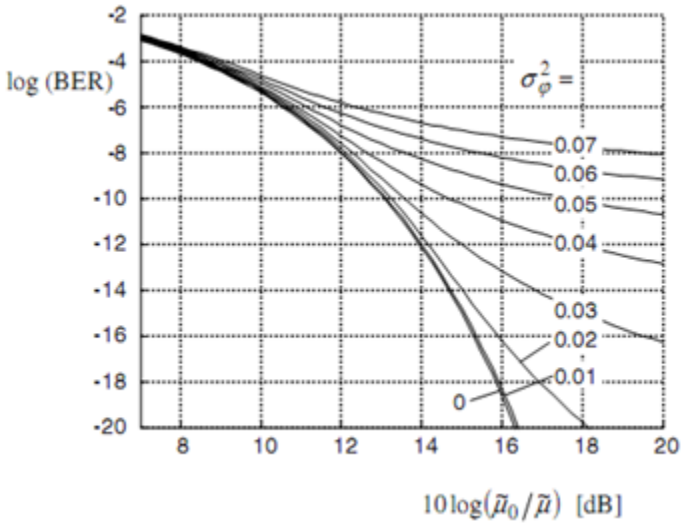

Fig. 2-25. BER performace for synchronous PSK (homodyne and heterodyne) in presence of phase noise with a variance σ^2 [100].

2.5.3 Implementation of an Optical Coherent Receiver

We have already presented in previous chapters the basic scheme of a heterodyne receiver (Fig. 2-24.c). In order to implement it we will reproduce exactly the same design, but substituting each

block for commercial devices. One important difference to mention is that we will use part of the power sent by the transmitter as a local oscillator on the receiver. This way we will only need one laser source on the complete system, which makes the system more affordable. This is called self-heterodyne detection.

Table 2-5. Description of the commercial devices used to implement the coherent receiver.

Description	Brand & Model	Parameter	Typical Value	Units
Variable Attenuator	Thorlabs VOA50-FC	Attenuation Range	1.5-50	dB
		Attenuation Resolution	0.1	dB
		Insertion Loss	< 1..5	dB
		Return Loss	> 55	dB
		Max. Power	300	mW
RF RX Amplifier	Mini-Circuits ZFL-1000G	Frequency Range	10-1000	MHz
		Gain	19	dB
		Max. Ouput Power @1dB Compression	3	dBm
3dB Coupler	Thorlabs 10202A-50-FC	Coupling ratio	50/50	
		Insertion Loss	3.8	dB
		Excess Loss	0.2	dB
		Directivity	>60	dB
Manual Polarization Controller	Thorlabs FPC032	Loop Diameter	27	mm
		Paddle Rotation	+117.5	º
		Bend Loss	< 0.1	dB
Oscilloscope	Agilent Infiniium DSO9104A	Analog Bandwidth	2	GHz
		Max analog sample rate	10	GSa/s
		Analog Input Channels	4	
		Vertical Resolution	12	Bits
		Input impedance	50	Ω
		Input Sensitivity	1	mV/div
		Maximum Input Voltage	5	V
		Time Resolution	1	Ps
Balanced Photodetector	U2T BPDV2150R	3 dB Cut-Off Frequency	40	GHz

		Operation Wavelength	1550	nm
		Responsivity	0.5	A/W
		Optical Return Loss	27	dB
		Polarization Dependent Loss	0.4	dB
		CMRR	15	dB
		Responsivity Imbalance	1.5	%
		Photodiode Reverse Voltage	3.5	V

The experimental setup shown in Fig. 2-24 is implemented by using the commercial devices described in Table 2-5. At the receiver, a Thorlabs VOA50-FC variable attenuator, which provides attenuations up to 50 dB, is used to control the LO power. Then the LO signal is sent through a Thorlabs FPC032 polarization controller that allows us to modify the polarization state of the LO beam to match the polarization of the transmitted signal and, maximizing the output of the mixing efficiency stage. To perform the heterodyne mix a 3 dB optical coupler is used to combine the LO and transmitted signal. The resulting optical output is transformed into an electrical signal using a U2T BPDV2020R 40 GHz balanced photo detector with a responsivity of 0.5 A/W. The resulting electrical signal is amplified by a broadband Mini-Circuits ZFL-1000G variable amplifier in order to maximize the adaptation to the D/A converter.The electrical signal coming from the balanced photo detectors is converted into the digital domain by using an Analog to Digital Converter (ADC). The device used is an Agilent Infiniium 9000 Series Osciloscope (DSO9104A) with an analog bandwidth of 2GSa/s, which acquires the electrical signal and delivers it to the DSP stage. At this point we are able to apply the digital processing algorithms explained in previous sections in order to recover the transmitted data. These algorithms are implemented by using the National Instruments Labview 2012. The system parameters defined for the transmitter will be used in the receiver (number of symbol pilots, pulse shaping, constellation, etc). The software implemented is responsible for the data acquisition, impairment compensation and system BER performance evaluation.

To calculate and calibrate the clock deviation that exists between our digital transmitter and digital receiver we need an external reference that, independently of its own deviation, will measure the central frequency generated by each device at a single frequency. The objective is to see if this clock deviation generates a constant frequency deviation through the working

frequency range. For that, the central frequency of the generated sine is progressively shifted and a measurement of the deviation for each frequency and each channel is performed (Fig. 2-26). In this figure we observe that the deviation increases as the central frequency grows up. The results are almost identical for both channels. From this graph we can extract that the deviation is linear and depends on the working frequency. Other parameters that could influence this deviation were studied, as output power, pre-distortion filters or output filters, but no dependences were found. From this graph we can extract that the deviation can be modeled as a percentual deviation around 0.0015%. With this calibration the clock of both systems are synchronized by using a digital fractional re-sampling stage, which compensates this static deviation.

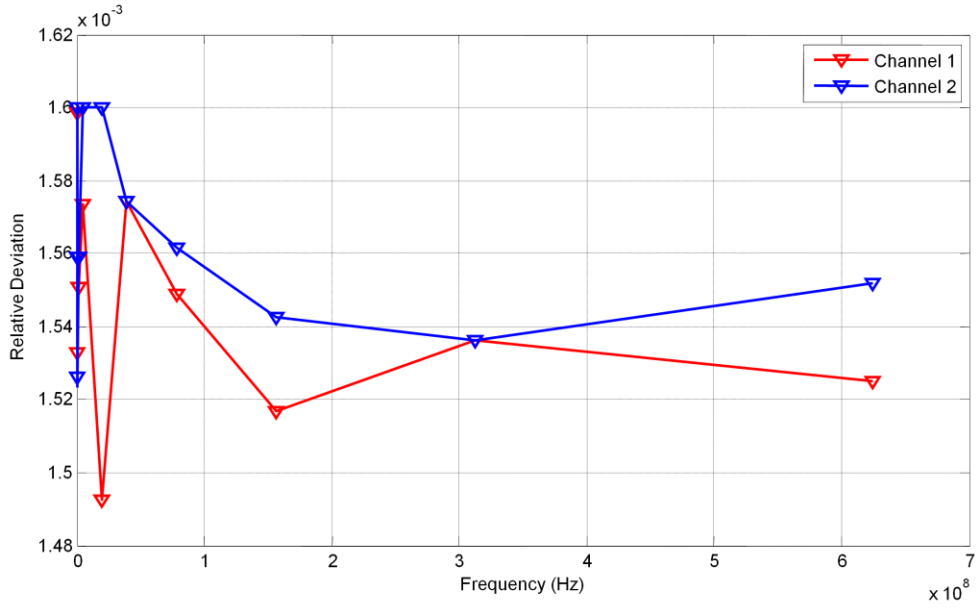

Fig. 2-26. Relative Clock Deviation between N8241A and DSO9104A

2.5.4 Software Front End

In order to test the behavior of the transmitter and receiver implementation a LabView control software is implemented. The data and symbol generation involved in the transmitter as well as the acquisition and impairment compensation blocks are developed using LabView 2012. This software also allow us to perform the control of the hardware equipment involved in the transmitter (AWG Agilent N8241A) and in the receiver (Agilent Infiniium DSO9104A) by using standard drivers and functions provided by the constructor. The implemented transmitter and receiver control panels are shown in Fig. 2-27 and Fig. 2-28, respectively.

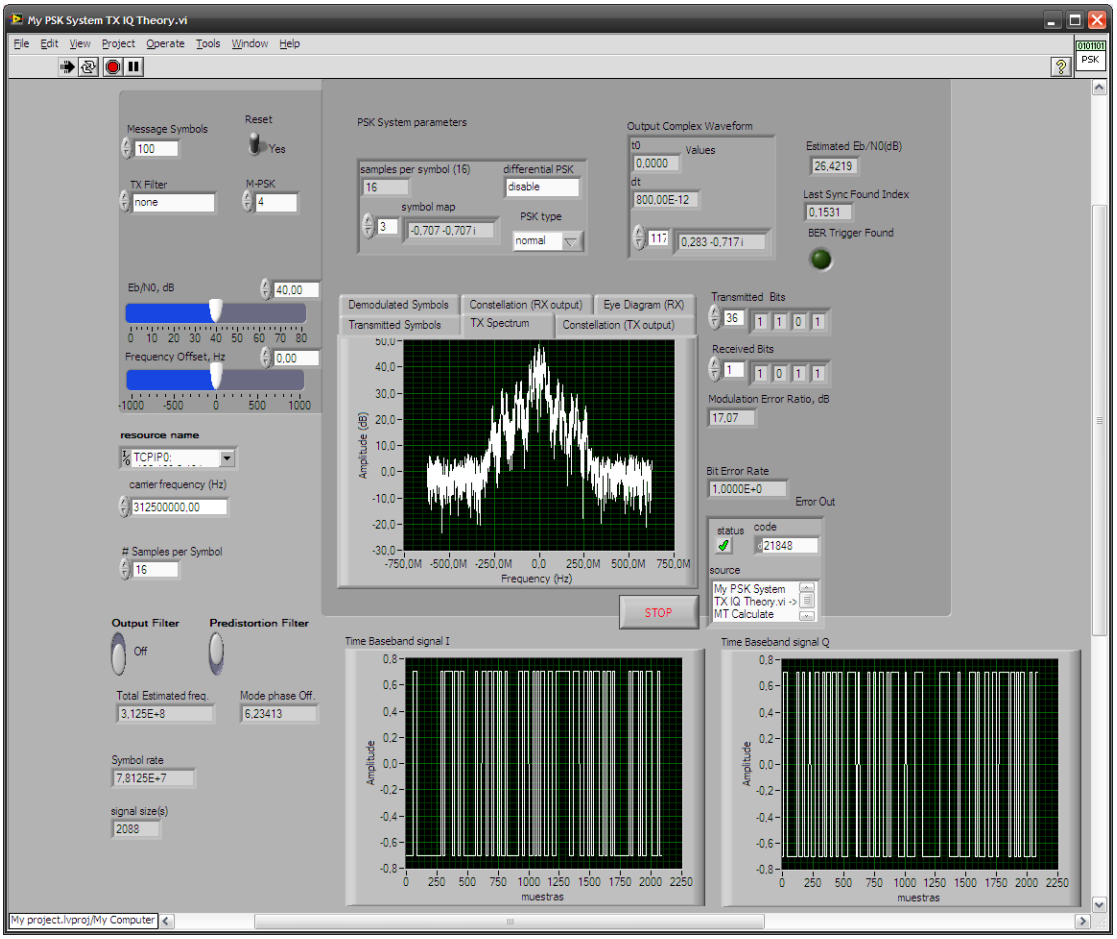

Fig. 2-27. Transmitter control panel using Labview. From this panel the digital transmission parameters are configured as well as the control over the arbitrary waveform generator.

The prototype is designed with the main objective of validating the transceiver of an optical coherent system that uses complex modulation formats as well as direct methods at a maximum symbol rate of 625 MHz on single polarization. The 312.5 Msymbols/s baseband data signal is modulated by a carrier frequency at 312.5 MHz. The number of symbols sent is based on the laser line width characterization previously derived, implying that at this data rate we are able to send a maximum of $5x10^3$ symbols assuming a constant phase offset. The data rate is chosen to be the maximum allowed by the AWG, which implies that the transmitter will be using 2 samples per symbol resulting into a baseband signal of 312.5 MHz bandwidth. The AWG is configured to work in the optimal scenario using a pre-distortion filter, maximum amplification and no filter at 500MHz.

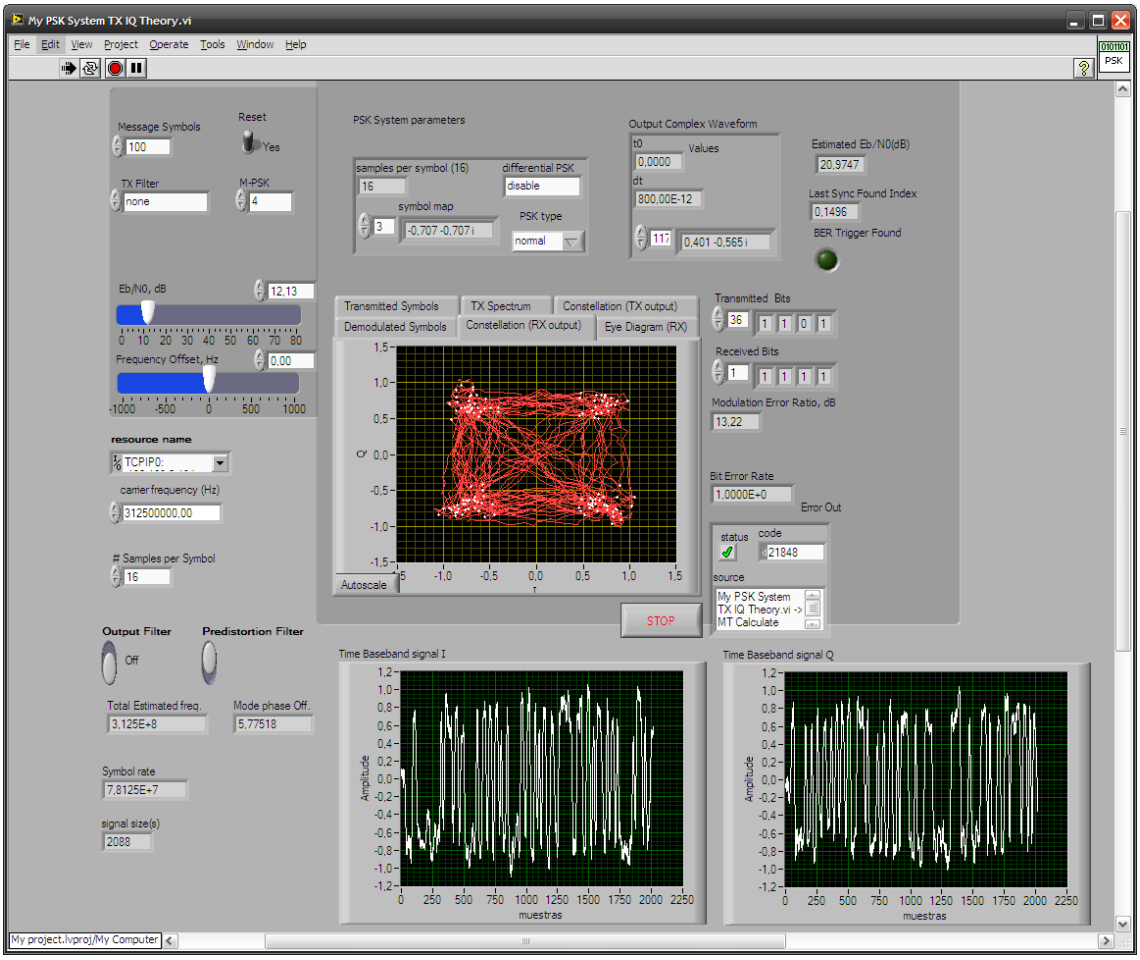

Fig. 2-28. Receiver control panel using Labview. This panel controls the receiver parameters, the ADC acquisition configuration and the DSP for impairment compensation. It also performs the demodulation process, showing the demodulated IQ diagram and system BER.

The shape filter used can be modified by parameterization, being able to use raised cosine, root raised cosine, Gaussian filter or none. The fixed preamble used to solve the phase ambiguity at the receiver is chosen to be eleven symbols and it is configured to be unique. In the transmitter it is also possible to configure other parameters such as frequency deviation, white noise addition or IQ impairments. The communication system parameters are shown in Table 2-6. Digital filtering is applied by re-sampling and channel impairments are optionally applied using additive and multiplicative noises. The digital signal processing algorithms previously explained in this chapter are used applying the system parameters defined in the transmitter. After demodulation in burst mode the system BER can be calculated under different SNR scenarios and system parameters, which allow us a high flexibility on the system definition.

Table 2-6. Communication system parameters.

Parameter	Typical Value	Units
Modulation Format	M-PSK	
Modulation Order (M)	4	
Intermediate Carrier Frequency	312.5	MHz
Baseband Signal Bandwidth	312.5	MHz
Transmission Rate	625	Mb/s
Communication Mode	Burst Mode	
TX Filter	None	
Symbols per Packet	5000	S/packet
Number of Pilot Symbols	11	S/packet
Packet Duration	0.016	ms
Computational Delay	52	ms
Predistortion Filter	ON	
Output Filter	OFF	
Fractional Re-sampling Factor	0.0015	%

2.6 Experimental System Performance for the Fiber Coherent Communication System

In this section the robustness of the coherent system is tested. First of all, the functionality of the receiver in absence of impairments is checked to demonstrate the system validation for then compare its performance with the one of an ideal receiver working in a quantum limited scenario (Eq. 2.55). It is demonstrated that the system is able to send and receive information using a QPSK single polarization complex modulation, achieving different data rate as a function of the system parameters used. We test the BER performance of the system under AWGN in absence of each compensation block, which shows the performance improvement and penalization introduced by each one. From this study it is shown that the phase and frequency estimator achieves a good practical performance by averaging the information along the symbols sent in a packet.

First, the experiments are performed by using the parameters described in the previous section and reaching a total number of bits transmitted above 10^6 for each SNR scenario. This way the BER can be analyzed as the SNR per bit is modified by adding AWGN through computation. The BER obtained for each case can be seen in Fig. 2-29.

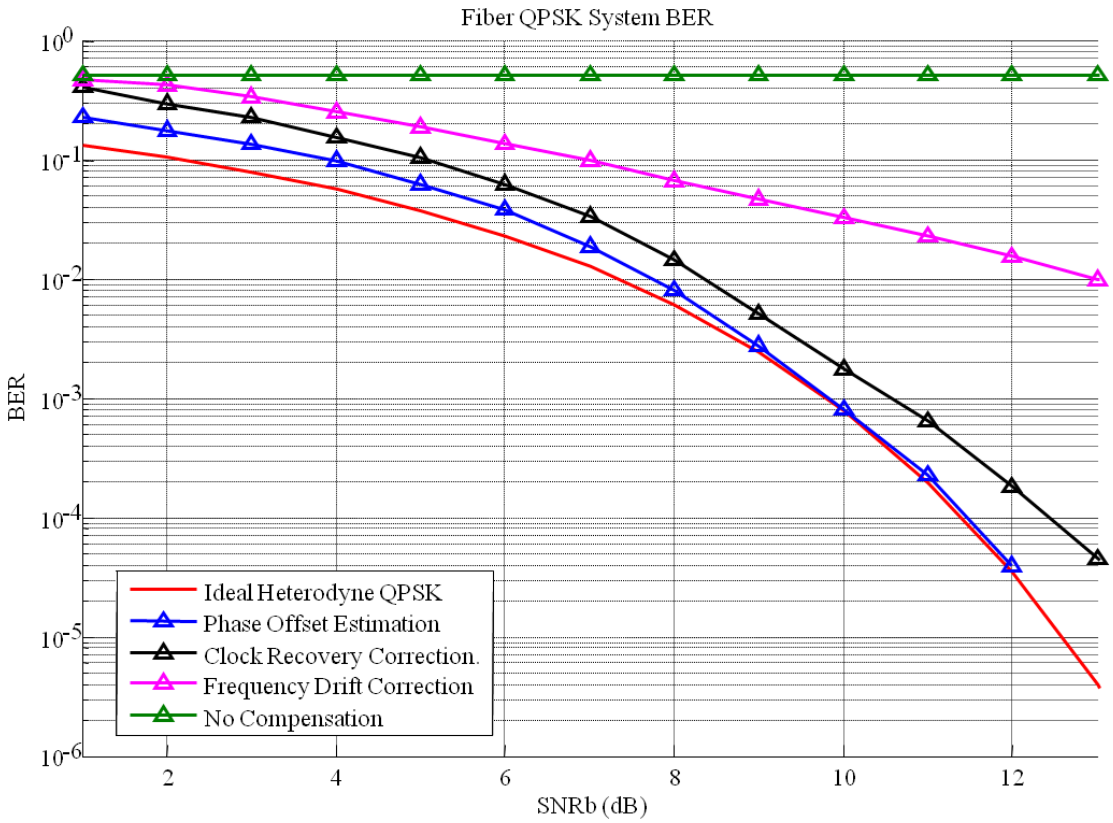

Fig. 2-29. System performance in the presence of compensation algorithms. The system BER is obtained for different SNR scenarios and compensation techniques. When compensation techniques are not applied, data demodulation becomes random. By introducing a frequency offset estimator the system is able to demodulate data correctly. The clock recovery block improves the receiver performance, but the system becomes optimal when the phase offset estimator is applied. In this situation, for SNR higher than 8 dB the sensitivity penalization is around 0.1dB in compare to the theoretical limit.

When no frequency correction is applied the demodulated symbols are completely random. This means that a small frequency deviation, if it is not compensated this effect can destroy completely the transmitted data. Even when no additive noise is present, the demodulated phase is not correct due to the phase drift. The frequency offset present in our system is due to the instantaneous difference between the transmitter and receiver carrier frequencies. This difference is caused by the deviation between the AWG reference clock and the oscilloscope reference clock. When the frequency offset is compensated by estimating the residual carrier described in Section 2.4.2, the receiver is able to demodulate correctly the transmitted data.

Still, the difference with the theoretical limit is large. This is because the sampling rate is not matched with the one at the transmitter. The effect is that, at the receiver, the shape filter is

not optimal and it introduces an error due to inter-symbol-interference (ISI). When the clock recovery block is included, the behavior of the receiver improves up to 6dB, obtaining a closer curve to the theoretical results. At this point we still have a penalization close to 1.5 dB, which can be improved by estimating the phase offset over a higher number of symbols. The resulting BER after averaging over 5000 symbols almost matches the theoretical limit when the SNR is higher than 8dB. The residual deviation present at higher SNR may be caused by some of the impairments such as asymmetric hybrids, limited bandwidth, small frequency deviations or by the clock parameter estimation.

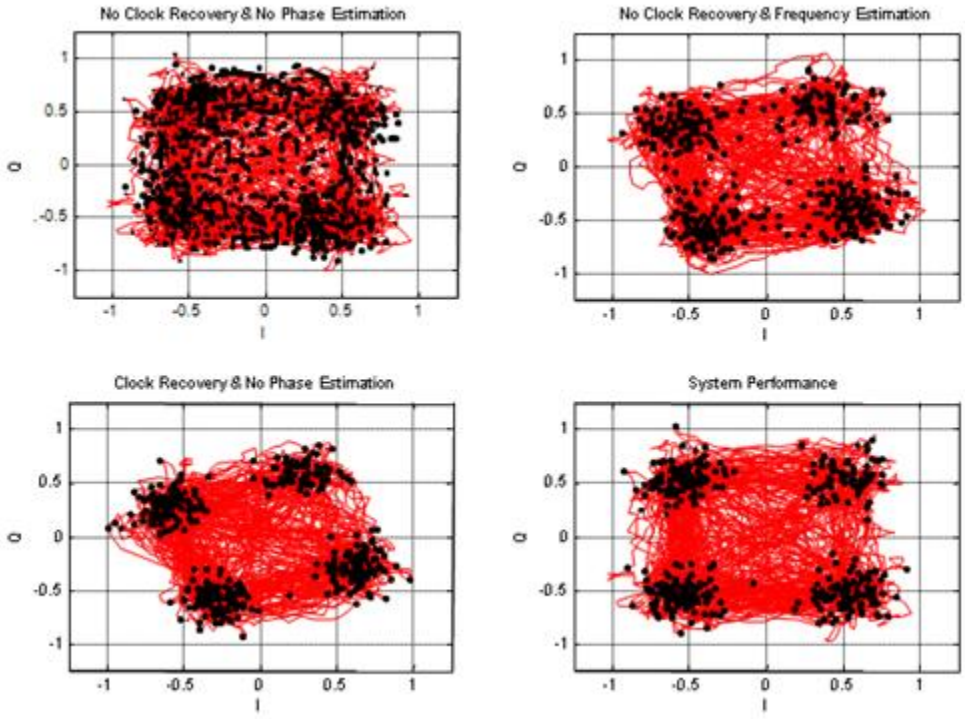

Fig. 2-30. Demodulated QPSK IQ diagram working with an SNR of 10 dB when (a) No clock recovery and no phase estimation (b) no clock recovery and frequency estimation (c) clock recovery and no phase estimation (d) frequency and phase compensation and clock recovery.

Working with a SNR of 8 dB the penalty introduced over the SNR is 1.02 dB. For lower SNR the phase estimator losses some accuracy and the differences are higher. The maximum penalization introduced by this block is around 2dB in the worst scenario considered. This additional error is mainly due to the phase unwrapping stage, which transform a continuous phase into a circular one. At low SNR, phase jumps are not detected and contribute significantly to the

calculated average. When the SNR is good enough to avoid this jumps the penalty introduced is less than 0.1 dB.

By taking a look to the IQ diagrams (Fig. 2-30) we can visualize the effects already mentioned. When clock recovery is not applied the sampled point are not optimally chosen so we have a high dispersion around each ideal symbol. By adding the frequency estimation at this point we see that the performance improves but there is a residual phase offset that is not correctly estimated. This is due to the fact that the phase offset is calculated by using the sampled points. If these points contain an error, it will be transmitted to the phase offset estimator. When clock recovery is applied, the sampled points are chosen to be optimal and they are closer to the original constellation points. Still, the IQ diagram is phase shifted and the phase estimator is needed is order to avoid errors. We get the optimum scenario by applying both algorithms. Here, the IQ diagram presents the demodulated symbols around the ideal constellation points. The distance to the ideal point is mainly due to the particular AWGN noise added by computation.

From this study, the functionality of the system and blocks has been validated. The results demonstrate the viability of the system and the BER performance is close to the theoretical values presented in previous sections. The compensation algorithms have been shown to be crucial for the proper symbol demodulation. The penalization introduced by these algorithms has been experimentally measured and it has been shown that, when the SNR is above a certain threshold, this penalization can be neglected and the system achieves an optimal performance.

3 Atmospheric Turbulence in Free Space Optical Coherent Systems

In this chapter we describe the fundamentals of atmospheric turbulence and its effects on laser beam propagation. The Kolmogorv theory of turbulence, as well as the Zernike polynomials and Noll's phase fluctuation model are presented. Then, the effects of phase fluctuations over FSO systems are addressed by modelling the resulting mixing efficiency under atmospheric turbulence. For simulating in the laboratory the influence that the turbulent atmosphere has on light beams, we introduce a practical method for generating atmospheric wavefront distortions that considers digital holographic reconstruction using a programmable micromirror array. We present the theoretical background of the method and we analyze the limits of the approach for different configurations of the micromirror array. An experimental set-up is then implemented in order to demonstrate the benchtop technique experimentally.

3.1 Turbulence Theory in the Earth's Atmopshere

3.1.1 The Kolmogorov Model of Turbulence

Any light beam that propagates through the atmosphere gets distorted by this random turbulent medium. The optical path of the light coming from any light source (laser, star, etc.) is altered by the varying refraction index of the Earth's atmosphere, which fluctuates randomly as a function of different parameters such us pressure, temperature, humidity, wind velocities and many other factors. In order to model this random channel, the atmosphere is considered a locally homogenous medium that temporally changes following a quasi-random behavior. This motion has been proved to present some statistical consistency that allows us to extract mathematical expressions to model the atmospheric turbulence.

The main approach has been the Kolgomorov statistical model, proposed by the Russian mathematician Andre Kologmorov in 1941 [101] in the paper "The local structure of turbulence in incompressible viscous fluid for very large Reynolds numbers". Here the atmosphere is

considered as a turbulent media where the kinetic energy of large scale motions is handed over smaller scale motions and an statistical homogeneity and isotropy can be assumed when the Reynolds number of the flow is sufficiently large. It also shows the well-known "two-third power law", responsible for the unusual power coefficients that appear when working with atmospheric turbulence. The complex nature of the atmospheric turbulence has been applied to a great variety of simulations [26] and has been supported by many experimental measurements [102]. One of the most important applications of this model has been described by Tatarskii in [103], where he completely defines the propagation of electromagnetic waves in a turbulent medium. Nowadays, the study of the atmospheric statistics is an active research field, covering from novel mathematical models to new experimental measurements.

In order to model mathematically the spatial fluctuations of the refraction index of the atmosphere, Kolgomorov proposed statistical expressions to emulate the turbulent atmosphere for different strength scenarios. Its model is based on a type of energy transfer called *energy cascade theory* that considers the atmosphere as a water mass which is heated by the encircling air. This model is based on the fluctuations of the refraction index on the velocity fluctuations derived from considering the atmosphere as a turbulent medium where the fluid movement and dissipation of energy goes from a macro scale (L_0) to a micro scale (l_0). These two regions are called outer scale and inner scale, respectively. The process can be understood as a continuous transfer of energy where the big masses are broken down into smaller particles, passing the inertial forces from one scale to another. Any region above or below these scales are considered statistically homogeneous and isotropic, so when the particles are smaller than l_0, the remaining energy is transformed into heat [103]. This structure for the transfer energy can be visualized in Fig. 3-1.

To give a brief mathematical of the Kolgomorov approach, let us start considering one single atmospheric wind layer that can be defined in terms of its velocity v, its viscosity ɳ an its outer length scale L_0. Assuming that the fluctuation occurs in a layer with composed by particle of size l, the motion energy for unit mass is ${v_l}^2$ and the time scale associated to its occurrence is $\tau = l/v_l$ [101]. The energy per unit transported is estimated as

$$\varepsilon \sim {v_l}^2/\tau = {v_l}^3/l \qquad 3.1$$

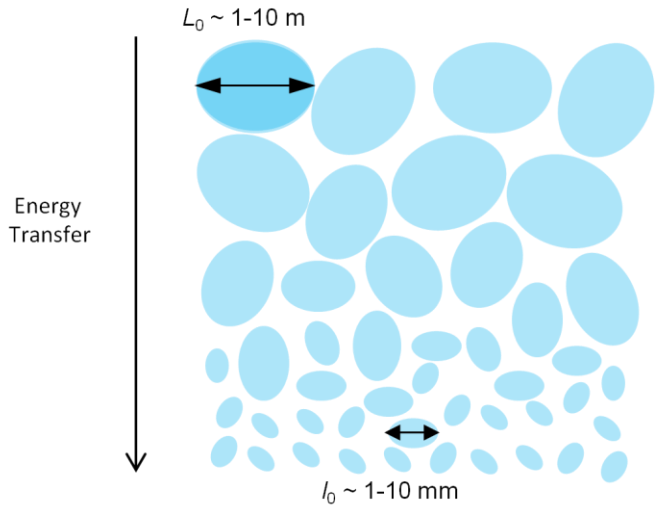

Fig. 3-1. Kolgomorov model of turbulence known as the *cascade energy theory*. The outer scale region particles (L_0) are broken down into smaller particles (l_0), passing the inertial forces and energy from one scale to another. After this stage, the energy is dissipated to heat.

An opposite effect to this wind motion energy is the viscosity of the medium itself. The total energy per unit time ε that is dissipated from this fluctuation is given by [101]

$$\varepsilon \sim \eta v_l{}^2 / l^2 \tag{3.2}$$

So the fluctuations can only carry on if $\xi > \varepsilon$. This condition can be assumed if we consider that $v_l l/\eta$ is sufficiently large [101]. This parameter is known as the Reynolds number. In this case, the fluctuations between layers become unstable and the big structures (L_0) are broken down into smaller ones until they reach a boundary scale (l_0) where the energy is dissipated. Typical values for these scales are 20 m and 1 mm, respectively. The atmospheric turbulence is a stochastic process, so its description must be essentially statistical. We can assume that the fluctuations of any physical property of the atmosphere (e.g. wind velocity, temperature, refractive index) is defined as $f(\vec{x})$, where $\vec{x}$ is a point in the x, y and z coordinates. The statistical characteristics can be described in terms of the structure function based on an average over a time span T [103]

$$D(\vec{x}_1, \vec{x}_2) = E\{|f(\vec{x}_1) - f(\vec{x}_2)|^2\} \cong \frac{1}{T}\int_{-T/2}^{T/2} |f(\vec{x}_1) - f(\vec{x}_2)|^2 \, dt \tag{3.3}$$

Considering that the turbulence is equal at all locations (homogeneous) and in all directions (isotropic), it can be shown that $D(\vec{x}_1, \vec{x}_2) = D(|\vec{x}_1 - \vec{x}_2|)$. Therefore, the structure function characterizes the fluctuations strength of $f(\vec{x})$ with a length scale comparable to $|\vec{x}_1 - \vec{x}_2|$. To

derive a more precise expression for the structure function we use the observations performed for the wind velocity structure function $D_v(\vec{x}_1, \vec{x}_2)$. From [103] we can assume that: first, the dominant contribution to the velocity difference between $\vec{x}_1$ and $\vec{x}_2$ are originated in particles with size $l \sim |\vec{x}_1 - \vec{x}_2|$, and, second, the energy dissipation for $l > l_0$ can be neglected. As a result, the energy in a single layer is maintained constant, so Eq. 3.1 must be hold between every scale from L_0 to l_0, thus leading to

$$D_v(\vec{x}_1, \vec{x}_2) \sim (\mathfrak{C}|\vec{x}_1 - \vec{x}_2|)^{2/3} = {C_v}^2(|\vec{x}_1 - \vec{x}_2|)^{2/3} \quad 3.4$$

where ${C_v}^2$ is defined as the structure constant and indicates the strength of the turbulence. The previous equation is widely known as "Kolgomorov's two-thirds law". Same conclusions could be achieved by using a dimension analysis [103]. Similarly, we can define the structure functions and constants for other physical properties of the atmosphere such us temperature, having:

$$D_T(\vec{x}_1, \vec{x}_2) = {C_T}^2(|\vec{x}_1 - \vec{x}_2|)^{2/3} \quad 3.5$$

where T corresponds to the temperature of the atmosphere.

For imaging systems, the motion of atmospheric cells presenting the same temperature does not influence the observations due to the fact that gas motion does not change the refraction index by itself. The problem is that the atmosphere is a pressure equilibrium medium. The change on the atmospheric pressure automatically implies a change on the temperature, creating time varying inhomogeneities in the refractive index $n(\vec{x}, t)$ that can be expressed as [103]

$$n(\vec{x}, t) \approx 1 + 0.00029 \frac{p(\vec{x}, t)}{1.3 \cdot 10^{-3}} \quad 3.6$$

where $1.3 \cdot 10^{-3}$ is the air density at 1 bar and 0 degrees Celsius measured in $g \cdot cm^{-3}$. Consequently, we can define a parameter, known as the structure parameter $C_n^2[m^{-\frac{2}{3}}]$, that can be expressed as a function of the pressure, *P [mb]*, the temperature of each layer *T [K]* and the temperature structure constant $C_T[K/m^{2/3}]$ obtained from measurements of the temperature variations between two points separated by a constant distance. The expression of the structure parameter is defined as:

$$C_n^2 = \left(79 \cdot 10^{-6} \frac{P}{T^2}\right)^2 C_T^2 \qquad 3.7$$

The value of C_n^2 is also a measurable quantity which usually take values from $1 \cdot 10^{-17} m^{-2/3}$ to $1 \cdot 10^{-13} m^{-2/3}$ under weak or strong turbulent conditions. Usually, the minimum values of C_n^2 occur near sunrise and sunset, while the highest values are present during midday [42]. Also, the highest turbulence is found in positions close to the earth surface, while it decreases for higher altitudes. Many accepted models to obtain C_n^2 as a function of the altitude have been proposed and accepted. One of the most complete models is the modified Hufnagel-Valley [104], which describes de turbulence strength taking into account the observation height and the height of the ground station. The expression given in this model is given by

$$C_n^2 = 0.00594 \cdot \left(\frac{V_{RMS}}{27}\right)^2 \cdot (10^{-5} \cdot h)^{10} exp\left(\frac{h}{1000}\right) + 2.7 \cdot 10^{-16} exp\left(\frac{h}{1500}\right) + \\ + A \cdot exp\left(\frac{H_{GS}}{700}\right) \cdot exp\left(\frac{-(h - H_{GS})}{100}\right) \qquad 3.8$$

Where h is the observation height, V_{RMS} is the square root of RMS value of the wind velocity difference between 5 km and 20 km height, H_{GS} is the ground station height and A is a parameter for ground near values observed that depends on the location and the hour.

In general, the Kolgomorov model of turbulence is often used in calculations due to its simplicity. Other models present a more precise description of the atmospheric turbulence by considering inner and outer scale effects. Two representative models are the modified Von Karman model and the modified atmospheric spectrum [105], but the study of these models is beyond the scope of this project.

3.1.2 Wavefront Distortions through Turbulent Atmosphere

The atmospheric turbulence distorts a transmitted light beam in several ways. The beam wander distortion shifts the centroid of the transmitted beam due to the influence of turbulent cells larger than the beam. The beam spreading effect reduces the averaged intensity at the receiver by broadening the beam radius. Constructive and destructive interferences effects within a beam redistribute the intensity inside a beam. These effects can be grouped as scintillation effects. In [105], a profound study of the effects of phase and amplitude fluctuations was performed to

evaluate FSO coherent systems. In this paper, the effects of amplitude fluctuations and wavefront phase distortion on the system performance were quantified, leading to two different regimes of turbulence depending on the receiver aperture diameter normalized to the coherence diameter of the received wavefront. When the normalized aperture diameter is small, amplitude scintillation dominates and, as phase fluctuations have little impact. In the other hand, for larger aperture sizes, amplitude fluctuations become minor, and phase fluctuations become dominant. So, for most typical link designs, wavefront phase fluctuations are the dominant impairment and amplitude fluctuations effects can be ignored as they are a second order effect [105]. Consequently, wavefront distortions, cannot be neglected as they degrade the overall performance of any optical system, particularly in coherent communications systems [106][107]. This approach is a good estimation for most applications and it is sustained by experimental studies previously performed on the atmosphere [105].

Noll developed a mathematical analysis to describe the phase fluctuations produced by atmospheric turbulence [102]. For that, he used the Fried's parameter r_0, which can be seen as a statistical measure of the coherence length of the turbulence introduced by the atmosphere. The Fried parameter r_0 is defined as a function of the turbulence strength C_n^2 and is given by [105]

$$r_0 = \left[0.423 \cdot k^2 \cdot sec\,(\gamma) \int_0^\infty C_n^2(z)dz\right]^{-3/5} \tag{3.9}$$

Based on r_0, Noll proposed an intuitive representation of the coherence function $B_w(\vec{r})$ of an specific wavefront $W(\vec{x}) = exp\big(j\varphi(\vec{x})\big)$. The coherence function is defined as

$$B_w(\vec{r}) = \langle W(\vec{x}+\vec{r})W^*(\vec{x})\rangle = \langle exp\big(j\varphi(\vec{x}) - \varphi(\vec{x}+\vec{r})\big)\rangle = exp\left[-3.44\left(\frac{r}{r_0}\right)^{5/3}\right] \tag{3.10}$$

The resulting structure function of the phase wavefront, defined as $D_\varphi(\vec{r}) = |\varphi(\vec{x}) - \varphi(\vec{x}+\vec{r})|^2$, can then be expressed as

$$D_\varphi(\vec{r}) = 6.88\left(\frac{r}{r_0}\right)^{5/3} \tag{3.11}$$

The phase structure function goes with the five-thirds power of the distance between two points, and the 6.88 factor is selected a value such the wavefront is distorted around 1 radian of root-

mean square (RMS) phase difference over a distance r_0. In order to obtain a general expression for the image distortion introduced by the atmospheric turbulence we introduce a imaging concept in which the measured flux of the aberrated wavefront $W(\vec{u})$, where $\vec{u} = \vec{x}/\lambda$, entering through a telescope [105] is given by:

$$\langle S(\vec{f})\rangle = B_w(\vec{f})T(\vec{f}) \tag{3.12}$$

Where $\vec{f} = \vec{r}/\lambda$, $T(\vec{f})$ is the transfer function of the telescope and $B_w(\vec{f})$ is the autocorrelation of the wave at the aperture plane. If we consider a Gaussian beam with beam with beam waist w_0, the random variations previously described result into a broadening of the beam. The relation between r_0 and w_0 is given by [21]

$$\frac{w_0}{r_0} = \frac{\sqrt{(w_{le}/w_{dl})^2 - 1}}{3} \tag{3.13}$$

where w_{dl} and w_{le} are the *1/e* radius of the diffraction limited beam and averaged broadened beam. As an example on how turbulence degrades optical systems we consider the ideal case of a point source correctly focused on the focal plane. This source will produce an airy pattern and its diameter is defined by [108]:

$$d_{airy} = 2.44 \cdot \frac{f \cdot \lambda}{D} \tag{3.14}$$

Being f the focal length of the optical system. After this light beam is propagated through the atmosphere, the airy disc will become wider at the focal plane as a consequence of the turbulence. The averaged spread function of the airy pattern diameter over a long period of time is determined by [109] and can be expressed as

$$d_{spread} = 0.98 \cdot \frac{f \cdot \lambda}{r_0} \tag{3.15}$$

This means that the well-focused spot becomes a random Function of smaller spots that vary in time and space depending on the atmospheric perturbation. A representative set of possible different scenarios are shown in Fig. 3-2.

Consequently, r_0 has become an important parameter in free space optical systems as it provides a very intuitive measure of the *seeing* condition at the receiver plane in a particular site. The resulting coherence length, usually from 5cm for poor seeing conditions and 25 cm in excellent seeing conditions, provides a suitable metric of the telescope aperture *D* needed in a specific optical system in order to have a well defined light spot in the focal plane. If r_0 is much lower than *D* the telescope will receive many different coherent regions, which will imply a degradation of the received image. If r_0 is equal or higher than *D*, it would imply that only one coherent region is entering the receiver telescope and the image can be recovered perfectly.

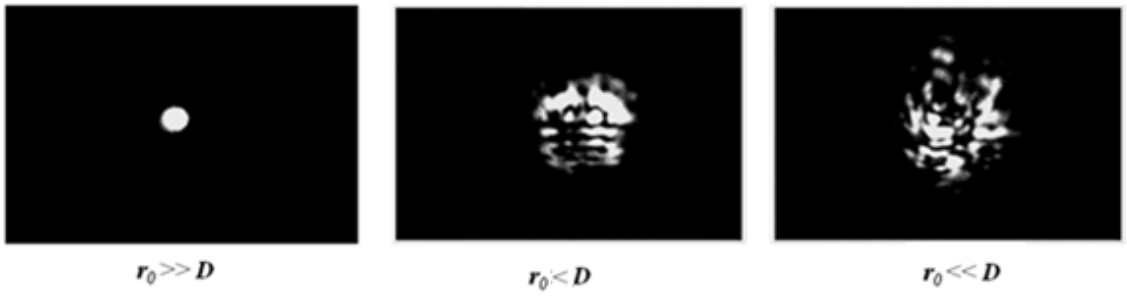

Fig. 3-2. Instantaneous image of a point source at the receiver plane under different turbulent scenarios depending on the Fried's parameter r_0 and the receiver telescope diameter *D*.

3.1.3 Zernike Polynomials and Noll's Phase Fluctuation Model

The most commonly used way of expressing wavefront aberrations is by means of specific set of polynomials with special characteristics. In this project we use a set of polynomials called Zernike Polynomials, which have been widely used due to the fact that they represent the typical optical aberrations such defocus, astigmatism, etc. Any wavefront aberration can be expressed as the sum of an orthonormal set of polynomials. Zernike polynomials form a complete set of functions or modes that are orthogonal over the unit circle, which make it very useful to work with circular apertures, the ones that we will be essentially considering. These polynomials are convenient for serving a set of basis due to several reasons. They are expressible in polar and Cartesian coordinates, they can be scaled so that non-zero order modes have zero mean and unit variance and they are recommended for describing wave aberration functions and data fitting for experimental measurements for the eye. Also, the terms are normalized so that the coefficient of a particular mode is the RMS contribution of that term, putting modes in a common reference frame for meaningful relative comparison.

Table 3-1. Zernike Polynomial expressions

mode j	order n	frequency m	$Z_n^m(\rho,\theta)$	Description
0	0	0	1	Piston
1	1	-1	$2\rho\sin(\theta)$	Tip
2	1	1	$2\rho\cos(\theta)$	Tilt
3	2	-2	$\sqrt{6}\rho^2\sin(2\theta)$	Defocus
4	2	0	$\sqrt{3}(2\rho^2-1)$	Astigmatism X
5	2	2	$\sqrt{6}\rho^2\cos(2\theta)$	Astigmatism Y
6	3	-3	$\sqrt{8}\rho^3\sin(3\theta)$	Coma X
7	3	-1	$\sqrt{8}(3\rho^3-2\rho)\sin(\theta)$	Coma Y
8	3	1	$\sqrt{8}(3\rho^3-2\rho)\cos(\theta)$	Trefoil X
9	3	3	$\sqrt{8}\rho^3\cos(3\theta)$	Trefoil Y
10	4	-4	$\sqrt{10}\rho^4\sin(4\theta)$	Spherical
11	4	-2	$\sqrt{10}(4\rho^4-3\rho^2)\sin(2\theta)$	2nd Astigmatism X
12	4	0	$\sqrt{5}(6\rho^4-6\rho^2+1)$	2nd Astigmatism Y
13	4	2	$\sqrt{10}(4\rho^4-3\rho^2)\cos(2\theta)$	Quadrafoil X
14	4	4	$\sqrt{10}\rho^4\cos(4\theta)$	Quadrafoil Y
…	…	…	…	…

The Zernike polynomials are frequently defined in polar coordinates (ρ,θ), being ρ the radial coordinate, ranging from 0 to 1, and θ the azimuthal component, ranging from 0 to 2π. Each polynomial consists of three components: a normalization factor, a radial dependent component and an azimuthal dependent component. The radial component is a polynomial and the azimuthal component is sinusoidal. A double indexing format is practical for unambiguously describing the functions, with the index *n* describing the highest power or order of the radial polynomial and the index *m* describing the azimuthal frequency of the azimuthal component. The Zernike polynomials are defined as [15]:

$$\begin{aligned} Z_n^m(\rho,\theta) &= N_n^m R_n^{|m|}(\rho)\cos(m,\theta) \quad for\ m \geq 0 \\ &= -N_n^m R_n^{|m|}(\rho)\sin(m,\theta)\ for\ m < 0 \end{aligned} \tag{3.16}$$

For a given *n: m* can only take values of *–n, -n+2, -n+4,…, n* and N_n^m is the normalization factor that can be expressed as:

$$N_n^m = \sqrt{\frac{2(n+1)}{1+\delta_{m0}}}\ \ with\ \delta_{m0} = 1\ for\ m = 0,\ \delta_{m0} = 0\ for\ m \neq 0 \tag{3.17}$$

and $R_n^{|m|}(\rho)$ is given by:

$$R_n^{|m|}(\rho) = \sum_{s=0}^{(n-|m|)/2} \frac{(-1)^s (n-s)!}{s!\,[0.5(n+|m|)-s]!\,[0.5(n-|m|)-s)!}\rho^{n-2s} \tag{3.18}$$

By following this expression, we can obtain the Zernike polynomials for each mode as a function of *m* and *n*. The first 14 modes are shown in a convenient order in Table 3-1.

The index *j* is a mode ordering number that can be obtained as a function of *n* and *m*. This ordering in terms of *j* classify the aberrations from low to high orders and it is suitable to express the modal orthogonality as

$$\delta_{jj^*} = \int P(r) Z_j Z_{j^*} d^2 r \tag{3.19}$$

where $P(r) = 1/\pi$ if $r \leq 1$ and $P(r) = 0$ elsewhere. So any arbitrary phase function can be expresses as a function of the Zernike polynomials over a circle of unity radius:

$$\varphi(\rho,\theta) = \sum_j a_j Z_j(\rho,\theta) \tag{3.20}$$

where a_j are the weights for each Zernike mode and are given by

$$a_j = \int P(r) Z_j \varphi(\rho, \theta) d^2 r \qquad 3.21$$

In Fig. 3-3 the Zernike wavefront aberrations for the first 21st modes ordered by the azimuthal and radial orders *(m,n)*. Using the Fried parameter and the Kolgomorov model, we can define any phase aberrated wavefront $W(\rho, \theta) = exp(j2\pi\varphi(\rho, \theta))$ by using the Noll's approach [102]. Using the phase structure function derived in Eq. 3.11 and considering that it is related with the Weiner spectrum $\Phi(k)$ as

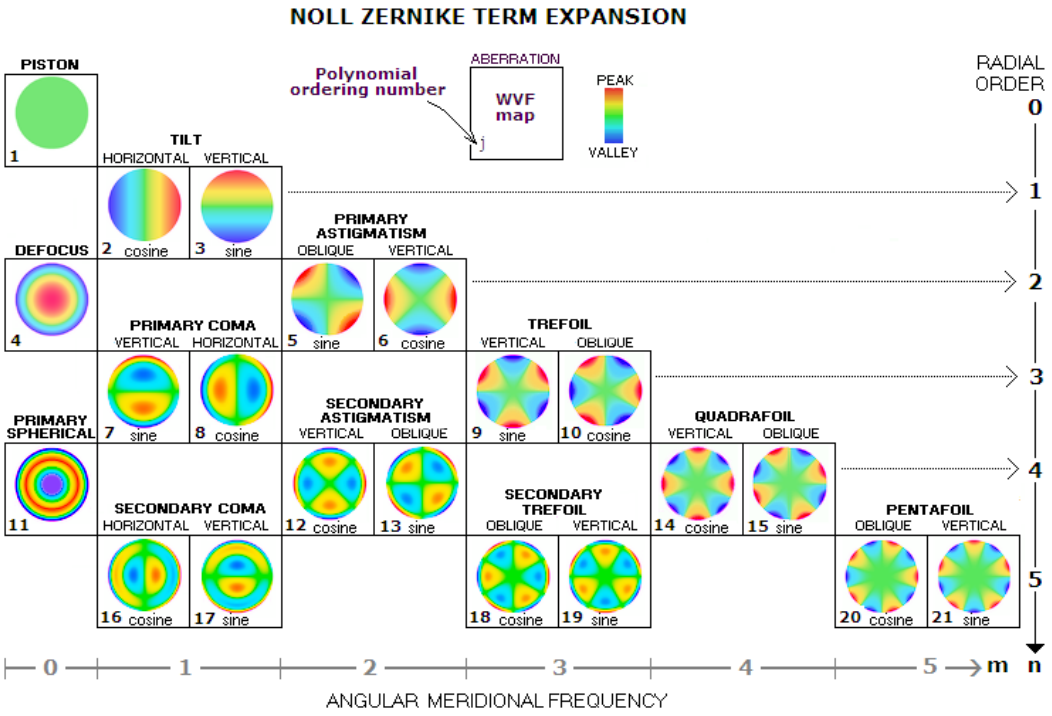

Fig. 3-3. Noll Zernike wavefront aberration for the first 21st modes ordered by the azimuthal and radial orders *(m,n)* [26].

$$D_\varphi(\vec{r}) = 2 \int \Phi(k) \left[1 - cos(2\pi k r)\right] dk \qquad 3.22$$

We obtain that the Wiener spectrum of the phase fluctuations using the Kolgomorov model of turbulence is [102]

$$\Phi(k) = \left(0.023 / r_0^{5/3}\right) k^{-11/3} \qquad 3.23$$

To represent this spectrum in terms of the Zernike modes we can evaluate the covariance of the coefficients in Eq. 3.20 and by considering them zero mean Gaussian variables. So, using Eq. 3.21 we obtain:

$$\langle a_j{}^* a_j \rangle = \int\int \Phi(k,k') Q_j{}^*(k) Q_{j^*}(k') dk dk' \tag{3.24}$$

where Q_j is the Fourier transform of Z_j and $\Phi(k,k') = \left(0.023/r_0^{5/3}\right) k^{-11/3} \delta(k-k')$. By using that [102]

$$Q_{even,j}(k,\theta) = K(-1)^{\frac{n-m}{2}} i^m \sqrt{2}\, cos(m\theta) \tag{3.25}$$

$$Q_{odd,j}(k,\theta) = K(-1)^{\frac{n-m}{2}} i^m \sqrt{2}\, sin(m\theta) \tag{3.26}$$

$$Q_{m=0,j}(k,\theta) = K(-1)^{\frac{n}{2}} \tag{3.27}$$

where $K = \sqrt{n+1} J_{n+1}(2\pi k)/\pi k$ and $J_l(x)$ is the lth order Bessel function and we obtain the Zernike matrix representation for the Kolgomorov phase spectrum [102]

$$\langle a_j{}^* a_j \rangle = \left(\frac{0.046}{\pi}\right)\left(\frac{1}{r_0}\right)^{\frac{5}{3}} [(n+1)(n' + 1)]^{\frac{1}{2}} (-1)^{\frac{n+n'-2n}{2}} \delta_{mm'}\, x \int \frac{J_{n+1}(2\pi k) J_{n'+1}(2\pi k)}{k^2} k^{-\frac{8}{3}} \tag{3.28}$$

This representation allow us to easily describe the residual phase error after performing the correction of the first J Zernike modes as

$$\sigma_J = \int P(r) \langle \varphi(\rho,\theta) - \varphi_{c,J}(\rho,\theta) \rangle \, d\rho = \sigma_\varphi^2 - \sigma_{c,j}^2 \tag{3.29}$$

where σ_φ^2 is the phase variance, $\varphi_c(\rho,\theta)$ is the applied phase map correction, and $\sigma_{c,j}^2$ is the applied phase variance. The correction phase map can be defined as

$$\varphi_{c,J}(\rho,\theta) = \sum_{j=1}^{J} a_{c,j}\, Z_j \tag{3.30}$$

$a_{c,j}$ are the Zernike coefficients of the correcting phase map. The resulting residual phase error from Eq. 3.29 is then:

$$\sigma_j^2 = \sigma_\varphi^2 - \sum_{j=1}^{J} \left| a_{c,j} \right|^2 \qquad 3.31$$

These residual errors σ_j^2, widely known as Zernike-Kolgomorov residual errors, can then be directly calculated using this expression and are given in Table 3-2.

Table 3-2. Zernike-Kolgomorov residual errors, σ_j^2, and their relation to *D/r0* for a Zernike Mode j

Zernike Mode	Zernike-Kolgomorov residual error
Tip	$\sigma_1^2 = 1.0299(D/r0)^{5/3}$
Tilt	$\sigma_2^2 = 0.5820(D/r0)^{5/3}$
Focus	$\sigma_3^2 = 0.1340(D/r0)^{5/3}$
Astigmatism X	$\sigma_4^2 = 0.0111(D/r0)^{5/3}$
Astigmatism Y	$\sigma_5^2 = 0.0880(D/r0)^{5/3}$
Coma X	$\sigma_6^2 = 0.0648(D/r0)^{5/3}$
Coma Y	$\sigma_7^2 = 0.0587(D/r0)^{5/3}$
Trefoil X	$\sigma_8^2 = 0.0525(D/r0)^{5/3}$
Trefoil Y	$\sigma_9^2 = 0.0401(D/r0)^{5/3}$
Spherical	$\sigma_{10}^2 = 0.0401(D/r0)^{5/3}$
Secondary Astigmatism X	$\sigma_{11}^2 = 0.0377(D/r0)^{5/3}$
Secondary Astigmatism Y	$\sigma_{12}^2 = 0.0352(D/r0)^{5/3}$
Larger Orders (j>12)	$\sigma_j^2 \simeq 0.2944\, j^{\sqrt{3/2}}(D/r0)^{5/3}$

The 5/3 exponent is a consequence of the Kolgomorov power law previously described in this chapter. Therefore, the phase variance over an aperture with diameter *D*, excluding piston errors, is given by

$$\sigma_1^2 = 1.0299(D/r0)^{5/3} \qquad 3.32$$

The resulting phase variance when correcting the tip and tilt components (j=1, 2) is

$$\sigma_3^2 = 0.134(D/r0)^{5/3} \quad 3.33$$

By using this approach we can calculate the phase of any wavefront after being distorted by the atmosphere and emulate the earth's atmosphere for different perturbation scenarios as a function of the normalized turbulence strength (D/r_0). The resulting wavefront phase can be expressed as

$$\varphi_g(\rho,\theta) = \sum_i X_i d_i Z_i(\rho,\theta) \quad 3.34$$

Where X_i is a random coefficient for the i^{th} mode using a zero-mean Gaussian distribution and unitary variance, and d_i is the total error associated to the *i-th* Zernike mode for a specific D/r_0 factor whose variance is $\sigma_{d_i}^2 = \sigma_i^2 - \sigma_{i+1}^2$.

3.2 Mixing Efficiency of Distorted Wavefronts

In Chapter 2 we assumed a perfect spatial phase matching between local oscillator and incoming signal in order to derive the expressions that describe the electrical intensities produced by the mixing and balanced photodetection stages. In FSO, it is of particular interest to understand the impact of atmospheric aberrations in these stages. When a laser beam propagates through a turbulent medium like the atmosphere several effects such as absorption, scattering, beam spreading and beam wander, scintillation, and phase front distortions degrade the mixing efficiency or the coupled power into a fiber as both spatial fields present any mismatch in terms of phase and amplitude. Knowledge of this mixing efficiency is therefore important to assess the feasibility of coherent receivers or systems using coupling stages into a fiber. It is relevant to note that the mixing efficiency and the coupling efficiency into a single mode fiber can be treated as the same problem [110]. The LO field in a coherent receiver is given by the fundamental Gaussian mode of the single mode fiber used, so the degradation on the mixing efficiency of coherent receivers can be calculated as the coupling efficiency into a single mode fiber degraded by atmospheric effects. In this section we try to perform a more realistic description of the mixing efficiency by taking into account the wavefront phase perturbations introduced by the atmosphere.

For two complex electrical fields, the mixing efficiency η at a specific time can be described as:

$$\eta(E_S(r), E_{LO}(r), t) = \frac{|\int E_S(r,t) {E_{LO}}^*(r,t)\, dr|^2}{\int |E_S(r,t)|^2 \int |E_{LO}(r,t)|^2} \quad 3.35$$

where $r^2 = x^2 + y^2$. $E_S(r,t)$ and $E_{LO}(r,t)$ can be expressed as:

$$E_S(r,t) = W_0(r) A_S(r) \cdot exp\,[i(w_S(t) + \varphi_S(r) + \emptyset_S)] \quad 3.36$$

$$E_{LO}(r,t) = W_0(r) A_{LO}(r) \cdot exp\,[i(w_{LO}(t) + \varphi_{LO}(r) + \emptyset_{LO})] \quad 3.37$$

with $w_S(t)$ and $w_{LO}(t)$ the temporal frequencies, $\varphi_S(r)$ and $\varphi_{LO}(r)$ are the spatial phases, and $\emptyset_S(t)$ and $\emptyset_{LO}(t)$ are the respective phases. $A_S(r)$ and $A_{LO}(r)$ are the field amplitudes filtered by the aperture

$$A_S(r), A_{LO}(r) = \begin{cases} A_{S,0}(r), A_{LO,0} & if\ r < D/2 \\ 0 & otherwise \end{cases} \quad 3.38$$

where D is the aperture diameter and $A_{S,0}(r)$ and $A_{LO,0}$ are the field amplitudes. Also, we can assume that the LO source presents a constant spatial phase $\varphi_{LO}(r)$ as it is not aberrated by the media. From here we assume heterodyne detection, where $w_S(t) \neq w_{LO}(t)$. Substituting Eq. 3.36 and Eq. 3.37 into Eq. 3.36 and taking the time average over the residual beat frequency $\Delta w = w_S(t) - w_{LO}(t)$ we obtain that the heterodyne efficiency is expressed

$$\bar{\eta}\big(E_S(r), E_{LO}(r)\big) = \frac{\left|\int A_S(r) A_{LO}(r) \cdot exp\big[i\big(\varphi_S(r)\big)\big]\, dr\right|^2}{\int |A_S(r)|^2 dr \int |A_{LO}(r)|^2\, dr} \quad 3.39$$

The resulting averaged heterodyne efficiency can be expressed as [111]

$$\bar{\eta}\big(E_S(r), E_{LO}(r)\big) = \eta_g\big(A_S(r), A_{LO}(r)\big) \cdot SR\big(E_S(r), E_{LO}(r)\big) \quad 3.40$$

Where $\eta_g\big(A_S(r), A_{LO}(r)\big)$ is the geometrical efficiency, which depends only on the relationship between the amplitudes and it is defined as

$$\eta_g\left(A_S(r), A_{LO}(r)\right) = \frac{\left|\int A_S(r)A_{LO}(r)\,dr\right|^2}{\int|A_S(r)|^2 dr \int|A_{LO}(r)|^2\,dr} \tag{3.41}$$

This efficiency is basically defined by the lens-to-fiber coupling geometry. The parameter $SR\left(E_S(r), E_{LO}(r)\right)$, usually known as Strehl ratio (SR), depends on the relationship between both, phase and amplitude, and it is defined as

$$SR\left(E_S(r), E_{LO}(r)\right) = \frac{\left|\int A_S(r)A_{LO}(r)\cdot exp\left[i\left(\varphi_S(r)\right)\right]dr\right|^2}{\left|\int A_S(r)A_{LO}(r)\,dr\right|^2} \tag{3.42}$$

We can also expand the averaged heterodyne efficiency from Eq. 3.39 by using $exp\left[i\left(\varphi_S(r)\right)\right] = cos\left(\varphi_S(r)\right) + isin\left(\varphi_S(r)\right)$:

$$\bar{\eta} = \frac{\left[\int A_S(r)A_{LO}(r)\cdot cos\left(\varphi_S(r)\right)dr\right]^2 + \left[\int A_S(r)A_{LO}(r)\cdot sin\left(\varphi_S(r)\right)dr\right]^2}{\int|A_S(r)|^2 dr \int|A_{LO}(r)|^2\,dr} \tag{3.43}$$

Therefore, the heterodyne efficiency can be expressed in terms of

$$\bar{\eta} \equiv \alpha^2 = \alpha_r^2 + \alpha_i^2 \tag{3.44}$$

Where α_r^2 and α_i^2 represent the integrals over the collecting aperture of the real and imaginary parts of the normalized optical field at the receiver and are defined by

$$\alpha_{r=} \frac{\int A_S(r)A_{LO}(r)\cdot cos\left(\varphi_S(r)\right)dr}{\sqrt{\int|A_S(r)|^2 dr \int|A_{LO}(r)|^2\,dr}} \tag{3.45}$$

$$\alpha_{r=} \frac{\int A_S(r)A_{LO}(r)\cdot sin\left(\varphi_S(r)\right)dr}{\sqrt{\int|A_S(r)|^2 dr \int|A_{LO}(r)|^2\,dr}} \tag{3.46}$$

3.2.1 Mixing Efficiency in the Absence of Atmospheric Turbulence

Let us first assume a perfect phase matching between both signals, so $\varphi_S(r) = 0$. In a single mode fiber-coupling system, the $E_{LO}(r)$ has the shape of the Gaussian profile contained in the fundamental mode. For coherent homodyne/heterodyne $E_{LO}(r)$ is the field of the LO laser, which can be also described as a Gaussian profile. Therefore, in both cases [21]

$$E_{LO}(r) = Aexp\left(\frac{-r^2}{{w_0}^2}\right) \quad 3.47$$

where w_0 is the mode radius. In Fig. 3-4 the coupling geometry for a plane wave over a circular aperture with diameter D is shown. An incoming aberrated plane wavefront $E_S(r)$ is focused by a lens into the core of a single mode fiber and $E_{LO}(r)$ is the inverse Fourier transform of the

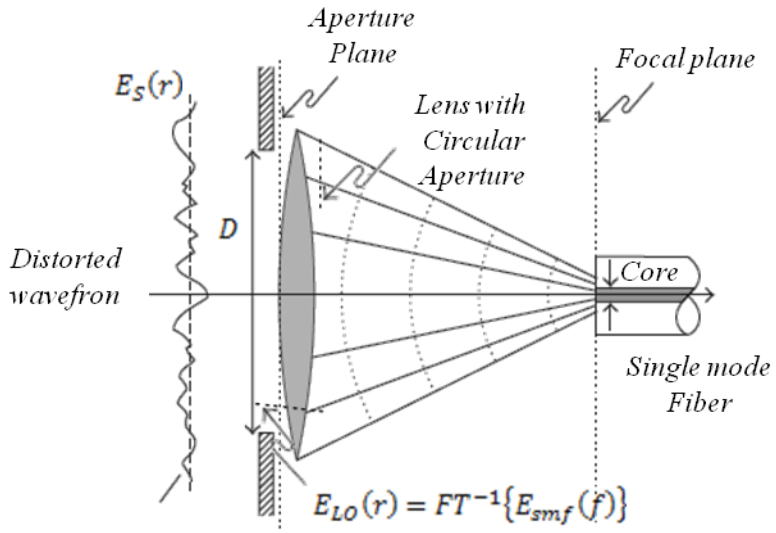

Fig. 3-4. Coupling geometry for a plane wave over a circular aperture with diameter *D*. An incoming aberrated wavefront $E_S(r)$ is focused by a lens into the core of a single mode fiber. In this case, $E_{LO}(r)$ is the inverse Fourier transform of the fundamental mode on the fiber $E_{smf}(r)$ [113].

fundamental mode on the fiber $E_{smf}(r)$. In the case where $E_S(r)$ is a plane wave, the field distribution of the focused plane wave is an airy distribution

$$E_S(r) = \frac{J_1\left(\frac{\pi Dr}{f\lambda}\right)}{\frac{\pi Dr}{f\lambda}} \quad 3.48$$

Where J_1 is the first Bessel function, and f is the focal length of the lens. It has been shown that for an optimum focal length selection and perfect alignment the maximum achievable mixing efficiency with perfect phase matching for an incoming plane wave is $\eta \approx 0.8$ [112]. In this case, the optimum focal length to achieve a maximum coupling efficiency is [112]

$$f \approx 1.408 \frac{Dw_0}{\lambda} \tag{3.49}$$

In the case of a plane wave, the mismatch between the incoming plane wave and the LO Gaussian in the aperture plane profile produces an efficiency loss. The same conclusion can be extracted in the focal plane, where the mismatch is due to the differences between the Airy distribution of the focused plane wave and the Gaussian mode of the single mode fiber.

3.2.2 Heterodyne Efficiency under Atmospheric Phase Fluctuations

In case we consider phase fluctuations ($\varphi_S(r) \neq 0$) a more complex analysis has to be performed. Here, we model the effect of phase fluctuations on the incoming wavefront by summarizing the statistical model described in [18], where exact expressions of the probability density functions of the log-normal amplitude fluctuations and Gaussian phase fluctuations were provided. In this study we simplify the analysis as scintillations effects are not considered.

In Eq. 3.44 the heterodyne efficiency, often known as fading intensity when considering phase fluctuations, was express as the sum of two magnitudes, α_r and α_i, that integrate over the collecting aperture the real and imaginary parts of the normalized optical field at the receiver. By assuming that both signals are normalized plane waves and considering that we can express those integrals as a finite sum of *N* independent cell, we can express Eq. 3.45 and Eq. 3.46 as:

$$\alpha_r = \frac{1}{N} \sum_{k=1}^{N} cos(\varphi_{S,k}) \tag{3.50}$$

$$\alpha_i = \frac{1}{N} \sum_{k=1}^{N} sin(\varphi_{S,k}) \tag{3.51}$$

By considering that *N* is sufficiently large, both components can be approximated as two jointly normal random variables [18]

$$p_{\alpha_r,\alpha_i} = \frac{1}{2\pi\sigma_r\sigma_i} exp\left(-\frac{(\alpha_r - \bar{\alpha}_r)^2}{2{\sigma_r}^2}\right) exp\left(-\frac{(\alpha_i - \bar{\alpha}_i)^2}{2{\sigma_i}^2}\right) \tag{3.52}$$

Being $\bar{\alpha}_r, \bar{\alpha}_i$ and σ_r, σ_i the means and variances of α_r and α_i, respectively. These means and variances can be calculated by using the statistical model for speckle with non-uniform distribution phases [115], resulting in

$$\bar{\alpha}_r = \frac{1}{2}\left[M_\varphi(1) + M_\varphi(-1)\right] \tag{3.53}$$

$$\bar{\alpha}_i = -\frac{j}{2}\left[M_\varphi(1) - M_\varphi(-1)\right] \tag{3.54}$$

$${\sigma_r}^2 = \frac{1}{4N}\left[2 + M_\varphi(2) + M_\varphi(-2)\right] - \frac{1}{4N}\left[2M_\varphi(1)M_\varphi(-1) + M_\varphi^2(1) + M_\varphi^2(-1)\right] \tag{3.55}$$

$${\sigma_i}^2 = \frac{1}{4N}\left[2 - M_\varphi(2) - M_\varphi(-2)\right] - \frac{1}{4N}\left[2M_\varphi(1)M_\varphi(-1) - M_\varphi^2(1) - M_\varphi^2(-1)\right] \tag{3.56}$$

where $M_\varphi(w)$ is the characteristic function of the phase. The phase fluctuations due to atmospheric turbulence follow a zero-mean Gaussian statistics, so the characteristic function can be expressed as:

$$M_\varphi(w) = exp\left(\frac{-\sigma_\varphi^2 w^2}{2}\right) \tag{3.57}$$

Using the Noll's approach (Eq. 3.31), the phase variance can be expressed in terms of the residual error when compensating *j* Zernike modes, so

$$\sigma_\varphi^2 = \sigma_j^2 \tag{3.58}$$

Substituting Eq. 3.57 into Eqs. 3.53-3.56 the resulting means and variances are

$$\bar{\alpha}_r = exp\left(\frac{-\sigma_\varphi^2}{2}\right) \tag{3.59}$$

$$\bar{\alpha}_i = 0 \tag{3.60}$$

$${\sigma_r}^2 = \frac{1}{2N}\left[1 + exp\left(-2\sigma_\varphi^2\right) - 2exp\left(-\sigma_\varphi^2\right)\right] \tag{3.61}$$

$${\sigma_i}^2 = \frac{1}{2N}\left[1 - exp\left(-2\sigma_\varphi^2\right)\right] \tag{3.62}$$

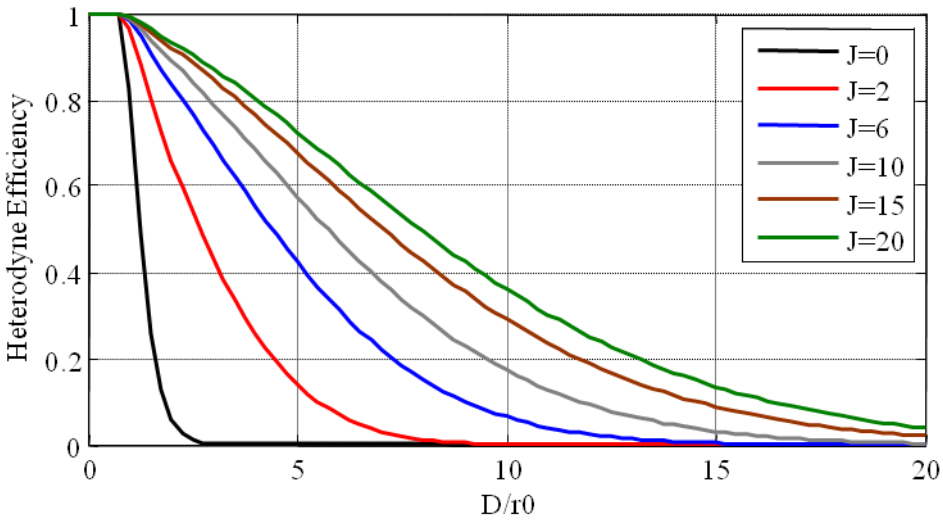

Fig. 3-5. Mixing efficiency under phase fluctuations when *J* modes are corrected.

It is important to note that the heterodyne efficiency averaged over the beat frequency, expressed as $\bar{\eta} \equiv \alpha^2 = \alpha_r^2 + \alpha_i^2$, is a random variable with probability density function $p_{\alpha^2}(\alpha^2)$ and mean $\overline{\alpha^2}$. At this point we use $\bar{\eta} = \alpha^2$ in order to do not mistake mean with time average. As σ_r and σ_i are jointly normal random variables, the resulting mean and variance of the mixing efficiency under phase fluctuations are given by

$$\overline{\alpha^2} = {\sigma_r}^2 + {\sigma_i}^2 + {\bar{\alpha}_r}^2 \tag{3.63}$$

$$\sigma_{\alpha^2}^2 = 2({\sigma_r}^4 + {\sigma_i}^4) + 4\sigma_r^2 {\bar{\alpha}_r}^2 \tag{3.64}$$

This way we can express the first order statistics of the mixing efficiency as a function of the phase variance and the parameter *N*. In [18] an analytic expression for *N* is provided:

$$N = \left\{1.09\left(\frac{r_0}{D}\right)^2 \Gamma\left[\frac{6}{5}, 1.08\left(\frac{D}{r_0}\right)^{5/3}\right]\right\}^{-1} \tag{3.65}$$

where $\Gamma(a, b)$ is the lower incomplete gamma function. By calculating *N*, we can substitute its value in Eq. 3.61 and Eq. 3.62 to obtain the mean heterodyne efficiency and variance from Eqs. 3.63-3.64. In Fig. 3-5 the averaged heterodyne efficiency calculated using Eq. 3.63 is shown for different normalized turbulence strengths and number of corrected modes. When no correction is applied, the wavefront phase variations produce a complete loss of the power resulting from the

coherent mix or the fiber coupling stage even at $D/r_0 < 3$. A more exhaustive analysis about the mixing efficiency and its repercussions on FSO is provided in Chapters 4 and 5, where an evaluation of AO under atmospheric turbulence is performed. By now, this theoretical model provides the mathematical basics to evaluate the performance of optical turbulence generators, being able to compare experimental results with theoretical models.

3.3 Optical Turbulence Generators for Evaluating FSO

3.3.1 Introduction to Optical Turbulence Generators for FSO

The development of adaptive optics for FSO is a complex discipline encompassing many challenging problems and, in general, every new adaptive system needs to be fully calibrated and tested in the workshop to ensure quality deployments. In order to characterize different types of adaptive optical systems, an optical turbulence generator (OTG) that introduces optical aberrations which presents characteristics close to the atmospheric turbulence becomes suitable in the laboratory, specially for astronomical and FSO communication system applications. The main advantages of using OTG is that they allow us to carry out a performance analysis of AO systems without the necessity of a real atmospheric link, saving telescope time and not being limited by the specific atmospheric condition at a certain time. Also, these OTG systems may be integrated in a functional AO setup and they can be used to perform the calibrations and maintenance required in mounted telescopes.

To guarantee that the performance analysis of an AO obtained by using an OTG can be compared with model predictions, the wavefront aberrations introduced by these systems must emulate Kolgomorov statistics. For that, the most important parameter to achieve by an OTG is the ratio between the telescope diameter and the Fried's parameter D/r_0, also known as normalized turbulence strength. This parameter defines the wavefront phase by using Eq. 3.34 and characterizes the spatial and temporal properties of the OTG output field.

Different methods to generate atmospheric aberrations have been proposed, including wind chambers [116], phase screens [117], moving plates [118][119] and spatial light modulators (SLMs) [120][121]. However, these methods present some limitations in compare to the characteristics that an ideal turbulence generator should present in terms of creating dynamic and

deterministic wave-front aberrations working at a sufficient rate to emulate both spatial and temporal atmospheric disturbances in the receiving light. Wind chambers, phase screens and moving plates are well defined methods to simulate dynamic atmospheric aberrations, but they present problems when introducing deterministic aberrations. In the other hand, SLMs show a good behavior in terms of repeatability and deterministic aberration generation, but they are limited by a frame refresh-rate of about 60 Hz, which considerably limits the speed of operation of any system based on this technology. Recently, a new technology based on digital micro-mirrors, which main characteristic is that they perform binary amplitude modulation [122], has been developed and a set of variations of digital micro-mirrors devices (DMDs) are commercially available for a fraction of the cost of a phase-only SLM. In this project we present a new technique based on the use of DMD devices that, in junction with binary computer-generated holography (BCGH), are able to provide wavefront phase modulation by just modifying the amplitude of the incoming light. In this section we provide a brief description of the different OTG methods and present a short discussion about their performance by explaining the main conclusion from the review performed by Jolissaint [123].

Static Phase screens: The main concept of this OTG is to introduce an optical path difference by means of an aberrated transparent plate or a modified mirror, emulating a turbulent layer with Kolgomorov statistics (Fig. 3-6.a). These physically modified surfaces present as main limitation that they are not reconfigurable, so in order to achieve a dynamic performance external motion has to be applied. This can be achieved by introducing a displacement or a rotational movement [124] (Fig. 3-6.b). The limitation by doing this is that the phase pattern is repeated after a certain time. To increase the repetition time more phase screens can be added. It has been shown that better performances can be achieved by rotating each phase screen at a different rate or introducing a lateral oscillation [125][126]. The main manufacturing options provided until now are: Polymer plate molding [127], where the optical path is modified by a plastic screen previously molded by a metallic pattern; Fluid-Jet-Polished Glass [128], where a glass plate is modified by using a jet of water with polishing sand; Photographic plate methods [124], where the modulation is achieved by illuminating a photo-sensitive material that modifies its refraction index; and Near-index-matching [129], where two optical medias with similar refractive index are put together, which makes it less expensive than the other methods. The main advantages of this method are that the phases introduced in the plate are deterministic and they can be integrated into the optical system without much complexity. In the other hand, each phase plate can only

generate a specific D/r_0 for a specific light beam. Still, the beam light could be expanded or contracted [130] to modify that ratio at the cost of higher complexity in the optical system. Also it is important to note that these phase screens must be perfectly aligned to do not introduce any residual tip/tilt component.

Spatial light modulators: This type of OTGs is defined by the fact that their surface characteristics can be modified by applying a specific voltage or current in each of the compounding parts of the device. These devices are widely known as spatial light modulator (SLM) (Fig. 3-6.c). The first approach was to use liquid crystals (LC), in which the refraction index is changed by applying a certain voltage [131]. These OTGs provide a deterministic and dynamic wavefront modulation, allowing repeatability and reconfiguration of the turbulence strength. In the other hand, they present low configuration rates (around 10 ms), high cost and they are polarization dependent. A different approach is to used ferroelectric LC SLMs, which present an increased frequency rate (kHz) but with the limitations that they only provide a phase modulation of 0 or π [132]. Its functionality is based on binarizing the sum of a phase map and a tip/tilt. Then, the resulting diffracted orders are separated by means of a lens and the first diffracted order is isolated by using a pinhole. The filtered mode is retrieved by another lens, resulting into a collimated containing the phase and tilt information. In [132] D/r_0up to 30 were achieved with a 256x256 FLC-SLM. The main drawbacks are that this method is wavelength dependent, as the diffracted order position change with the wavelength, the system increases the complexity of the setup and the power efficiency is low due to the fact that most of the power is directed to the zero-*th* order. Another option is the use of deformable mirrors (DM) [133]. These devices introduce a phase modulation by generating a delay on a specific pixel. The main advantage is that they are achromatic, but their cost and low spatial resolution, limited by the actuator pitch, make them a not very suitable solution for testing AO systems.

Turbulent Fluid Chambers: In this technique the objective is to create a physical turbulence by mixing flows at a different temperature of a specific media to generate variations on the refraction index. The main advantages is that Kolgomorov statistics are naturally achieved and the parameter D/r_0 can be modified by selecting the differential temperature between fluids. Also, this is an achromatic solution as is wavelength independent and the cost of these systems is low in compare with other options. In the other, they present a non-determinist approach to the problem and a profound calibration must be performed. Two main solutions have been proposed:

water chambers [134], which are able to produce stronger turbulences due a larger refractive index, and hot air chambers [135] (Fig. 3-6.d), which are widely used due to their implementation simplicity.

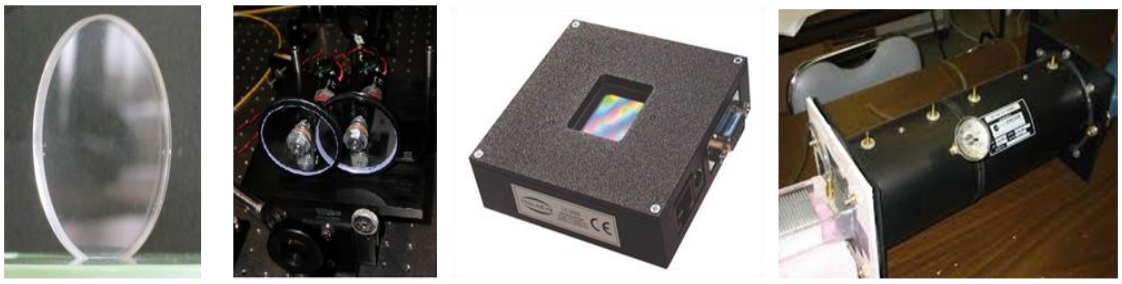

Fig. 3-6. Examples of optical turbulence generators. a) Phase screens, b) moving plates, c) spatial light modulator and d) wind chamber.

BCGH using Binary DMDs: For simulating in the laboratory the influence that the turbulent atmosphere has on light beams, we introduce a practical method for generating atmospheric wavefront distortions that considers digital holographic reconstruction using a programmable micromirror array. The main characteristic of these DMDs is that they are able to modulate the amplitude of the incoming beam only in two levels, cero or one, depending on the state ("on" or "off") of each micro mirror. The binary nature of the device increases the simplicity of the electronics involved, which results into an increased speed of the reconfiguration rates. It also presents a wide optical spectral bandwidth, good spatial resolution, and high power damage thresholds, which make it very useful for many light-control applications[136][137].

DMDs are by definition amplitude-modulation devices with reduced capabilities due to the binary nature of the micromirror array. To overcome this limitation, DMDs can be paired with binary computer-generated holographic (BCGH) techniques since they are able to provide wavefront phase modulation through binary amplitude modulation [138]. In this technique, the light beam coming from an optical source is separated into different spatial modes by interfering it with a holographic pattern composed by a set of binary gratings. These binary gratings are calculated using a computer, which encodes the phase information of the desired wavefront onto the holographic pattern [139]. The generated hologram is a grating that diffracts the incoming light into several orders. The first diffracted order is isolated and it contains the phase and amplitude information encoded on the hologram. This technique has been traditionally

implemented by using high-quality printing machines [140], what made it a very interesting solution due to its simplicity, low cost and high spatial bandwidth. In the other hand, it was limited by the slow process of printing and exchanging the printed slides, and dynamic wavefront generation was difficult to achieve due to the fact that the orientation between the laser and the hologram must be kept constant. By generating these binary grating using a DMD device we overcome this limitations and provide a equilibrate solution to the problem. In the other hand, the pixelated nature of the DMD devices influences the quality and spatial bandwidth. Also, this technique present a low power efficiency as most of the power is directed to the zero-*th* order.A study of these limitations is performed in this chapter. The combination of BCGH methods with DMD technology has been recently proposed and successfully validated in several optical setups [138][139].

3.3.2 Holographic systems: Method Overview

Holography is a technique that has been widely used for many applications since it was discovered in 1940 by the Hungarian-british physicist Dennis Gabor. This technique can record the three dimensional image of an object on an interferogram by producing interferometry between a reference laser beam and the reflected light coming from this object. Also, it is possible to regenerate this image by illuminating the recorded hologram containing the interferogram information with a coherent source [141]. In concrete, digital holography is defined by the fact that the interferogram is recorded onto a digital detector array (i.e. CMOS, CCD, etc.), which contains the amplitude and the phase of the complex field of the object.

In order to record the complex field of an object two waves must interfere onto a hologram recorder. The standard procedure to generate a hologram is shown in Fig. 3-7, where a plane illuminating beam hits an object and it interferes with the reference beam. The interference pattern between these two waves is recorded into a hologram.

In our case, the object to be reproduced is a plane wave aberrated by atmospheric turbulence that is defined by

$$W(x,y) = \sqrt{I_\alpha} exp\left(j\varphi_g(x,y)\right) \qquad 3.66$$

where I_α is the intensity and $\varphi_g(x,y)$ is the phase map of the aberrated wavefront. The illumination beam $P(x,y)$ can be mathematically described as a plane wave with an incident angle α and intensity I_r:

$$P(x,y) = \sqrt{I_r} exp(jksin(x)\alpha) \tag{3.67}$$

where k is the wave number ($2\pi/\lambda$). The interference pattern $G(x,y)$ recorded on the hologram is expressed as:

$$\begin{aligned} G(x,y) &= \left|\sqrt{I_r} exp\ (jksin(x)\alpha) + \sqrt{I_\alpha} exp\ (j\varphi_g(x,y))\right|^2 \\ &= I_\alpha + I_r + 2\sqrt{I_r I_\alpha} cos\left[\varphi_g(x,y) - ksin(\alpha)x\right] \end{aligned} \tag{3.68}$$

The basic scheme to generate wavefront aberration by using this recorded hologram is seen in Fig. 3-8. There, a collimated beam hits the hologram with an α angle and it is diffracted in several orders. By selecting the first mode using a focus lens and an aperture, we are able to recover aberrated waveform that is used as input for the adaptive optical system.The recovered wavefront can be expressend mathematically as follows:

$$\begin{aligned} W(x,y) &= [T_0 - tG(x,y)]\sqrt{I_b} exp\ (jksin(x)\alpha) \\ &= (T_0 - tI_\alpha - tI_r) exp\ (jksin(x)\alpha) \\ &\quad -t\sqrt{I_r I_\alpha I_b} exp\ (j\varphi_g(x,y)) \\ &\quad -t\sqrt{I_r I_\alpha I_b} exp\ (-j\varphi_g(x,y) + jksin(x)\alpha) \end{aligned} \tag{3.69}$$

where I_b is the intensity of the input reference beam, T_0 is the amplitude transmittance of the recorded hologram and t is the transmittance modulation depending on the technology used. The first term in Eq. 3.69 represents the zeroth-order light. The second and third terms represent the desired wavefront having phase $\varphi_g(x,y)$ and it's conjugated with an additional tilt, respectively. By filtering the second term of the equation, the complex field of the object can be recovered.

3.3.3 Binary Computer Generated Holograms

The BCGH is based on the principle that the generated holograms are composed of only two values: zeros or ones. These holograms are quite similar to interferograms, where the incoming light hits a grating pattern and it generates maximum and minimum values onto a screen

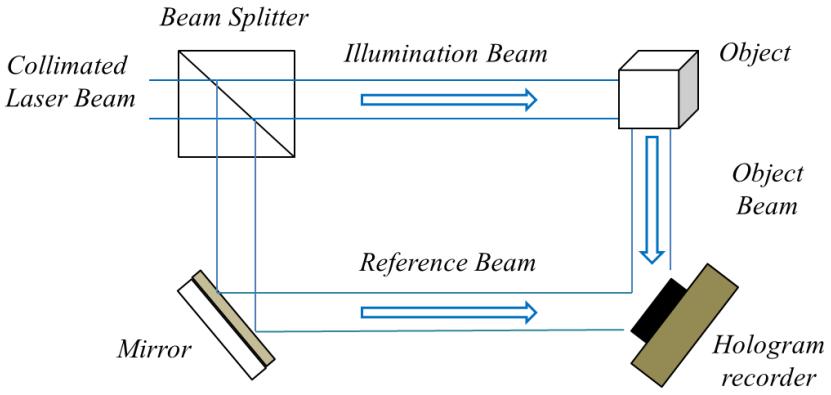

Fig. 3-7. Record of a complex field of an object into a hologram. A plane illumination beam hits an object and it interferes with the reference beam. The interference pattern between this two waves is recorded into a hologram.

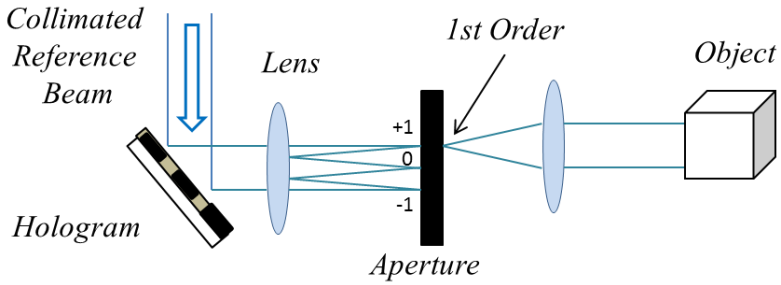

Fig. 3-8. Wavefront aberration generation using a recorded hologram. a collimated beam hits the hologram with a α angle and it is diffracted in several orders. By selecting the first mode using a focus lens and an aperture, we are able to recover aberrated waveform that will be used as input for the adaptive optical system.

depending on the grating parameters. The objective is to transform into zeros or ones the interference pattern $G(x,y)$ from Eq. 3.68 by using a non-linear process. Lee showed in [141] that the amplitude transmittance $t(x,y)$ that has to be recorded onto a hologram to produce a specific wave-front phase $\varphi_g(x,y)$ can be also expressed as:

$$t(x,y) = \frac{1}{2}\left(1 + cos\,(2\pi\alpha x - \varphi_g(x,y))\right) \qquad 3.70$$

where α is the linear tilt introduced by computation on the holographic pattern and acts as the carrier spatial frequency, and $\varphi_g(x,y)$ is the desired phase map to generate. Due to the constraint of the binary nature of the DMD, the function $cos\,(2\pi\alpha x - \varphi_g(x,y))$ has to be translated into 0's or 1's using a nonlinear function during the computation process. This function translates the

sinusoidal amplitude transmittance into a binary fringe pattern. The desired transmittance function [142] can be expressed as:

$$h(x,y) = \begin{cases} 1 \; if \; cos\left(2\pi\alpha x - \varphi_g(x,y)\right) > cos(\pi q(x,y)) \\ 0 \; if \; cos\left(2\pi\alpha x - \varphi_g(x,y)\right) < cos(\pi q(x,y)) \end{cases} \quad 3.71$$

where $q(x,y)$ is a parametric function that controls the width of the rectangular pulses coming out from the limiter and the positions the pulses in the grating are defined by $\varphi_g(x,y)$. The non-linear process of an analog hologram line can be seen in Fig. 3-9 for *q=0.5*.

It has been shown that this binary grating, allows amplitude and phase modulation [143]. This can be observed by expanding Eq. 3.71 as a Fourier series:

$$h(x,y) = \sum_m \frac{sin\pi mq(x,y)}{\pi m} exp\,(jm\left(cos\left(2\pi\alpha x - \varphi_g(x,y)\right)\right) \quad 3.72$$

where m is the diffracted mode. We can represent $h(x,y)$ as

$$h(x,y) = \sum_m U_m = \sum_m |U_m| exp\,\left(j\left(w_m x + \varphi_m(x,y)\right)\right) \quad 3.73$$

where U_m is the electrical field for diffracted mode m and $|U_m|$, w_m and $\varphi_m(x,y)$ are the amplitude, carrier and phase components for each mode, respectively. It is important to note that each one of these modes is spatially modulated by a spatial carrier $w_m = 2\pi\alpha m$, a phase modulation of $\varphi_m(x,y) = m\varphi_g(x,y)$ and amplitude equal to $|U_m| = \frac{sin\pi mq(x,y)}{\pi m}$. Therefore, each mode contains both, phase and amplitude information. A representation of these modes is shown in Fig. 3-10. By selecting the first positive diffracted order we can completely recover the modulated wavefront phase $\varphi_g(x,y)$ and modulated amplitude $q(x,y)$. In our study we are focused on wavefront aberrations, so the amplitude modulation function $q(x,y)$ can be considered a constant parameter that just controls the diffraction efficiency of each mode m.

When q is 0.5, all the even terms of Eq. 3.72 become zero, except the $m = 0$ term, which allows us to have a maximum diffraction efficiency of 10% at the first diffracted order [143].

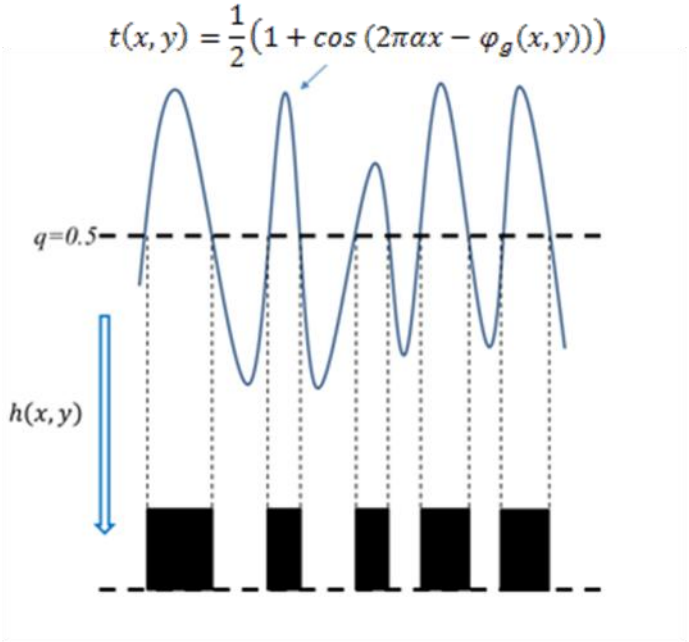

Fig. 3-9. Non-linear process $h(x,y)$ from an analog to a binary hologram when $q=0.5$.

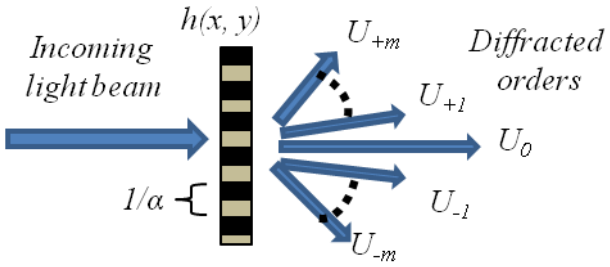

Fig. 3-10. Diffracted modes U_m produced by a binary hologram $h(x,y)$ with grating period $T = 1/\alpha$. The angular separation between adjacent modes is $2\pi\alpha$.

These binary holograms can represent the recorded wavefront, and, in the case that the wavefront contains only phase variations, the resulting hologram has the appearance of an interferogram. The resulting grating consists on a set of rectangular pulses of period T, pulse width qT and a relative location $\delta(x,y)$ for each fringe which:

$$\delta(x,y) = \frac{\varphi_g(x,y)}{2\pi} \qquad 3.74$$

The fringe location is the key parameter that encodes the phase information in a binary hologram. It is important to notice that, as a binary hologram can only take two possible values (one or

zero), the only way of encoding information in a pulse period is to modify the position on which the transition between both states occurs.

3.3.4 Performance of BCGH using finite arrays

We have introduced the binary holography theoretical background considering that a hologram can take one out of two possible values at any position of the recorded interferogram. Historically, this have been useful due to the fact that the holograms where printed using a computer [142] and the pixel resolution of the images where high enough to assume that the pixilation effect can be disregarded. In our proposal, we are using DMD devices that present a specific pixels size. This implies that any hologram must be discretized in both, *x* and *y* directions, before been sent to the DMD. First, in the *y* axis, the limitation is imposed by the fact that the maximum spatial frequency produced by the hologram fulfills the Nyquist criteria. The sampling frequency in the *y* direction is $fs_{\varphi_g,y} = 1/dy_p$, where dy_p is the pixel vertical size. This means that the maximum spatial bandwidth that can be represented without any loss of information is:

$$BW_{\varphi_g,y} = \left\{\frac{\partial \varphi_g(x,y)}{\partial y}\right\}_{max} \leq \frac{fs_{\varphi_g,y}}{2} \qquad 3.75$$

In the *x* axis the requirements are far more restrictive. From Eq. 3.72, the *x* axis is composed by a set of binary gratings having a period *T*. This period must be an integer number of pixels *N* in order to be able to implement it in a finite array and not loss information during the process [143]. This parameter *N* imposes a set of possible linear tilts α, or angular separation between modes, that can be expressed as:

$$\alpha = \lambda/T = \lambda/(N * dx_p) \qquad 3.76$$

where dx_p is the pixel size and N is an integer. This linear tilt, which acts as the spatial carrier frequency, must be higher than twice the maximum spatial frequency of the phase map in order to avoid aliasing between the different modes generated. This imposes a design restriction in the holographic generation process:

$$\frac{1}{(N * dx_p)} \geq 2\left\{\frac{\partial \varphi_g(x,y)}{\partial x}\right\}_{max} \qquad 3.77$$

To avoid mode aliasing, *N* must be small enough to introduce a minimum angular modulation. This requirement set a lower limit to the parameter selection of *N*.

In order to encode phase information into a digital binary device we need to convert the continuous phase map $\varphi_g(x,y)$ onto a discrete implementation. As the modulation is introduced in the fringe position of each grating, two direct limitations arise:

1. Re-sampling of $\varphi_g(x,y)$at a frequency $1/(N * dx_p)$ in the *x* axis. The fact that the information is encoded in the fringe location implies that only one phase value per grating period is allowed. The resulting down-sampled phase map symbols S_{ij} for a grating period *T* can be obtained by averaging the phase map over periods of *N* pixels as

$$S_{ij} = \frac{\sum_{x=iN+1}^{i(N+1)} \varphi_g[x_n, y_n]}{N} \qquad 3.78$$

where i is the symbol index in the *x* axis and take values from 1 to N_x/N. N_x is the total number of pixels in the *x* axis, j is the symbol index in the *y* axis and take values from 1 to N_y and $\varphi_g[x_n, y_n]$ is the original phase map to be generated represented in a grid of $N_x x N_y$ dimensions where x_n goes from 1 to N_x and y_n from 1 to N_y. The resulting downsampled phase map can be expressed as $\varphi_{g,T}[i,j] = S_{ij}$.

2. The fact that a grating period is composed by *N* pixels implies that the fringe location $\delta(x,y)$ from Eq. 3.74 can only take an integer value from *0* to *N-1*. Therefore, the phase information $\varphi_{g,T}[i,j]$ must be quantizated in *N* levels:

$$\varphi_{g,q}[i,j] = \varphi_{g,T}[i,j]\Big]_{q=2\pi/N} \qquad 3.79$$

This effect can be modeled as an additive random noise with zero mean and variance $\Delta^2/12$, being Δ the quantization step ($\Delta = 2\pi/N$).

In Fig. 3-11 the discrete implementation of a binary grating onto a DMD is shown. Each symbol is defined as a set of *N* pixels, which compose one period of the binary grating. The light coming with an incident angle β is separated into different modes U_m with an angular deviation α between them, each one containing different phase information. For example, to achieve a phase modulation of π on the first diffracted orders, the relative location δ has to be *N/2* pixels.

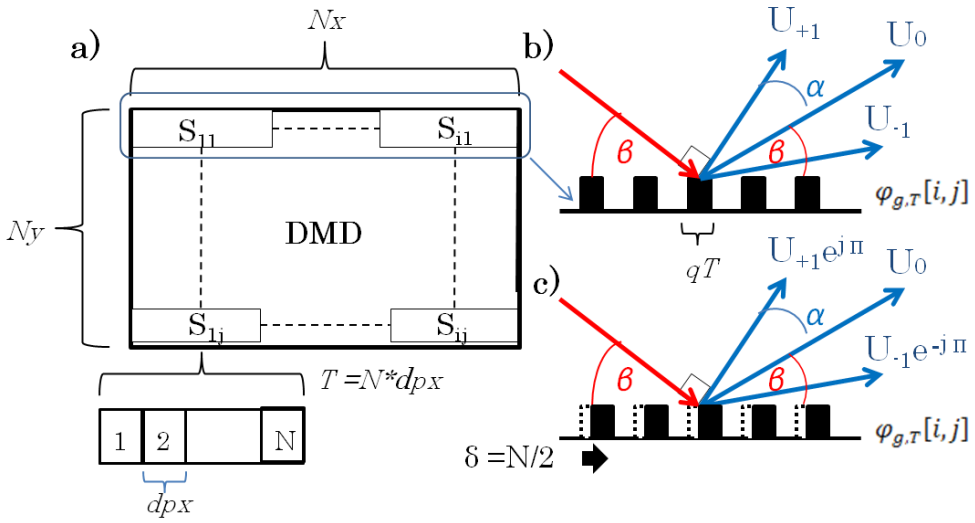

Fig. 3-11. a) Discrete implementation of a binary grating onto a DMD with Nx×Ny pixels. Each symbol S_{ij} is defined by a set of 1×N pixels, and generates one period on the binary grating. b) The light coming with an incident angle β is separated into different modes $(U_0, U_1, \dots)$ with an angular separation of α, each one containing different phase information. c) An example of phase modulation is shown: the relative fringe location δ is shifted by N/2 to produce a resulting phase modulation of π on the first diffracted orders.

Selecting an optimal parameter *N* will determine the characteristics of the resulting wavefront. A high number of pixels per grating period will diminish the separation between the diffracted orders and, also, will set an upper limit to the spatial bandwidth that can be generated due to the necessity of fulfilling the Nyquist criteria. In the other hand, a low number of pixels per period results in higher quantization errors while encoding the phase because the phase information for each symbol must be encoded in less quantization levels. We can conclude that it exists a tradeoff between generating high resolution aberrations and high spatial frequency aberrations, so the parameter *N* has to be chosen depending on the characteristics of each application.

In Fig. 3-12 the process to generate a binary hologram and its adaptation to a finite array is shown. First, an adequate grating period *T* is selected as a parameter. This parameter depends on the application and the different characteristics of the DMD. We will study this parameter

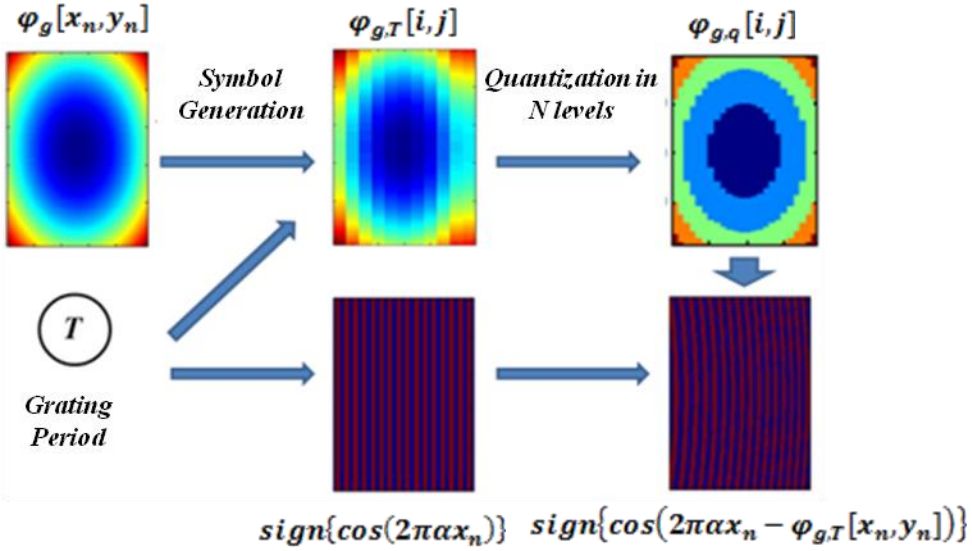

Fig. 3-12. Process to generate a binary hologram and its adaptation to a finite array DMD is shown. First, an adequate grating period *T* is selected as a parameter. Then the phase map $\varphi_g[x_n, y_n]$ has to be resampled with grating period *T* to obtain $\varphi_{g,T}[i,j]$ and quantizated in *N* levels $\varphi_{g,q}[i,j]$. The downsampled and quantizated phase map is added to the carrier spatial frequency to obtain the desired holographic pattern.

selection in the next section. To reproduce a phase map $\varphi_g[x_n, y_n]$ first it has to be resampled with grating period *T* and then quantizated in *N* levels. The downsampled and quantizated phase map is then added to the carrier spatial frequency to obtain the desired holographic pattern. We have stated that, due to the pixelation effect of the finite array, this technique introduces a set of limitations that may affect the quality of the generated wavefront in compare to desired wavefront. The efficiency of the method depends highly on the grating period *T* selected, which, at the same time, depends on the pixel size dx_p and the number of pixels per period *N*. The objective now is to evaluate how this set of parameters influences the efficiency for generating atmospheric turbulence using Zernike polynomials and Kolgomorov statistics. Considering these characteristic we can perform an analytical study to determine a functional set of parameters for our application, which will allow us to study the performance of the device when generating a specific wave-front aberration. For that, a measure to evaluate the error introduced by the digital holographic process is needed. The RMS error per pixel is proposed as a way of measuring the difference between the final phase map recorded onto the hologram, $\varphi_{g,q}[x_n, y_n]$, and the original phase map $\varphi_g[x_n, y_n]$, defined by the Kolgomorov model of turbulence. It can be expressed as:

$$e_{RMS} = \sqrt{\frac{\sum(\varphi_g[x_n, y_n] - \varphi_{g,q}[x_n, y_n])^2}{N_x N_y}} \qquad 3.80$$

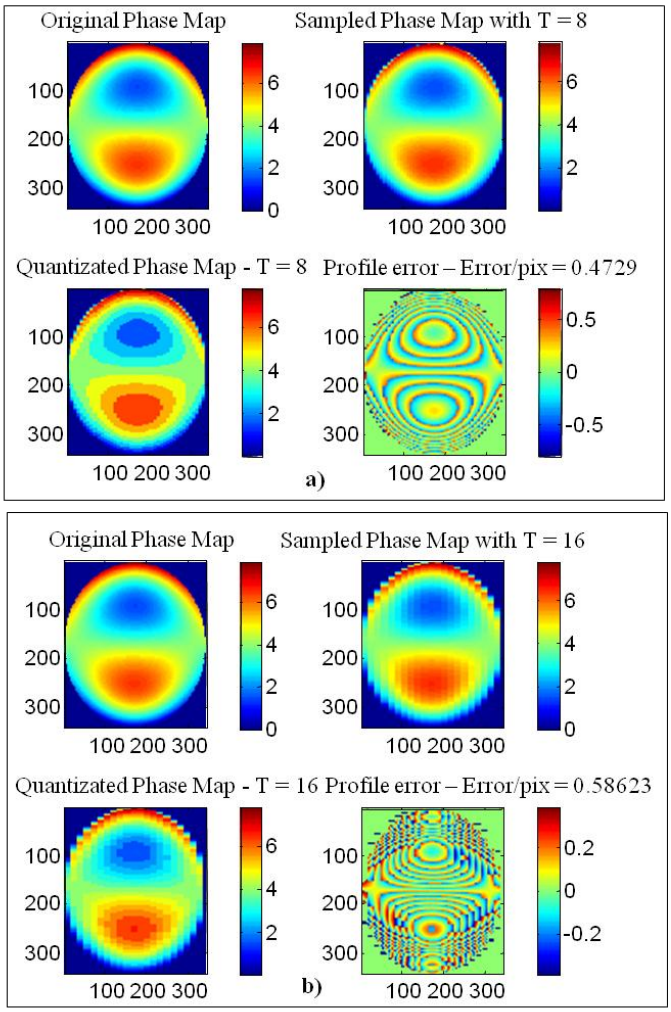

Fig. 3-13. Phase map adaptation to finite micro arrays for the vertical coma with weight 5 for a) T=8 and 2) T=16. The original phase maps are downsampled and quantizated in T levels. The resulting phase map error introduced is shown in each case.

In Fig. 3-13 the RMS error per pixel is shown for two different grating periods ($N = 8, 16$) when the selected aberration is a vertical coma. In this particular case, the RMS error is higher when the period is composed by 16 pixels in compare to the 8 pixels one. Here, the dominant error is produced by the high spatial frequencies needed to implement this phase map. Even if the quantization errors are higher for *N*=8, the total computed error is lower because a lower grating period allows an improved re-sampling spatial frequency in compare to *N*=16. It

might be other cases where the spatial frequencies of the original phase map are lower and a higher N is preferred as the error is dominated by the quantization process. This implies that a numerical analysis is needed in order to evaluate the optimal grating period for generating Kolgomorov wavefronts in each case.

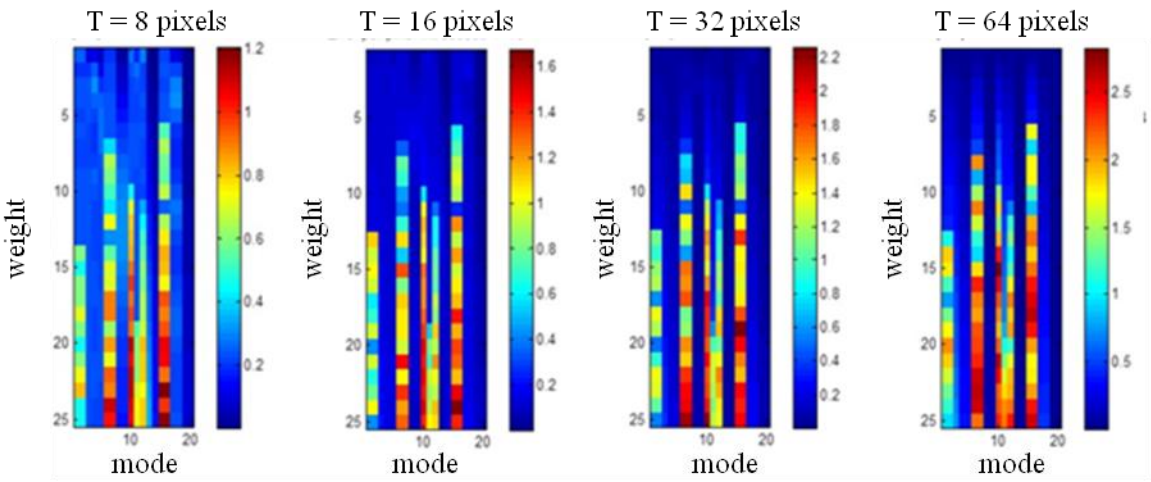

Fig. 3-14. Mean error per pixel for each mode and weight as a function of the grating period.

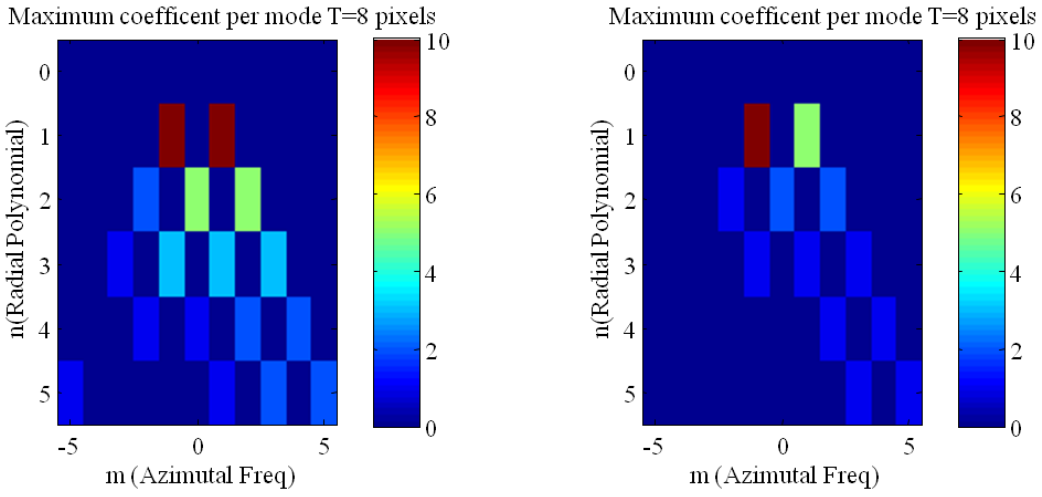

Fig. 3-15. Maximum weight per mode without introducing aliasing for a specific aperture of 3.6mm (DLP3000 DMD).

To evaluate correctly what is the optimal parameter N for our application we have to calculate the particular phase map to reproduce in each case. For each Zernike polynomial and for each different weight the optimum parameter the result may vary. Therefore, to study the influence of the main parameters (N_x, N) on the system performance we need to fix the

additional parameter, the pixel size. In this case we will use the standard pixel size that these devices present nowadays. The main manufacturer is Texas Instruments, which devices have a 10.8µm effective pixel size [144]. In Fig. 3-14 the error per pixel is shown for each mode and weight as a function of the grating period. The most visible consequence of the holographic process is that the error is not equally distributed between the modes. The modes which contain higher spatial frequencies along the *x* axes present a higher penalization due to the discretization. As an example, the mode 2 (Tip) never presents a limit in terms of weight to reproduce because its phase map is constant in the *x* direction. In the other hand, mode 3 (Tilt) presents aliasing with weight below 3.

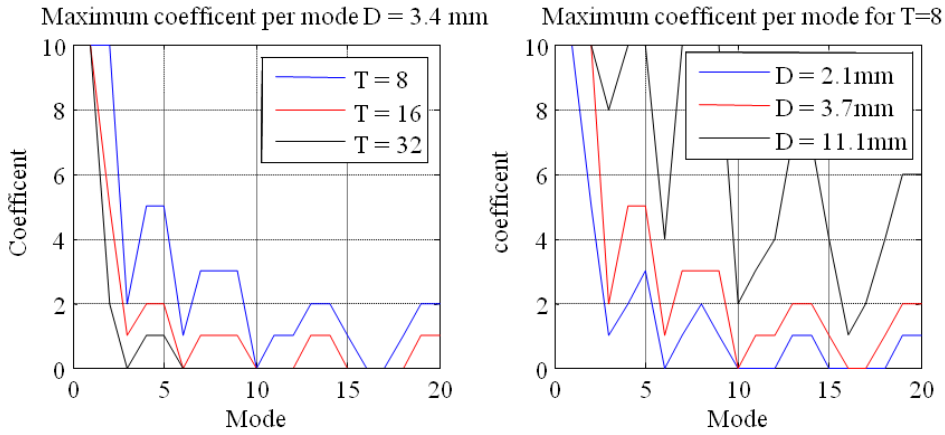

Fig. 3-16. Maximum weight per mode for (a) Aperture of 2.1mm and T= 8, 16 and 32. (b) T=8 and apertures of 2.1 mm, 3.7 mm and 11.1 mm.

In general, the mean error increases by increasing *N* due to aliasing in the re-sampling process but this cannot be assumed for every mode and weight. As an example, for weights below 5, the error diminishes when *N* is increased. The fact that the spatial bandwidth of these phase maps is very narrow implies that they can be correctly re-sampled and the error is minimized by performing the quantization process with more levels. For weights above 10 it occurs the opposite: the error diminish when a higher sampling frequency is used, even if the quantization levels are low. In Fig. 3-15 the maximum weight per mode without introducing aliasing in the discretization process is shown for a specific aperture of 3.6mm (DLP3000 DMD). As the grating period increases, the holographic pattern is not able to generate high weights for each mode. Also, when the azimutal frequency and radial mode increases (dependency with *x* increases) the maximum weight per mode decreases.

In figure Fig. 3-16 the other parameter N_x is analyzed. By increasing the number of pixels in the array (aperture size) the number of symbols per row increases while keeping the same grating period. This means that the relative spatial frequency of the phase map diminish in compare to the re-sampling frequency, so the errors introduced by the discretization process are reduced. It becomes obvious that a higher number of total pixels increase the efficiency of the process: it increases the re-sampling relative frequency and allows a higher number of quantization levels, which makes possible to reproduce the modes with higher weight.

In Fig. 3-17.a) the calculated RMS error per pixel is shown for different grating periods and turbulence scenarios for a specific MEM (DLP3000 DMD TI) of 342 pixels (3.4mm aperture). For $D/r_0 < 3$, the error is dominated by the quantization effect, so a higher number of pixels per grating period is preferred in order to increase the quantization levels. The mean error for $D/r_0 = 1$ matches almost exactly the theoretical error predicted by the quantization error model. The quantization mean error for $T = 8$ and $D/r_0 = 1$ is defined by the model to be $(2\pi/N)/\sqrt{12} = 0.226$ [rad/px]. In Fig. 3-17 it can be seen that the error is almost plane for $T = 8$ and $D/r_0 < 6$, so in this region it can be considered there is no aliasing. In the other hand, for $T = 16, 32$ this plane error region does not exist as the error increases for higher D/r_0. The RMS error in both cases for $D/r_0 = 0$ corresponds to the predicted value for the quantization error of 0.1134 [rad/px] and 0.0567[rad/px] for $T = 16, 32$ respectively. When the turbulence strength increases, the spatial bandwidth of the wave-front is broader and the error introduced by the aliasing dominates over the quantization error. For these grating periods the dominant error is strictly due to the aliasing practically from the beginning. For scenarios where $D/r_0 > 3$, a lower grating period increase the performance of the method.

The wave front phase efficiency generation for different perturbation scenarios and grating periods can be seen in Fig. 3-17.b). The phase efficiency is calculated as $\eta = 1 - e_{RMS}/2\pi$, where 2π is the maximim posible error. Our objective is to reproduce a wide variety of perturbation scenarios, so a lower grating period (N = 8 pixels) is preferred for this application and device. By choosing $N = 8$, we ensure efficiency above 82% for $D/r_0 < 12$. To see how the error is distributed between the different modes when a holographic binary pattern produces a Kolgomorov distribution, a comparison between the resulting weights associated with the generated wavefront and the weights of the original phase map is performed. In Fig. 3-18 the total error is decomposed into the different Zernike modes. Equivalently as in the analysis performed

by modes, the dependency of the x direction for each mode corresponds to a higher percentual error. Also, the error tends to increase as the mode number increases. This can be explained by the fact that higher modes correspond to higher spatial frequencies, which lead to an increase of the error introduced by aliasing.

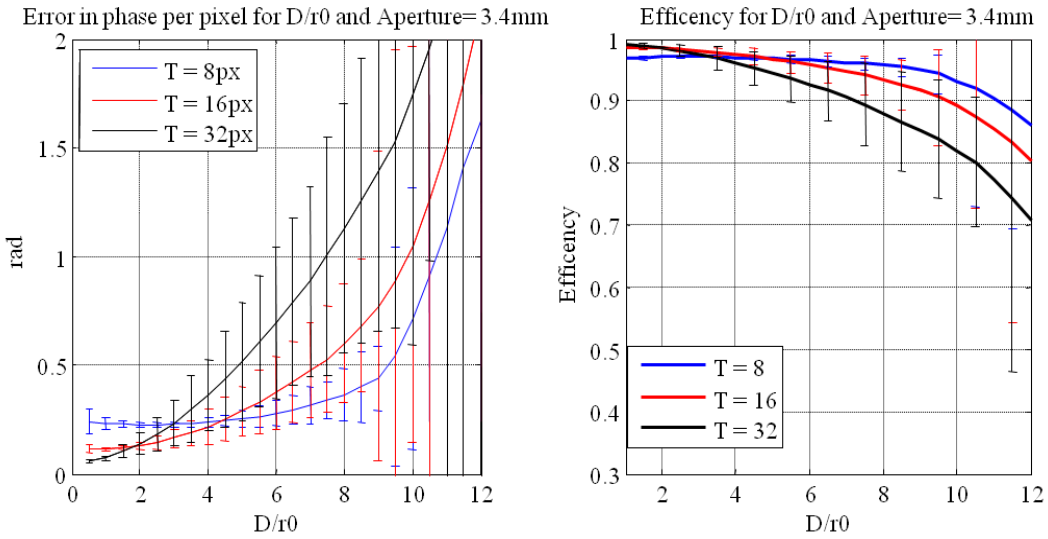

Fig. 3-17. Root mean square error per pixel (a) and wavefront phase efficiency for different grating periods and turbulence scenarios for a specific DMD (DLP3000 DMD TI).

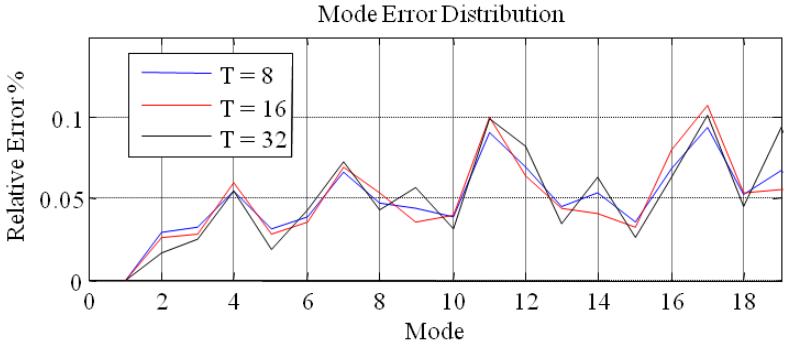

Fig. 3-18. Relative error decomposed into the different Zernike modes for DLP3000 DMD and different grating periods.

Better performance can be achieved by using newer generations of DMDs (TI DLP 7000, TI DLP 9500) that are available with higher resolution characteristics. For a specific grating period, the resulting coherence length r_0 that can be generated by a DMD can be calculated as a function of dx_p, N_p and aperture diameter D. Through simulations, we can obtain the resulting r_0 generated by the discrete and quantizated phase map that each device is able to generate. For that

calculation we use the seld coherence function (SCF) definition for an electric field measured at two points $(\boldsymbol{x_1}, \boldsymbol{x_2})$ in the observation plane at an specific time [21]

$$\Gamma(\boldsymbol{x_1}, \boldsymbol{x_2}) = \langle E(\boldsymbol{x_1}) E^*(\boldsymbol{x_2}) \rangle \tag{3.81}$$

By considering $E(\boldsymbol{x}, t) = exp\,(j\varphi(\boldsymbol{x}, t))$ a stationary field that only depends on the difference between $\boldsymbol{\tau} = \boldsymbol{x_1} - \boldsymbol{x_2}$ and that the field $E(\boldsymbol{x}, t)$ is isotropic, so it only depends on the magnitude of $|\boldsymbol{\tau}|$ we obtain that the self coherence function can be obtained as

$$\Gamma(\boldsymbol{x_1}, \boldsymbol{x_2}) = \Gamma(\boldsymbol{\tau}) = \langle E(\boldsymbol{x}) E^*(\boldsymbol{x} - \boldsymbol{\tau}) \rangle \tag{3.82}$$

The coherence length, or r_0, can then be derived by defining it as the maximum distance where $|\Gamma(\boldsymbol{\tau})| \geq 1/e$. This coherence length is calculated as [105]

$$\bar{r_0}^2 = \frac{\int \boldsymbol{\tau^2} |\Gamma(\boldsymbol{\tau})|^2 d\,\boldsymbol{\tau}}{\int |\Gamma(\boldsymbol{\tau})|^2 d\,\boldsymbol{\tau}} \tag{3.83}$$

In our case, to estimate the coherence length of the wavefront generated on the first diffracted order we substitute $E(\boldsymbol{x})$ in Eq. 3.82 by $E_{g,q}[x, y] = exp\,(j\varphi_{g,q}[x_n, y_n])$ and perform the integral from Eq. 3.83 in the discrete domain. The estimated coherence length of the output field from our OTG $\left(\bar{r}_{0_{g,q}}\right)$ is compared to the $\bar{r}_0$ calculated from using $E_g[x, y] = exp\,(j\varphi_g[x_n, y_n])$ in Eq. 3.82 and Eq. 3.83. In Fig. 3-19, the perturbation efficiency generation $(\bar{r}_{0_{g,q}}/\bar{r}_{ideal})$ can be seen for different DMDs with different resolution parameters and a grating period of 8 pixels. It is shown that just by upgrading the DMD we can provide a wider set of scenarios. By using the DLP3000 we can achieve perturbation scenarios up to $D/r_0 < 10$ by using a set of 192x192 picels (aperture of 2.1 mm) with generation efficiencies above 90%. The same device presents a higher performance by using its maximum resolution of 342x342 pixels (aperture 3.6 mm), which allow us to generate perturbations up to $D/r_0 < 15$. The DLP9500 is able to achieve the same efficiency up to $D/r_0 \approx 18$ thanks to its 1920x1080 pixel resolution.

This shows that the technique is adequate to produce wavefront aberrations with spatial characteristics similar to the ones generated by the atmosphere. The wavefront generation efficiency is highly dependent on the array size, which depends on the device characteristic, and

on the grating period selected, which is a design parameter that controls the trade-off between high spatial resolution and quantization error.

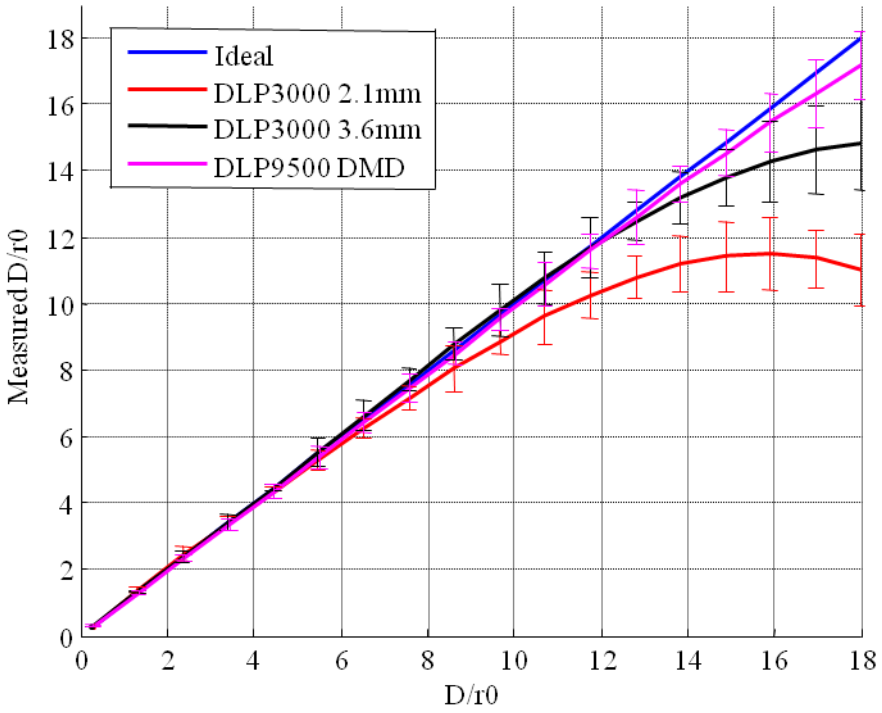

Fig. 3-19. Perturbation efficiency generation (r_0/r_{ideal}) for different DMDs with different resolution parameters and a grating period of 8 pixels. By using the DLP3000 we can achieve perturbation scenarios up to $D/r_0 < 10$ using a set of 192x192 pixels (aperture 2.1 mm) with generation efficiencies above 90%. The same devices presents a higher performance using 342x342 pixels (aperture 3.6 mm), which allow us to generate perturbations up to $D/r_0 < 15$. The DLP9500 is able to achieve the same efficiency for $D/r_0 \approx 18$ thanks to its 1920x1080 pixel resolution.

3.4 Experimental Set-Up for Generating Atmospheric Aberrations using DMDs

In Fig. 3-20 an optical turbulence generator setup using BCGH and a binary DMD device is shown. The experimental set up is based on the holographic principles presented in the previous section. The objective is to build an experimental OTG using commercially available devices that introduces wavefront phase aberrations similar to the ones introduced by the atmosphere. This stage is crucial to evaluate the performance of FSO coherent systems under atmospheric turbulence.

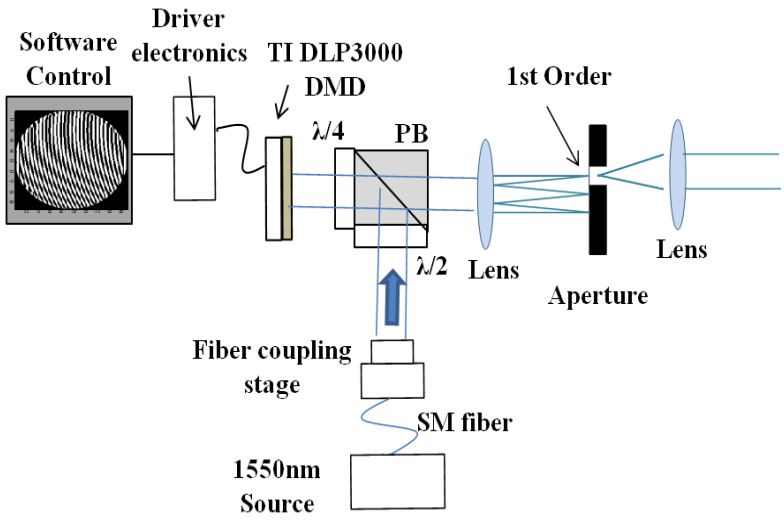

Fig. 3-20. Optical turbulence generator set up using BCGH and a binary DMD device.

Table 3-3. Description of the optical devices used in the OTG set up

	Commercial name	Parameter	Value	Units
Aspheric Lens	Thorlabs C660TME Mounted Lens	Focal length	2.97	mm
		Clear Aperture	3.60	mm
Free-Space Fiber	Thorlabs KT110	x-y-z Translation	0.5	µm/Div
Polarization Beam Splitter	Thorlabs CM1-PBS254	Reflection Efficiency	99.5	%
		Transmission Efficiency	90	%
λ/2 Waveplate	Thorlabs WPH10M-1550	Clear Aperture	25	mm
		Reflectance	0.25	%
λ/4 Waveplate	Thorlabs WPQ10M-1550	Clear Aperture	25	mm
		Reflectance	0.25	%
Lens		Focal Length	40	mm
Variable Aperture	Thorlabs SM2D21	Aperture	0.7-5	mm

The laser beam is collimated into the fiber space by using a coupling stage. The coupling stage is composed by a *x-y-z* translator where the fiber is connected and a 2.97 mm focal aspheric lens. The resulting beam presents a diameter of 2.1 mm and an additional loss of 0.5 dB due to insertion losses on the coupling stage. By manually configuring the translation stage the resulting beam present a 0.2 mrad divergence. After collimation, the laser is sent through the λ/2, configured to maximize light reflected by the PBS. This stage, composed by the λ/2, λ/4 and the

PBS act as a free space optical circulator that redirects the light perpendicularly to the DMD, maximizing the effective area of the TI 3000DMD. The DMD introduces a phase modulation by generating diffracted orders. As it has been explained in this chapter, the wavefront phase aberration introduced by the DMD is controlled by the use of a PC, which generates a specific phase map in the first diffracted order. The first positive order is isolated by using two 40 mm focal lenses and a variable aperture with a minimum and maximum aperture of 0.7 mm and 5 mm respectively. The main optical parameters of the setup are shown in Table 3-3.

By using this scheme we obtain a deterministic aberrated wavefront that can be used to evaluate the performance of FSO systems. In this section we describe the hardware and software details to implement a OTG using BCGH and DMDs.

3.4.1 Software Control

To generate the holographic patterns a software package has been developed and implemented using Matlab. The application generates the original aberrated phase map $\varphi_g[x_n, y_n]$ in a $N_x x N_y$ array and adapts it to the device in use by applying the procedures explained Eq. 3.78 and 3.79 to obtain $\varphi_{g,q}[x_n, y_n]$. The input parameter of the program can be divided in two groups: (1) phase map generation and (2) implementation of the binary holography. To generate the phase wavefront we can select between the Kolgomorov approach, which will generate a random phase map based on the value of D/r_0 introduced using Eq. 3.34, or the mode approach, which will generate a phase map composed by the weights w_g and Zernike modes Z_i:

$$\varphi_g[x_n, y_n] = \sum_i w_g Z_i \qquad 3.84$$

Once the phase map is calculated, the application transforms it into a holographic pattern. For that it is necessary that the user indicates the finite array characteristics: number of pixels N_x, pixel size d_{px} and pixels per grating period N.

Once the input data is fulfilled, the program calculates the re-sampled and quantizated phase map $\varphi_{g,q}[x_n, y_n]$. Then, the binary holographic pattern $h[x_n, y_n]$ is calculated by adding the linear tilt to the phase and performing the operation described in Eq. 3.71.

$$h[x_n, y_n] = sign\{cos(2\pi\alpha x_n - \varphi_{g,q}[x_n, y_n])\} \quad 3.85$$

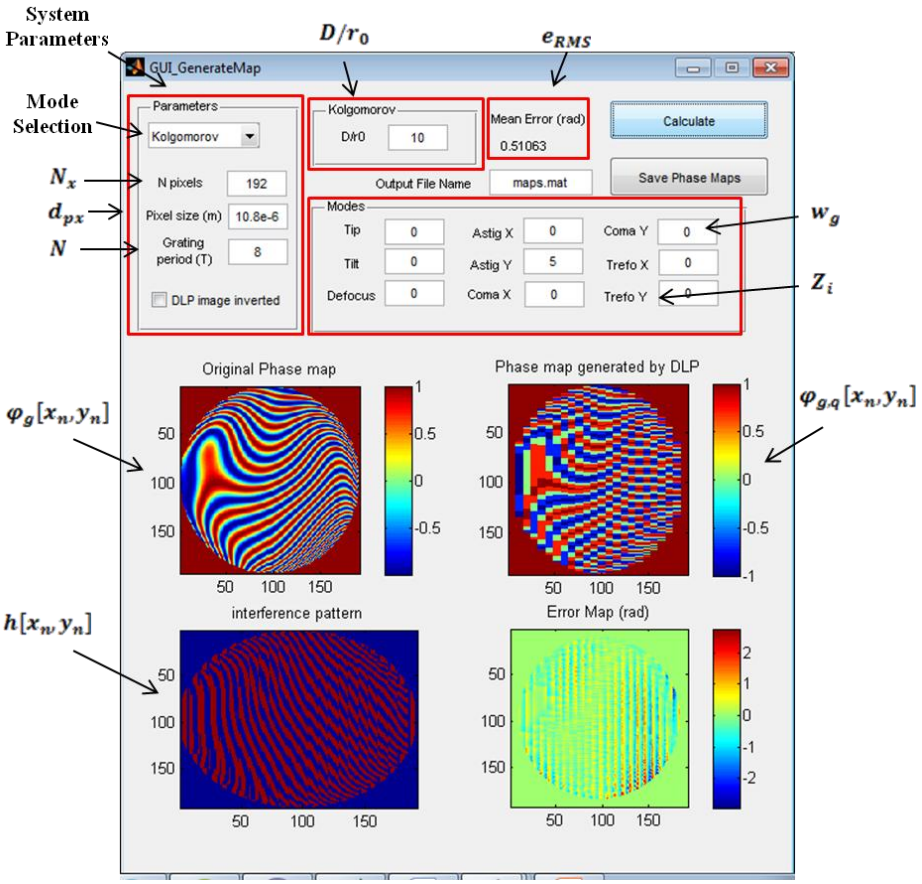

Fig. 3-21. Phase Map and Holographic pattern generation software. The application generates the original aberrated phase map and adapts it to the device in use. The input parameters are the number of pixels, the pixel size and grating period. Option of generating Kolgomorov distributions or separate Zernike modes.

Four different graphs are shown through the user interface: the original phase map aberration to be recorded, the re-sampled and quantizated map achieved using these parameters, the holographic pattern that will be loaded to the DMD and the phase error map, which corresponds to $(\varphi_g[x_n, y_n] - \varphi_{g,q}[x_n, y_n])$. By taking a look to the discrete phase map and error phase map, the user is able to visualize at first sight how the method is able to reproduce the wavefront aberration. Also, the mean error per pixels e_{RMS} from Eq. 3.80 is shown to give the user a quantitative measure of the method's efficiency for a specific phase map. In Fig. 3-21 the user interface of the program is shown.

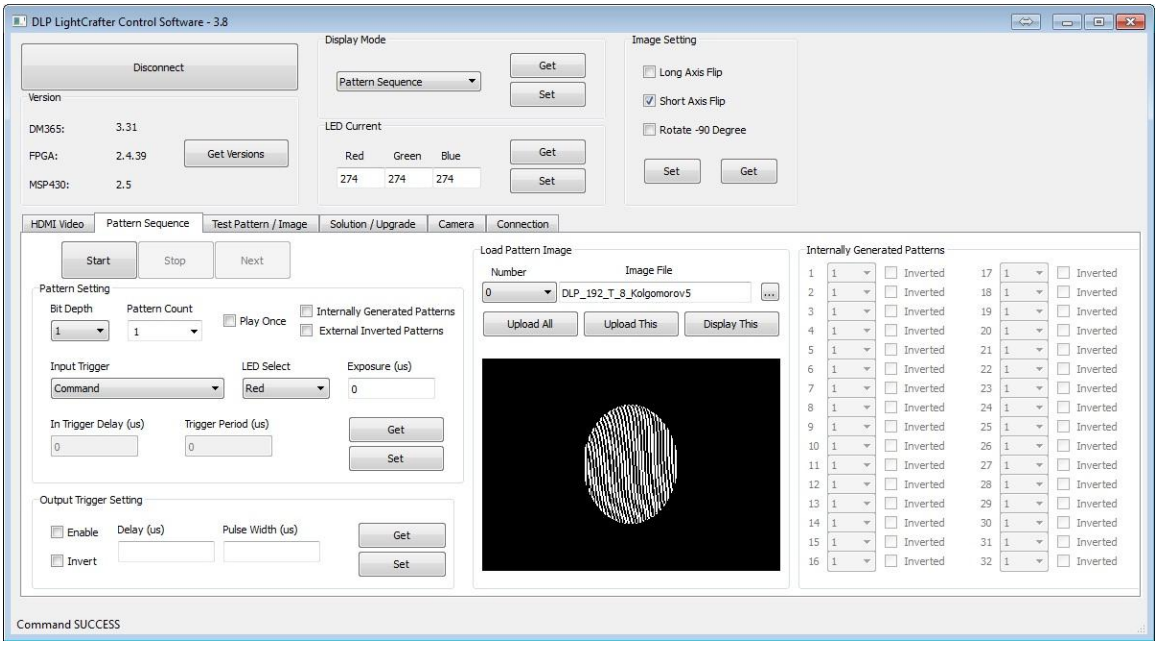

Fig. 3-22. DLP LightCrafter Control Software used to control the Texas Instrument DLP3000 DMD,

The holographic pattern generated by this application is then loaded using the software control of the DMD. In this case we use the Texas Instruments DLP3000 DMD, which includes the control software *DLP Lightcrafter Control Software 3.8*, shown in Fig. 3-22. This software allows us to connect, transfer and configure the output of the DMD. The options of this software are many, but in this project we will use only two of the main options: Static image, which loads and shows an image generated by the user, or a pattern sequence, in which the user uploads a set of images that are shown sequentially with an exposure time indicated by the user. The maximum frame rate achievable by this device is 4 kHz for a maximum set of 96 binary images.

3.4.2 DMD Characterization

The DLP3000 digital micro mirror device (DMD) is a digitally controlled MOEMS (micro-opto-electromechanical system) spatial light modulator (SLM) composed by a reconfigurable screen (DLP 0.3 WVGA DMD) and the electronic driver to control it (DLP WVGA 0.3 Chipset). When coupled to an appropriate optical system, the DLP3000 can be used to modulate the amplitude and direction of incoming light. The DLP3000 creates light patterns with speed, precision, and efficiency. The main characteristic of these DMDs is that they are able to modulate the amplitude of the incoming beam only in two levels, cero or one, depending on the state (“on” or “off”) of each micro mirror. The binary nature of the device increases the simplicity of the electronics

involved, which results into an increased speed of the reconfiguration rates. It also presents a wide optical spectral bandwidth, good spatial resolution, and high power damage thresholds, which make it very useful for many light-control applications [145][146].

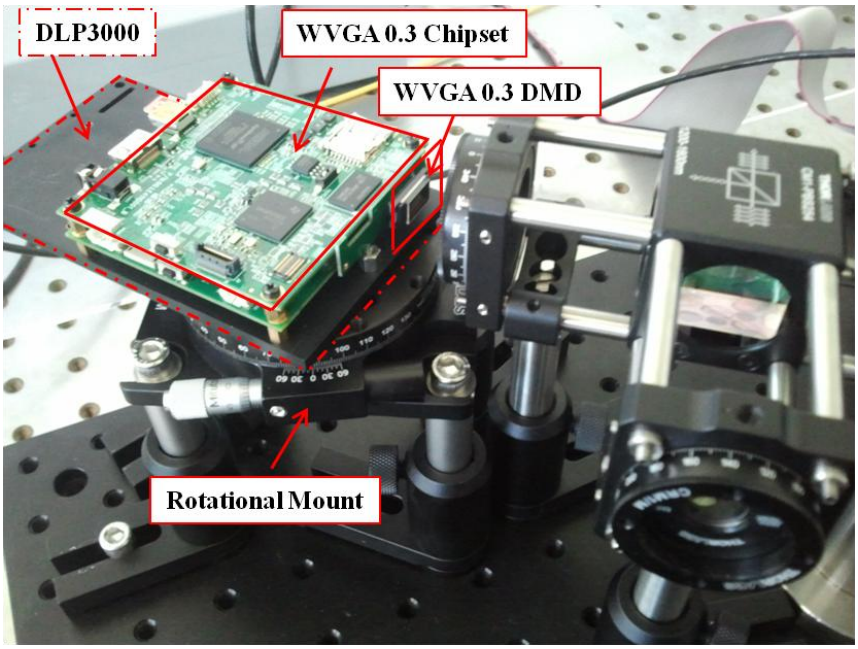

Fig. 3-23. The DLP300 DMD TI, composed by a reconfigurable screen (DLP 0.3 WVGA DMD) and the electronic driver to control it (DLP WVGA 0.3 Chipset) over an angular rotation stage. Micro mirror array distribution on a 608x684 diamond pixel configuration (right).

The device under test (Fig. 3-23) is a 608 × 684 resolution DMD from Texas Instruments (DLP3000 DMD) with a micro-mirror diagonal size of 10.8 µm and 7.6 µm micromirror pitch which reflects the incoming light in two angular positions of 12° (on state) and −12° (off state) [144]. Optically, the DLP3000 consists of 415,872 highly reflective, digitally switchable, micrometer-sized mirrors (micromirrors) organized in a two-dimensional array. The micromirror array consists of 608 micromirror columns (N_{xT}) by 684 micromirror rows (N_{yT}) in diamond pixel configuration. The diamond pixel configuration introduces a set of considerations that have to be taken into account. The diamond pixel configuration implies that the columns of each odd row are offset by half a pixel from the columns of the even row. The main consequence is that odd rows do not contribute to the effective size of the DMD area used, so the effective number of rows for the designer from a spatial point of view is $N_y = N_{yT}/2 = 342$ pixels. The pixel index in the y direction considered in previous equations y_n corresponds only to the even rows of the DMD. Also, as we are using Gaussian beams, the effective area used is a circle, so $N_x = N_y$=

342. This leads to a loss of the effective area used in the DMD, wasting a total of 608-342=266 lateral columns. The resulting diameter of the beam is then 342x10.8µm = 3.69 mm.

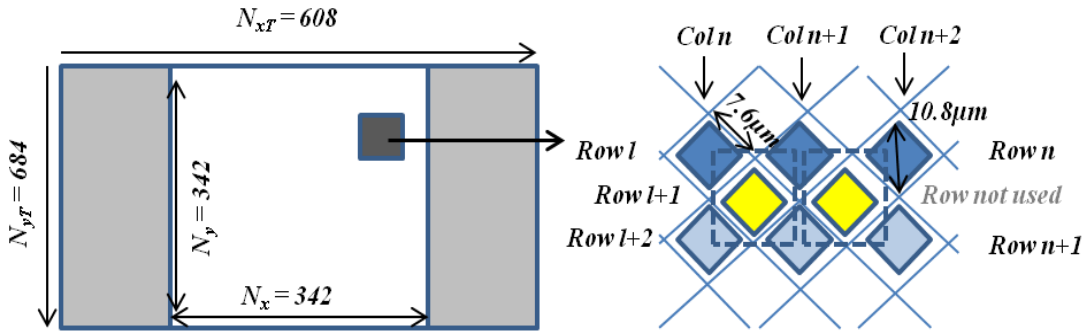

Fig. 3-24. Diamond pixel configuration of the DMD. The columns of each odd row are offset by half a pixel from the columns of the even row so they do not contribute to the effective size of the DMD area used. The effective number of rows for the designer from a spatial point of view is $N_y = N_{yT}/2 = 342$ pixels. The pixel index in the y direction considered in previous equations y_n corresponds only to the even rows of the DMD. Also, as we are using Gaussian beams, the effective area used is a circle, so $N_x = N_y$= 342.

Each aluminum micromirror is approximately 7.6 microns in size, and is switchable between two discrete angular positions: –12° and +12°. The angular positions are measured relative to a 0° flat reference when the mirrors are parked in their inactive state. The tilt direction is perpendicular to the hinge-axis. Each individual micromirror is positioned over a corresponding CMOS memory cell. The angular position of a specific micromirror is determined by the binary state (logic 0 or 1) of the corresponding CMOS memory cell contents, after the mirror clocking pulse is applied. The angular position (–12° or +12°) of the individual micromirrors changes synchronously with a micromirror clocking pulse, rather than being coincident with the CMOS memory cell data update. Therefore, writing a logic 1 into a memory cell followed by a mirror clocking pulse results in the corresponding micromirror switching to a +12° position. Writing a logic 0 into a memory cell followed by a mirror clocking pulse results in the corresponding micromirror switching to a –12° position.

To analyze the efficiency of the generated first diffracted order we have to take into account several effects present in these devices. First, residual effect to be considered on these devices is the multiple slit diffraction effect [21]. The space between micro mirrors creates a two dimensional grating structure that introduces a residual modulation that diffracts the incoming light into additional modes, which are translated into power losses. The residual diffracted order locations will be determined by the grating pitch (*d*), the wavelength and the incident angle. The

theory that we have previously developed in this chapter to model the diffracted mode generation by using binary gratings can be similarly applied to explain this residual effect. From Eq. 3.72 and assuming a periodic grating with period *d*, the residual diffraction grating in the *x* direction $h_{r,x}(x,y)$ can be expressed as

$$h_{r,x}(x,y) = \sum_{m} \frac{sin\pi m q_r(x,y)}{\pi m} exp\ (jm\left(cos\left(2\pi\frac{\lambda}{d}x\right)\right) \tag{3.86}$$

where m is the diffracted mode. As we did for Eq. 3.73, $h_{r,x}(x,y)$ can be expressed as

$$h_{r,x}(x,y) = \sum_{m} U_{r,m} = \sum_{m} \left|U_{r,m}\right| exp\ (jmw_{r,m}x) \tag{3.87}$$

where $U_{r,m}$ is the residual *m* mode with amplitude $\left|U_{r,m}\right|$ and phase $w_{r,m}x$, where $w_{r,m} = \lambda/d$ is the spatial carrier modulation. By extending this equations to a two dimensional grating, the resulting effect is a 2-D grid of diffracted orders separated by λ/d in both, the *x* and *y* directions, due to the residual space between micromirrors. The effect is shown in Fig. 3-25. The amplitude of each mode is defined by

$$\left|U_{r,m}\right| = \frac{sin\pi m q_r(x,y)}{\pi m} \tag{3.88}$$

where $q_r(x,y)$ is the function that defines the width of the residual gratings as

$$h_{r,x}(x,y) = \begin{cases} 1\ if\ cos\left(2\pi\frac{\lambda}{d}x\right) > cos(\pi q_r(x,y)) \\ 0\ if\ cos\left(2\pi\frac{\lambda}{d}x\right) < cos(\pi q_r(x,y)) \end{cases} \tag{3.89}$$

The resulting array diffraction efficiency is a parameter given by the constructor and it is defined to be 86 % for this device. Another parameter is the array fill factor, which measures the effective area with reflectivity in the device. The DLP3000 presents a fill factor of 92%. Also, the micro mirror reflectivity is optimized for the 420 nm-700 nm range, reaching a 88% reflectivity for these frequencies. The effective reflectivity drops to about 75% at 1550 nm. The result is a total loss of about 45% loss for the cumulative inbound pass plus outbound pass through the glass. Considering that binary holography is implemented with this device, the maximum

achievable efficiency that a binary hologram can provide for the first diffracted order is 10.1% [142][147]. This results in a total efficiency that can be expressed as:

$$\eta_{tot} = {\eta_{sp}}^2 \cdot \eta_r \cdot \eta_{fill} \cdot \eta_{dif} \cdot \eta_{holo} \qquad 3.90$$

where η_{sp} is the single pass window efficiency, η_r is the mirror reflectivity, η_{fill} is the array fill factor, η_{diff} is the diffraction efficiency and η_{holo} is the first diffracted order holographic efficiency. To measure the efficiency we compare the power of the first diffracted order with the output power of the fiber-to-free-space stage by means of a broadband InGaAs photodetector from OEC GmbH that presents a large responsive area (*D*=12mm), which presents a variable effective responsivity up to $3x10^5$ [V/W]. The resulting efficiency after measuring both signals leads to a -14.2 dB of losses. The low efficiency for generating holography is one of the disadvantages of using this technology, but it is not critical for our design due to the fact that, in general, the laboratory the laser sources can provide as much optical power as needed. Also, the motivation is to generate artificial aberrated wavefronts, so this technology is not intended to be implemented in real systems, where the link budget is generally critical.

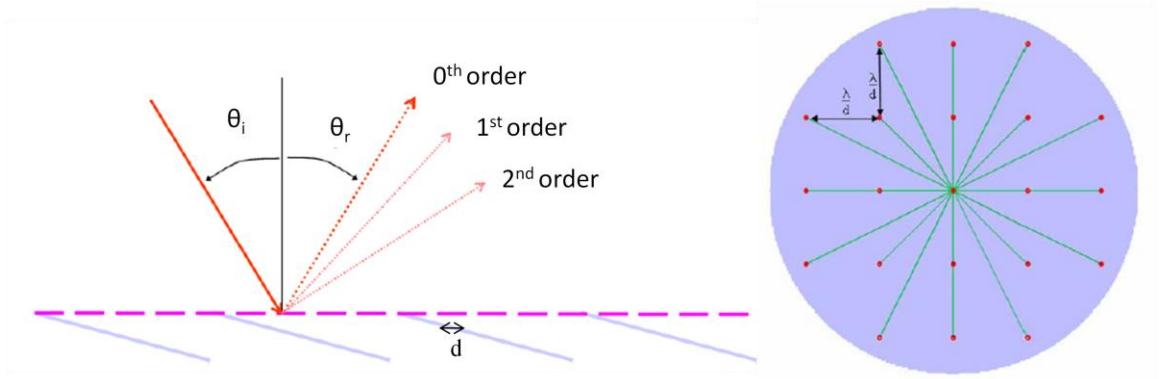

Fig. 3-25. Dimensional grating structure introduces a residual modulation that diffracts the incoming light into additional modes, which are translated into power losses [21].

3.4.3 Wavefront Phase Measurements using Mach-Zehnder Interferometers

An experimental setup to demonstrate the functionality of the method have been developed using the TI DLP3000 DMD. In order to verify the phase patterns of the generated beams we have implemented a Mach-Zehnder interferometer. The experimental set-up can be seen in Fig. 3-26. A collimated plane-wave reference beam coming from the same laser is interfered with the

filtered mode generated by the DMD and the interference pattern is recorded by a CCD Camera of 752x528 pixel resolution. The atmospheric aberrations are generated by loading the computer generated holographic patterns onto the DMD. By selecting a grating period of 8 pixels, the resulting angular separation between modes is 0.0179 rad working at 1550nm. The angle formed by the incident beam and the mirrors on 'on' state is 0.7675 rad. This incident angle is set at this value in order to have the first diffracted order perpendicular to the incident beam. Then, the first order beam must be filtered and isolated from the other diffraction orders by using a set of two lenses of equal focal length (40mm) and a variable aperture. A ND filter is introduced in the reference branch to control the intensity of the reference beam. The interferences were recorded by the CCD image with an integration time of 1/60Hz ≈ 17ms.

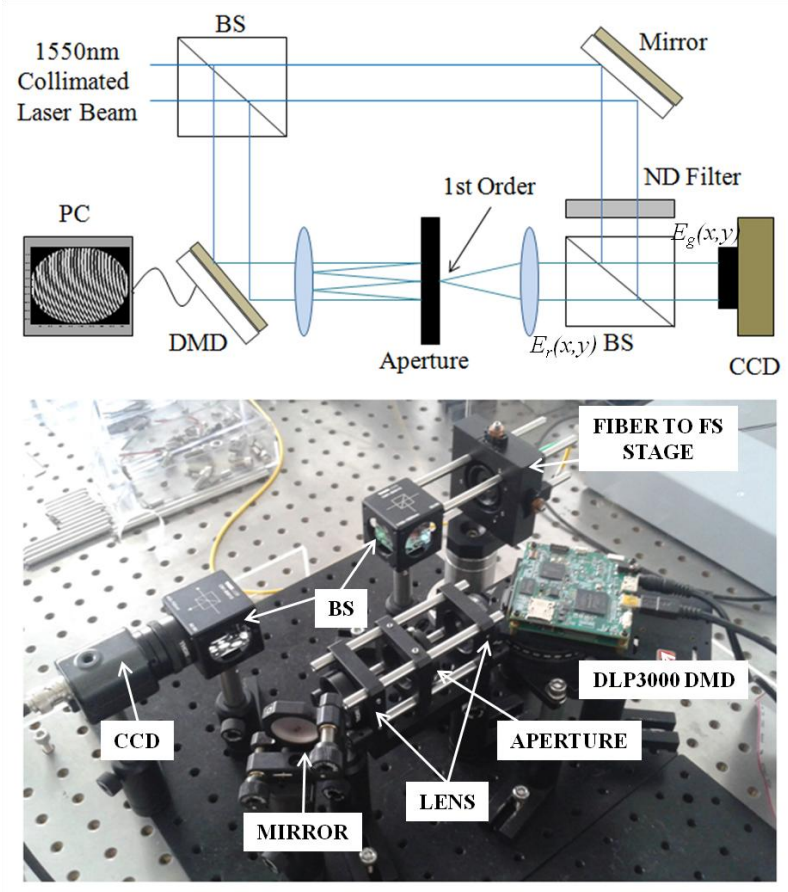

Fig. 3-26. Experimental Set-up for a Match-Zenhder self interferometer. A collimated beam is divided into two beams. The first beam hits the DMD and the resulting first spatial mode is filtered using two lenses and a variable aperture. The reference beam interferes with the aberrated beam using a beam splitter and the interference pattern is recorded using a CCD camera.

In this configuration, the incoming field in the evaluation branch is the output of the OTG and is defined as

$$E_{g,o}(x,y) = \left|E_g(x,y)\right| exp\left(j\varphi_{g,o}(x,y)\right) \tag{3.91}$$

where $\varphi_{g,o}(x,y)$ and $\left|E_{g,o}(x,y)\right|$ are the wavefront phase and amplitude, respectively. A second field, which will be known as reference wave $E_r(x,y)$, is equivalently defined as

$$E_r(x,y) = |E_r(x,y)| exp\left(j\varphi_r(x,y)\right) \tag{3.92}$$

The intensity recorded by the CCD camera is given by

$$\begin{gathered} I_{CCD}(x,y) = \left|E_{g,o}(x,y) + E_r(x,y)\right|^2 \\ I_{CCD}(x,y) = I_r(x,y) + I_{g,o}(x,y) + 2\sqrt{I_r(x,y)I_{g,o}(x,y)}cos\left(\varphi_{g,o}(x,y) - \varphi_r(x,y)\right) \end{gathered} \tag{3.93}$$

where $I_r(x,y) = E_r(x,y)E_r(x,y)^*$ and $I_{g,o}(x,y) = E_{g,o}(x,y)E_{g,o}(x,y)^*$. In the case of the reference branch, we assume that the wavefront phase $\varphi_r(x,y)$ is space-constant and it is defined by the path difference between both branches. This factor introduces a phase offset that has to be calibrated in order to extract the exact phase. In our case it is enough to extract the information about the variations of $\varphi_{g,o}(x,y)$, so this term can be neglected. It is important to note that this configuration cannot be implemented with a PBS because both signals would have orthogonal polarizations and they would not interfere in the CCD.

From Eq. 3.93 it can be seen that the phase difference between both branches influence the resulting intensity on the CCD. The performance of an interferometer is an important concern when we deal with phase measurements. The performance can be measured as the capability of the interferometer to visualize the resulting fringes or perceive the contrast on the interference images [105]. For that we use the term visibility, which is defined as

$$V_{IS} = \frac{I_{CCD,max} - I_{CCD,min}}{I_{CCD,max} + I_{CCD,min}} \tag{3.94}$$

It can be easily derived from Eq. 3.93 and Eq. 3.94 that the maximum visibility that can be achieved is for $I_r(x,y) = I_{g,o}(x,y)$. The ND filter selected performs this equilibration. As the

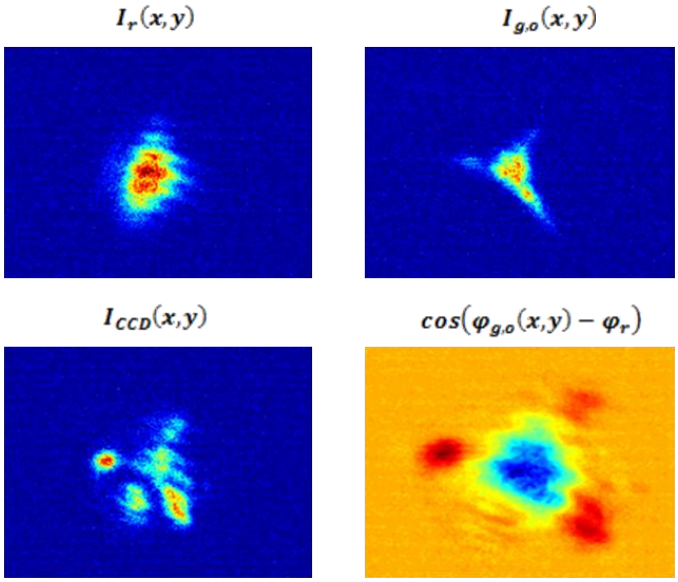

Fig. 3-27. Procedure for extracting the phase information in a Mach-Zehnder interferometer. First, the profile intensities of both branches are recorded. Then, the intensity profile is acquired and the phase profile is calculated by using Eq. 3.95.

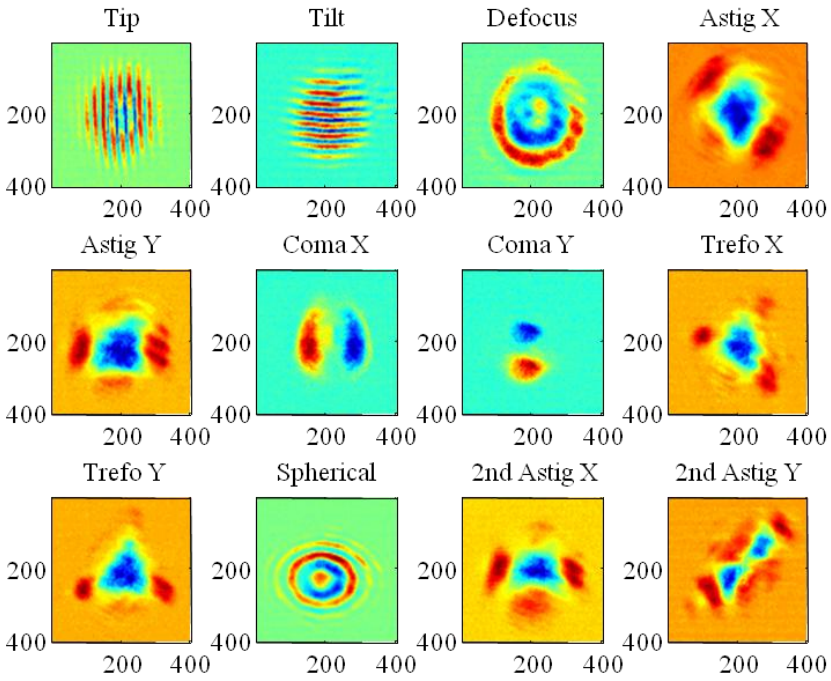

Fig. 3-28. First twelve Zernike modes generated by the DLP3000 DMD obtained using the Mach-Zehnder interferometer. The measured phase maps match the wave-front aberration profile that is introduced for each mode.

aberrated wavefront presents 14.2 dB losses, the ND filter is selected to introduce an attenuation of 15 dB, close to the perfect value. This slight difference leads to a loss of the practical visibility.

From Eq. 3.93 it can be also derived that for extracting the phase information we have to substract the intensity profile of both branches and normalize it by the intensity profiles as

$$cos\left(\varphi_{g,o}(x,y) - \varphi_r\right) = \frac{I_{CCD}(x,y) - I_r(x,y) - I_{g,o}(x,y)}{2\sqrt{I_r(x,y)I_{g,o}(x,y)}} \qquad 3.95$$

Therefore, first we have to record the profile intensities of both branches separately. Then, the intensity profile is acquired and the phase profile is calculated by using Eq. 3.95. This procedure can be seen in Fig. 3-27.

Several factors influence the resulting phase information, introducing some uncertainties on the final image. First, the best response of the CCD camera is achieved with a low exposure time due to the fact that phase variations of the laser degrade the averaged image [148]. In the other hand, the image noise increases as only few images are taken in a single acquisition. To increase the quality of the final image we perform a two-dimensional averaging, or low-pass filtering, of $cos\left(\varphi_{g,o}(x,y) - \varphi_r\right)$.

The second main limitation is the dynamic range of the camera in junction with the intensity pattern on the far field of both branches. On the reference branch, as we are using Gaussian beams, the intensity profiles concentrate higher power levels in the center than in the surrounding areas. Also, the far field intensity of the aberrated wavefront introduces variations on the recorded profile. From Eq. 3.93, it can be seen that the phase information in areas with low intensity in any of both branches present lower SNR, while for areas with high power this SNR would be dramatically increased. Therefore, to obtain a good resolution the dynamic range of the camera needs to be sufficiently large to not introduce saturation at the maximum power regions, which would lead to a loss of phase information, and to obtain information intensity even when the reference intensities are low. This introduces specific hardware requirements to measure the phase profile in detail. In the other hand, this scheme is enough to provide a qualitative approach to experimentally demonstrate the viability of the OTG. A more detailed and robust analysis of the generated phases is performed in Chapter 4 by using the free-space to fiber coupling stage and comparing the results of the mixing efficiency with the model provided in Section 3.2.2.

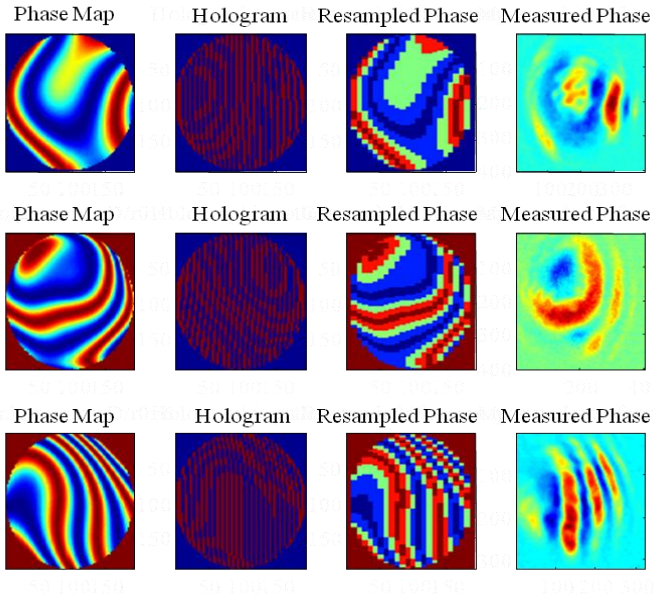

Fig. 3-29. Atmospheric turbulence aberrations generated using Kolgomorov statistics and different turbulent scenarios D/r_0= 2, 4 and 6. Ideal aberration to be generated, holographic patterns, quantizated and downsampled phase map implemented by the DMD and interference recorded.

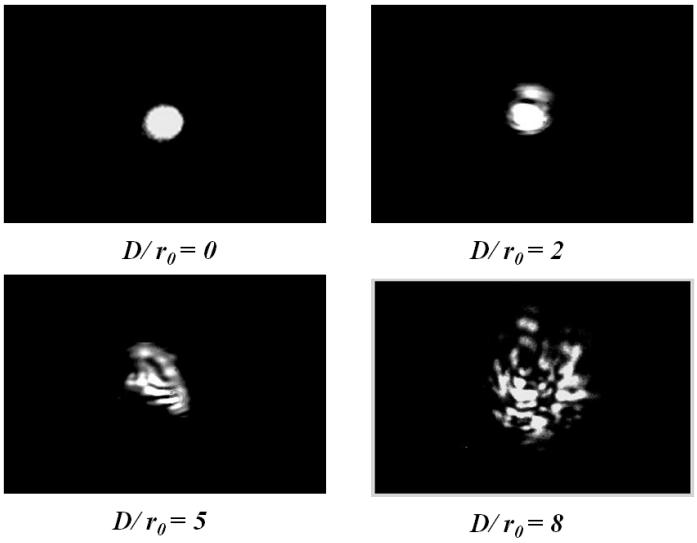

Fig. 3-30. Intensity recorded patterns for several Kolgomorov wavefront aberrations with normalized turbulence strength D/r_0 = 0, 2, 5 and 8.

Several Zernike modes were introduced into the DMD and interference patterns were obtained by using the Mach-Zehnder interferometer. In Fig. 3-28 the resulting phase maps obtained for each mode are shown. The measured phase maps match the wave-front aberration that is introduced for each mode. In some areas the phase information is difficult to extract due to the absence of intensity. Still, the generic profile for each Zernike mode is successfully achieved.

Using the first 120 modes and the Noll approach [102] random wave-front aberrations can be generated on the laboratory for different turbulence strength scenarios.

In Fig. 3-29 we present different realizations for Kolgomorov aberrations. The figure shows the ideal phase map to be generated, the downsampled and quantizated phase map that can be generated by the DLP3000 and the interference pattern recorded by the CCD camera. Slightly differences are observed between the obtained phase map and the ideal perturbation due to the dynamic range limitation of the CCD and the Gaussian shape of the beam. Still, it can be seen that the interference patterns obtained match the phase maps introduced by computation, which ensures that the method and the devices are working properly. In Fig. 3-30 the intensity pattern of several Kolgomorov wavefront aberrations is shown. These images were obtained with the same CCD camera but, instead of using the interferometric set-up, the first diffracted order light beam was filtered and its intensity was directly recorded. In these images it can be appreciated how the coherence diameter progressively diminishes. For $D/r_0 = 2$ the intensity pattern is slightly modified in compare to the reference image. In the other hand, the intensity profile results into an speckle pattern for $D/r_0 = 8$.

In this section we have studied the feasibility of generating atmospheric aberrations by using binary digital holography and commercially available DMDs. We have developed the theoretical background behind the application of BCGH techniques with micromirror arrays, identifying the required assumptions and input parameters. Then, an experimental set-up of the technique has been implemented and we detailed the different trade-offs of the method. In doing so, we highlighted the main advantages and weaknesses of the wavefront generation technique. We have also demonstrated experimentally its practicability by creating atmospheric aberrations using a complex set of Zernike modes and the Kolgomorov model of turbulence. As a part of the next chapter, and taking advantage of the coherent FSO system, we provide detailed results on the accuracy of the phase wavefronts generated by this method by measuring the mixing efficiency of the LO source with the aberrated wavefront.

4 Adaptive Optics in Free Space Optical Systems

In this chapter we present the principles of AO systems, the main architectures used and the spatial and temporal requirements for its application on real systems. Then we perform the design and implementation of a wavefront sensor-less optical system driven by a blind search algorithm, the parallel gradient descendent algorithm (SPGD), and we study its performance under different SNR scenarios and system parameters. Then, the AO is used to compensate phase wavefront distortions introduced by the OTG implemented in the previous chapter and its performance is evaluated under different turbulent strength scenarios.

4.1 Principles of Adaptive Optics

Refractive index variations of the earth's atmosphere introduce wavefront aberrations in laser beams that are propagated through the atmosphere. These distortions degrade the signal that arrives to the optical receiver, which diminishes the performance of the free space optical system. In order to increase this performance, wavefront distortions can be mitigated by using adaptive optics [149][150]. The main objective of any adaptive optical system is to introduce a phase correction in the incoming wavefront that converts the aberrated wavefront into a plane wave. This compensation principle is visually expressed in Fig. 4-1. The adaptive optics technology was primarily used in astronomy in order to improve the image quality of the outer space, but nowadays we can find applications in many different fields such as free space communications communication, lidar systems, optical tomography, etc. In our project we are focused on free space optical coherent communications, which performance is severely degraded by these distortions. The atmospheric turbulent channel results into a link deterioration and an increase of the BER [18], which is considered the defining parameter on any communication system. Typical fiber optical communications systems are able to improve the BER by applying data coding techniques, which are able to diminish the errors related to electro-optical noise. In FSO communications these techniques are not enough to ensure a good system performance and adaptive optics become mandatory in order to maximize the communication efficiency. In FSO

systems the receiver collects the optical power through small photo diodes or single mode fibers coupled to a lens. In order to maximize the focusing efficiency a plane wave on the incident plane is needed, so the collected power in the fiber can be increased. In coherent communications systems, the incoming beam has to be mixed with the local oscillator. This problem can be treated equivalently as the coupling stage of a laser beam into a single mode fiber [26]. The mixing efficiency, as it has been shown in Chapter 3, is highly dependent on the wavefront coherence of these two light beams, so the wavefront control becomes a crucial stage to achieve a successful communication performance.

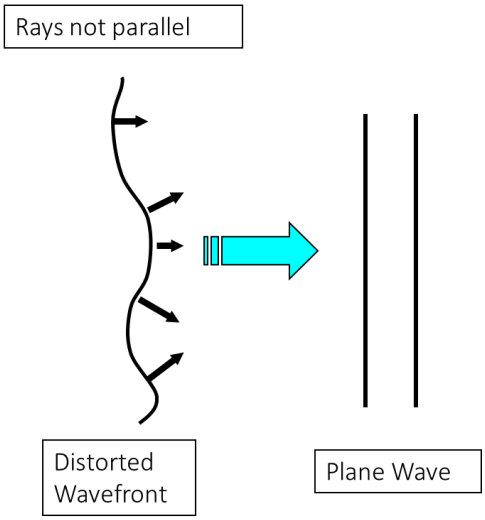

Fig. 4-1. Principle of wavefront correction. The incoming distorted wavefront is converted into a plane wave by introducing adaptive optics.

4.1.1 Modal and Zonal Correction of Atmospheric Aberrations

As we stated on Chapter 3, one of the main parameter to describe the wavefront phase aberrations on the aperture plane of the receiver is the phase variance σ_{φ}^2. When AO is applied, a correcting phase map $\varphi_c(\rho)$ is substracted from the incoming phase wavefront. The resulting residual variance σ_{res}^2 of the corrected wavefront is then expressed as

$$\sigma_{res}^2 = \frac{1}{\pi}\int \left(\varphi(\rho) - \varphi_c(\rho)\right)^2 d\rho \qquad 4.1$$

Two main techniques are used to characterize the wavefront error over a two-dimensional aperture: zonal and modal. The modal approach is based on the principle that the actuator is able

to completely compensate j Zernike modes. The theoretical basics were presented in Chapter 3, where the phase variance was expressed in terms of the normalized turbulence strength D/r_0 and the number of corrected modes j. Using the expressions derived in Chapter 3, the correction phase map $\varphi_c(\rho,\theta)$ can be defined as

$$\varphi_{c,J}(\rho,\theta) = \sum_{j=1}^{J} a_{c,j}\, Z_j \qquad 4.2$$

where $a_{c,j}$ are the Zernike coefficients of the correcting phase map and Z_j is the j Zernike mode. The resulting residual phase error is then:

$$\sigma_j^2 = \sigma_\varphi^2 - \sum_{j=1}^{J} \left|a_{c,j}\right|^2 \qquad 4.3$$

where σ_φ^2 is the phase variance of the incoming signal. The residual errors σ_j^2, widely known as Zernike-Kolgomorov residual errors, can then be obtained from Table 3-2. In Fig. 4-2 we represent the phase variance of a corrected wavefront when j modes are corrected for $j = 0, 2, 6, 10, 15, 20$.

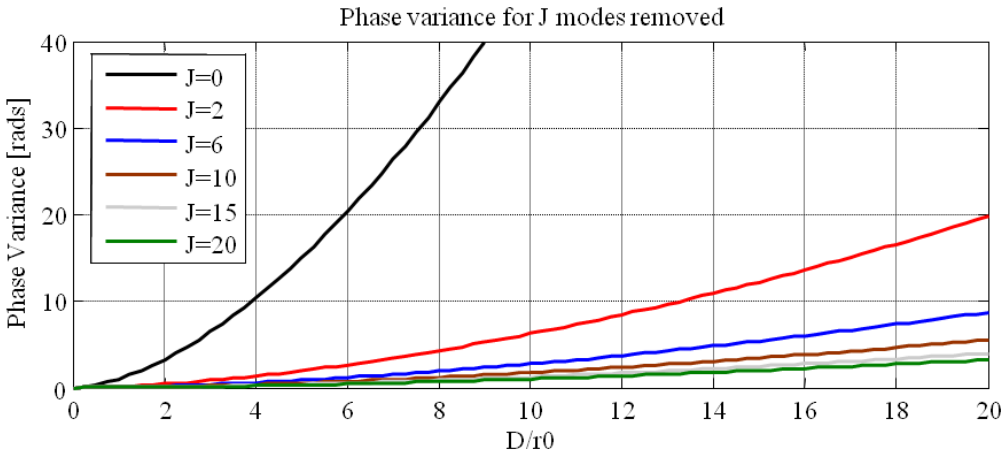

Fig. 4-2. Wavefront phase variance for atmospheric turbulence when j modes are corrected for $j = 0, 2, 6, 10, 15, 20$.

The wavefront correction is usually performed by two separated set of mirrors: first a steering mirror, which performs the correction for the tip/tilt components, and a deformable mirror, which try to compensate higher order modes. The reason for this is that the phase variance

it is not equally distributed over all Zernike modes. Actually, by removing the first two Zernike modes, the resulting phase variance is reduced by a factor of $\sigma_3^2/\sigma_1^2 = 7.685$. A representation of the variance for the 20 first Zernike modes is shown in Fig. 4-3, where it can be seen the greater impact of the tip and tilt components on the total phase variance of the wavefront.

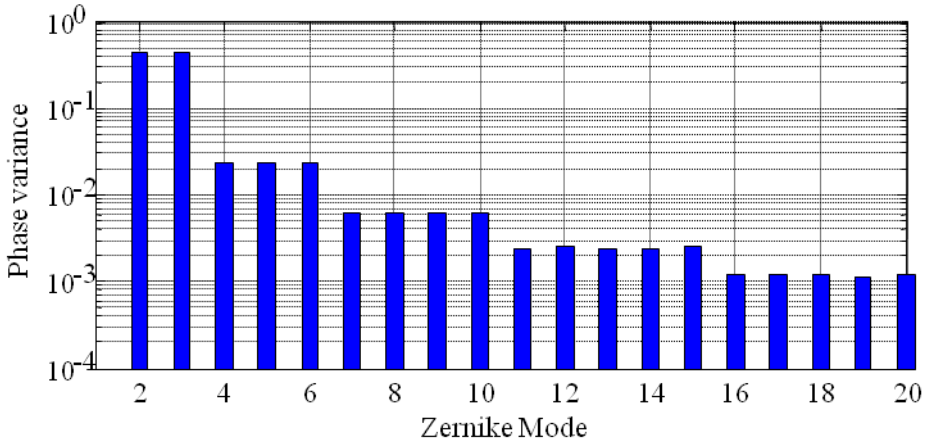

Fig. 4-3. Variance magnitude of the first 20 Zernike modes. The two first Zernike modes (tip/tilt) have a greater impact over the total phase variance.

The lowest orders aberrations (tip and tilt), which are the responsible for moving the beam centroid around the focal plane, are in general mitigated by using a steering mirror. This allows increasing the AO efficiency as higher orders can be mitigated by using a separated deformable mirror. By doing so, the AO system exploits the maximum dynamic range of the DM stroke as it does not have to compensate the strongest phase distortions. In some cases, correcting just the two first Zernike modes may be sufficient to increase the power received in applications with large photo-detector areas and low dependency on phase information [102], but in free space optical coherent communications, a higher resolution phase compensation is required in order to avoid signal fading due to the necessity of coupling the focused beam into a single mode fiber, as it was derived from Fig. 3-5.

Assuming that modal compensation can be applied to the tip/tilt components by using a fast steering mirror, the rest of the compensation is generally implemented by using zonal correction. In the zonal approach the aperture is composed by an array of independent subapertures or zones. In each of these zones the wavefront phase applied is estimated to minimize the resulting phase variance by performing a spatial average on each independent actuator [151]. The phase variance after zonal correction is expressed by

$$\sigma_z^2 = \frac{1}{\pi}\int \left(\varphi(\rho) - \varphi_z(\rho)\right)^2 d\rho \qquad 4.4$$

where $\varphi_z(\rho)$ is the phase map applied by the zonal corrector. In the next section we describe the analytical expressions to evaluate the performance of these techniques.

4.1.2 Spatial requirements for AO Systems

In order to define the spatial requirements of an adaptive optical system, first, the expected perturbation on the aberrated wavefront must be analyzed. The compensation optics stage, as it has been stated in the previous section, is composed by two different mirrors in order to maximize the efficiency of the system. First, a fast steering mirror (FSM) is focused on the compensation of the two first Zernike modes: Tip and Tilt, which basically corrects pointing errors and perturbations on the angle of arrival. The highest orders are meant to be corrected by using a deformable mirror (DM), which is composed by a set of micro-mirrors that introduce a phase modulation in each one of them. In the previous section, the partition of the compensation stage into these two mirrors has been demonstrated to be a practical solution to maximize the spatial performance of the DM. If no FSM is used, the consequence is that most of the correction potential of the DM is employed on correcting the lowest orders. Also, pointing problems will occur due to the fact that the incoming beam doesn't hit the center of the DM. Further in this chapter the efficiency loss using only the DM will be shown.

Let us first describe the requirements for the FSM. In [26], an expression to estimate the standard deviation of the atmospheric tilt σ_{tilt} as a function of the telescope aperture is given by:

$$\sigma_{tilt} = \sqrt{0.184\left(\frac{D}{ro}\right)^{5/3}\left(\frac{\lambda}{ro}\right)^2} \qquad 4.5$$

Fig. 4-4 shows σ_{tilt} as a function of the coherence length r_0 for $\lambda = 1550\text{nm}$ and different telescope apertures. The maximum atmospheric Tilt can be expressed as $M_{tilt} = \pm 2.5\sigma_{tilt}$ [26], so for the given apertures and considering realistic values of r_0>10 mm, the maximum tilt is around 1mrad. Also we need to include a 0.5 factor due to the fact that an angular movement of the mirror corresponds to twice the beam angular shift. Assuming that no amplification is used, the maximum angular deplexion needed in our system is ±0.5mrad.

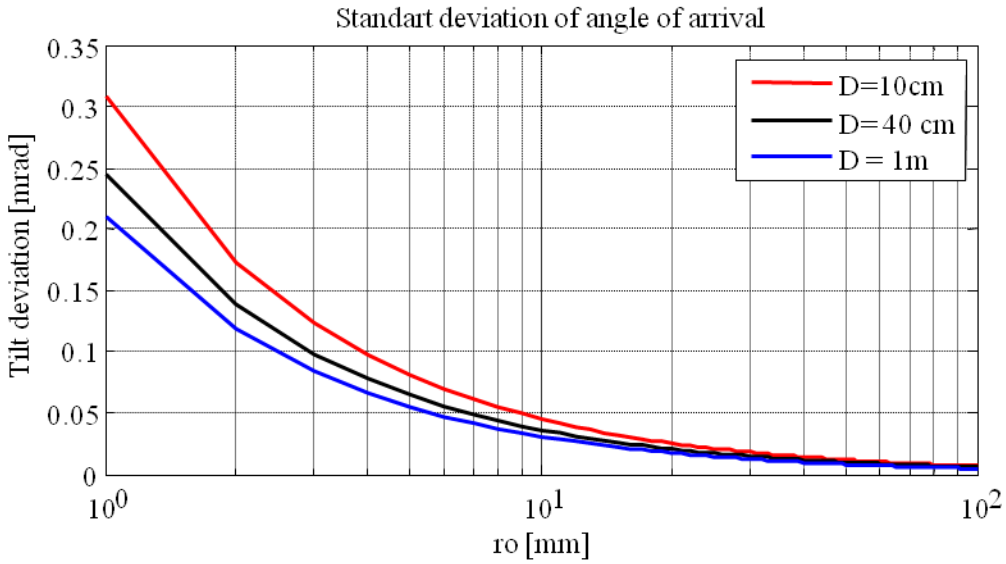

Fig. 4-4. Standard deviation of the atmospheric tilt as a function of the coherence length r_0 for $\lambda = 1550$nm and different telescope apertures.

The spatial requirements for the DM are calculated assuming that the whole tip-tilt is corrected by the FSM. Using the Noll's approach, the tip/tilt corrected phase wavefront presents a phase variance expressed as:

$$\sigma_{DM}{}^2 = \sigma_3{}^2 = 0.134\left(\frac{D}{ro}\right)^{5/3} \tag{4.6}$$

In [26] it is shown that the required actuator stroke S_{DM} for a deformable mirror is estimated as

$$S_{DM} = \frac{\lambda}{2\pi} \cdot 2.5 \cdot \sigma_{DM} \tag{4.7}$$

The rule to obtain this calculation is to consider that the peak to peak aberration is approximately 5 times the standard deviation of the tip-tilt corrected, but the phase change on the DM mirrors implies a double phase change, resulting into the 2.5 factor. The required DM Stroke for compensating tip/tilt corrected wavefronts as a function of the normalized turbulence strength can be seen in Fig. 4-5. To completely correct a turbulence of $D/r_0 = 10$ the required stroke is around 1.5µm. A typical stroke of 3.5µm is able to completely correct up to $D/r_0 = 27$.

Another key parameter that influences the performance of a DM is the interactuator spacing r_s, which defines the DM response in terms of spatial bandwidth. An analysis performed

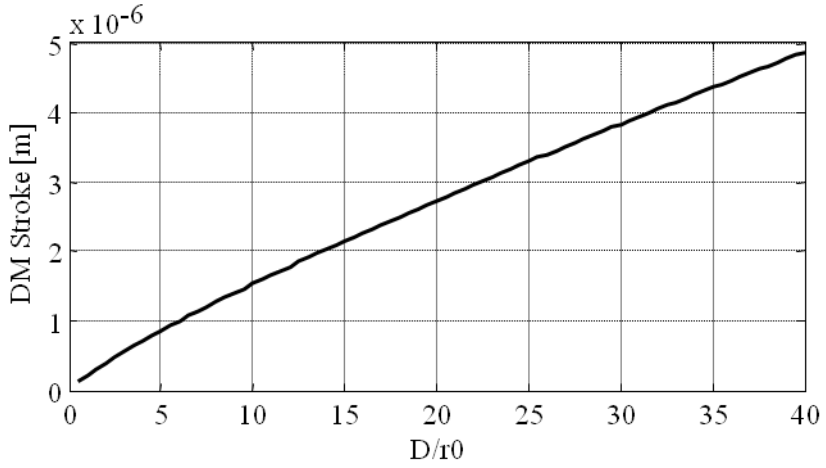

Fig. 4-5. DM Stroke required for compensating tip/tilt corrected wavefronts versus the normalized turbulence strength. To completely correct a turbulence of $D/r_0 = 10$ the required stroke is around 1.5μm. A typical stroke of 3.5μm is able to completely correct up to $D/r_0 = 27$.

in [152] derived that the residual phase variance after applying zonal correction by a DM is given by

$$\sigma^2_{res,m} = k\left(\frac{r_s}{r_0}\right)^{5/3} \tag{4.8}$$

This description quantifies the residual error in terms of the interactuator spacing r_s and the Fried parameter r_0. The k parameter is a constant that depends on the specific wavefront actuator architecture, and it usually takes values from 0.23 in segmented mirrors up to 0.35 with continuous membrane deformable mirrors [153]. The interactuator spacing is closely related with the number of independent actuators N_a needed to perform the correction over a specific aperture of diameter *D*. The formula that gives an estimation of the number of actuators is derived by using the strehl ratio (SR) from Eq. 3.42 and approximating it by using [154]

$$SR \approx exp\,(-\sigma^2) \tag{4.9}$$

So the *SR* for the residual variance from Eq. 4.8 is given by

$$SR \approx exp\left[-k\left(\frac{r_s}{r_0}\right)^{5/3}\right] \tag{4.10}$$

Therefore, r_s can be approximated by

$$r_s \approx r_0 \left(\frac{-ln\,(SR)}{k} \right)^{3/5} \tag{4.11}$$

By selecting a minimum *SR* and r_0 we can calculate a specific value for r_s. Given an aperture D, the number of independent cells can then be estimated as

$$N_a = \frac{\pi}{4} \left(\frac{D}{r_s} \right)^2 \tag{4.12}$$

The residual phase variance as a function of the Fried parameter r_0 and the interactuator spacing r_s is shown in Fig. 4-6. Typical values of r_0 between 2 and 40 cm and r_s between 0.2 mm and 1 mm were considered.

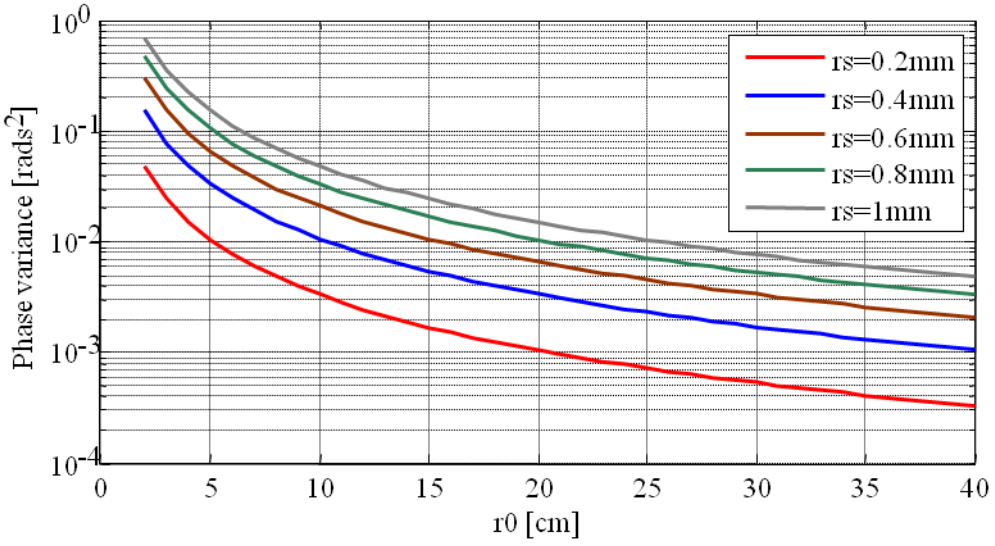

Fig. 4-6. Residual phase variance as a function of the Fried parameter r_0 and the interactuator spacing r_s for typical values of r_0 between 2 and 40 cm and r_s between 0.2 mm and 1 mm.

4.1.3 Temporal Requirements

The first study that completed the theoretical analysis to estimate the temporal performance of an AO system was presented by Greenwood [155]. In that study, the characteristic frequency f_G that describes the temporal behavior experienced by the AO system was presented. This frequency, widely known as Greenwood frequency, can be considered as the bandwidth at which the residual

wavefront error is limited to 1 rad. In this study, the residual phase error of the corrected wavefront under bandwidth limitations is expressed by

$$\sigma_G^2 = \left(\frac{f_G}{f_{3dB}}\right)^{5/3} \tag{4.13}$$

where f_G is the Greenwood frequency and f_{3dB} is the cut-off frequency of a first order RC-filter that models the closed-loop response of the AO. In Eq. 4.13, f_G is defined by [155] as

$$f_G = 2.31 \cdot \lambda^{-6/5} \left(\int C_n^2(z) v^{\frac{5}{3}}(z) dz \right)^{3/5} \tag{4.14}$$

being v the transversal wind velocity. Using this work, the tilt frequency f_{TG} (known as G-tilt) was derived in [156]. Therefore, the tracking frequency of a FSM can be estimated by using the G-tilt frequency, which is given by [156]

$$f_{TG} = 0.331 * D^{-01/6} * \lambda^{-1} * sec\,(\varphi) \int C_n^2(h) * V^2 dh \tag{4.15}$$

Typical tracking frequencies are not larger than a few *Hz*. For a typical turbulence scenario of $HV_{5/7}$ and average wind velocities we have that $f_{TG} = 7.44\ Hz$. The servo bandwitdth is recommended to be at least four times this frequency. The reason is that tracking control of the order of one fourth λ/D is adequate for most atmospheric applications. The resulting bandwidth required for a steering mirror is around 30Hz. The phase variance due the servo bandwith can be equivalently calculated using Eq. 4.13.

Using the Greenwood frequency obtained from [156], we can also set the temporal requirements for the DM using the approximation of the SR. The expression is derived by substituting Eq. 4.9 into Eq. 4.13. The resulting DM bandwidth is

$$f_{DM} = \frac{f_G}{(-ln\,(S_{DM}))^{3/5}} \tag{4.16}$$

Considering a typical perturbation scenario of $D/r_0 = 10$ a minimum bandwidth of 650 Hz is required. If the four times rule associated with a practical system is applied, the frequency rate of the DM should be at least 2.6 KHz.

4.2 Adaptive Optics Architectures for Free-Space Optical Systems

The adaptive optics (optical elements –typically mirrors– that can adapt their optical surface and performance to compensate for phase and poor optical quality of the light reflecting from them) technology to be considered in free-space coherent optical communications improve the quality of the received beam in order to obtain more power at the receiver and increase the mode matching efficiency between the received signal and the local oscillator. Deformable mirrors and wavefront sensors have been around almost as long as lasers. However, the use of adaptive optics has been limited by their significant complexity, and correspondingly high cost. These realities narrowed the application of adaptive optics to only the highest priced lasers or imaging systems. Still, new manufacturing process and designs brings affordable adaptive optics to a broader range of applications. Using dynamic faces with time-varying control are able to optimize or change the characteristics of reflected light for a specific application, one of these optical elements provides sharper images and tighter laser beams, even in a dynamic environment.

Typical adaptive optical systems are implemented with a deformable mirror to perform the correction of the phase wavefront profile, a wavefront sensor to estimate the wavefront error, and a feedback control algorithm to connect these elements in real time [26]. This technique, known as wavefront sensing, is based on the conjugation principle and it has been used in a wide number of systems, especially in astronomical applications [157].

A second approach is wavefront control using optimization of a performance metric by a blind search algorithm. Instead of implementing a phase conjugation by measuring the residual phase error, the phase correction strategy is based on the direct optimization of a system performance metric (received power, image sharpening, etc.). This approach is known as wavefront sensorless architecture [45]. Problems related with the use of the wavefront sensing technique have encouraged this adaptive system architecture for a wide set of optical applications. Also, the emergence of affordable wavefront correctors based on MOEMS technology and liquid-crystal (LC) phase modulators provide the potential to define fast, small, and inexpensive adaptive systems which can eliminate the problems associated with the wavefront sensor architecture. The development of capable blind search algorithms offers efficient signal processing architectures for adaptive optics applications. In this section we present the basics of these architectures and the optical components involved.

4.2.1 Direct Wavefront Sensing

Historically, the most commonly used architecture used to implement optical compensation is known as Direct Wavefront Sensing (DWS) [151][157]. The architecture is shown in Fig. 4-7. Its main characteristic is that it is composed by a wavefront sensor which is able to extract the wavefront phase profile. The measured wavefront is sent to the feedback control algorithm, which generates the information to the controller that feeds the actuators (usually consisting on deformable mirrors, steering mirrors, etc.).

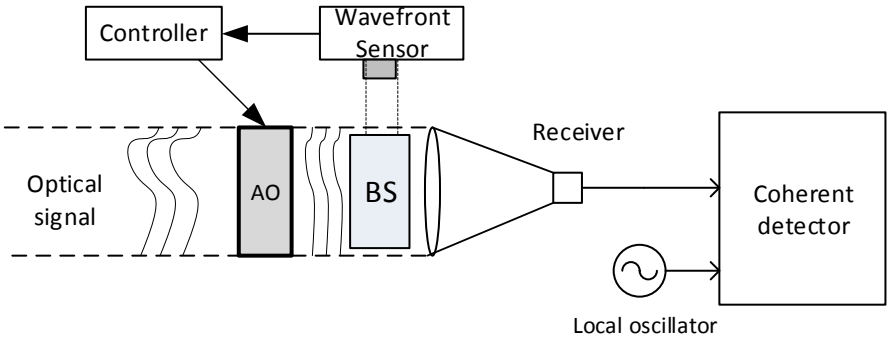

Fig. 4-7. Architecture of a direct wavefront sensing approach in AO coherent communication systems. The wavefront distortion is measured using a wavefront sensor and the data is sent to a feedback algorithm, which calculates the conjugated phase profile to apply in the AO.

The function of the feedback control algorithm is to generate the conjugated phase map by applying a principle of reciprocity to correct the aberrations. The control of the deformable mirror is based on the multivariate control theory [26]. If we define X_a as the set of mirror control command, the resulting phase introduced by the AO is given by

$$\varphi_M = A_M X_a \tag{4.17}$$

where A_M is the matrix mirror, which has been previously calibrated by the manufacturer. Using this expression, we can describe the optimal control command set to match a required measured wavefront φ_R as

$$X_A = {A_M}^{-1} \varphi_R \tag{4.18}$$

being ${A_M}^{-1}$ the pseudo-inverse matrix of A_M described by

$$A_M{}^{-1} = VS^{-1}U^T \tag{4.19}$$

Here, U, S and V are the singular value decomposition of A_M

$$A_M = USV^T \tag{4.20}$$

The coefficients of the diagonal matrix S are the singular values of the decomposition, which define the gain of each mirror control. The columns U and V represent an orthonormal set of the mirror deformation.

To achieve a good measurement performance, a part of the incoming light has to be re-directed to the wavefront sensor. Actually, these sensors also introduce some noise in the measurements that can be translated into a phase variance on the corrected wavefront. The phase variance for a wavefront sensor is given by [157] as

$$\sigma_{WFS}^2 \cong \left(\frac{2\pi\gamma_n w_i}{N_{ph}}\left(1+\frac{4n_d^2}{N_{ph}}\right)^{1/2}\frac{\lambda_b}{\lambda_i}\right) \tag{4.21}$$

γ_n is the noise reduction factor of the closed loop, w_i is the image width factor, λ_b and λ_i are the wavefront sensor and incoming beam wavelength, respectively, and N_{ph} is the averaged number of photons at each sensor aperture.

In these architectures the most important characteristic devices are the wavefront sensors (WFS). Nowadays, it is not possible to directly measure the wavefront phase at optical wavelengths with direct methods. Instead, optical detector can extract the phase information by measuring the resulting intensity signals derived from interferometry processes. Based on this principle, a wide set of WFSs are available. In this section we present a brief description of the two main types of WFS: the Shack-Hartmann (SH) sensor and the curvature sensor (CS). Other wavefront sensors, like the lateral shearing interferometer [158] or the pyramid WFS, are not widely used in AO, so their explanation is beyond the scope of this study.

4.2.1.1 Shack-Hartmann Sensor

The SH sensor is composed by a matrix of smaller subapertures, each one containing identical lenses used to produce multiple images. If the incoming beam presents a plane wavefront, every

image is located at the center of each cell of the grid, which is defined by the geometry of the subapertures. In the other hand, an aberrated wavefront will cause a displacement of the focused point in each cell, which is proportional to the wavefront slope displacement over the subaperture. This device often needs a reference plane wave generated from a reference source in order to adjust accurately the reference focus positions on the detector array. The images formed by the lenslet array are recorded by a charged-coupled device (CCD) simultaneously. A main disadvantage is that they require a high number of pixels per subaperture [151].

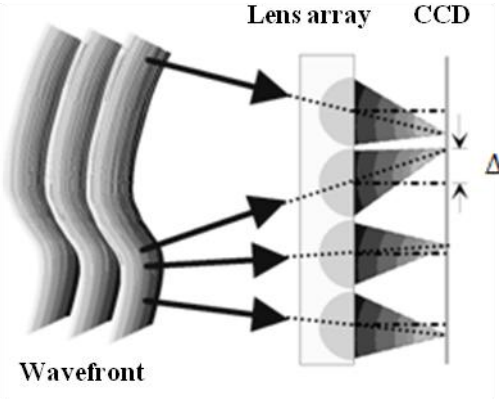

Fig. 4-8. Principle of SH sensor. The incoming wavefront is imaged into a CCD camera by a lenset grid. The detector measures the displacement Δx_i, which is proportional to the wavefront gradient [159].

For a given input phase wavefront $\varphi(x, y)$, the SH sensor measures the averaged displacement for each cell. The centroid displacement in the *x* direction for each cell Δx_i is given by [160]

$$\Delta x_i = \frac{\lambda}{2\pi A} \int \frac{\partial \varphi(x, y)}{\partial x} dx \qquad 4.22$$

where *A* is the subaperture area. A similar expression is used for the displacements in the *y* direction. The measurements of these displacements from its reference positions are directly proportional to the wavefront gradient. The principle is shown in Fig. 4-8. The most important drawback of SH sensors is their inflexibility with respect to wavefront tilt sensitivity and dynamic range, which cannot be changed during operation. Also, under strong scintillation, the intensity fading makes the use of these devices ineffective. Still, the SH sensor has become the standard wavefront sensor for adaptive optics systems.

4.2.1.2 Curvature Sensors

The principle of curvature sensing was presented by Roddier [161][162]. It is based on measuring the intensity distribution in two different planes and calculating the normalized difference between them, which, based on geometrical optics approximation, it is a measure of the curvature of the wavefront in the entrance pupil of the optical system and of the wavefront tilt at the pupil edge. The main goal for achieving compensation is making these both intensity profiles identical, which occurs when the phase wavefront is plane [163].

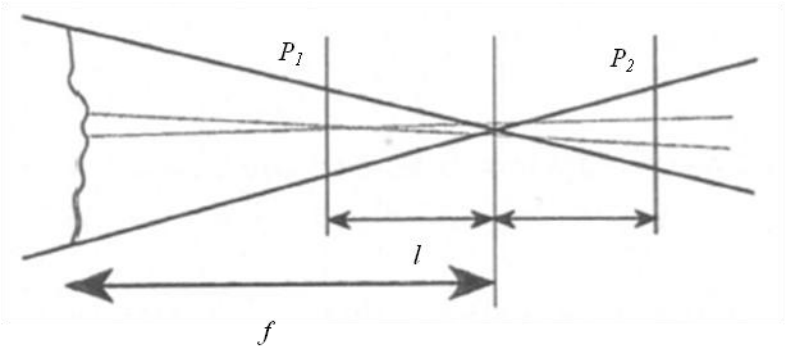

Fig. 4-9. Curvature Sensor principle. Two intensity distributions are obtained at P_1 and P_2, separated by a distance l from the focal plane. The phase wavefront is obtained from calculating the normalized difference between both intensity profiles.

The principle is shown in Fig. 4-9. Two intensity distributions are obtained at P_1 and P_2, separated by a distance l from the focal plane. The resulting normalized difference between both signals relates to the phase wavefront as [161]

$$\frac{I_1 - I_2}{I_1 + I_2} \propto \left[\frac{\partial}{\partial \rho}\varphi(\rho)\Psi - \nabla^2\varphi(\rho)\right] \qquad 4.23$$

where ∇^2 is the Laplacian operator representing the wavefront curvature and Ψ is the impulse response. This equation is derived by applying a geometrical optical approximation known as transport theory. The main advantage of the CS is that its output can be directly connected to a correction device without the use of a computer [164]. In the other hand, the spatial requirements for this devices are high, as the distance l needs to be sufficiently large to avoid having an intensity profile very small, fact that increases the requirements on the pixel resolution of the intensity recorder used.

4.2.2 Wavefront Sensorless Architecture

A second approach is wavefront control using direct system performance metric optimization (Fig. 4-10). Rather than performing explicit phase conjugation by equalizing the residual phase through measurement, reconstruction and conjugation of the wavefront, the phase correction strategy can be based on direct optimization of a system performance metric (received signal strength, Strethl ratio, image quality, etc.). This approach is known as wavefront control based on model-free optimization. Problems related with the use of the wavefront sensing technique, as mentioned above, have stimulated this adaptive system architecture for a number of optical applications. Also, the appearance of inexpensive wavefront correctors based on MOEMS technology and liquid-crystal (LC) phase modulators has the potential to define fast, small, and inexpensive adaptive systems if we can eliminate the obstacle of wavefront sensor hardware.

Also, efficient parallel model-free optimization algorithms offer efficient signal processing architectures for adaptive optics applications. This, in junction with the technological advances is electronic hardware and processing, have overcome the main limitation of this architecture: the control bandwidth that is necessary to compensate the atmospheric effects under realistic conditions [165][166].

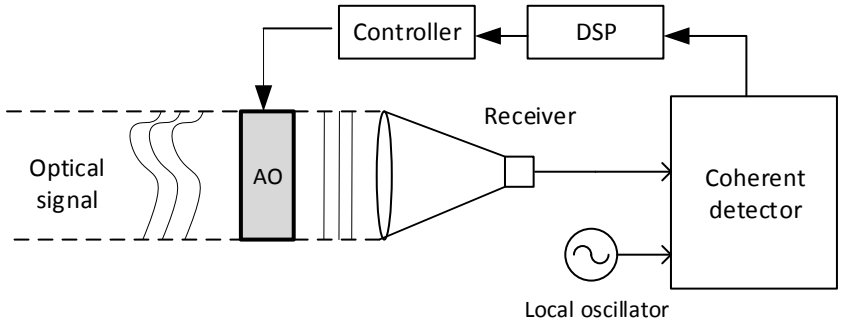

Fig. 4-10. Architecture of an indirect wavefront sensing approach in AO coherent communication systems. The wavefront distortion is compensated using a blind optimization of the performance metric generated by the coherent detector using digital signal processing (DSP).

For free space communications this architecture has several advantages in compare to the wavefront sensing design. The first and most intuitive one is that a wavefront sensor is not required, so the complexity and cost of the system is reduced. Second, as the feedback system is based on the maximization of a metric signal, there is no need to re-direct part of the incoming light to the wavefron sensor, which implies an increase of the received SNR. Also, information of

the received power is often available at the communication terminal, so no new hardware devices are needed to extract the metric signal. In addition, iterative algorithms usually demand less computation than the complex matrix calculations required in wavefront reconstruction. As a result we also have a great reduction in the cost and the size of the system. In the other hand, this architecture may present some inconveniences. First, it requires a set of iterations in order to achieve an optimal compensation while the WFS technique requires just one. Second, the noise present in the measured metric signal may affect the compensation performance of the blind search algorithms. An analysis of these subjects is provided in the next sections.

The stochastic parallel gradient descendent (SPGD) algorithm has been demonstrated to be a valid blind search algorithm that improves the efficiency of AO systems whose architectures do not include a wavefront sensor. First developed by Vorontsov [167], SPGD method has been successfully used in many scenarios [168][169]. In the next section we provide the description of this algorithm. Further in this chapter we analyze its performance and convergence rate as a function of the algorithm parameters and the SNR at the receiver.

4.2.2.1 Fundamentals of the SPGD Blind Algorithm

The SPGD is an improved algorithm which is based on typical steepest descendent algorithms. The concept is to apply random perturbations to the control parameters of all actuators at the same time and estimate the gradient variation of a previously defined performance metric signal. Many different metric signals (*J*) have been used in AO systems in previous studies, being the most common ones the optical power at the detector plane and the image sharpening ratio. From the change in the performance metric, the SPGD estimates the value of the gradient of the performance metric for each mirror control channel. The control signals are updated in each iteration following the next expression:

$$u^{m+}{}_n = u^m{}_n + \gamma^m{}_n \cdot \delta \cdot u \qquad 4.24$$

Where u_n represent the input commands to the actuator array, *n* is the actuator index (*n=1, 2, …, N*) and *N* is the total number of actuators on the AO system. The subscript *m* corresponds to the iteration number, and $m+$ and $m-$ indicate the positive and negative perturbations at the iteration number *m*. The parameter $\gamma^m{}_n$ is a random sign perturbation (+1 or -1) and δ is the

perturbation size parameter, which indicates the temporal offset quantity that is added to the control signal. Once the J^{m+} is recorded, the perturbation offset is reversed:

$$u^{m-}{}_n = u^m{}_n - \gamma^m{}_n \cdot \delta \cdot u \tag{4.25}$$

And the new metric value J^{m-} is recorded. Then, the gradient can be calculated as:

$$\delta J^m = J^{m+} - J^{m-} \tag{4.26}$$

The control signal for the next iteration is calculated to be:

$$u^{m+1}{}_n = u^m{}_n + G \cdot \delta \cdot J^m \cdot \gamma^m{}_n \cdot \delta \cdot u \tag{4.27}$$

where *G* is a gain parameter defined by the user. This iterative process drives the controller to a position that maximizes or minimizes the performance metric *J*. Typically, a trade-off between the perturbation size and the controller gain is present. Low controller gain and low perturbation amplitudes usually lead to reach the global maximum of the performance metric, but the convergence time increases. By increasing the controller gain and perturbation size the SPGD algorithm converges faster, but the variance of the metric signal increases and it is less likely to completely achieve the maximum value. Other methods based in this algorithm have been proposed and successfully validated [170], presenting slightly better performance in terms of convergence time. The implementation of these techniques could be a future improvement on the system developed on this project.

4.2.3 Wavefront Correctors

Wavefront correctors are devices that introduce an optical phase modulation on the applied optical beam with the purpose of removing wavefront phase aberrations. These correctors are usually divided into two classes depending on the compensation method used, zonal and modal. Modal correctors, such as piston mirrors or tip-tilt mirrors, allow individual control of a Zernike mode applied. In the other hand, zonas correctors, such as deformable mirrors, use a set of micro-mirrors to approximate the conjugated aberrated phase [171]. Both types of correctors are presented in this section.

4.2.3.1 Deformable Mirrors

Deformable mirrors are devices that produce an optical phase shift φ_l by introducing an optical path difference δ_l in each actuator. The phase shift produced is defined by

$$\varphi_l = \frac{2\pi}{\lambda}\delta_l \qquad 4.28$$

Deformable mirrors normally provide a stroke of a few microns in astronomical applications and up to 10 microns for atmospheric compensation (see Fig. 4-5), where they must respond within the coherence time of the aberrations. Deformable mirrors can be divided into five main groups depending on their characteristics (Fig. 4-11).

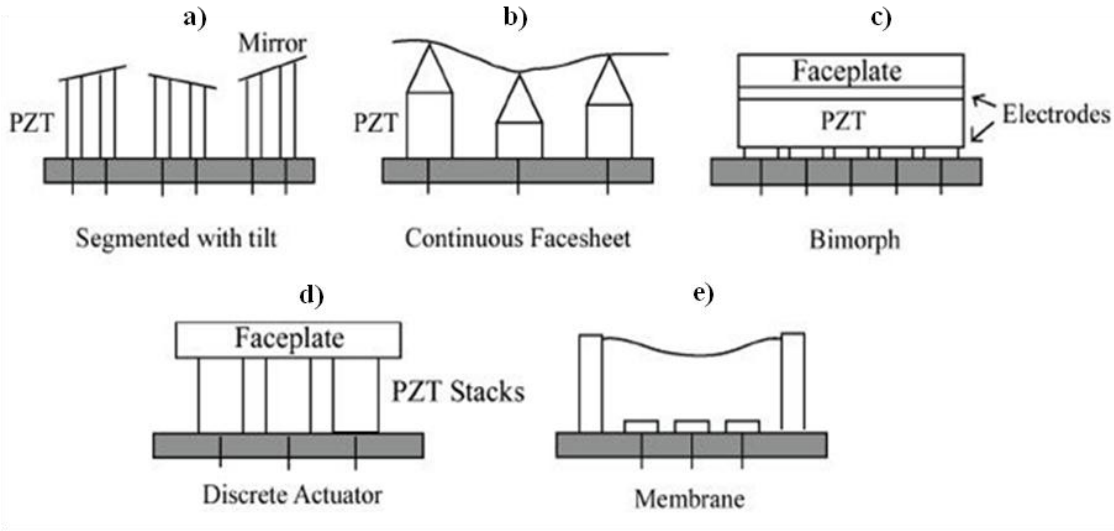

Fig. 4-11. Classes of deformable mirrors: segmented with tip/tilt (a), continuous membrane (b, c, e) and discrete actuators (d) [175].

First, segmented mirrors with single tip/tilt actuators, in which each mirror applies an independent tip/tilt phase modulation (Fig. 4-11.a). The main advantages are that each mirror is independent from the surrounding mirrors and they can be easily replaced in case of malfunction. In the other hand, the discontinuous nature of their surface produced diffraction effects due to the space between mirrors and also, it may provide a residual piston modulation.

Deformable mirrors with continuous surface are composed by a set of discrete actuators positioned at a stable mirror base which are tied to a thin flexible mirror [172]. They can be divided into and piezo-electric (PZT) mirrors (Fig. 4-11.b), where a set of actuators behind the mirror surface pushes the mirror by applying a force perpendicular to the surface, and bimorph

mirrors (Fig. 4-11.c) where the shape of the surface is modified by applying a force parallel to the surface [173][174]. This type of mirrors has been widely used due to several reasons: they provide above 100s actuators and the bandwidth is in the range of KHz with typical strokes of 5μm. Also, this technology has been well tested and it provides a very reliable solution for practical systems. In discrete actuators DMs (Fig. 4-11.d) the actuators are usually multilayer stacks of piezoelectric material. They are mounted on a massive baseplate and at the top of each actuator is a coupling that forms the interface between the actuator and the faceplate.

A recent type of deformable mirror - membrane mirror, usually known as MEMs (Micro-Electro-Mechanical system) [176] has lately attracted lot of attention. These DMs are composed by a thin membrane surface that can be directly manipulated by applying a certain voltage. The main advantage of these devices is that they can be produced at lower prices than their continuous membrane predecessors. On the other hand, their membrane is fixed at its corners, so correction cannot be performed on those areas. OKO Technologies [177 and Boston Micromachines [178] produce a wide set membrane mirrors for a relatively low cost. The main manufactured mirrors and their details are shown in Table 4-1

Table 4-1. Details of Commercial DMs [179]

Mirror	Technology	Diameter (mm)	Actuators	Stroke (μm)	Aprox.Price ($)
OKO37	Electrostatic	15	37	3.5	5000
OKO19	Piezoelectric	30	19	3, 7-9	8000
AOptix35	Electrorestrictive	10.2	35	16	30000
MIRA O52	Magnetic	15	52	50	26000
BMC140	Electrostatic	3.3 x 3.3	140	3.5	35000
BMC32	Electrostatic	2.1 x 2.1	32	5.5	12000

4.2.3.2 Tip/Tilt Compensation Devices

Critical to any FSO system is the ability to adjust the beam pointing and removing Tip/Tilt deviations, as it has been demonstrated in Section 4.1.1. In real systems, beams need to be centered in position and angle, and adjustments have to be performed in real time to compensate the movement of the transmitter and receiver as well as the angular deviation introduced by the atmosphere. In this project we are focused on compensating atmospheric effects, so compensating techniques for beam pointing are beyond the scope of this project. Tip/Tilt compensation systems are generally electrically driven, and are controlled by feedback systems to achieve dynamic

correction. The spatial and temporal requirements obtained from Sections 4.1.2-4.1.3 are crucial for achieving a correct compensation. The main parameters that define the performance of a Tip/Tilt corrector are: maximum steering angle, angle resolution, aperture and maximum bandwidth. Typical kinds of tip/tilt correctors are fast steering mirrors [180][181][182] and Risley prisms [183][184].

Fast steering mirrors (Fig. 4-12.a) have been traditionally used in FSO systems and their performance has been widely validated. They are typically light mirrors controlled by electromechanical actuators on the back of the mirror. The choice of actuation mechanism is influenced by the required frequency response of the mirror. High frequency movements with high load lead to small deviation angles, while for achieving maximum deviation angles at higher frequencies a light mirror is preferred. Also, these systems generally include a sensor and feedback system that increases the achievable resolution and minimizes the error on the applied angle at the cost of diminishing their frequency response. Under atmospheric turbulence, the frequency response requirement for tracking the tip/tilt components (around 100 Hz) is not even close to the typical frequency response of these devices (around 1 KHz), so they present an optimal solution for these applications.

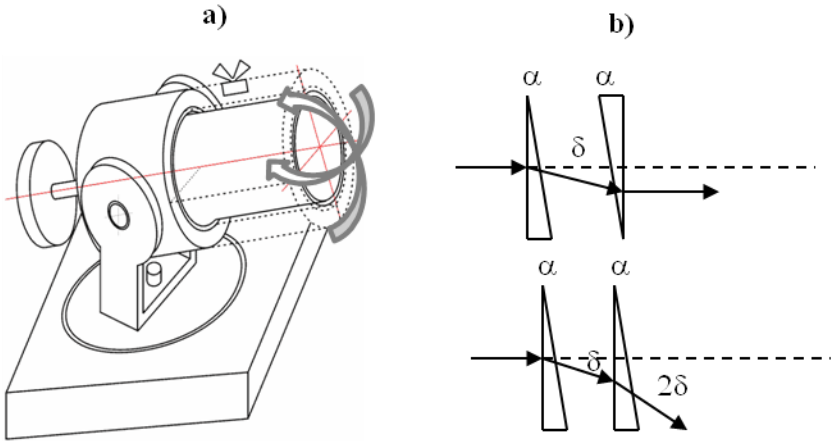

Fig. 4-12. Tip/tilt compensation schemes. Fast Steering Mirror (a) and Risley prisms (b).

Other possible solutions are Risley prisms (Fig. 4-12.a). In this architecture two identical prisms are able to move circularly one respect the other. The prisms are electromechanically controlled and perform the compensation by rotating one or both prisms, being able to modify the output angle up to a maximum angle of 2δ. The beam path follows a Lissajou type pattern that

depends on the angle parametric angle δ, that depends on the prisms selected, and the rotation angle α. If the prisms are not matched there can be blind zones that cannot be pointed to. Typical parameters for these systems are a maximum deviation angle of 7º, pointing resolution of 100 µrads and control bandwidth below 40 Hz [185].

4.3 System Model and Implementation of Wavefront Sensorless AO for Coherent Communication Systems

Following the general architecture explained in Section 4.2.2, our objective is to design an AO wavefront sensorless system for compensating atmospheric aberrations. The main benefits of this architecture have been already exposed. First, a low cost implementation as the WFS is not required. Second, it provides a maximization of the power received in the aperture plane as no power has to be redirected to the WFS. Also, it can achieve compensation under fading channels due to the use of a LO source acting as an optical amplifier, which increases the signal power after the mixing stage. In the other hand, issues related to the convergence performance of blind algorithms have to be considered and analyzed. The design process is based on the principle of choosing the adequate devices that fulfill the system parameters derived from the spatial and temporal requirements obtained in sections 4.1.2 and 4.1.3 by using commercially available wavefront correctors, which were introduced in section 4.2.3. A balanced solution between fulfilling those requirements and assuming a tolerable cost of the hardware is key in our design. Also, the set-up arrangement must be design to maximize the performance of each device inside the complete system. Of special interest is to provide a closed and compact design, crucial for embedding those systems in typical FSO applications.

4.3.1 AO Block System Model

In this section we describe the system arrangement of generic devices and provide the mathematical description for the optical and electrical fields involved in wavefront sensorless AO architectures for coherent systems. The objective is to translate the general architecture from Fig. 4-10 to a specific system arrangement and formulate a mathematical description for each signal.

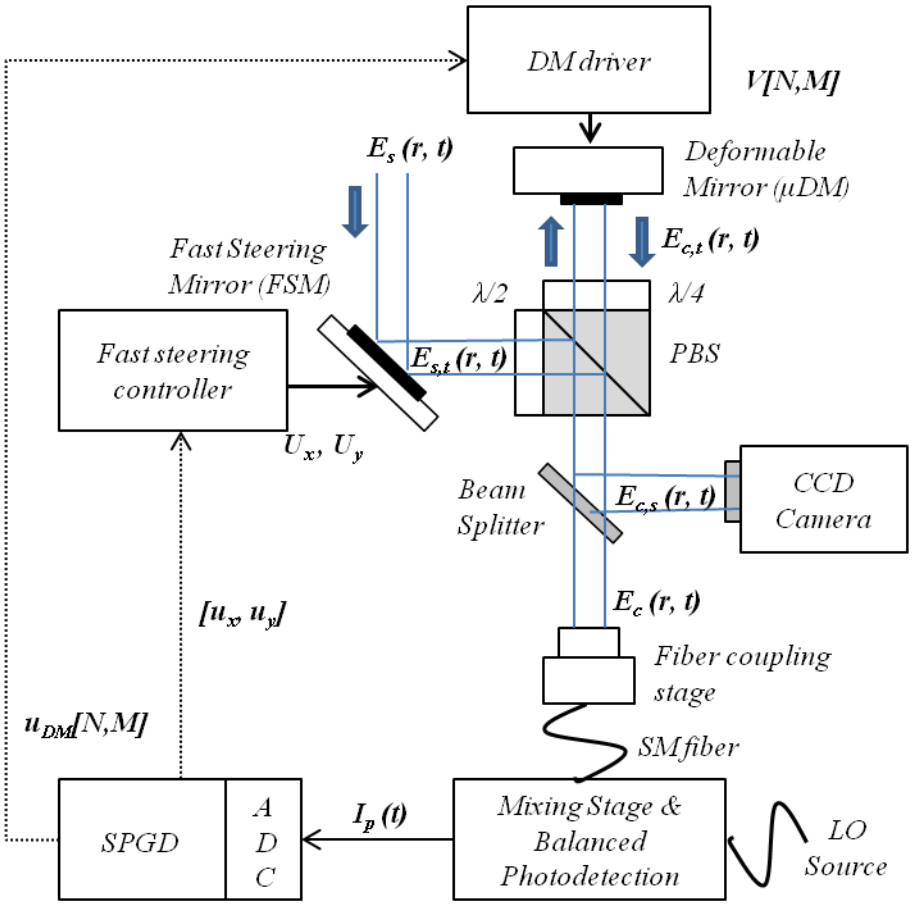

Fig. 4-13. An incoming laser beam $E_s(t)$ hits the FSM, which compensates the tip/tilt components producing $E_{s,t}(t)$. The light is sent through an optical circulator, composed by a half wave plate, a PBS and a quarter wave plate. The objective of this stage is to maximize the use of the DM surface (beam direction perpendicular to the surface) while maximizing the compact design of the system. The corrected wavefront $E_{c,t}(t)$ is sent through a beam splitter, which sends part of the beam to a CCD camera, acting as monitoring signal $E_{c,s}(t)$, and the other beam $E_c(t)$ to the fiber coupling stage. The coupled signal is mixed with the LO source and the resulting signal is translated to an electrical photocurrent $I_p(t)$ by a balanced photodetector and converted to the digital domain by an ADC. Then, the SPGD is applied using $I_p(t)$ as the performance metric. The SPGD generates the control signals ($u_x[n], u_y[n]$) for the FSM controller, that generates the analog control signals $U_x(t), U_y(t)$], and the phase map ($\varphi_{DM}[N,M]$) for the DM driver, which translates it into the voltage matrix signal $V(t)[N,M]$.

Our proposed design is shown in Fig. 4-13. In this figure we show the AO architecture and the electrical fields and signals related. The incoming laser beam $E_s(r,t) = A_s exp\,(j[w_s t + \varphi_s(r)])$ hits the FSM, which compensates the tip/tilt components. The resulting beam is expressed as

$$E_{s,t}(r,t) = R_{FSM} A_s exp(j[w_s t + \varphi_s(r) + \varphi_{FSM}(r)]) = A_{s,t} exp\,(j[w_s t + \varphi_{s,t}(r)]) \qquad 4.29$$

where R_{FSM} is the FSM mirror reflectivity and $\varphi_{FSM}(r)$ is the phase wavefront applied by the FSM. The selection of the FSM platform is based on the high frequency response and convenient angular resolution that these devices provide [182]. Also, these platforms usually present a large reflective area fact. This allows the designer to place them forming a 45º angle, making the input and output beams perpendicular one from the other at the reference position, fact that minimizes the space used. The light is then sent through an optical circulator, composed by a half wave plate, a PBS and a quarter wave plate. The objective of this stage is to maximize the use of the DM surface (beam direction perpendicular to the surface) while maximizing the compact design of the system. The effect is that the whole actuator surface and stroke are being fully used, which increases the compensation efficiency [150]. The half wave plate is configured to set the output polarization on the one that maximizes the reflected power on the PBS. Then, the linearly polarized signal is sent to the quarter wave-plate, which converts it to circular polarization. The light beam hits the DM, where a correction is introduced and the handedness of the polarized light is reversed. Then, it is translated into horizontal polarization by the quarter wave plate in order to go through the PBS. The corrected wavefront, described as

$$E_{c,t}(r,t) = R_t A_{s,t} exp\left(j\left[w_s t + \varphi_{s,t}(r) + \varphi_{DM}(r)\right]\right) = A_{c,t} exp\ (j[w_s t + \varphi_c(r)]) \qquad 4.30$$

where R_t is the efficiency of the circulator and DM and $\varphi_{DM}(r)$ the phase map applied by the DM, is sent through a beam splitter that sends part of the beam to a CCD camera, acting as monitoring signal $E_{c,s}(r,t)$

$$E_{c,s}(r,t) = R_{BS} A_{c,t} exp\ (j[w_s t + \varphi_c(r)]) \qquad 4.31$$

being R_{BS} is the reflectivity of the beam splitter. The corrected beam $E_{c,s}(r,t)$ described by

$$E_c(r,t) = T_{BS} A_{c,t} exp\left(j\left[w_s t + \varphi_{c,t}(r)\right]\right) = A_c exp(j[w_s t + \varphi_c(r)]) \qquad 4.32$$

where T_{BS} is the beam splitter transmittance, is sent to the fiber coupling stage. The configuration of the coupling stage is critical in order to maximize the power coupled into the fiber. Any misalignment introduced by the beam pointing or any residual aberration (e.g. beam divergence) will be compensated by the AO system, and this AO configuration serves as the reference state when no aberration is introduced. The coupled power is mixed with the LO source, $E_{LO}(r,t) =$

$A_{LO}exp\ (j[w_{LO}t])$, and translated into an electrical current $I_{het}(t)$ by a balanced photodetector. The resulting intensity is

$$I_{het}(t) = I_S(t) + i_N(t) \tag{4.33}$$

where $I_S(t)$ is the intensity related to the input signal and $i_N(t)$ is the intensity associated to the noise after balanced photodetection. $I_S(t)$ can be expressed as

$$I_S(t) = \eta_q A_c A_{LO} \int W(r) cos\ (\Delta wt + \Delta\emptyset + \varphi_c(r)) dr \tag{4.34}$$

where η_q is the quantum efficiency of the balanced photodetector, $W(r)$ the aperture function which equals unity for $|r| \leq D/2$ and zero elsewhere, and Δw and $\Delta\emptyset$ are the frequency and temporal phase difference between the incoming beam and the LO source. Using that $\cos(u - v) = \cos(u)\cos(v) + \sin(u)\sin(v)$ we can express that

$$\begin{aligned} I_S(t) = \eta_q A_c A_{LO} \Big\{ & cos(\Delta wt + \Delta\emptyset) \int W(r) exp\big[cos\big(\varphi_c(r)\big)\big] dr \\ & + sin(\Delta wt + \Delta\emptyset) \int W(r) exp\big[sin\big(\varphi_c(r)\big)\big] dr \Big\} \end{aligned} \tag{4.35}$$

By averaging the signal by the beat frequency Δw, the averaged signal power is obtained as

$$\overline{I_S{}^2} = \frac{1}{2}\left(\eta_q \frac{\pi}{4} D^2 A_c A_{LO}\right)^2 \alpha^2 \tag{4.36}$$

Where α^2 is the averaged mixing efficiency under phase fluctuations obtained in Eq. 3.44 from section 3.2. As we are using a LO source, we can assume that we are working in a shot noise limited scenario, where the dominant noise is shot noise and other noise sources can be neglected, as we stated in section 2.1.2. From Eq. 2.10, we obtain the noise power per bandwidth in a shot limited scenario. Inserting Eq. 4.36 into Eq. 2.10, the resulting averaged noise power is

$$\overline{i_N{}^2} = \frac{e\eta_q \pi}{4} D^2 A_{LO} \tag{4.37}$$

where e is the electronic charge. The intensity $I_p(t)$ containing both, signal and noise intensities, is converted to the digital domain by an ADC. Then, the SPGD is applied using DSP. The averaged power $\overline{I_{het}(t)^2}$ act as the performance metric for the SPGD algorithm, which generates

the control signals for the FSM and DM drivers. The SNR per unit bandwidth of the metric signal is given by

$$\gamma = \frac{\overline{I_S{}^2}}{\overline{\iota_N{}^2}} = \frac{\eta_q}{2e} \cdot \frac{\pi}{4} D^2 {A_c}^2 \alpha^2 \tag{4.38}$$

It is important to note that the SNR in presence of phase fluctuations γ can be given as a function of the SNR in absence of turbulence $\gamma_0 = \frac{\eta_q}{2e} \cdot \frac{\pi}{4} D^2 {A_c}^2$

$$\gamma = \gamma_0 \cdot \alpha^2 \tag{4.39}$$

Using Eq. 2.19, which express the SNR per bit for a shot noise limited scenario in absence of turbulence in terms of the number of photons per bit (N_p), we can obtain that the SNR per bit under turbulence γ_b is given by

$$\gamma_b = \eta_q \cdot N_p \cdot \alpha^2 \tag{4.40}$$

Equivalently, we can define the SNR per symbol in the shot limited scenario γ_S as

$$\gamma_s = \eta_q \cdot N_s \cdot \alpha^2 \tag{4.41}$$

where N_s is the number of photons per symbol. The SNR of the performance metric *J* is a crucial parameter to evaluate the performance of the SPGD algorithm under turbulent channels. The SPGD algorithm, as it have been stated in section 4.2.2.1, consists on applying, in parallel, stochastic perturbations on the different mirrors involved and the measurement of the subsequent change in the performance metric. From the change in the performance metric, the SPGD estimates the value of the gradient of the performance metric for each mirror control channel. All the mirror control channels can then be updated in parallel based on the gradient estimates. The SPGD generates the tip/tilt control signals u_x and u_y for the FSM controller and the $u_{DM}[N, M]$ for the DM driver. Then, the FSM controller translates these digital signals into control voltages, U_x and U_y, that feed the FSM. Also, the DM driver, generates the voltage matrix signal $V[N, M]$ for the DM actuator grid. Each SPGD loop iteration consists of two different perturbations, positive and negative, so, considering that the FSM is included as an additional mirror of the SPGD, the maximum theoretical loop rate is equivalent to half the FSM frequency rate.

4.3.2 Active Components of the AO Set-Up

4.3.2.1 Fast Steering Mirror

The selected device in order to fulfill the requirements calculated in sections 4.1.2 and 4.1.3 is the S-330.2SL from Physik Instrument (PI) GmbH & Co. KG. The S-330 platform is a fast and compact tip/tilt unit that provides precise angular motion of the top platform around two coplanar, orthogonal axes. This platform can provide high accelerations, enabling step response times in the sub-millisecond range, achieving a maximum of 1.3 kHz frame rate. The main parameters of this device are: maximum open-loop tip/tilt angles of 3.5 mrad, maximum closed-loop tip/tilt angles of 2 mrad, a open-loop angular resolution of 0.02 µrad and a closed loop angular resolution of 0.05 µrad. These characteristics, shown in Table 4-2, fulfill the requirements derived in sections 4.1.2 and 4.1.3, where the maximum tip/tilt required deviation was below ± 0.5 mrad and the required frequency rate was around 30 Hz. Therefore, we can assume that the phase variance due to bandwidth resolution on the tip/tilt components can be ignored. The maximum error arising from angular deviation after correction is half the angular resolution α_{res}, so the residual phase variance due to the tip/tilt components after correction is ${\sigma_{tt}}^2 = \alpha_{res}^2/2 \approx 10E-16$, leading to a perfect tip/tilt compensation. The expected phase variance and mixing efficiency after tip/tilt correction can be seen in Fig. 4-17. The theoretical phase variance and the resulting mixing efficiency (Eq. 3.44) when applying the correction with the FSM matches the theoretical values predicted by the Kolmogorov residual errors after tip/tilt compensation (σ_3^2 in Table 3-2).

Fig. 4-14. S-330.2SL Tip/tilt Platform from Physik Instrumente (PI) GmbH.

On closed-loop operation, high-resolution strain gauge sensors (SGS) are applied to appropriate places on the drive train and feed the platform position information back to a piezoelectric controller. The sensors are connected in a full-bridge configuration to eliminate

thermal drift; they assure optimal position stability and rapid response with nanometer resolution. This PI tip/tilt platform is based on a parallel-kinematics design with coplanar rotational axes and a single moving platform driven by two pairs of differential actuators [186].

The platform must be controlled by an external voltage source. Each tilt axis of the tip/tilt platform system requires one controlled operating voltage in the range of 0 to +100 volts and one constant voltage of +100 V. At the zero position (tilt angle zero) both actuators of a pair are expanded to 50% of their maximum expansion. Control voltages below 50 volts cause tilting in one direction, above 50 volts, tilting in the other. For that purpose, the E-616.SS0G controller and amplifier, in junction with the National Instruments data acquisition board NI DAQ 6221, is used (Fig. 4-15.

The NI DAQ 6221 is a low-cost multifunction data acquisition board that provides four analog outputs at 16 bits resolution, 833 KS/s update rate and ± 10 V output range [189]. Two of these outputs are used to control the Tip/Tilt components, respectively. The control signals are generated by using Mathwork's Matlab and the libraries provided by National Instruments.

Table 4-2. Tip/Tilt S-330.2SL Platform & E-616 Driver Specifications

	Value	Units
Active Axes	$\emptyset_x, \emptyset_y$	
Integrated Sensor	4 x SGS	
Open-loop Tip/Tilt angle	3.5	mrad
Closed-loop Tip/Tilt angle	2	mrad
Open-loop Resolution	0.02	µrad
Closed-loop Resolution	0.05	µrad
Max Frame Rate Closed-Loop	1.253	kHz
Resolution	14	bit
Mirror Diameter	8	mm
Mirror Thickness	2	mm

The E-616 is a special controller for piezo based tip/tilt mirrors and tip/tilt platforms containing two servo controllers, amplifiers and sensor channels in a compact unit. High-resolution SGS position sensors within the piezo mechanics provide optimum position stability and fast response (3 kHz) in nanometer respectively µrad-range. A high output power of 10 W per channel allows dynamic operation of the tip/tilt mirrors. This driver operates in a differential drive design, where

the actuators operate in pairs in a push/pull mode. Two orthogonal rotation axes share a common pivot point. The differential drive design provides an improved linearity and resolution [186]. This operational configuration would require the transformation of the tilt/tip angles into separated voltage control. This operation is provided by the E-616, eliminating the need of additional software computation before creating the digital control signals.

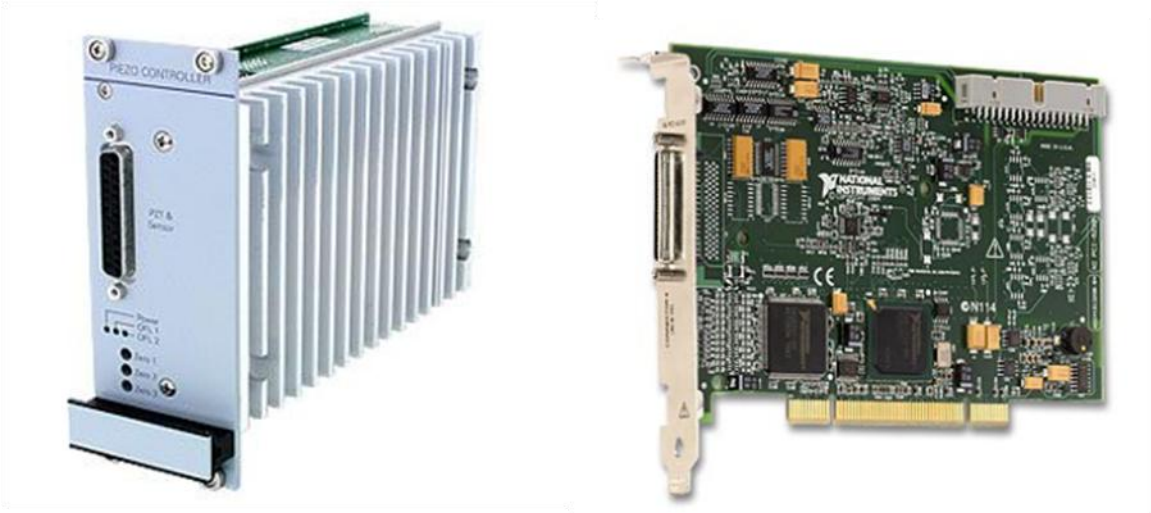

Fig. 4-15. The E-616.SS0G controller (left) and NI DAQ 6221 (right), needed to provide the control signal for the S-330.2SL Tip/tilt Platform.

In addition to the amplifier, controller and sensor bandwidths, the maximum operating frequency of a tilt platform depends on its mechanical resonant frequency. To estimate the effective resonant frequency of the tilt mirror system (platform + mirror), the moment of inertia of the mirror substrate is calculated as [186]:

$$I_M = m\left[\frac{3R^2 + H^2}{12} + \left(\frac{H}{2} + T\right)^2\right] \qquad 4.42$$

Where m is the mirror mass, R is the mirror radius, H is the mirror thickness and T is the distance from the pivot point to platform surface. The moment of inertia for the mirror used (a golden coated mirror of 2 g, 8 mm radius and 2 mm thickness) is calculated using Eq. 4.42, resulting into a inertia of 106.667 [g$\cdot mm^2$]. Using the frequency of the platform f_0 and the moment inertia of the platform I_0, the system resonant frequency is calculated as:

$$f' = \frac{f_0}{\sqrt{1 + I_M/I_0}} \tag{4.43}$$

The resulting maximum achievable frequency working in closed-loop is 1.257 kHz. This ensures that the temporal requirements for the Tip/tilt correction are fulfilled.

4.3.2.2 Deformable Mirror

One of the most validated and widely used technologies in wavefront phase modulation is the micro-electro-mechanical (MEMs) deformable mirrors (DMs). The wide technological background and the versatility of these devices make them a popular solution for adaptive optic systems.

Table 4-3. BMC32 Multi-DM specifications

	Value	Units
Actuator Count	32	
Actuator Pitch	300	µm
Max Stroke	5.5	µm
Mirror Coating	Gold	
Clear Aperture	2.1	mm
Membrane Surface	Continuous	
Max Frame Rate	4.6	kHz
Resolution	14	bit

In our project, the specific DM used to compensate part of the test phase aberrations generated by the wavefront generator stage is a 6x6 Multi-DM gold coated 5.5µm actuator stroke from Boston Micromachine's (BMC's), shown in Fig. 4-17. Its main characteristics are shown in Table 4-3. The BMC32 DM is a continuous face-sheet deformable mirror controlled by hysteresis-free electrostatic actuators located on a square grid [188]. The mirror grid is composed by a 6x6 actuator array with four inactive corner actuators. Each actuator provides up to 5.5 µm of mechanical stroke, which corresponds to about 3 waves of phase control, and each one can be controlled individually with low influence of the surrounding actuators.

By using figure Fig. 4-5, we showed the DM stroke required for different normalized turbulence strength scenarios, this device is able to compensate turbulence strengths up to $D/r_0 \approx 40$ in terms of the stroke. Also, the DM is characterized by an actuator pitch of 300 µm, a

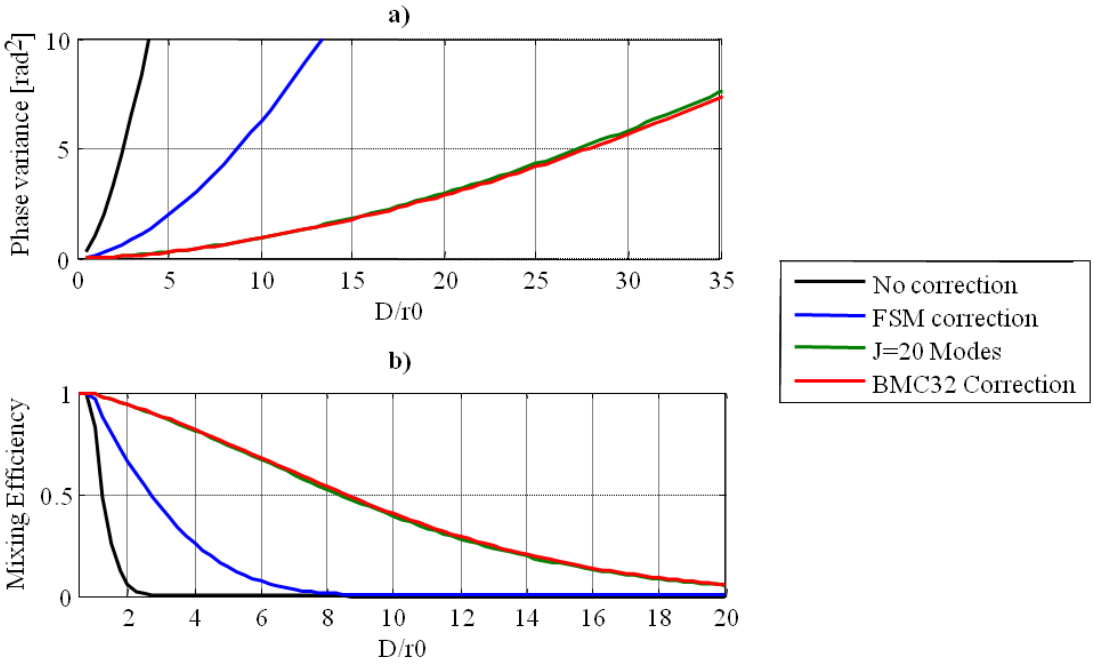

Fig. 4-16. Phase variance (a) and mixing efficiency (b) for: no correction, FSM correction, BMC32 correction and J=20 modes removed. The use of the FSM in junction with the DM is estimated to provide a correction similar to the theoretical correction when removing 20 modes.

2.1mm clear aperture, a 20% interactuator coupling, a surface quality below 40 nm RMS and 32 actuators (N_{act}). The resulting interactuator spacing r_s can be approximated as $r_s = D/\sqrt{N_{act}} \approx$ 0.371 mm. Using Eq. 4.8 we can calculate the estimated residual phase variance after the DM correction. The results for the residual phase variance and the resulting mixing efficiency (Eq. 3.44) after applying DM correction are shown in Fig. 4-17. The estimated correction of the FSM in junction with the DM is similar to the Kolgomorov residual error when removing 20 modes (σ_{21}^2).

The Multi-DM is fabricated using polysilicon surface micromachining fabrication methods [188]. The MEMS device is packaged and wire bonded to a ceramic chip carrier and sealed using a window enclosure. A pin grid array on the back of the package interfaces with the socket inside the mirror box, shown in Fig. 4-17. The electrostatic actuator array is driven using independent high voltage channels with 14-bit resolution. The standard drive electronics are controlled via a USB 2.0 PC connection, providing DM frame rates of about 4.6 kHz. High speed X-CL drive electronics are also available which operate over a Camera- Link interface providing DM frame rates of up to 100 kHz.

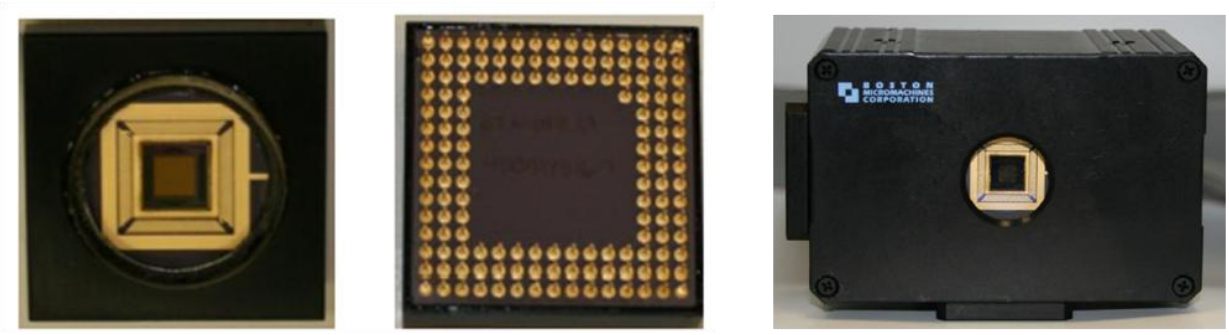

Fig. 4-17. 6x6 Multi-DM gold coated 3.5µm actuator pitch from Boston Micromachine's (BMC's).

A host PC, connected with a USB 2.0 interface, controls each output channel independently. The control software for the DM is based in Mathwork's Matlab, and runs on platforms using Windows 32-bit operating systems. In Windows, the actual achievable frame rates for USB 2.0 communication is platform dependent. In our set-up, the maximum achievable closed-loop frame rate measured for the DM system is about 1 kHz, which consists of two Multi-DM driver commands, two power measurements and the corresponding Matlab computation.

4.3.3 Experimental AO Set Up

Following the design described in Fig. 4-13 an experimental set up is implemented. The experimental setup for the adaptive optical system is illustrated in Fig. 4-18. A 2.1-mm-diameter collimated laser beam at 1550nm coming from the Thorlabs KT110 fiber-to-free space stage acts as the incoming beam. A first mirror acts, in conjugation with the Tip/Tilt S-330.2SL platform, as a Z-Mirror that allows us to calibrate the system when no aberration is introduced in order to maximize the coupled power at the fiber coupling stage. The Tip/Tilt S-330.2SL platform presents a resulting frequency rate of 1.257 kHz, a closed loop tilt angle of 2 mrad and an angular resolution of 0.05 µrad. The reflected beam is directed into a structure that acts as a free space circulator consisting on a Thorlabs WPH10M-1550 half wave-plate, a Thorlabs CM1-PBS254 PBS, the BMC32 DM, and a Thorlabs WPQ10M-1550 quarter wave-plate. The light beam hits the BMC32 DM, where the correction is introduced. The mirror is composed by 36 micro-mirrors guided each one by actuators with 5.5µm of mechanical stroke working at a maximum frame rate of 4.6 KHz. A 8% reflection beam splitter divides the light beam into two beams, one going to the fiber coupling stage and the other going to the CamIR CCD camera from Applied Scintillation Technologies. A fiber coupling stage adapts the free space light beam into a single fiber. This stage is equivalent to the one used in the fiber to free-space stage, and is composed by a x-y-z

translator platform and an aspherical lens with 2.97 mm effective focal length, 3.6 mm clear aperture and 0.6 numerical aperture specially designed to work at 1550 nm. Then, the coupled signal is mixed with the LO source using a Thorlabs 10202A-50-FC 3 dB coupler. $I_p(t)$ is obtained using a U2T BPDV2150R balanced photodetector, and it is then translated to the digital domain by the DSO9104A Agilent Infiniium Osciloscope. This down-convertion and ADC stages are the ones used for the coherent receiver implemented in section 2.5.3.

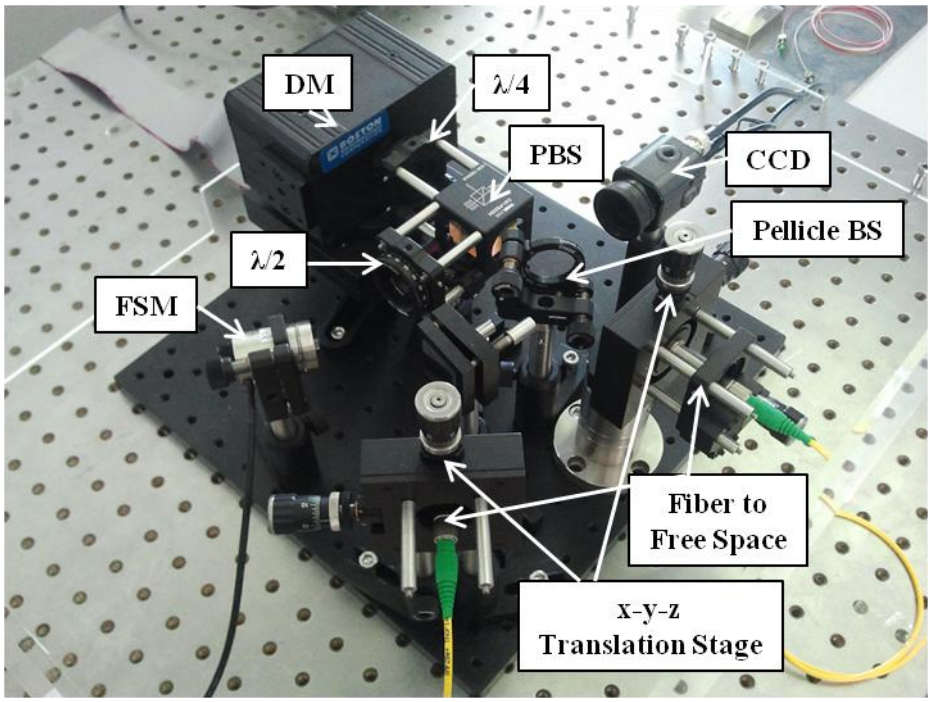

Fig. 4-18. Experimental AO Set Up. A 2.1-mm-diameter collimated laser beam at a wavelength of 1550nm arrives to the system. A first mirror acts, in conjugation with the fast steering mirror as a Z-Mirror that allows us to calibrate the system when no aberration is introduced. The light is sent through a half wave plate to change its polarization. The output polarization must be that one that maximizes the reflection on the PBS. Then, the whole linearly polarized signal is sent to the quarter wave-plate, which converts it to circular polarization. The light hits the DM, where the handedness of polarized light is reversed and then translated into horizontal polarization. A beam splitter send a sample to a CCD camera and the 92% of the power is sent to the coherent receiver stage (section 2.5.3) through a fiber coupling stage. The SPGD uses the metric value J to generate the control signal to the Tip/Tilt S-330.2SL and BMC32 DM.

The wavefront correction using the SPGD is then performed at a maximum rate of 500 iterations per second. This rate does not reach the maximum rate of the devices (4.6 KHz for the DM and 1.2 kHz for the FSM) for several reasons. First, even if the DM is able to work at high frame rate, the DSP is driven by a PC which is not able to exploit the maximum performance of the DM. The PC receives the data from the DSO9104A and performs the SPGD calculation. Each SPGD iteration consists of two different perturbations, positive and negative, which leads to a

maximum iteration rate of half the DM frequency rate. Also, two power measurements from the oscilloscope must be performed for each iteration along with the correspondent computational calculation, leading to an increase of the iteration latency. The minimum iteration latency achieved by our system is 2 ms. This latency could be improved by using high speed electronics, such as field programmable gate arrays (FPGAs) or digital signal processors (DSPs), to provide an optimum performance of the AO, but these techniques are beyond the scope of this project. In the other hand, the iteration rate for the FSM control is enough to fulfill the temporal requirements. The maximum iteration rate achieved for this device reaches the 500 iter/s.

Table 4-4. Parameters of the commercial devices used in the AO set up

	Commercial name	Parameter	Value	Units
Aspheric Lens	Thorlabs C660TME Mounted Lens	Focal length	2.97	mm
		Clear Aperture	3.60	mm
Free-Space Fiber	Thorlabs KT110	x-y-z Translation	0.5	µm/Div
Polarization Beam Splitter	Thorlabs CM1-PBS254	Reflection Efficiency	99.5	%
		Transmission Efficiency	90	%
λ/2 Waveplate	Thorlabs WPH10M-1550	Clear Aperture	25	mm
		Reflectance	0.25	%
λ/4 Waveplate	Thorlabs WPQ10M-1550	Clear Aperture	25	mm
		Reflectance	0.25	%
CCD Camera	Applied Scintillation Technologies CamIR	Resolution	752 x 582	pixels
		Active Area	1/2'	
		Effective Dynamic range	20	dB
Pellicle Beam Splitter	Thorlabs BP108 - Ø1	Split/Ratio	8/92	%

The adaptive optical system implemented is demonstrated by first measuring the signal power coupled into the single-mode fiber. The maximum coupling efficiency achieved without perturbation is 79% of the total power arriving to the receiver. The power at the receiver was measured by placing the same photodetector used in section 3.4 to obtain the efficiency of the holographic process. The loss of efficiency in the absence of phase fluctuations is due to an amplitude mismatch between the signal and LO source (see section 3.2.1), and can be

approximated to the geometrical losses of the coupling stage, η_g in Eq. 3.41. At this optimum pointing position, we connect the SM fiber to the mixing efficiency stage and obtain the averaged power $\overline{I_S{}^2}$ (Eq. 4.36) when no aberration is introduced. This value acts as the reference power to obtain the mixing efficiency in presence of phase fluctuations.

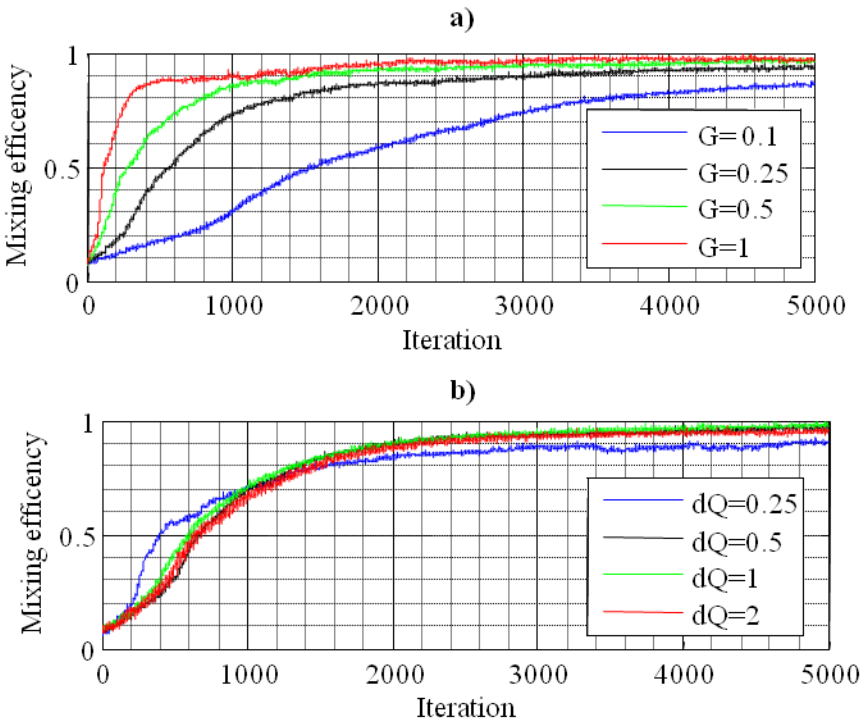

Fig. 4-19. Convergence of the SPGD is shown for the an arbitrary perturbation and for different values of the gain *G* (a) and for different values of the perturbation size *dQ (b)*.

To test the performance of the AO we first perform a self-correction procedure. In this procedure, a random phase map is introduced into the steering and DM actuators. From this arbitrary state, the SPGD performs the wave-front correction. The SPGD control software is provided with the BMC32, while the metric signal is acquired using the Agilent Infiniium DSO9104A (section 2.5.3) and the Labview control software developed in section 2.5.4. The SPDG key control parameters are the perturbation size (*dQ*), which defines the stochastic perturbation magnitude applied by the DM during the blind search, and the loop gain (*G*), which determines the weight value of the applied correction for each iteration. In Fig. 4-19 the convergence of the SPGD is shown for an arbitrary perturbation and for different values of *dQ* and *G*. In this case, γ_s is calibrated to be around 80 dB by adjusting the LO power, so the noise

present can be considered negligible. This allows us to measure the convergence on the performance metric and evaluate the AO response in optimal conditions.

The gain parameter is evaluated in Fig. 4-19.a. When a low gain is applied, the convergence rate of the SPGD diminishes. In the other hand, the variance of the signal increases with a higher gain. The SPGD efficiency is close to 0.98 when a perturbation size higher than 0.25V is applied having a gain parameter of 0.5. Under this situation, the convergence of the system has a greater slope at the beginning of the compensation, achieving a correction from 8% to 55% in the first 500 iterations. Therefore, the performance of the AO system run by the SPGD is highly dependent on two parameters, the perturbation size and the gain control, which define the performance slope of the adaptive system. In Fig. 4-20 the beam profile is shown for different stages of the compensation process. In this figure we can appreciate how the wavefront is progressively corrected and gradually increases the optical power around the center of the image. In the final SPGD steps the beam is completely corrected, recovering its original Gaussian shape, and the resulting mixing efficiency achieves its maximum.

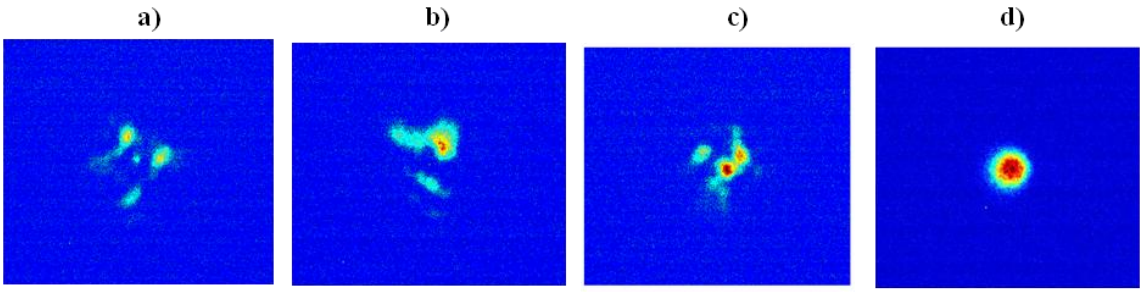

Fig. 4-20. Beam profile for different stages of the compensation process shown in Fig. 4-19 when the mixing efficiency is 0.23 (a), 0.43 (b), 0.67 (c) and 0.98 (d).

This characterization might be not enough to describe the complete behavior of this algorithm in FSO communication applications, where usually the receiver power is very low, leading to poor SNR. Analyzing the performance of the SPGD algorithm for different SNR of the performance metric *J* is crucial to understand its efficiency on real applications.

In order to study the SPGD performance under different SNR of the metric signal we use the mixing efficiency parameter. Assuming a shot noise limited scenario, the SNR per symbol γ_s, defined in Eq. 4.41, is controlled by adding digital noise to the metric signal *J*. The fact that the noise is added digitally does not lead to any loss of generality and could be equally performed by

adjusting the power in the LO. The reason for introducing the noise digitally is to modify γ_s without introducing any change in the hardware, fact that allow us to automate the experimental measurement process. Starting from a random perturbation scenario, the efficiency of the system is calculated by running the SPGD a maximum of 5000 iterations. The coupled power achieved in the last iteration is compared to the maximum achievable at the optimal point and the efficiency is calculated for each scenario. For each γ_s step the process is repeated 100 times in order to improve the statistical data. In Figure 4-13 the SPGD efficiency and its convergence time is evaluated for different perturbation sizes and SNR of the metric signal. As it was previously shown, a lower perturbation size implies a higher efficiency for γ_s >50 dB, but at the cost of higher convergence times. After a specific value of the γ_s for each perturbation size, the efficiency of the SPGD decreases at a constant rate in compare to the SNR. These points are 45 dB, 40 dB, 35 dB, 30 dB and 25 dB for the perturbation sizes of 0.2 V, 0.4 V, 0.8 V, 1.2 V and 1.6 V respectively, reaching a maximum efficiency of 0.97, 0.96, 0.937, 0.9 and 0.867 in each case. The convergence time also start increasing after these break points.

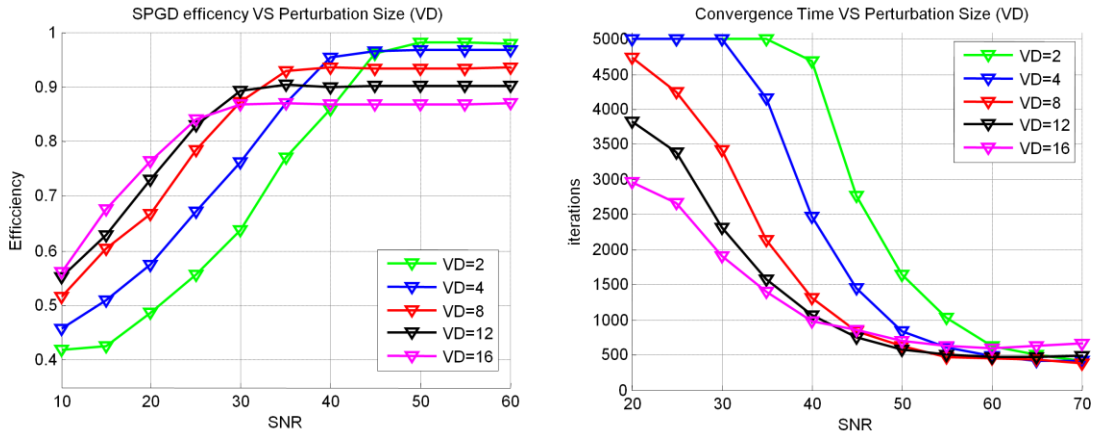

Fig. 4-21. SPGD efficiency and its convergence for different perturbation sizes and SNR per symbol at the receiver.

For γ_s below 25 dB, the SPGD efficiency decreases and the situation is reversed: higher perturbation sizes present higher efficiencies due to their robustness against the AWGN. Also the convergence time is faster for these higher perturbation sizes. It can be concluded that it exists a tradeoff between the performance efficiency in a good γ_s scenario and the efficiency in low γ_s scenarios, which also affects the convergence time. So depending on the application different SPGD parameters should be chosen. In Fig. 4-22 the same analysis is performed by modifying the gain parameter and evaluating the algorithm performance for a fixed perturbation gain of 0.8

V. In terms of efficiency, the gain parameter does not have much influence if its value is above a certain threshold (0.6 V in our case). On the other hand, the convergence time is drastically reduced by increasing this parameter. After a certain point, for gains above 1 V, the system response is not stable and the algorithm does not converge in many cases due to the high variance obtained in the signal metric. For a gain equal to 1 V and γ_s above 30 dB, the convergence rate is below 500 iterations, while, for the same SNR and gain equal to 0.4 V it needs around 2.000 iterations. By selecting a balanced response in terms of efficiency and convergence rate (e.g. perturbation size 0.8V and gain 1 V) and assuming the most restringing temporal requirement of the DM, which was calculated to be 650 corrections/second, a real wavefront sensorless architecture using the implemented AO should achieve an effective rate of 325 kHz. This performance is nowadays achievable by using commercial devices, such as the *BMC X Driver*, which achieves frame rates up to 400 kHz. This implies that a wavefront sensorless architecture can be an attractive solution for real systems due to its benefits in terms of cost, complexity, power efficiency and temporal response.

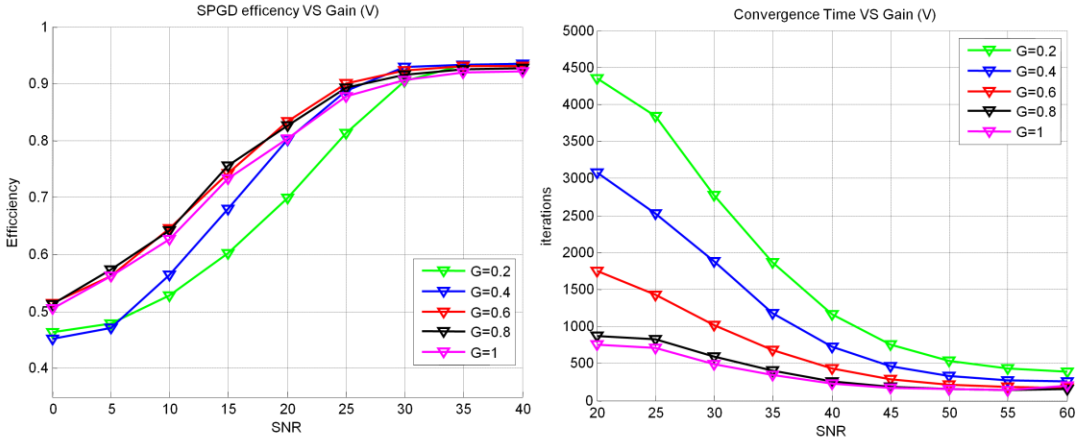

Fig. 4-22. SPGD efficiency and its convergence for different gain parameters and SNR for a fixed perturbation gain of 0.8 V.

In Fig. 4-23 the SPGD algorithm convergence is spatially represented for Tip/Tilt aberration compensations of equal magnitude and random directions. Here, the FSM control signal for each component are shown for different sets of 1000 FSM iterations. The FSM is driven by the SPGD, which searches for the maximal point ($x = 0, y = 0$). It can be seen that for γ_s of 45 dB and 35 dB, the convergence of the Tip/Tilt components is ensured. The paths followed by the step algorithm are quite direct in compare to the ones working with γ_s=25 dB, which also converges but with at a lower rate. In the other hand, for γ_s= 15dB, some of the

realizations do not converge to the optimal point, which lead to an efficiency loss. In these situations, the paths that converge present a higher convergence time.

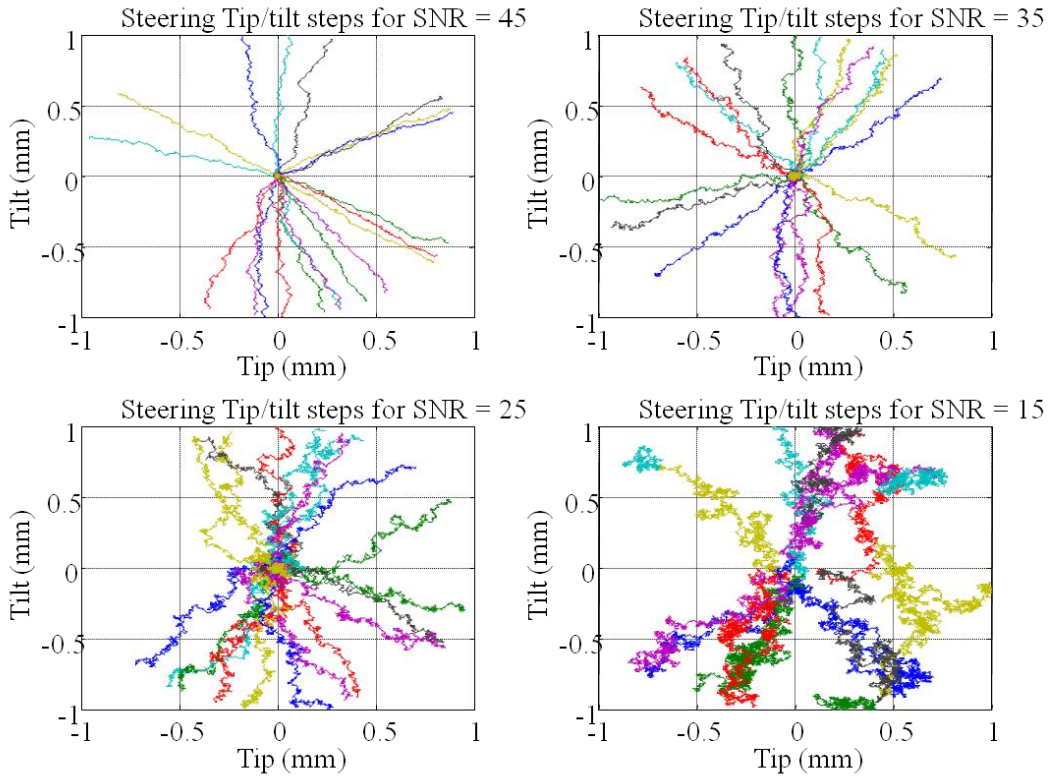

Fig. 4-23. SPGD algorithm convergence spatially represented for Tip/Tilt aberration compensations of equal magnitudes and random directions for different SNR of the metric signal.

We can conclude that the use of wavefront sensor-less architecture increases the mixing efficiency at the receiver by maximizing a performance metric. The behavior of the algorithm strongly depends on these two parameters (perturbation size and gain) selected for each application and the SNR of the signal metric (γ_s). The compensation algorithm has been demonstrated to achieve efficiencies close to 0.97 by using an optimal perturbation size and working with γ_s above a certain threshold. This γ_s threshold depends on the gain and perturbation size parameters used in each scenario. Once the perturbation size is fixed, the convergence rate is defined by the gain parameter, which can take values up to 1 V, point where the algorithm does not converge anymore.

4.4 Mitigation of Atmospheric Turbulence with AO for Coherent FSO

One of the objectives of this project is to provide the theoretical background and experimental demonstration of a free space optical coherent communication system with atmospheric turbulence generation and adaptive optics compensation. The development of this testbed is intended to experimentally demonstrate the viability of free space optical coherent communications as well as to provide a complete experimental setup that allows us to perform future research in all the different fields involve: communication modulation formats, compensation algorithms, dynamic wavefront generation and so on.

The development of a deterministic wavefront generator presents a set of advantages that this project tries to exploit. First, repeatability can be performed, which means that the wavefront aberration system can create exactly the same perturbation as many times as needed in order to compare different compensation techniques. Also, the OTG developed is able to introduce deterministic aberrations. Therefore, the system has a complete knowledge of the phase aberration introduced and the AO is able to generate the conjugated map, emulating this way an ideal WFS. This allows us to perform an experimental study of the maximum correction achievable by the AO as well as study the performance of the AO driven by the SPGD algorithm.

In this section the complete free space system is implemented by joining the OTG, the AO system and the coherent detector. The main parameter used to evaluate the performance of the OTG and the AO is the heterodyne efficiency (Eq. 3.44). Even when we are not able to perform a direct measure of the phase variance introduced by the OTG or the phase variance after AO correction, the measure of the mixing efficiency provides a full characterization of the effects of atmospheric phase fluctuations. The phase variance and mixing efficiency are related using Eq. 3.45 and Eq. 3.46, which allows us to compare the experimental results against the theoretical models. First, we evaluate the performance of the OTG by measuring the mixing efficiency in the absence of AO compensation. Then, the maximum performance of the AO is obtained by introducing complementary phase maps in OTG and in the AO system. Then, the efficiency of the wavefront sensorless AO controlled by the SPGD algorithm is studied. The resulting system performance is obtained for a wide set of scenarios depending on the signal to noise at the receiver plane and the turbulence strength present on the atmosphere.

4.4.1 Complete Coherent FSO Set Up

To evaluate the performance of free space optical coherent systems under atmospheric turbulence we take advantage of the previously developed stages in this project. The objective is to generate aberrated wavefronts and correct them with the AO system that performs the compensation by using two different methods: phase map conjugation and SPGD algorithm. This allows us to perform an experimental study of the performance of the different stages and algorithms as well as analyze the spatial limits of the AO system.

Table 4-5. Coherent FSO System Parameters

Parameter	Value	Units
Wavelength	1550	nm
Output Laser Power	19.03	dBm
Link Budget	-26.05	dBm
Max Coupled Signal Power	-7.02	dBm
LO power	9.03	dBm
SNR per symbol with no turbulence ($\gamma_{s,0}$)	60.78	dB
AO Iteration Rate	500	Iter/s
Laser Beam Width	2.1	mm

The FSO experimental set up scheme is shown in Fig. 4-24. The complete set-up is composed by a laser source working at 1550nm that provides a high power light beam of 80 mW (19.03 dBm). The light beam is separated in two fibers using a 90/10 beam splitter that introduces a 0.9 dB losses due to insertion loss of the device and its FC connectors. The 10% branch is sent to the coherent receiver stage and acts as a local oscillator. This light beam passes through an attenuator that controls the amount of power that arrives to the mixing stage. This device presents an attenuation range from 1.5 to 50 dB. The LO beam is then sent through a polarization stage that sets the beam polarization at a position that maximizes the mixing efficiency by matching its polarization with one of the light beam coming from the free space stage. The 90% beam is sent to the OTG set up, which was described in detail in section 3.4. The beam presents a diameter of 2.1 mm and an additional loss of 0.5 dB due to insertion losses on the coupling stage. By manually configuring the translation stage the resulting beam present a 0.2 mrad divergence. After collimation, the laser is sent through free space optical circulator that redirects the light perpendicularly to the DMD, maximizing the effective area of the TI 3000DMD. The DMD, driven by a PC, introduces a phase modulation by generating diffracted orders.

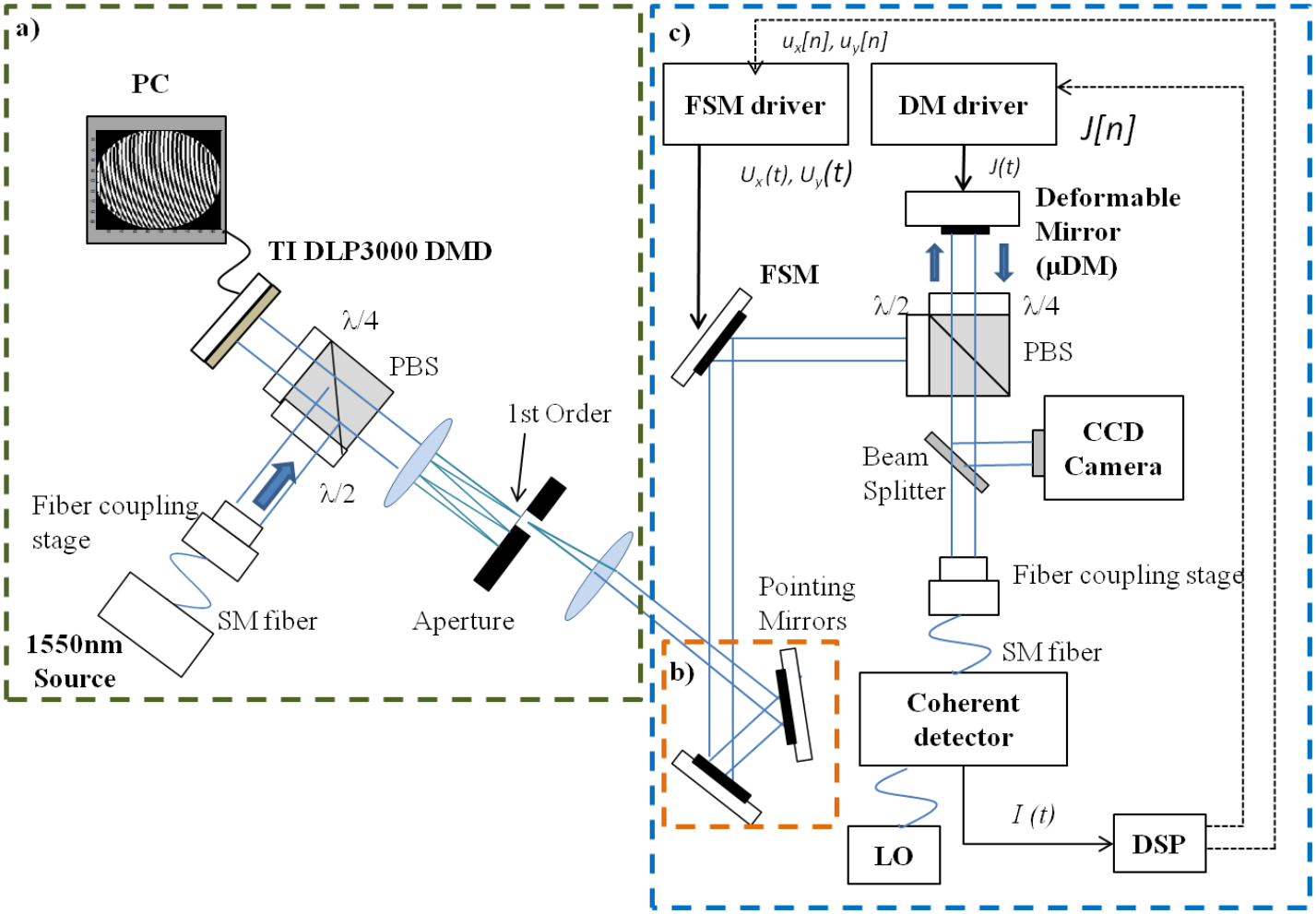

Fig. 4-24. FSO Experimental Set-Up scheme. The OTG stage (a) and the coherent AO stage (c) see 4.3.3) are joint by using a Z-mirror pointing stage (b). This set up emulates a FSO Coherent system under the influence of atmospheric phase fluctuations.

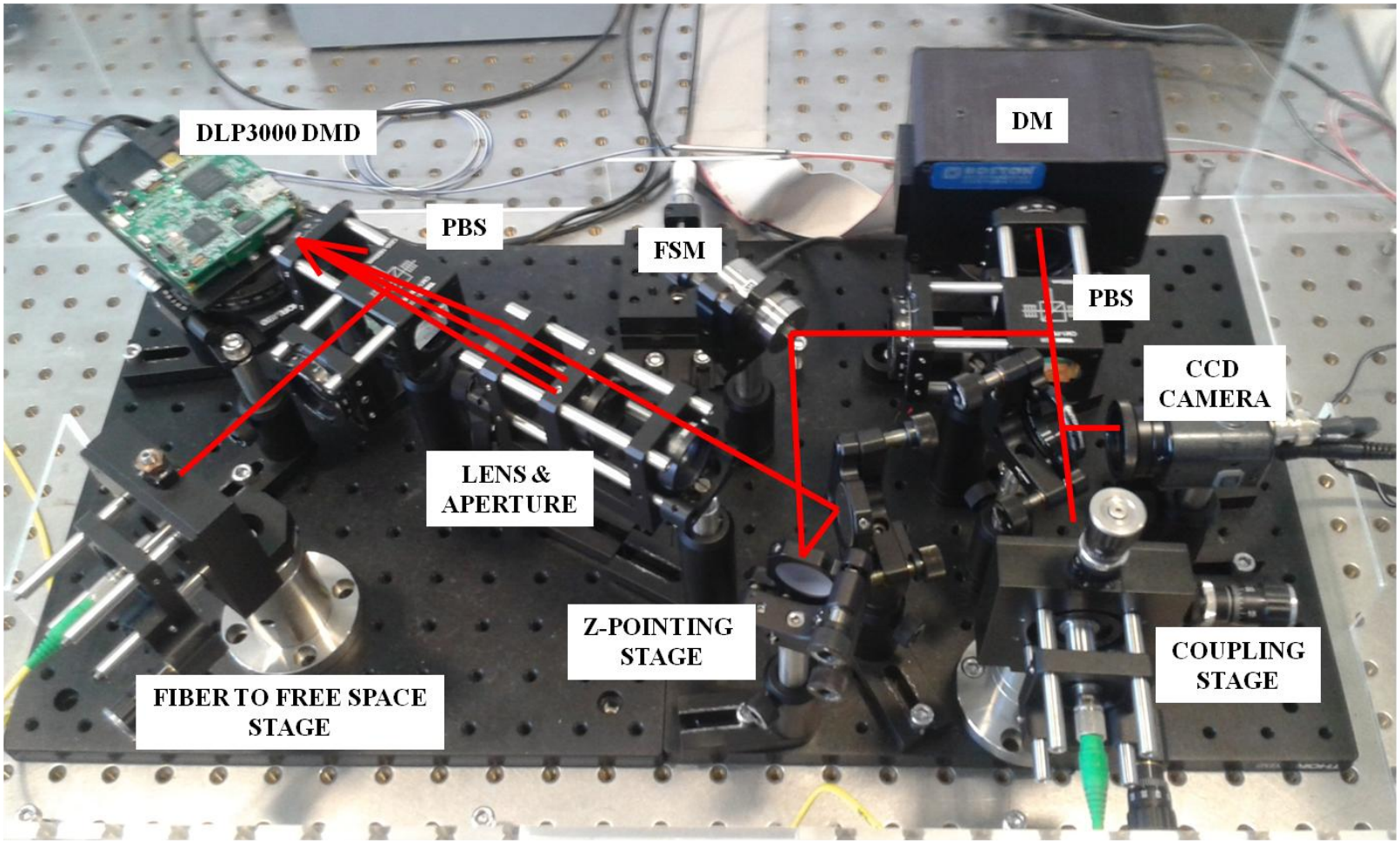

Fig. 4-25. FSO experimental set up. The set up is composed by the OTG and AO stages previously developed. These two stages are joint using a Z-mirror pointing stage. This set up emulates a FSO Coherent system under the influence of atmospheric phase fluctuation.

The first positive order is isolated by using two 4 mm focal lenses and a variable aperture with a minimum and maximum aperture of 0.7 mm and 5 mm respectively. The resulting aberrated beam is then sent to the AO system by using a Z-pointing stage. This Z-stage is composed by two broadband dielectric mirrors optimized for the 1280-1600 nm range and each mirror exhibits a 98% reflectivity at 1550 nm. This stage performs the beam pointing between the atmospheric aberration and the AO stages without introducing any additional reconfiguration on these systems. These mirrors are set in such way that the aberrated beam hits the center of a 96% reflectivity, 12 mm diameter golden coated mirror fixed to the FSM platform. The AO stage is the one developed in section 4.3.3. This stage applies the correction in order to mitigate the atmospheric. The corrected wavefront is then sent through a 8/92 free space beam splitter that separates the incoming beam into two beams. The 8% beam feeds the infrared 752x582 pixel resolution CCD camera that collects the beam intensity profile at 50 frames per second and act as a monitoring stage. The 92% branch is collected by the free space-to-fiber stage and the beam is coupled into a 10.5 µm mode field diameter single mode fiber. Adjustments must be made to maximize the coupled power, reaching a maximum of -7.02 dBm at the optimal point and when no aberration is introduced. The rest of the power lost in the free space stage is due to the holographic efficiency (less than 1%, see section 3.4.2), the insertions losses on the free space circulator stage (13% in each pass), the Z-mirror stage reflectivity (96.04%), the FSM (96%) and DM (82% @ 1550nm) reflectivities, the pellicle beam splitter losses (92%) and the coupling stage efficiency (73.2% efficiency). The estimated link budget looses is around -25.038 dB, close to the -26.05 dB measured at the reference position. The coupled beam is sent to the coherent receiver and mixed with the LO beam by using a 50/50 beam splitter, which produces two beams that feed the balanced photodetector. The photodetector is a BPDV2R integrated balanced photodectector developed by U2T photonics and it presents a 0.6 A/W responsivity at 1550nm and 40 GHz bandwidth. The resulting electrical signal $I_{het}(t)$ (Eq. 4.33) is sent to acquisition stage (see section 2.5.3), which feeds the coherent demodulator. The SPGD algorithm uses the averaged power $\overline{\overline{I_{het}(t)}}^2$ over a symbol period as the performance metric J to be maximized. The maximum γ_s at the receiver in a shot noise limited scenario is obtained using Eq. 2.17 and substituting $P_{in} = -7.02\ dBm$, $R = 0.6$ and $\Delta f = 625\ MHz$. The resulting γ_s in the absence of turbulence is $\gamma_{s,0} = 60.78\ dB$. .

The maximum loop rate achieved for the compensation stage is 500 iter/s (see section 4.3.3). The DSP designed after the acquisition stage allows us to introduce AWGN generated by computation to control the SNR per symbol, defined in Eq. 4.41 for a shot noise limited scenario. The advantage of doing this is that the SNR arriving to the demodulation stage and compensation algorithm can be set by the user without modifying any hardware configuration. Other option would be to use the optical attenuator positioned in the LO branch to control the signal to noise ratio arriving at the photodetector, which slows down the process. The heterodyne intensity coupled in the optimal position act as a reference to measure the efficiency of the AO system under different turbulent scenarios and for different compensation methods. In the next sections a complete characterization of the OTG and AO system is performed by measuring the mixing efficiency.

4.4.2 OTG Performance Analysis

To calibrate and verify the OTG we first perform measurements of the heterodyne efficiency in absence of AO compensation. Through this analysis the objective is to verify that the aberrations introduced by the OTG follow the predicted model developed in section 3.2.2. The procedure to measure the OTG performance is executed in three steps:

1. *Theoretical heterodyne efficiency calculation:* We first consider the Kolmogorov theory of turbulence and the residual errors after correcting *J* modes. The phase variance after correcting *J* modes (σ_J^2) is obtained from Table 3-2. Then, by replacing σ_φ^2 by σ_J^2 in

$$\bar{\alpha}_r = exp\left(\frac{-\sigma_\varphi^2}{2}\right) \tag{4.44}$$

$$\bar{\alpha}_i = 0 \tag{4.45}$$

$$\sigma_r{}^2 = \frac{1}{2N}\left[1 + exp\left(-2\sigma_\varphi^2\right) - 2exp\left(-\sigma_\varphi^2\right)\right] \tag{4.46}$$

$$\sigma_i{}^2 = \frac{1}{2N}\left[1 - exp\left(-2\sigma_\varphi^2\right)\right] \tag{4.47}$$

We can obtain theoretical mean mixing efficiency for each scenario using

$$\overline{\alpha^2} = {\sigma_r}^2 + {\sigma_i}^2 + {\bar{\alpha}_r}^2 \qquad 4.48$$

The objective of the OTG is to generate always a full turbulence (*J=1*), but this scenario is not enough to verify the correct phase modulation because the mixing efficiency decays too fast, providing a very low resolution of the measurements. To increase the reliability of the method we evaluate the phase map generation for *J*=3, 6, 10 and 20.

2. *Estimated heterodyne efficiency:* The OTG generates a set of 10 phase maps for each scenario as a function of the *J* modes removed and the normalized turbulence strength. The phase map is a 1024x1024 pixel grid that is re-sampled onto a 192x192 pixel phase map. This factor is chosen to match the diameter of the incoming light beam and the pattern diameter of the DLP image (192 pixels x 10.8μm ≅ 2.1 mm). The resulting phase map is downsampled in the *x* direction using a grating period of 8 pixels and quantizated in 8 levels (0, 2π/8, 2π/4, …), obtaining $\varphi_{g,q}[i,j]$ from Eq. 3.79. From section 3.3.4, we demonstrated that this procedure introduces a set of limitations that diminish the performance of the generated phase maps. We can calculate the phase variance associated to each downsampled and quatizated phase map σ_{DLP}^2 in order to obtain an estimation of the resulting heterodyne efficiency (α_{DLP}^2) by replacing σ_φ^2 by σ_{DLP}^2 in Eqs. 4.44-4.48.

3. *Direct measurement of heterodyne efficiency:* The last step is to introduce the phase maps $\varphi_{g,q}[i,j]$ in the DMD and measure the mixing efficiency for each scenario using the experimental set up from Fig. 4-25. The results are given in Fig. 4-26.

In Fig. 4-26, the theoretical (black dashed line), estimated (colored line) and measured (color dashed line) heterodyne efficiency are shown. Small deviations between the theoretical and estimated mixing efficiency are present for $D/r_0 > 10$ due to the DMD limitations. In this case, the grating period selected is 8 pixels, which was shown to be an optimal value for our application, and the aperture is equal to the beam width, 2.1 mm. The limitations are consistent with the results obtained in section 3.2.2, which imposed an upper level in the phase variance that the OTG is able to reproduce. Still, the heterodyne efficiency measurements achieve close values to the ones estimated by assuming the DMD limitations. Therefore, this experiment validates two principles: first, the model developed in [18] (see section 3.2.2) to describe the mean heterodyne

efficiency under atmospheric phase fluctuations is validated. Second, the BCGH using binary finite arrays is demonstrated as a valid method to perform wavefront phase modulation.

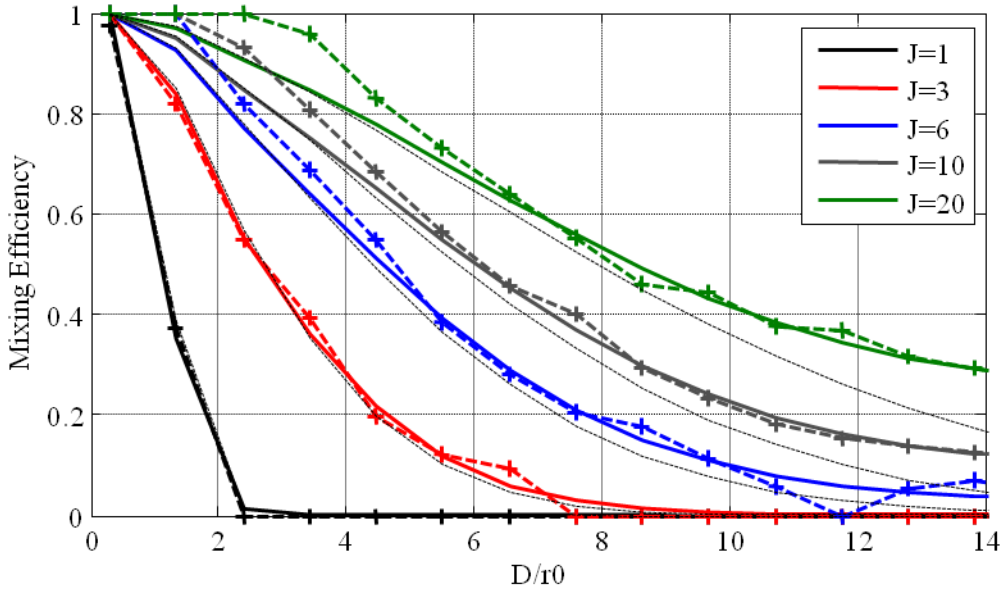

Fig. 4-26. OTG Characterization. To verify that the phase maps are correctly generated by the OTG we reproduce a set of turbulence scenarios for J modes removed and different D/r_0. The theoretical (black dashed line), estimated (colored line) and measured the heterodyne efficiency are shown. Small deviations between the theoretical and estimated mixing efficiency are present for $D/r_0 > 10$ due to the DMD limitations.

4.4.3 AO Performance under Atmospheric Turbulence

The same procedure used in the previous section for measuring the OTG performance can be used to validate the AO stage under the effects of atmospheric turbulence. In this case, the OTG generates random aberrations for a specific D/r_0 and the AO correction is switched on. After the AO compensation, some residual phases are present in the wavefront, which leads to losses in the heterodyne efficiency. The theoretical results of the compensation stage were provided in section 4.3.2. In Fig. 4-16, the theoretical phase variance of the corrected wavefront and resulting heterodyne efficiency were shown. The AO is able, in theory, to perform a complete correction for the first 20 first modes. To experimentally demonstrate the AO compensation we first apply the phase conjugation method. We generate a set of 100 ideal phase maps, each one composed by a 1024x1024 grid, for each turbulence scenario. The phase map is re-sampled and quantizated onto a 192x192 pixel phase map to match the DLP resolution. The phase map introduced in the

DLP is then re-sampled to match the 6x6 DM mirror matrix. The conjugated values of the phase map are calculated and sent to the DM driver. The phase map applied by the DM is $\varphi_c[i,j]$.

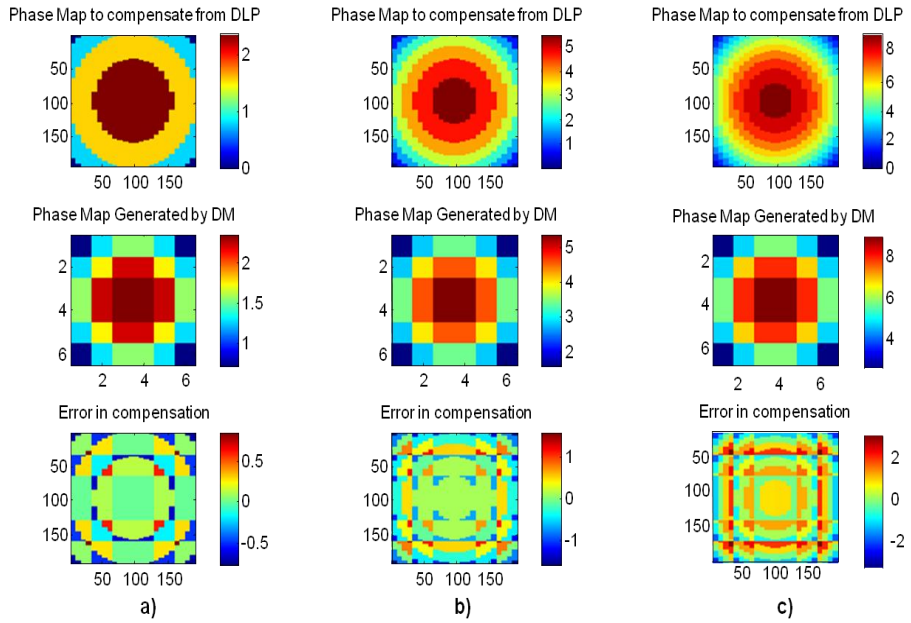

Fig. 4-27. Residual phase estimation after correction for three different defocus aberrations. The residual phase map is obtained by substracting the phase map generated by the DM to the one generated by the DLP.

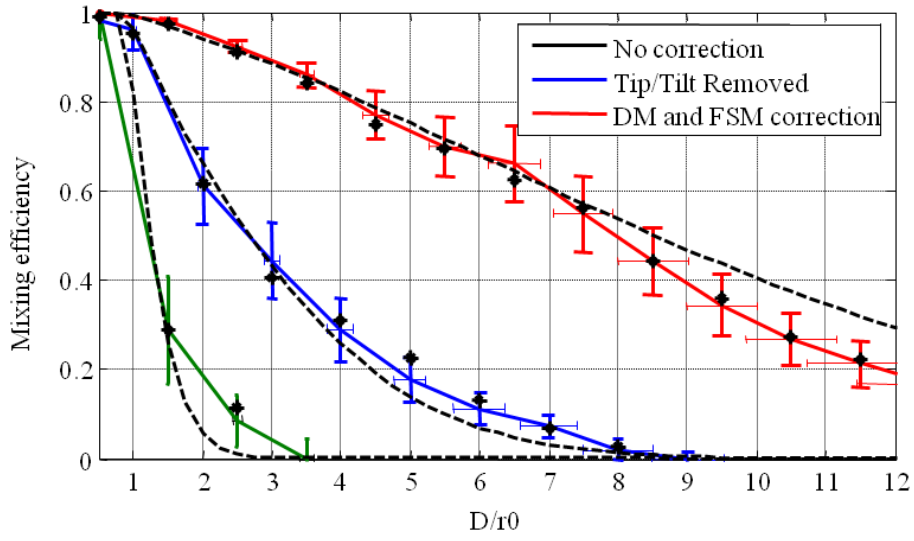

Fig. 4-28. Theoretical (dashed), estimated (coloured) and measured (point) heterodyne efficiency after applying AO correction under different normalized turbulence strength scenarios and compensation schemes. The measured values are close to the ones estimated by computation. In the other hand, the DM response is suboptimal in compare to the theoretical performance for $D/r_0 > 8$.

At this point, calibration must be performed in order to translate from phase [rad] to driver values [0-230 V]. The equivalence used is that the DM presents a maximum of 5.5 µm stroke at 230 V, which is approximately 3 times λ @ 1550 nm, or 6 π rads. The phase difference between the DLP and the DM phase maps is then calculated obtaining the residual phase. Substituting its phase variance in Eqs. 3.59-3.62, the theoretical mean mixing efficiency after applying correction can be obtained using Eq. 3.63. A graphical example of how the residual phase maps are calculated is shown in Fig. 4-27.

The theoretical, estimated and measured heterodyne efficiency for each D/r_0 are shown in Fig. 4-28 for a set of 100 realizations per measured point. When correction is only performed by the FSM, the tip/tilt weights are extracted from each phase map and are translated into control signal signals that feed the FSM driver. The heterodyne efficiency for the tip/tilt corrected scenario is then measured. When full correction is applied, the estimated error phase map is mainly due to the DM when correcting higher Zernike modes. The compensation then is performed by separating the compensation phase maps into two, one sent to the FSM, which calibrates the Tip/Tilt modes, and the other containing the higher orders, sent to the DM.

In Fig. 4-28 the statistical model and experimental results of the heterodyne efficiency over different normalized turbulence strength is shown. For $D/r_0 = 0.5$ the heterodyne efficiency is 0.64 when no correction is introduced, 0.902 by just correcting the Tip/Tilt and 0.987 with the complete AO system. In this case, the AO system is able to completely compensate the aberration introduced. For $D/r_0 > 2$, the heterodyne efficiency is below 0.1 in absence of AO, implying that the coherent system is severely degraded even for very low perturbation scenarios when no compensation is introduced. For $D/r_0 < 3$, the AO system is able to achieve efficiencies above 0.9, but it continuously decreases as the turbulence strength increases. For $D/r_0 > 8$, the AO exhibits compensation efficiencies below 0.5. Also, after this point, the theoretical and estimated mixing efficiencies present slightly differences. Let us remember that the theoretical dashed line for the DM and FSM correction corresponds to the efficiency loss associated with the residual variance due to the interactuator spacing (see Fig. 4-16), which was found to be equivalent to completely compensating a set of J=20 modes. The observed result indicates that the DM is not able to fully correct those orders and, after a break point situated around D/r_0= 8, its compensation is suboptimal, achieving half the theoretical efficiency at $D/r_0 = 12$. This practical difference may be due to the interactuator coupling (20% in the BMC32), which degrades the

spatial response of the DM. This effect becomes more significant at stronger turbulences, as the wavefront spatial bandwidth increases and differences between adjacent mirrors of the DM increase. From this graph we can also extract that, even for $D/r_0 < 3$, the tip/tilt correction it is not enough to provide decent heterodyne efficiencies. Therefore, it has been demonstrated that phase fluctuations severely degrade the performance of a coherent system. For these systems, AO becomes mandatory to compensate the effects of atmospheric turbulence.

Until now, we have analyzed the AO compensation performance using the conjugation principle. The incorporation of a blind search algorithm that controls the AO introduces an efficiency penalization that depends on the SNR of the metric signal *J* used and on the parameters selected to run the SPGD algorithm. Now, the objective is to measure the mixing efficiency of the AO system and SPGD algorithm under different turbulence strength scenarios for a set of specific compensation parameters.

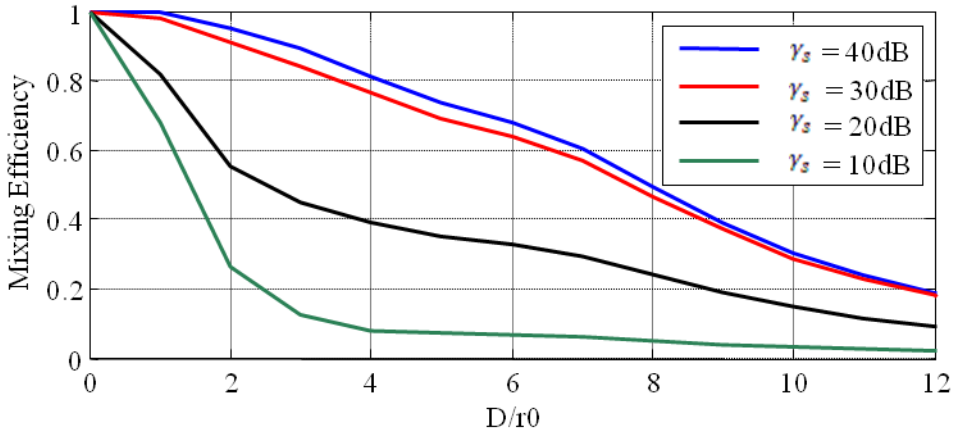

Fig. 4-29. Heterodyne efficiency for different values of D/r_0 for SNR per symbol (γ_s) of 10, 20, 30 and 40 dB. When γ_s is high enough (>40 dB) the efficiency matches the optimal compensation in every turbulent scenario. For SNR below 20 dB, the penalization introduced by the SPGD increases and the efficiency of the system is drastically reduced.

Also, the spatial limits of the AO compensation in junction with the SNR dependency of the SPGD generate a combined effect that impacts the system efficiency. No previous studies have experimentally evaluated this dependency on real systems. To perform this analysis, a set of 50 phase wavefronts were generated for each D/r_0 from 0 to 14. For each phase map the compensation is performed for a set of 100 repetitions adding AWGN and 5000 iterations per SPGD compensation realization. The SPGD parameters used were 0.8 V for the perturbation size

and 1 V for the gain. These parameters present an equilibrate response in terms of efficiency and convergence time (see section 4.3.3). In Fig. 4-29 the mean heterodyne efficiency is shown for different values of D/r_0 for γ_s of 10, 20, 30 and 40 dB. When γ_s is high enough (>30 dB) the efficiency matches the conjugation compensation in every turbulent scenario. For γ_s below 20 dB, the penalization introduced by the SPGD increases and the efficiency of the system is drastically reduced, even for $D/r_0 <$ 2. Considering an efficiency threshold of 0.4, the implemented AO is able to compensate $D/r_0 <$ 8.5 for $\gamma_s >$ 30 dB, $D/r_0 <$ 4 for a $\gamma_s =$ 20 dB and $D/r_0 <$ 1.75 for $\gamma_s <$ 10 dB. The efficiency loss is not equal for each perturbation scenario. A 6.54 dB penalization is introduced when γ_s decreases from 40 to 10 dB at D/r_0 = 1 while, for the same values of γ_s and D/r_0 = 8, the penalization reaches 7.08 dB. These differences are due to the spatial resolution of the DM and its effect on the metric signal *J*. For high D/r_0 the DM actuators stroke are consumed on compensating the lower Zernike modes, which contain higher power and have stronger influence over the metric signal. For low D/r_0 the DM has more capacity to introduce more accurate perturbations and compensate higher orders.

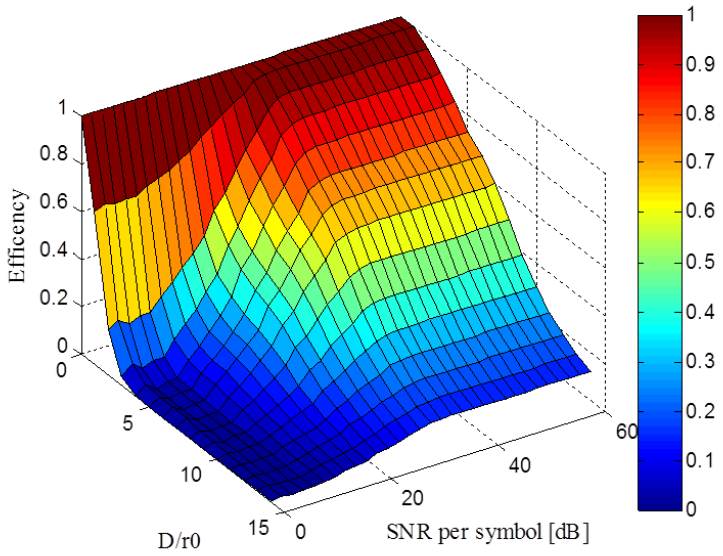

Fig. 4-30. Mixing efficiency for a wavefront sensorless architecture driven by the SPGD algorithm for dQ=0.8 V and G=1 V for different D/r_0 and γ_s.

The resulting effect is that the maximum heterodyne efficiency achievable by a specific set of actuators is decreased by the use of the blind algorithm when γ_s is below a threshold. In Fig. 4-30 the complete set of results obtained by using the same parameters and methods is

shown. For that, a set of 10 phase maps for each integer value of D/r_0 were generated and 100 compensation repetitions per phase map were performed by adding AWGN to control γ_s from 0 dB to 60 dB using a 2 dB increase step. The combined effect of the turbulence and γ_s produces a mixing efficiency equal to the one achieved by the conjugation method when $\gamma_s > 30$ dB. In these cases no penalization is introduced by the SPGD algorithm. For $\gamma_s < 30$ the efficiency decreases differently for each D/r_0. The mixing efficiency exhibits a higher change rate for increasing perturbation strengths at low γ_s. The maximum loss gradient is introduced for $D/r_0 \approx 4$ and SNR ≈ 22 dB.

5 Performance of FSO Coherent Communications under Atmospheric Turbulence

In this chapter the objective is to develop theoretical understanding and experimental demonstration of the coherent communication performance achievable using AO under atmospheric turbulence. For that, our purpose is to validate the theoretical models with experimental results obtained in the laboratory. We first introduce the model developed in [18], which describe the performance of synchronous receivers under atmospheric turbulence. Then, we develop an experimental set-up that involves the fiber coherent system, the OTG and the AO system, which have been described in previous chapter. The coherent FSO system performance is then experimentally evaluated using two different techniques: full optimal compensation and wavefront sensorless architecture using the SPGD algorithm. The resulting SERs are obtained and the experimental results are compared against the theoretical model. The analysis and results related to this chapter have been recapitulated in [49].

5.1 Introduction to Coherent Free Space Optics using AO

The system BER of a coherent system, which can be defined as the main characteristic of a communication system, is affected by the short-term effects produced by the electrical noise of the devices and by the long-term atmospheric effects that yield to signal fading at the receiver. Many data coding techniques developed for microwave wireless and optical fiber communication systems can partially compensate the errors due to short-term effects [190]. In the other hand, atmospheric turbulence induced errors present a much more complex problem which cannot be solved using these traditional techniques.

In a free space coherent receiver, the phase fluctuations introduced by the atmosphere on the transmitted signal may severely degrade the system performance. Adaptive optics has been demonstrated to be a potent method to reduce the effect of atmospheric turbulence in many different areas such as astronomical observations [191], imaging [192], etc. The improvement

that this tool can provide to laser communications has been demonstrated in different studies and experiments for direct detection methods [193][194].

For coherent communications in FSO, theoretical studies and analytical expressions have been developed in terms of heterodyne efficiency and error probability depending on different parameters such turbulence strength, signal strength, receiver aperture size and wavefront compensation [195][196]. However, experimental results have not been reported up to now. Evaluating this performance is usually difficult due to the complexity of the atmospheric effects, the precise experimental set-ups required to introduce the wavefront compensation and the multiple effects that have to be taken into account (vibrations, noise, laser linewidth, etc.). The objective of this project is to develop theoretical understanding and experimental demonstration of the coherent communication performance achievable by using AO under atmospheric turbulence as well as validate the theoretical models with experimental results. Also, the development of a complete bench top is intended to provide the researchers a useful tool to evaluate every block, method or algorithm involved in these systems.

In this project, the downconvertion from the optical domain to the electrical domain is achieved by using heterodyne detection. The modulation used is a QPSK modulation, so the SNR and BER performance can be extrapolated also to the homodyne case. Also, a shot noise limited scenario is considered, where the dominant noise is the local oscillator shot noise. By making these assumptions, the objectives are to explain the theory behind the mixing efficiency and BER performance of coherent detection using AO and demonstrate experimentally how a specific experimental AO set-up can increase the efficiency and BER of a coherent receiver in the presence of atmospheric turbulence and additive Gaussian noise.

The use of AO has been demonstrated to increase the heterodyne efficiency of the implemented coherent system under atmospheric turbulence. Now, by taking advantage of the coherent communication system, developed in section 2.5, we can analyze the BER statistics of a coherent FSO under atmospheric turbulence and different compensation techniques. First, we provide a mathematical description of the problem, which has been developed by [18]. The results obtained by this model are compared against the experimental data resulting from the experimental set up.

5.2 Statistical Model for Synchronous RX under Atmospheric Turbulence

In order to provide a model for the performance of synchronous receiver under atmospheric turbulence, first, it is crucial to summarize some of the concepts described in previous sections. In section 3.2 we derived the mathematical expressions that describe the mixing efficiency of coherent FSO systems under atmospheric turbulence. There, the mixing efficiency α^2 (Eq. 3.44) of a heterodyne system, also known as heterodyne efficiency, was described in terms of two random variables, α_r and α_i (Eq. 3.50 and Eq. 3.51), which represented the integrals over the collecting aperture of the real and imaginary parts of the normalized optical field at the receiver (Eq. 3.43). The mean and variance of these two terms were described as a function of the incoming wavefront phase variance (σ_φ^2) and the number of statistically independent cells (*N*, Eq. 3.65) present in the aperture. The relationships between these random variables were described in Eqs. 3.59-3.62. Similarly, when the AO correction is introduced, we can obtain the mean heterodyne efficiency by substituting σ_φ^2 by $\sigma_{\varphi_{res}}^2$ in these equations, where $\sigma_{\varphi_{res}}^2$ is the variance of the wavefront residual phase after correction ($\varphi_{res}(r) = \varphi(r) - \varphi_c(r)$).

Then, in section 4.3.1, we described the resulting SNR per unit bandwidth of a heterodyne detector in a shot noise limited scenario under atmospheric turbulence. In Eq. 4.41, the relationship between γ_s and α^2 was shown. It was shown that the SNR per symbol under atmospheric turbulence γ_s is proportional to the SNR per symbol in the absence of turbulence $\gamma_{s,0}$ and the heterodyne efficiency α^2

$$\gamma_s = \gamma_{s,0} \cdot \alpha^2 \tag{5.1}$$

where $\gamma_{s,0} = \eta_q \cdot N_s$. In an ideal coherent receiver, the symbol error probability (SEP), $p_s(E)$, is calculated by averaging the SEP conditioned to γ_s, ($p_s(E|\gamma_s)$), over the instantaneous γ_s, $p_s(\gamma_s)$.

$$p_s(E) = \int_0^\infty d\,\gamma_s p_s(E|\gamma_s) p_s(\gamma_s) \tag{5.2}$$

In this project we are focused on M-PSK modulations for M=4 (QPSK). For this case, the SEP conditioned to γ_s based on maximum-likelihood detection is 197]

$$p_s(E|\gamma_s) = \int_{-\pi/2}^{\pi/2-\pi/M} d\,\theta exp\left[-\gamma_s \frac{sin^2(\frac{\pi}{M})}{sin^2\theta}\right] \quad 5.3$$

By inserting Eq. 5.3 into Eq. 5.2, the SEP can be obtained as a function of $p_s(\gamma_s)$. In order to give a closed expression of Eq. 5.2, a full statistical description of γ_s need to be provided. Eq. 5.1 shows the dependency of γ_s and α^2, whose PDF are closely related as [18]

$$p_s(\gamma_s) = \frac{\overline{\alpha^2}}{\overline{\gamma_s}} p_{\alpha^2}\left(\gamma_s \frac{\overline{\alpha^2}}{\overline{\gamma_s}}\right) \quad 5.4$$

This implies that an statistical description of α^2 is required in order to evaluate the SEP performance of a coherent receiver. In Eq. 5.1, α^2 is a random variable with PDF $p_{\alpha^2}(\alpha^2)$. Using the PDF in Eq. 3.52, substituting $a_r = \sqrt{\alpha^2}cos\theta$, $a_i = \sqrt{\alpha^2}sin\theta$, multiplying the result by the Jacobian of the transformation (*1/2*) and integrating over θ, we obtain a joint PDF of α^2 and θ. The marginal PDF of the heterodyne efficiency α^2 is then obtained by integrating over θ [18]

$$p_{\alpha^2}(\alpha^2) = \frac{1}{4\pi\sigma_r\sigma_i}\int_{-\pi}^{\pi} exp\left(-\frac{(\alpha cos\theta - \bar{\alpha}_r)^2}{2{\sigma_r}^2}\right) exp\left(-\frac{(\alpha sin\theta)^2}{2{\sigma_i}^2}\right) \quad 5.5$$

This integral cannot be solved in a close form. Instead, it is possible to obtain the mean and variance of the intensity fading by assuming α_r and α_i jointly normal variables

$$\overline{\alpha^2} = {\sigma_r}^2 + {\sigma_i}^2 + {\bar{\alpha}_r}^2 \quad 5.6$$

$$\sigma_{\alpha^2}^2 = 2({\sigma_r}^4 + {\sigma_i}^4) + 4{\sigma_r}^2{\bar{\alpha}_r}^2 \quad 5.7$$

In [198], Eq. 5.5 was found to exhibit a Rice distribution for weak-turbulence scenarios, where α^2 was defined as the sum of a coherent term α_r with amplitude $\overline{\alpha_r}$ and a incoherent term α_i with zero mean and variance ${\sigma_i}^2$. The resulting PDF is given by

$$p_{\alpha^2}(\alpha^2) = \frac{1}{2\sigma^2} exp\left(-\frac{\alpha^2 + a^2}{2\sigma^2}\right) I_0\left(\frac{a\alpha}{\sigma^2}\right) \quad 5.8$$

being $a^2 = \overline{\alpha_r}^2$, representing the coherent intensity, and $2\sigma^2 = {\sigma_i}^2$, which represents the fluctuating radiance. In [18], this PDF was expressed in terms of $\overline{\alpha^2}$ and a parameter *r*, defined as

the contrast parameter, which relates the coherent intensity and the radiance fluctuating strength as $1/r = 2\sigma^2/a^2$, resulting in

$$p_{\alpha^2}(\alpha^2) = \frac{1+r}{\overline{\alpha^2}} exp(-r) exp\left(-\frac{(1+r)\alpha^2}{\overline{\alpha^2}}\right) I_0\left(2\alpha\sqrt{\frac{(1+r)r}{\overline{\alpha^2}}}\right) \quad 5.9$$

The resulting variance of the intensity fading is $\sigma_{\alpha^2}^2 = \overline{\alpha^2}(2r+1)/(1+r)^2$. In order to extend this description to higher turbulence strength scenarios, the $\overline{\alpha^2}$ and r parameters have to perform equal phase mean and variance for the PDFs expressed in Eq. 5.5 and Eq. 5.8, resulting into

$$\overline{\alpha^2} = \sigma_r{}^2 + \sigma_i{}^2 + \bar{\alpha}_r{}^2 \quad 5.10$$

$$\sigma_{\alpha^2}^2 (2r+1)/(1+r)^2 = 2(\sigma_r{}^4 + \sigma_i{}^4) + 4\sigma_r{}^2\bar{\alpha}_r{}^2 \quad 5.11$$

Using Eq. 5.11, the contrast parameter r can be calculated as a function of the wavefront phase variance and number of statistically independent cells using Eqs. 3.59-3.62. In general, for $D/r_0 \gg 1$, r tends to infinite, so the PDF can be approximated by a Gaussian with mean $\overline{\alpha^2}$. In the other hand, for values of r close to zero, α^2 approximates a negative-exponential distribution. Inserting Eq. 5.9 into Eq. 5.4 we obtain

$$p_{\gamma_s}(\gamma_s) = \frac{1+r}{\overline{\gamma_s}} exp(-r) exp\left(-\frac{(1+r)\gamma_s}{\overline{\gamma_s}}\right) I_0\left(2\sqrt{\frac{(1+r)r\gamma_s}{\overline{\gamma_s}}}\right) \quad 5.12$$

So the $p_{\gamma_s}(\gamma_s)$ is described as a noncentral chi-square distribution with two degrees of freedom [18].

Now, we can take Eq. 5.12 and Eq. 5.3 to obtain the SER described in Eq. 5.2. From [18] we obtain that

$$p_s(E) = \frac{1}{\pi}\int_{-\pi/2}^{\pi/2-\pi/M} d\,\theta \frac{(1+r)sin^2\theta}{(1+r)sin^2\theta - \overline{\gamma_s}sin^2\frac{\pi}{M}} exp\left[-\frac{r\overline{\gamma_s}sin^2(\frac{\pi}{M})}{(1+r)sin^2\theta - \overline{\gamma_s}sin^2\frac{\pi}{M}}\right] \quad 5.13$$

This integral has to be numerically solved. Still, considering that $sin^2\theta < 1$ we can obtain an upper bound to the integral on Eq. 5.3 to obtain [18]

$$p_s(E|\gamma_s) \leq \frac{M-1}{M} exp\left[-\gamma_s sin^2(\frac{\pi}{M})\right] \quad 5.14$$

So the upper bound for the SEP from Eq. 5.13 is given by [18]

$$p_s(E) \leq \frac{M-1}{M} \frac{(1+r)}{(1+r)-\bar{\gamma}_s sin^2\frac{\pi}{M}} exp\left[-\frac{r\bar{\gamma}_s sin^2(\frac{\pi}{M})}{(1+r)-\bar{\gamma}_s sin^2\frac{\pi}{M}}\right] \quad 5.15$$

The resulting Eq. 5.15 provides a theoretical upper bound to contrast the experimental results given in the next section.

5.3 Experiments on QPSK using FSO under Atmospheric Turbulence

The performance of an experimental QPSK under atmospheric turbulence can be obtained by joining together the different blocks presented in this work. The heterodyne QPSK coherent system on fiber, developed in Chapter 2, act as the communication front/end. The FSO, composed by the OTG and AO, performs the atmospheric turbulence generation and the AO compensation using the set up implemented in chapter 4 (see section 4.4). By using the coherent communication system developed in Chapter 2, the SER data can be computed for different scenarios. For each D/r_0, a set of 10 specific phase maps are generated. Then, for each phase map, the SER is obtained for four different cases. In the first case no correction is applied, obtaining the compensation free scenario. In the second case, only the tip/tilt correction is applied using the FSM. Then we perform a full optimal correction, where we introduce the OTG conjugated phase map in the FSM and DM compensating mirrors, being able to exploit the maximum achievable compensation of the AO system. As a final step, we apply the wavefront sensorless technique controlled by the SPGD algorithm. The phase maps chosen for each D/r_0 are selected to be representative in terms of phase variance. This means that the selected random phase maps match the mean heterodyne efficiency produced by a Kolgomorov distribution at a specific D/r_0.

For each phase map the SER is obtained in each compensation scenario as a function of the SNR per symbol γ_s, which takes values from 0 to 30 dB at 2 dB. The data acquisition follows the next procedure: in the absence of atmospheric turbulence the SER is obtained using the FSO set up and scanning every SNR scenario. The atmospheric turbulence is then introduced by the

OTG and the SER is evaluated in each compensation scenario: compensation free, tip/tilt correction, optimal correction and wavefront sensorless compensation.

In Fig. 5-1, Fig. 5-2 and Fig. 5-3the SER can be seen for different turbulence strength scenarios. The experimental data (∇) is compared to theoretical upper levels (coloured lines) derived from Eq. 5.15. In order to calculate the SER from Eq. 5.15, $\overline{\gamma_s}$ is obtained as $\overline{\gamma_s} = \gamma_0 \cdot \overline{\overline{\alpha^2}}$, where γ_0 is the SNR per symbol in absence of turbulence and $\overline{\alpha^2}$ is the averaged heterodyne efficiency measured with the experimental set up when AO correction is applied (see Fig. 4-28). For $D/r_0 = 2$ the measured SER achieved by the AO system with optimal compensation practically matches the SER of the AWGN channel. The AO provides efficiency gains around 7.5 dB in compare to the non-compensated scenario. A penalization of -2.3 dB in introduced when the tip/tilt correction is applied. When the optimal compensation method is substituted by the SPGD, the SER increases as a function of γ_0. For γ_0 below 5 dB the AO with SPGD does not introduce any additional correction. For SNR above 5 dB the SPGD starts compensating but, still, it does not reach the tip/tilt compensated scenario. In order to achieve a SER equal to 10^{-3} a $\gamma_0 >$ of 17 dB is required in the non compensated scenario, $\gamma_0 > 14.8$ dB with the AO and SPGD and a $\gamma_0 > 10.24$ dB with the optimal compensation. A loss of 0.23 dB is introduced in compare to the theoretical limit at that point. For $D/r_0 = 3$ the effect of the aberration introduced increases the system SER, requiring 25 dB to achieve a SER equal to 10^{-3}. The same analysis can be performed for the rest other turbulent scenarios. For turbulent strengths where $D/r_0 > 3$, the coherent receiver is not able to correctly demodulate the data and if no compensation is applied. Therefore, in these cases AO compensation becomes mandatory. From here, the performance of each compensation method is highly dependent on the γ_0. For $\gamma_0 < 25$ dB, the efficiency of the SPGD method introduces a significant penalization over the optimal compensation case. In the other hand, for higher γ_0 the penalization introduced by the SPGD diminishes. At a certain point, that has been calculated to be around 25 dB (see section 0), these two compensation techniques perform the same correction. It can also be appreciated how the compensation introduced by the AO with both techniques progressively decays as the D/r_0 increases due to the spatial characteristics of the AO. Also, as the D/r_0 increases, the system SER of both methods becomes similar due to their difficulties to compensate the wavefront aberrations and their SER curves progressively get closer to the one without compensation.

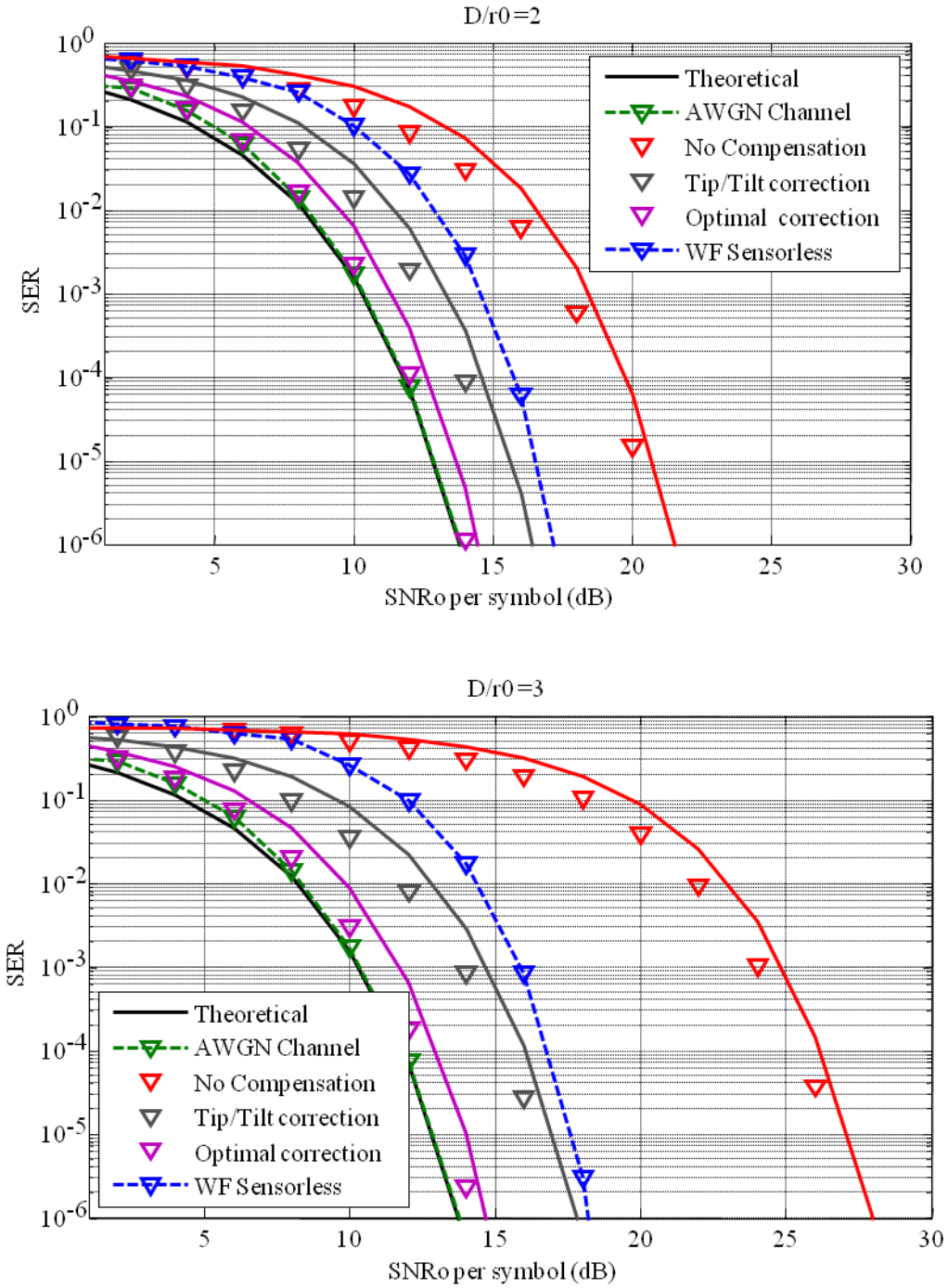

Fig. 5-1. SER versus $\gamma_{s,0}$ for $D/r_0 = 2$ and 3. Experimental data (∇) is compared to theoretical upper bounds (coloured lines) derived from the Eq. 5.15. The performance is evaluated with no turbulence, without compensation, with tip/tilt correction only, with AO using optimal compensation and with AO using SPGD.

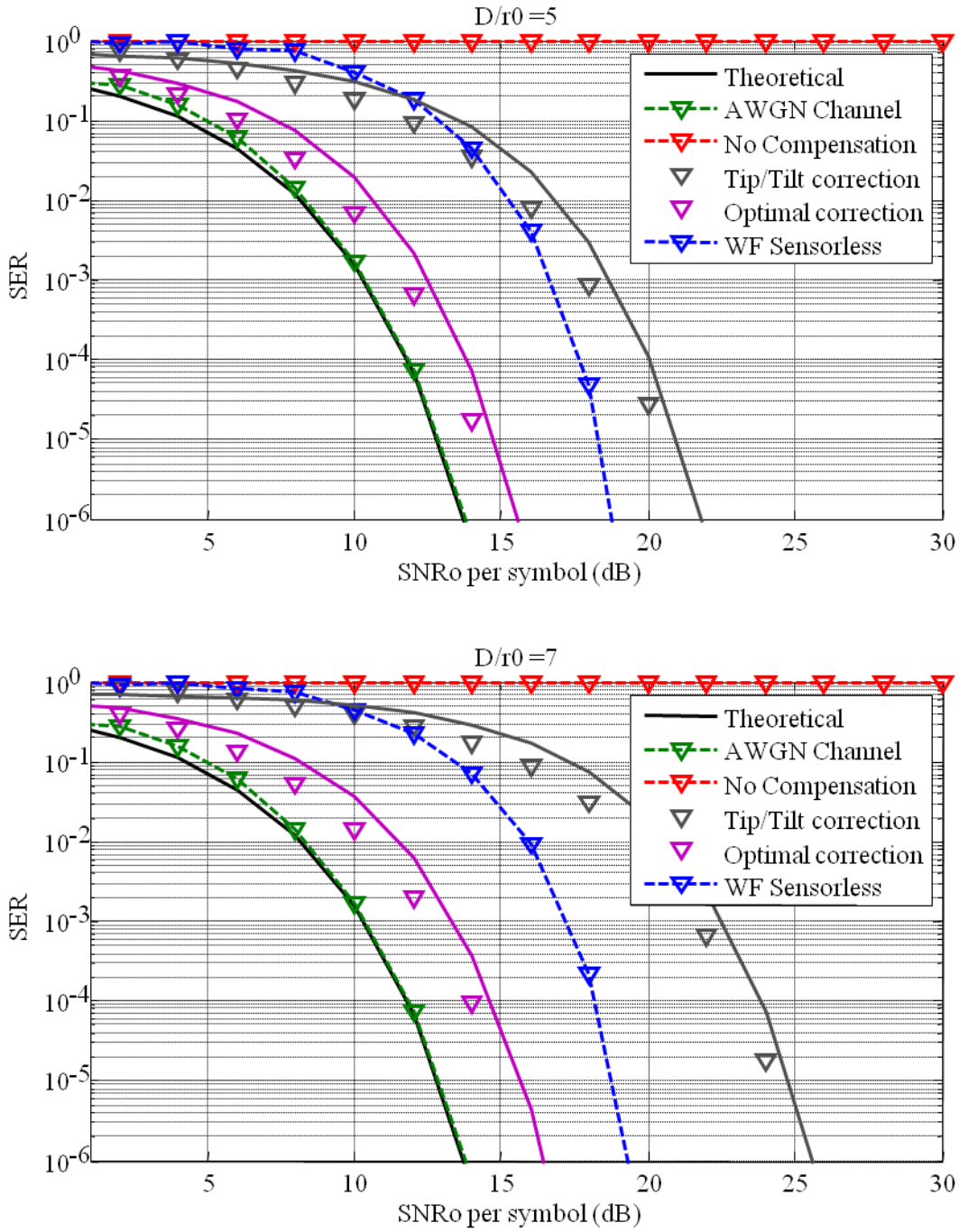

Fig. 5-2. SER versus $\gamma_{s,0}$ for $D/r_0 = 5$ and 7. Experimental data (∇) is compared to theoretical upper bounds (coloured lines) derived from the Eq. 5.15. The performance is evaluated with no turbulence, without compensation, with tip/tilt correction only, with AO using optimal compensation and with AO using SPGD.

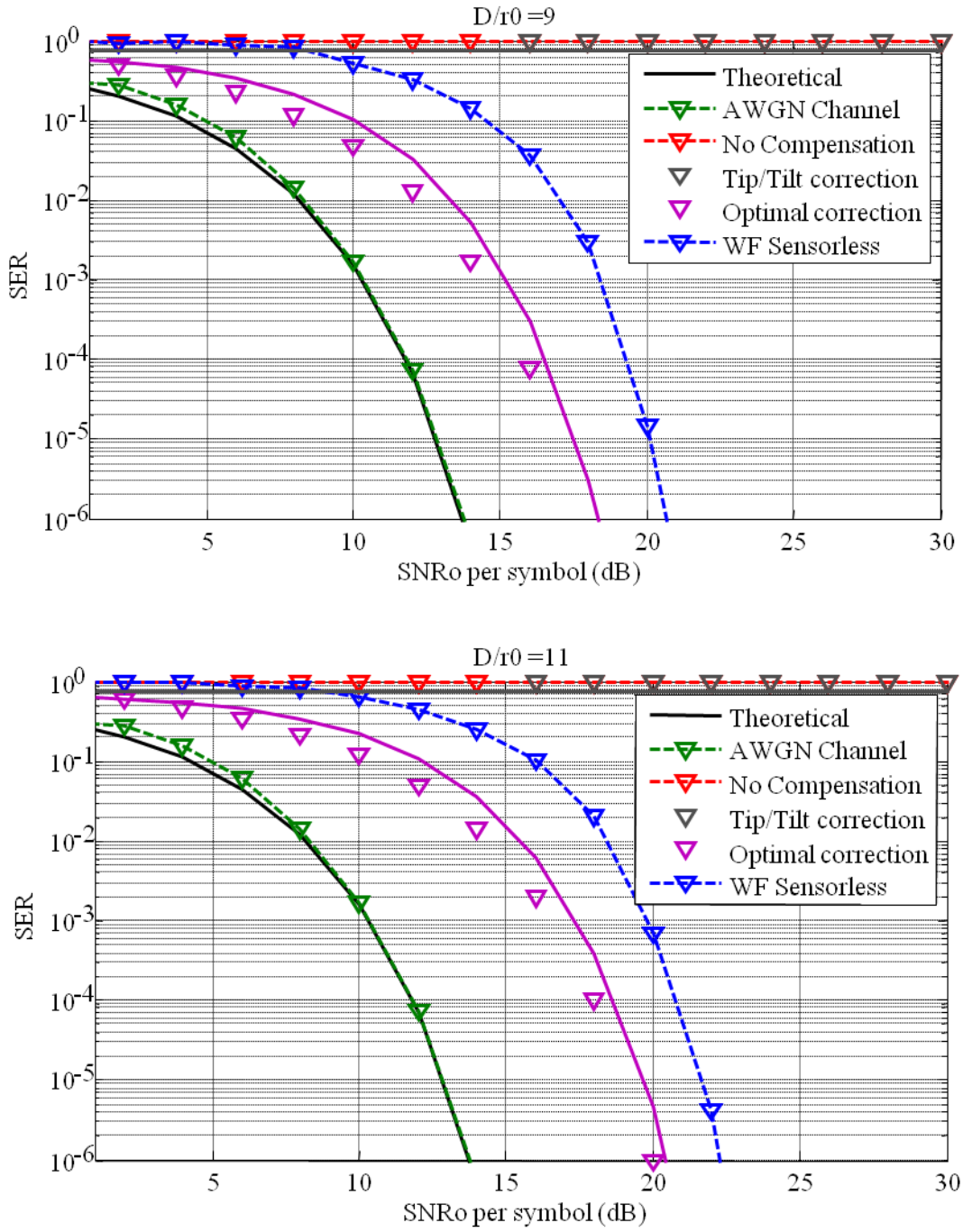

Fig. 5-3. SER versus $\gamma_{s,0}$ for $D/r_0 = 9$ and 11. Experimental data (∇) is compared to theoretical upper bounds (coloured lines) derived from the Eq. 5.15. The performance is evaluated with no turbulence, without compensation, with tip/tilt correction only, with AO using optimal compensation and with AO using SPGD.

When we compare the experimental results against the SER values predicted by the model, the performance of the experimental set up is demonstrated to follow the predicted upper bound derived from Eq. 5.15. In the other hand, this upper bound was found to be similar to the exact calculation of the SER from Eq. 5.13 in many practical situations [18]. In our case, small deviations arise between theoretical and experimental curves. A possible reason for these differences (below 1 dB in most cases) might be due to the statistical characteristics of the experiment performed. In the experiment, the number of realizations per turbulent scenario is limited, 10 for each D/r_0, due to the fact that SER measurements, up to 10^{-6}, are a slow process. These measurements have to be performed for each turbulent scenario and each compensation methods, which results into a time consuming task. At the same time, the phase wavefronts selected for the SER analysis were chosen to be representative, in terms of the mean, of the heterodyne efficiency achieved for each D/r_0. This may yield to a loss of accuracy in compare to the theoretical model as we are not evaluating a sufficiently large set of instantaneous α^2, required to perform a good description of atmospheric statistics.

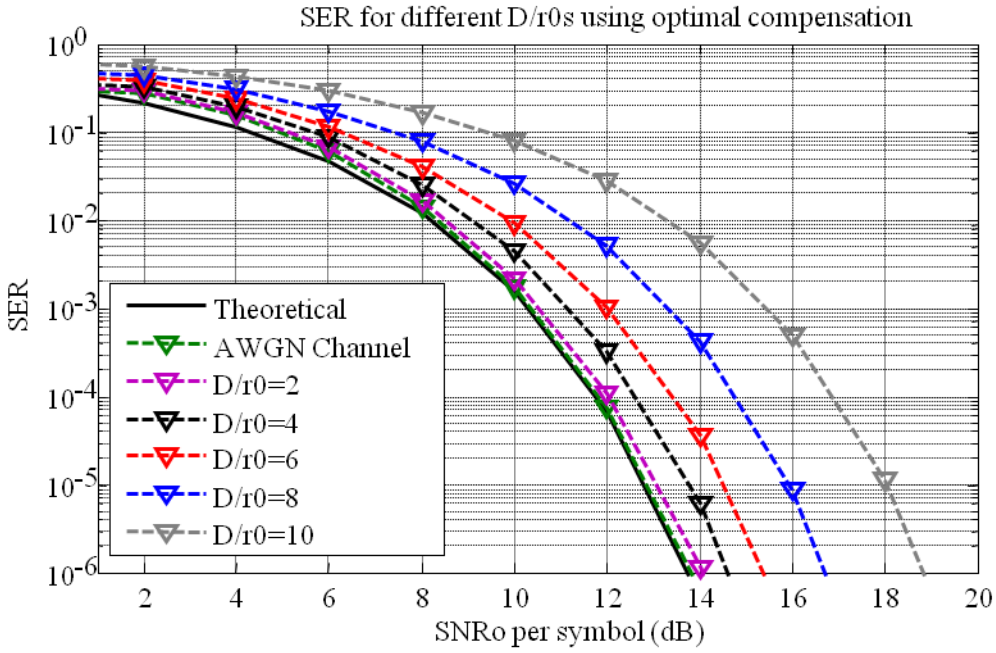

Fig. 5-4. SER performance of the QPSK FSO heterodyne system using AO and optimal correction for different turbulence strengths and SNR.

In Fig. 5-4, the SER performance of the QPSK heterodyne system is shown using AO with optimal compensation for different turbulence strengths and SNR. In this graph, the limit is

imposed by the maximum achievable performance in the AWGN channel. In this representation the spatial limits of the AO can be visualized. For increasing $D/r_0's$ the ability of the actuators to compensate the turbulence is reduced. This is due mainly to the hardware characteristics of the DM, which set a limit on the compensation results. The implemented AO can perform perfect compensation just when $D/r_0 = 1$. For higher values, the penalization introduced continuously increases from 2 dB for $D/r_0 = 0.1$ up to 5 dB when $D/r_0 = 10$. For $D/r_0 < 6$, the penalization can be considered almost lineal, and the system performance is degraded by only 2 dB at this point in compare to the theoretical limit.

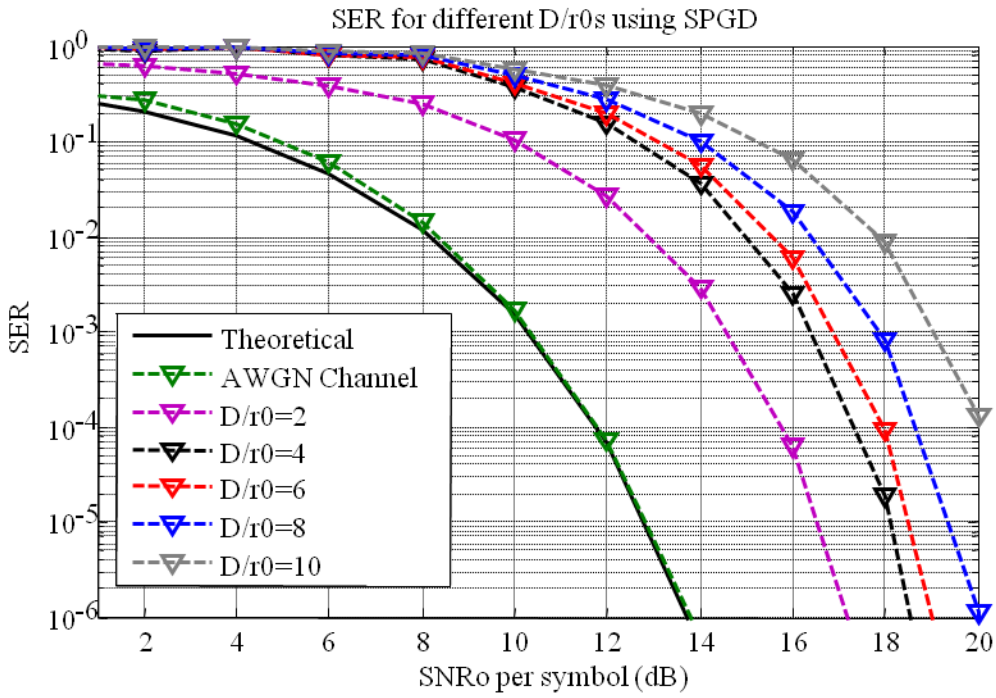

Fig. 5-5. SER performance of the QPSK FSO heterodyne system using a wavefront sensorless architecture driven by the SPGD algorithm for different turbulence strengths and SNR.

For the wavefront sensorless architecture using the SPGD algorithm, the SER performance is shown in Fig. 5-5. Here, the SER curves differ from the ones obtained with the optimal compensation. The penalty introduced by SPGD is dominant for SNR's below 15 dB. This is due to the fact that the SPGD algorithm works with differential magnitudes, which lead to a low performance when the metric signal presents low SNR. In the other hand, when the SNR at the receiver is high enough (above 25 dB), the system performance equals the wavefront sensor architecture. This is an interesting feature of this architecture, as its benefits on cost and complexity are evident. In this analysis we have only evaluated the convergence of the algorithm

in terms of the number of iterations. The ability of the receiver electronics to perform a sufficiently high rate of iterations per second is crucial for its implementation on practical systems.

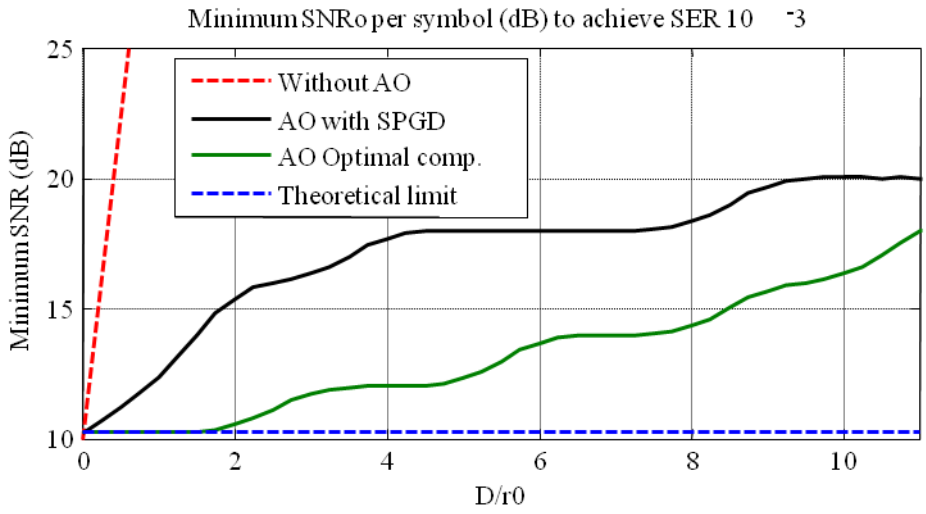

Fig. 5-6. Minimum SNR to achieve a SER equal to 10^{-3} for: ideal coherent detector, FSO under atmospheric turbulence, FSO under atmospheric turbulence with AO using optimal correction and FSO under atmospheric turbulence using SPGD algorithm.

In Fig. 5-6 the minimum SNR to achieve a SER equal to 10^{-3} is shown for different scenarios. When no aberration is generated, the penalization introduced by the FSO is around 0.2 dB in compare to the AWGN limit. This penalization, as it was shown in chapter 2, has its origin in the coherent detector, where the compensation algorithms introduce a residual error. For higher normalized turbulence factors, the SPGD algorithm introduces a penalization in compare to the optimal correction that continuously decreases until the 25 dB SNR threshold is achieved. In this range, the improvement introduced by the AO makes possible to reach the 10^{-3} BER threshold, which could not be achieved without active compensation.

The SER penalization of the SPGD algorithm is shown in Fig. 5-7. The strongest penalization introduced by the SPGD algorithm in compare to the ideal wavefront sensor architecture arises in scenarios where the SNR is below 25 dB and the normalized turbulence strength is above 8. For $D/r_0 < 10$ this threshold diminishes up to 20 dB.

From these results it is possible to extract several conclusions. First, the AO compensation becomes mandatory for $D/r_0 > 2$ if a coherent QPSK FSO that exhibits a system

SER below 10^{-3} needs to be implemented. Second, the introduction of AO drastically increases the coherent system performance allowing the viability of these FSO coherent systems. Still, a practical AO system introduces a penalization over its theoretical performance due to the limited spatial response of the active mirror actuators. Also, noise present on the metric signal used to feed the SPGD algorithm degrades the performance of wavefront sensorless arquitectures. For high SNR's, above 25 dB in our specific AO system, the SPGD blind search algorithm is able to achieve the same SER performance as the optimal correction method, allowing the designer to get rid of the wavefront sensor without any loss on the system performance. We can conclude that the theoretical upper bound for the SER in a FSO coherent QPSK has been validated by the experimental data obtained in the laboratory. Slight differences are present, mainly due by the limited set of phase aberrations used to obtain the SER. Therefore, the implemented testbed fulfills the specifications in order to consider it a valid tool to evaluate in the laboratory future research projects involving any coherent FSO system (increased modulation formats, improved blind search algorithms, etc.).

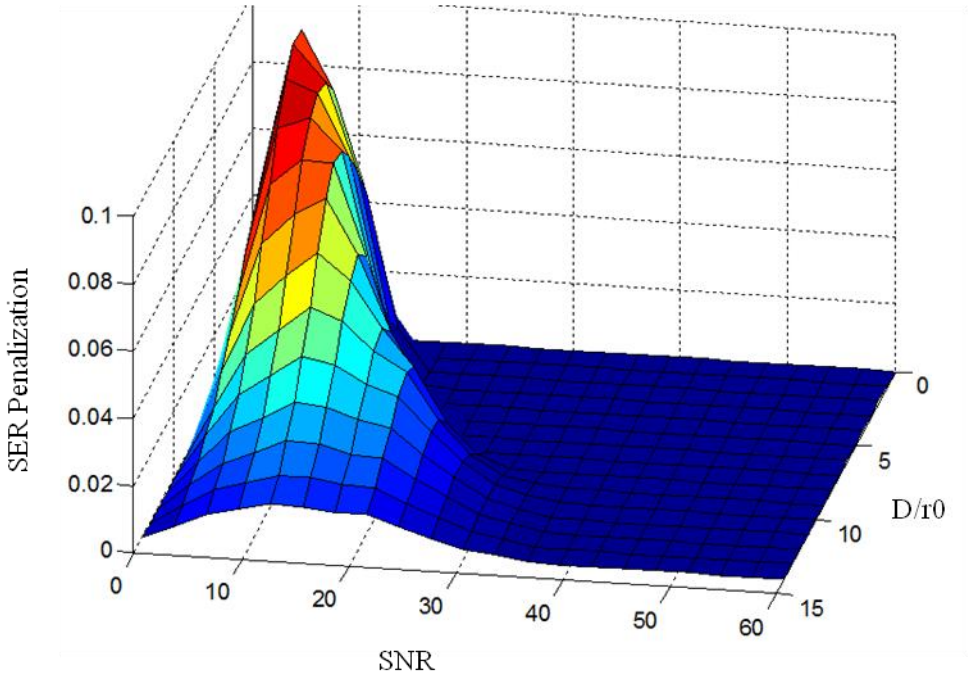

Fig. 5-7. SER penalization of the SPGD algorithm for different normalized turbulence strength and SNR per symbol.

6 Conclusions and Future Work

6.1 Conclusions and Comments

The main objective of the present work was to develop theoretical and experimental understanding of the performance of coherent FSO communications systems and to show how adaptive optics can mitigate the influence of atmospheric turbulence in free-space optical coherent communications. For that, our task has been focused on developing in the laboratory a complete experimental set-up that helps us to breakdown the communication system allowing us to study the performance of every block separated.

In chapter 1, we experimentally demonstrated the coherent optical infrastructure necessary to produce robust high-capacity optical communication links over the 1.5-micron wavelength spectral band using QPSK modulation and heterodyne detection. The system was able to send and receive information using a QPSK single polarization complex modulation, achieving a maximum 625 Mb/s communication data rate with low sensitivity penalization working in a shot noise limit scenario. The main source of errors is the loss of performance of the compensation algorithms when the incoming signal is weak in compare to the noise. For SNR per bit below 10 dB, the FF carrier recovery and phase offset compensation blocks loss accuracy and the system performance is deteriorated, leading to a maximum penalization of 2dB in the worst scenario considered (SNR equal to 1 dB). In the other hand, for SNR above 10 dB, the sensitivity penalization was around 0.1dB in compare to the theoretical limit. This showed that a practical coherent system is able to achieve performances close to the predicted by the theory by using digital compensation algorithms and modest SNR ratios. The main limitation of the implemented system is that it cannot perform a full real time demodulation due to the computational load of the impairment and demodulation schemes. Still, it is able to perform burst mode communications by adjusting the burst rate to the computational delay, which was calculated to be 50 ms in order to demodulate $5x10^3$symbols. In order to perform full-real time demodulation, the use of VLSI electronics is suggested but its implementation is beyond the scope of this project.

In order to generate atmospheric aberrations we have used recently developed technologies that allow us to create new implementation methods to emulate deterministic atmospheric conditions. The feasibility of generating atmospheric aberrations by using binary digital holography and commercially available DMDs has been proved and it has been shown that atmospheric turbulence, even with strong conditions, can be emulated by using commercially available devices at a fraction of the cost of the widely used SLMs. The trade-off between spatial resolution and quantization errors caused by the parameter selection has been addressed for a different set of parameters of the method. A normalized aperture (D/r_0) up to 18 can be generated with the Texas Instruments 9500DLP DMD. In the laboratory, an experimental set-up of the technique has been implemented and its practicability has been demonstrated by creating and measuring Zernike phase aberrations and Kolgomorov statistics. The experimental set-up uses a TI 3000DLP DMD that can generate turbulence aberrations up to D/r_0 = 10 with an efficiency above 0.92. The main disadvantage of the technique is the low power efficiency of the resulting signal (less that 1% of the incoming signal), but it is not critical due to the fact that this technique would only be applied in lab set ups and does not influence the link budget of real systems. An experimental Mach-Zehnder self-interferometer was implemented in order to verify and evaluate the generated phase wavefronts. This method just offered a qualitative verification of the phase wavefronts due to the high dynamic range required in the CCD camera to obtain accurate phase measurements. In order to precisely verify the phase wavefront generation we carried out experiments using the FSO coherent system and measuring the resulting heterodyne efficiency of the aberrated wavefront and the LO source. The experimental results were compared and verified against the theoretical models, which ensured that correct wavefront phase modulations were achieved. When higher turbulence scenarios are introduced, differences between the measured and theoretical heterodyne efficiency arises, leading to an upper limit of the turbulence generated.

A free space optical AO system to mitigate turbulence-induced phase fluctuations has been implemented by using a wavefront sensorless architecture driven by a blind search algorithm, the SPGD. The AO system was designed to correct the first 20 Zernike modes by using two separated active mirrors: a tip/tilt corrector and a DM with 32 actuators. In practice, the tip/tilt platform was demonstrated to compensate the tip/tilt aberrations with high accuracy for every turbulence strength under test. In the other hand, the observed result indicates that the DM is not able to fully correct the predicted orders and, after a break point situated around D/r_0= 8,

its performance is suboptimal. This practical difference is due to the inter-actuator coupling (20% in the BMC32), which degrades the spatial response of the DM, especially when the spatial bandwidth of the phase wavefront increase. We evaluated the heterodyne efficiency of the implemented AO system, achieving efficiencies above 0.5 for $D/r_0 < 8$. To perform an improved correction, a DM that presents higher capabilities in terms of number of actuators is required. The performance of the wavefront sensorless architecture was also experimentally evaluated, and it was shown that it is highly dependent on three parameters, the perturbation size applied, the gain control of the SPGD algorithm and the SNR of the metric signal used. These parameters define the convergence performance of the sensorless architectures. For our system, a perturbation size of 0.8 V and a 1 V gain has been proved to present the better performance in presence of AWGN. With these parameters, a heterodyne efficiency above 0.9 is achieved in compare to the ideal wavefront sensor architecture only when the SNR of the performance metric is above 30 dB. The convergence rate was below 500 iterations/correction in these scenarios. For lower SNR of the signal metric, the efficiency of the algorithm drastically diminishes, and for SNR below 10 dB the algorithm does not converge. In our system the iteration rate achieved is around 500 Hz, which it is not enough to provide compensation in real systems. Better performances could be achieved by using FPGA hardware or faster drive electronics. Assuming the most restringing temporal requirement of the AO, which was calculated to require a compensation bandwidth below 650 Hz, a real wavefront sensorless architecture using the implemented AO should achieve an effective loop rate of 325 kHz. This performance is nowadays achievable by using commercial devices, such as the *BMC X Driver*, which achieves frame rates up to 400 kHz. This implies that a wavefront sensorless architecture can be an attractive solution for real systems due to its benefits in terms of cost, complexity, power efficiency and temporal response. Also, other essential benefits, as compensation of aberrations introduced by the receiver optics or the capability to track pointing errors, may motivate the transition from wavefront sensor to wavefront sensorless architectures.

In chapter 5, by taking advantage of the OTG, the FSO with AO and the coherent transceiver, we were able to evaluate and experimentally quantify the performance achievable in term of the SER for coherent FSO systems using atmospheric compensation techniques. It was shown that the penalization introduced by phase fluctuations can introduce severe limitations in the system performance. A penalization of 15 dB in the absence of AO compensation is introduced by atmospheric effects for $D/r_0 = 3$ if a SER below 10^{-3} is required. For higher

turbulence strengths, the AO stage becomes mandatory. When AO compensation is introduced, it has been shown that the coherent system performs an efficient communication, making possible the coherent data transmission under atmospheric turbulence. To achieve a SER below 10^{-3} for $D/r_0 = 6$, the AO only introduces a penalization of 4 dB in compare to the non-perturbated scenario. To achieve the same SER for $D/r_0 = 10$, the penalization is 6.5 dB. By comparing these experimental results against the SER values predicted by the theoretical model, the performance of the experimental set up is demonstrated to follow the predicted upper bound derived in the literature. In the other hand, this upper bound was found to be similar to the exact calculation of the SER in many practical situations [18]]. In our case, small deviations arise between theoretical and experimental curves. A possible reason for these differences (below 1 dB in most cases) might be due to the statistical characteristics of the experiments performed as we did not evaluate a sufficiently large set of instantaneous α^2, required to perform a good description of atmospheric statistics. Still, the theoretical models have been validated by the results obtained with the experimental set-up implying that both, the experimental coherent FSO implemented and the theoretical model, successfully describe the performance of practical synchronous receivers under atmospheric turbulence.

6.2 Future work

The present work sets the theoretical and experimental basics of a free-space optical coherent communications system with deterministic turbulence generation. The development of this first experimental test-bed provides a starting point for future research in this field, allowing the improvement of each one of the stages involved as well as the implementation and analysis of new techniques in the field.

In this study we evaluated the performance of synchronous receiver assuming that we are working in a situation where the aperture telescope diameter (D) is larger than the coherence diameter of the wavefront (r_0). In this regime amplitude fluctuations effects become minor and phase fluctuations effects become dominant. Even if for most typical link designs, wavefront phase fluctuations are the dominant impairment and amplitude fluctuations effects can be ignored as they are a second order effect, a more extensive study could be performed by introducing scintillation effects into consideration. This evaluation would describe the effects and performance for situations where $D/r_0 < 1$. It is important to note that the BCGH technique

using binary arrays also allows the designer to also provide an amplitude modulation of the wavefront. This would imply a complete emulation of the atmospheric effects by introducing scintillation effects by using the same OTG and creating the software required to emulate them. Using the developed experimental set up, a further study could experimentally evaluate the performance in these scenarios, where the turbulence-induced distortions are responsible for severe fading of the received power at the receiver plane.

As an alternative to a single aperture coherent receiver with a full-size collecting area, as the one presented in this project, other techniques based on spatial and temporal diversity are becoming of special interest for free-space laser communication links. These techniques are generally based on the statistical properties of turbulence-induced signal intensity fading, as functions of both temporal and spatial coordinates. Spatial diversity combining, in which two or more copies of the same information bearing signal are combined in order to increase the overall SNR, offers a great potential for FSO communication link performance improvement [199]-[202]. With this technique, a large effective aperture can be achieved by combining the output signal from an array of smaller receivers. The advantage of a coherent array in terms of the coupling efficiency is that the number of turbulence speckles over each sub-aperture in the array is much smaller than it would be over a single large aperture. Because each receiver can now be smaller than the scale on which the signal wavefront varies, the local oscillator phase can be matched to the signal to achieve effective coherent reception. Output signals from these receivers can then be combined electronically to improve the detection statistics and can overcome turbulence-induced fading [199]-[202]. As the compensation is performed in the electrical domain, these techniques present several advantages in compare to the optical field conjugation techniques: improved loop rate and removal of adaptive mirrors. In the other hand, the receiver requires higher complexity in the electrical domain and a sufficiently high number of channels to perform compensation similar to the ones achieved by typical DMs [202]. By taking advantage of the communication set-up built in this project we could relate these FSO techniques with coherent communication systems and perform experimental comparing between single aperture and multiple aperture techniques.

In terms of the blind search algorithms for wavefront sensorless architectures, improved versions or modifications of the well-known SPGD algorithm could relax the hardware requirements on high-speed electronics at the receiver, which would facilitate the transition direct

to indirect wavefront sensor architectures. The optimization of the SPGD algorithm for AO systems has been proposed studied in the literature [203]-[205]. Improved blind search algorithms could be implemented by just modifying the control software designed at the receiver without introducing any additional cost while improving the temporal response of the AO. In [203], Vorontsov proposed an optimization technique based on the sub-division of the control channels into asynchronous SPGD clusters, demonstrating that it improves the AO system performance by exploiting individual and group characteristics of the AO system components. Also, in [204], the SPGD algorithm was demonstrated to provide a better performance by modifying the SPGD parameters in each iteration, decreasing the overall compensation time. Still, for most applications, the limited convergence rate of the algorithm in junction with important restrictions on the AO loop rate limit the performance of wave-front correction in real-time requirements. Future studies could take advantage of new high speed electronics and the SPGD optimization techniques to experimentally demonstrate wavefront sensorless correction for real applications.

References

[1] Killinger, Dennis. "Free space optics for laser communication through the air." *Optics and Photonics News* 13.10 (2002): 36-42.

[2] Kube, Erhard. "Information Transmission by light beams through the atmosphere." *Nachrichtentechnik* 6 (1968): 201-207.

[3] Schwartz, Jana L., Mason A. Peck, and Christopher D. Hall. "Historical review of air-bearing spacecraft simulators." *Journal of Guidance, Control, and Dynamics* 26.4 (2003): 513-522.

[4] Goodwin, Frank E. "A review of operational laser communication systems." *Proceedings of the IEEE* 58.10 (1970): 1746-1752.

[5] Chan, Vincent WS. "Space coherent optical communication systems-an introduction." *Journal of lightwave technology* 5 (1987): 633-637.

[6] Kiasaleh, Kamran. "Performance of APD-based, PPM free-space optical communication systems in atmospheric turbulence." *Communications, IEEE Transactions on* 53.9 (2005): 1455-1461.

[7] Hanzo, Lajos, et al. "Wireless myths, realities, and futures: from 3G/4G to optical and quantum wireless." *Proceedings of the IEEE* 100.Special Centennial Issue (2012): 1853-1888.

[8] Williams, W. Dan, et al. "RF and optical communications: A comparison of high data rate returns from deep space in the 2020 timeframe." (2007).

[9] Willebrand, Heinz, and Baksheesh S. Ghuman. *Free space optics: enabling optical connectivity in today's networks*. Sams Publishing, 2002.

[10] Kedar, Debbie, and Shlomi Arnon. "Urban optical wireless communication networks: the main challenges and possible solutions." *Communications Magazine, IEEE* 42.5 (2004): S2-S7.

[11] Liu, Qingchong, et al. "Optical wireless communication networks for first-and last-mile broadband access [Invited]." *Journal of optical Networking* 4.12 (2005): 807-828.

[12] Berk, Alexander, Lawrence S. Bernstein, and David C. Robertson. *MODTRAN: A moderate resolution model for LOWTRAN*. No. SSI-TR-124. SPECTRAL SCIENCES INC BURLINGTON MA, 1987.

[13] Henniger, Hennes, and Otakar Wilfert. "An introduction to free-space optical communications." *Radioengineering* 19.2 (2010): 203-212.

[14] Clark, Roger N. "Spectroscopy of rocks and minerals, and principles of spectroscopy." *Manual of remote sensing* 3 (1999): 3-58.

[15] Fried, David L. "Statistics of a geometric representation of wavefront distortion." *JOSA* 55.11 (1965): 1427-1431.

[16] Gregory, Mark, et al. "Commercial optical inter-satellite communication at high data rates." *Optical Engineering* 51.3 (2012): 031202-1.

[17] Belmonte, Aniceto, et al. "Performance evaluation of an adaptive optics free-space laser communications system from simulation of beam propagation." *Optics/Photonics in Security and Defence*. International Society for Optics and Photonics, 2006.

[18] Belmonte, Aniceto, and Joseph Khan. "Performance of synchronous optical receivers using atmospheric compensation techniques." *Optics express* 16.18 (2008): 14151-14162.

[19] Basch, E. E., and T. G. Brown. "Introduction to coherent optical fiber transmission." *Communications Magazine, IEEE* 23.5 (1985): 23-30.

[20] Li, Tingye. "Advances in lightwave systems research." *AT&T technical journal* 66.1 (1987): 5-18.

[21] Agrawal, Govind P. *Fiber-optic communication systems*. Vol. 1. 1997.

[22] Kazovsky, Leonid G., Georgios Kalogerakis, and Wei-Tao Shaw. "Homodyne phase-shift-keying systems: past challenges and future opportunities." *Journal of lightwave technology* 24.12 (2006): 4876-4884.

[23] Salz, J. "Modulation and detection for coherent lightwave communications." *Communications Magazine, IEEE* 24.6 (1986): 38-49.

[24] Okoshi, T., et al. "Computation of bit-error rate of various heterodyne and coherent-type optical communication schemes." *Journal of Optical Communications* 2.3 (1981): 89-96.

[25] Wagner, Richard E., Nim K. Cheung, and P. Kaiser. "Coherent lightwave systems for interoffice and loop-feeder applications." *Lightwave Technology, Journal of* 5.4 (1987): 429-438.

[26] Tyson, Robert K. *Introduction to adaptive optics*. Vol. 41. SPIE press, 2000.

[27] Ip, Ezra, et al. "Coherent detection in optical fiber systems." *Optics Express* 16.2 (2008): 753-791.

[28] Noe, Reinhold. "PLL-free synchronous QPSK polarization multiplex/diversity receiver concept with digital I&Q baseband processing." *Photonics Technology Letters, IEEE* 17.4 (2005): 887-889.

[29] Ip, Ezra, and Joseph M. Kahn. "Feedforward carrier recovery for coherent optical communications." *Journal of Lightwave Technology* 25.9 (2007): 2675-2692.

[30] Franz, Jürgen, and Virander K. Jain. Optical Communications: Components and Systems: Analysis--design--optimization--application. CRC press, 2000.

[31] Kazovsky, Leonid G. "Performance analysis and laser linewidth requirements for optical PSK heterodyne communications systems." *Lightwave Technology, Journal of* 4.4 (1986): 415-425.

[32] Wree, Christoph, et al. "Coherent receivers for phase-shift keyed transmission." *Optical Fiber Communication Conference*. Optical Society of America, 2007.

[33] Norimatsu, Seiji, and Katsushi Iwashita. "Damping factor influence on linewidth requirements for optical PSK coherent detection systems." *Lightwave Technology, Journal of* 11.7 (1993): 1226-1233.

[34] Xu, Chris, Xiang Liu, and Xing Wei. "Differential phase-shift keying for high spectral efficiency optical transmissions." *Selected Topics in Quantum Electronics, IEEE Journal of* 10.2 (2004): 281-293.

[35] Gnauck, Alan H., and Peter J. Winzer. "Optical phase-shift-keyed transmission." *Journal of lightwave technology* 23.1 (2005): 115.

[36] Jiang, Hong, and Ross Saunders. "Advances in SiGe ICs for 40G signal equalization." *Optical Fiber Communication Conference*. Optical Society of America, 2006.

[37] Dedic, Ian. "56 GS/s ADC: Enabling 100GbE." *Optical Fiber Communication Conference*. Optical Society of America, 2010.

[38] Ip, Ezra, et al. "Coherent detection in optical fiber systems." *Optics Express* 16.2 (2008): 753-791.

[39] Viterbi, Andrew. "Nonlinear estimation of PSK-modulated carrier phase with application to burst digital transmission." *Information Theory, IEEE Transactions on* 29.4 (1983): 543-551.

[40] Lee, Etty J., and Vincent W. Chan. "Diversity coherent and incoherent receivers for free-space optical communication in the presence and absence of interference." *Journal of Optical Communications and Networking* 1.5 (2009): 463-483.

[41] Belmonte, Aniceto, and Joseph M. Kahn. "Capacity of coherent free-space optical links using atmospheric compensation techniques." *Optics express* 17.4 (2009): 2763-2773.

[42] Andrews, Larry C. *Field guide to atmospheric optics*. Vol. 2. SPIE press, 2004.

[43] Motamedi, Ed, et al. "Special Section Guest Editorial: Emerging MOEMS Technology and Applications." *Journal of Micro/Nanolithography, MEMS, and MOEMS* 13.1 (2014): 011101-011101.

[44] Muller, Richard A., and Andrew Buffington. "Real-time correction of atmospherically degraded telescope images through image sharpening." *JOSA* 64.9 (1974): 1200-1210.

[45] Booth, Martin J. "Wavefront sensorless adaptive optics for large aberrations." *Optics letters* 32.1 (2007): 5-7.

[46] Belmonte, Aniceto. "Atmospheric compensation experiments on advanced free-space optical communication systems." *Technichal annex for non oriented fundamental research*, Spanish Department of Science and Innovation MICINN Grant No. TEC 2009-10025.

[47] Anzuola, Esdras and Aniceto Belmonte. "Generation of atmospheric wavefronts using binary micro-mirror arrays." *Submitted to Applied Optics*, February 2015.

[48] Anzuola, Esdras. "Digital coherent transceiver for optical communications. From Design to Implementation". *Master Thesis*. February 2012. ETSETB-230.82476

[49] Anzuola, Esdras and Aniceto Belmonte. "Experiments on free space optical communication systems using QPSK modulation." *Submitted to Applied Optics*, March 2015.

[50] Kazovsky, Leonid G., Sergio Benedetto, and Alan E. Willner. *Optical fiber communication systems*. Artech House, 1996.

[51] Schottky, Walter. "Über spontane Stromschwankungen in verschiedenen Elektrizitätsleitern." *Annalen der Physik* 362.23 (1918): 541-567.

[52] Bennett, William R. *Electrical noise*. Vol. 960. New York: McGraw-Hill, 1960.

[53] Robinson, Frank Neville Hosband. "Noise and fluctuations in electronic devices and circuits." *Oxford, Clarendon Press, 1974. 252 p.* 1 (1974).

[54] Okoshi, Takanori. *Coherent optical fiber communications*. Vol. 3. Springer, 1988.

[55] Yamamoto, Yoshihisa, and Tatsuya Kimura. "Coherent optical fiber transmission systems." *Quantum Electronics, IEEE Journal of* 17.6 (1981): 919-935.

[56] Kahn, Joseph M., and Keang-Po Ho. "Ultimate spectral efficiency limits in DWDM systems." *Optoelectronics communication conference, Yokohama, Japan*. 2002.

[57] Lyubomirsky, Ilya, and Cheng-Chung Chien. "Optical duobinary spectral efficiency versus transmission performance: Is there a tradeoff?." *Conference on Lasers and Electro-Optics*. Optical Society of America, 2005.

[58] Keiser, Gerd. *Optical fiber communications*. John Wiley & Sons, Inc., 2003.

[59] Lyuborminsky, I. ”Coherent Detection for Opical Duobinary Communication Systems.”, *Photonics Technology Letters, IEEE*, 18 (2006), 686-870.

[60] Taylor, Michael G. "Coherent detection method using DSP for demodulation of signal and subsequent equalization of propagation impairments." *Photonics Technology Letters, IEEE* 16.2 (2004): 674-676.

[61] Ramirez-Iniguez, Roberto, Sevia M. Idrus, and Ziran Sun. *Optical wireless communications: IR for wireless connectivity*. CRC Press, 2008.

[62] Ly-Gagnon, D., et al. "Coherent detection of optical quadrature phase-shift keying signals with carrier phase estimation." *Lightwave Technology, Journal of* 24.1 (2006): 12-21.

[63] Lee, Edward A., and David G. Messerschmitt. *Digital communication*. Kluwer, 1994.

[64] Foggi, Tommaso, et al. "Maximum-likelihood sequence detection with closed-form metrics in OOK optical systems impaired by GVD and PMD." *Journal of lightwave technology* 24.8 (2006): 3073.

[65] Ip, Ezra, et al. "Coherent detection in optical fiber systems." *Optics Express* 16.2 (2008): 753-791.

[66] Kahn, Joseph M., and Keang-Po Ho. "Spectral efficiency limits and modulation/detection techniques for DWDM systems." *Selected Topics in Quantum Electronics, IEEE Journal of* 10.2 (2004): 259-272.

[67] Nazarathy, Moshe, and Erez Simony. "Multichip differential phase encoded optical transmission." *Photonics Technology Letters, IEEE* 17.5 (2005): 1133-1135.

[68] Divsalar, Dariush, and Marvin K. Simon. "Multiple-symbol differential detection of MPSK." *Communications, IEEE Transactions on* 38.3 (1990): 300-308.

[69] Bar-David, I., and J. Salz. "On dual optical detection: Homodyne and transmitted-reference heterodyne reception." *Communications, IEEE Transactions on* 36.12 (1988): 1309-1315.

[70] Marsland, R. “Balanced Photoreceivers Challenge Shot-Noise Limit.” *Laser Focus World, Detector Handbook. (*1994). Supplement.

[71] Ebskamp F. and Pedersen R., “The Application of a balanced 6-15 GHz low noise Tuned Optical Front end in a 5 Gbits/s CPFSK Heterodyne System.”, *European Conference on Optical Communication.* Berlin (1992), 1375-1378.

[72] Smith, David W. "Techniques for multigigabit coherent optical transmission." *Lightwave Technology, Journal of* 5.10 (1987): 1466-1478.

[73] Abbas, Gregory Lew, Vincent WS Chan, and Ting Yee. "A dual-detector optical heterodyne receiver for local oscillator noise suppression." *Lightwave Technology, Journal of* 3.5 (1985): 1110-1122.

[74] Kazovsky, Leonid G. "Multichannel coherent optical communications systems." *Lightwave Technology, Journal of* 5.8 (1987): 1095-1102.

[75] Benedetto, Sergio, and Pierluigi Poggiolini. "Theory of polarization shift keying modulation." *Communications, IEEE Transactions on* 40.4 (1992): 708-721.

[76] Tsukamoto, Satoshi, Kazuhiro Katoh, and Kazuro Kikuchi. "Coherent demodulation of optical multilevel phase-shift-keying signals using homodyne detection and digital signal processing." *Photonics Technology Letters, IEEE* 18.10 (2006): 1131-1133.

[77] Linke, Richard A., and Alan H. Gnauck. "High-capacity coherent lightwave systems." *Lightwave Technology, Journal of* 6.11 (1988): 1750-1769.

[78] Barry, John R., and Edward A. Lee. "Performance of coherent optical receivers." *Proceedings of the IEEE* 78.8 (1990): 1369-1394.

[79] Barry, John R., and Joseph M. Kahn. "Carrier synchronization for homodyne and heterodyne detection of optical quadriphase-shift keying." *Lightwave Technology, Journal of* 10.12 (1992): 1939-1951.

[80] Chambers, William G. *Basics of communication and coding*. Oxford University Press, Inc., 1985.

[81] Proakis, John G., et al. *Communication systems engineering*. Vol. 2. Englewood Cliffs: Prentice-hall, 1994.

[82] Leven, Andreas, et al. "Coherent receivers for practical optical communication systems." *Optical Fiber Communication Conference*. Optical Society of America, 2007.

[83] Ly-Gagnon, D., et al. "Coherent detection of optical quadrature phase-shift keying signals with carrier phase estimation." *Lightwave Technology, Journal of* 24.1 (2006): 12-21.

[84] Henry, Charles H. "Theory of the phase noise and power spectrum of a single mode injection laser." *Quantum Electronics, IEEE Journal of* 19.9 (1983): 1391-1397.

[85] Tur, Moshe, Behzad Moslehi, and Joseph W. Goodman. "Theory of laser phase noise in recirculating fiber-optic delay lines." *Lightwave Technology, Journal of* 3.1 (1985): 20-31.

[86] Gardner, Floyd M. *Phaselock techniques*. John Wiley & Sons, 2005.

[87] Grant, M., W. Michie, and M. Fletcher. "The performance of optical phase-locked loops in the presence of nonnegligible loop propagation delay." *Lightwave Technology, Journal of* 5.4 (1987): 592-597.

[88] Ip, Ezra, and Joseph M. Kahn. "Carrier synchronization for 3-and 4-bit-per-symbol optical transmission." *Lightwave Technology, Journal of* 23.12 (2005): 4110-4124.

[89] Foschini, G. J., R. D. Gitlin, and S. B. Weinstein. "On the Selection of a Two-Dimensional Signal Constellation in the Presence of Phase Jitter and Gaussian Noise." *Bell System Technical Journal* 52.6 (1973): 927-965.

[90] Cao, Yinwen, et al. "Frequency estimation for optical coherent MPSK system without removing modulated data phase." *Photonics Technology Letters, IEEE* 22.10 (2010): 691-693.

[91] Hoffmann, Sebastian, et al. "Frequency estimation and compensation for coherent QPSK transmission with DFB lasers." *Coherent Optical Technologies and Applications*. Optical Society of America, 2008.

[92] Berrou, Claude, and Alain Glavieux. "Near optimum error correcting coding and decoding: Turbo-codes." *Communications, IEEE Transactions on* 44.10 (1996): 1261-1271.

[93] Massey, James L. "Optimum frame synchronization." *Communications, IEEE Transactions on* 20.2 (1972): 115-119.

[94] Lui, Gee, and Harry H. Tan. "Frame synchronization for Gaussian channels." *Communications, IEEE Transactions on* 35.8 (1987): 818-829.

[95] Cacciamani, E., and C. Wolejsza. "Phase-ambiguity resolution in a four-phase PSK communications system." *Communication Technology, IEEE Transactions on* 19.6 (1971): 1200-1210.

[96] Boone, Bradley G., et al. "Optical communications development for spacecraft applications: recent progress at JHU/APL." *Aerospace Conference, 2005 IEEE*. IEEE, 2005.

[97] Canny, John Francis. "Finding edges and lines in images." *Massachusetts Inst. of Tech. Report* 1 (1983).

[98] Erup, Lars, Floyd M. Gardner, and Robert A. Harris. "Interpolation in digital modems. II. Implementation and performance." *Communications, IEEE Transactions on* 41.6 (1993): 998-1008.

[99] Okoshi, T., Ki Kikuchi, and A. Nakayama. "Novel method for high resolution measurement of laser output spectrum." *Electronics letters* 16.16 (1980): 630-631.

[100] Goldfarb, Gilad, and Guifang Li. "BER estimation of QPSK homodyne detection with carrier phase estimation using digital signal processing." *Optics express* 14.18 (2006): 8043-8053.

[101] Kolmogorov, Andrey Nikolaevich. "The local structure of turbulence in incompressible viscous fluid for very large Reynolds numbers." *Dokl. Akad. Nauk SSSR*. Vol. 30. No. 4. 1941.

[102] Noll, Robert J. "Zernike polynomials and atmospheric turbulence." *JOsA* 66.3 (1976): 207-211.

[103] Tatarskii, V I. *Wave Propagation in a Turbulent Medium*.New York: McGraw-Hill, 1961.

[104] Karp, Sherman, and Larry B. Stotts. *Fundamentals of Electro-optic Systems Design: Communications, Lidar, and Imaging*. Cambridge University Press, 2012.

[105] Andrews, Larry C., and Ronald L. Phillips. *Laser beam propagation through random media*. Vol. 10. No. 3.626196. Bellingham: SPIE press, 2005.

[106] Fried, David L. "Optical heterodyne detection of an atmospherically distorted signal wave front." *Proceedings of the IEEE* 55.1 (1967): 57-77.

[107] Fried, D. L. "Atmospheric modulation noise in an optical heterodyne receiver." *Quantum Electronics, IEEE Journal of* 3.6 (1967): 213-221.

[108] Hecht, Eugene. *Theory and problems of optics*. McGraw-Hill, 1975.

[109] Glindemann, Andreas. "Relevant parameters for tip-tilt systems on large telescopes." *Publications of the Astronomical Society of the Pacific* (1997): 682-687.

[110] Ruilier, Cyril, and Frédéric Cassaing. "Coupling of large telescopes and single-mode waveguides: application to stellar interferometry." *JOSA A* 18.1 (2001): 143-149.

[111] Snyder, Allan W., and J. Love. *Optical waveguide theory*. Vol. 190. Springer, 1983.

[112] Cohen, Steven C. "Heterodyne detection: phase front alignment, beam spot size, and detector uniformity." *Applied optics* 14.8 (1975): 1953-1959.

[113] Franz, Fidler, and Wallner Oswald. "Application of single-mode fiber-coupled receivers in optical satellite to high-altitude platform communications." *EURASIP Journal on Wireless Communications and Networking* 2008 (2008).

[114] Buck, John A. *Fundamentals of optical fibers*. John Wiley & Sons, 2004.

[115] Cagigal, Manuel P., and Vidal F. Canales. "Speckle statistics in partially corrected wave fronts." *Optics letters* 23.14 (1998): 1072-1074.

[116] Keskin, Onur, Laurent Jolissaint, and Colin Bradley. "Hot-air optical turbulence generator for the testing of adaptive optics systems: principles and characterization." *Applied optics* 45.20 (2006): 4888-4897.

[117] Butler, David J., et al. "Broadband, static wave-front generation: Na-Ag ion-exchange phase screens and telescope emulation." *Applied optics* 43.14 (2004): 2813-2823.

[118] Rampy, Rachel, et al. "New method of fabricating phase screens for simulated atmospheric turbulence." *SPIE Astronomical Telescopes+ Instrumentation*. International Society for Optics and Photonics, 2010.

[119] Acosta, Eva, and Salvador Bará. "Variable aberration generators using rotated Zernike plates." *JOSA A* 22.9 (2005): 1993-1996.

[120] Tong, Xu. "Simulating Atmospheric Turbulence Using a Spatial Light Modulator based on Fourier Transform." *CLEO: Science and Innovations*. Optical Society of America, 2014.

[121] Phillips, James D., Matthew E. Goda, and Jason Schmidt. "Atmospheric turbulence simulation using liquid crystal spatial light modulators." *Optics & Photonics 2005*. International Society for Optics and Photonics, 2005.

[122] Lee, Wai-Hon. "Binary computer-generated holograms." *Applied Optics* 18.21 (1979): 3661-3669.

[123] Jolissaint, Laurent. "Optical turbulence generators for testing astronomical adaptive optics systems: A review and designer guide." *Publications of the Astronomical Society of the Pacific* 118.847 (2006): 1205-1224.

[124] Ragazzoni, Roberto, et al. "Adaptive optics module for TNG (AdOpt@ TNG): a status report." *Optical Telescopes of Today and Tomorrow*. International Society for Optics and Photonics, 1997.

[125] Harding, Cressida M., Rachel A. Johnston, and Richard G. Lane. "Fast simulation of a Kolmogorov phase screen." *Applied optics* 38.11 (1999): 2161-2170.

[126] Roddier, Francois J. "Variations on a Hartmann theme." *Optical Engineering* 29.10 (1990): 1239-1242.

[127] Ueno, Kousei, et al. "Fabrication and Characteristic Responses of Integrated Microelectrodes in Polymer Channel Chip." *Chemistry Letters* 8 (2000): 858-859.

[128] Amin, Alireza Esmaeili. "Fluid Jet Polishing of Glass Material."

[129] Ebstein, Steven M. "Adaptive optics: Index matching offers a low-cost route to complex optics." *Laser focus world* 42.1 (2006).

[130] McGuire, Patrick C., et al. "Full-system laboratory testing of the F/15 deformable secondary mirror for the new MMT adaptive optics system." *SPIE's International Symposium on Optical Science, Engineering, and Instrumentation*. International Society for Optics and Photonics, 1999.

[131] Dayton, David C., et al. "Theory and laboratory demonstrations on the use of a nematic liquid-crystal phase modulator for controlled turbulence generation and adaptive optics." *Applied optics* 37.24 (1998): 5579-5589.

[132] Lovea, Gordon D., et al. "Emulating multiconjugate turbulence." (2002).

[133] Tyson, Robert K., and Benjamin West Frazier. "Microelectromechanical system programmable aberration generator for adaptive optics." *Applied optics* 40.13 (2001): 2063-2067.

[134] Davis, Christopher C., et al. "Characterization of a liquid-filled turbulence simulator." *SPIE's International Symposium on Optical Science, Engineering, and Instrumentation*. International Society for Optics and Photonics, 1998.

[135] Gamo, Hideya, and Arun K. Majumdar. "Atmospheric turbulence chamber for optical transmission experiment: characterization by thermal method." *Applied optics* 17.23 (1978): 3755-3762.

[136] Yu, Wen-Kai, et al. "Adaptive compressive ghost imaging based on wavelet trees and sparse representation." *Optics express* 22.6 (2014): 7133-7144.

[137] Masson, A., et al. "Micromirror structured illumination microscope for high-speed in vivo drosophila brain imaging." *Optics express* 22.2 (2014): 1243-1256.

[138] Lerner, Vitaly, et al. "Shaping Laguerre–Gaussian laser modes with binary gratings using a digital micromirror device." *Optics letters* 37.23 (2012): 4826-4828.

[139] Mirhosseini, Mohammad, et al. "Rapid generation of light beams carrying orbital angular momentum." *Optics express* 21.25 (2013): 30196-30203.

[140] Otsubo, Masashi, Hideki Takami, and Masanori Iye. "Holographic atmospheric turbulence simulator for testing adaptive optics systems." *Publications of the astronomical society of the Pacific* (1997): 1057-1061.

[141] Brown, B. R., and A. W. Lohmann. "Computer-generated binary holograms." *IBM Journal of research and Development* 13.2 (1969): 160-168.

[142] Lee, Wai-Hon. "Binary synthetic holograms." *Applied optics* 13.7 (1974): 1677-1682.

[143] Lee, Wai-Hon. "III Computer-Generated Holograms: Techniques and Applications." *Progress in optics* 16 (1978): 119-232.

[144] Instruments, Texas. DLPS022A – Datasheet. s.l. : Texas Instruments Incorporated, 2012.

[145] Nesbitt, Ryder S., et al. "Holographic recording using a digital micromirror device." *Electronic Imaging'99*. International Society for Optics and Photonics, 1999.

[146] Instruments, Texas. Using Lasers with DLP® DMD technology. Sept. de 2008. TI DN 2509927.

[147] Lohmann, Adoph W., and D. P. Paris. "Binary Fraunhofer holograms, generated by computer." *Applied Optics* 6.10 (1967): 1739-1748.

[148] Teich, Malvin Carl, and B. E. A. Saleh. "Fundamentals of photonics." *Canada, Wiley Interscience* (1991): 3.

[149] Majumdar, Arun K. "Free-space laser communication performance in the atmospheric channel." *Journal of Optical and Fiber Communications Reports* 2.4 (2005): 345-396.

[150] Vorontsov, T. Weyrauch and M.A. "Free-space laser communications with adaptive optics: Atmospheric compensation experiments.", *Journal Opt. Fiber Commun, (*2004), págs. 355-379. Rep. I.

[151] Hardy, John W. *Adaptive optics for astronomical telescopes*. Oxford University Press, 1998.

[152] Hudgin, Richard. "Wave-front compensation error due to finite corrector-element size." *JOSA* 67.3 (1977): 393-395.

[153] Sawicki, Richard H., and William Sweatt. "Continuously deformable mirrors." *Technical Symposium Southeast*. International Society for Optics and Photonics, 1987.

[154] Mahajan, Virendra N. "Strehl ratio for primary aberrations in terms of their aberration variance." *JOSA* 73.6 (1983): 860-861.

[155] Greenwood, Darryl P. "Bandwidth specification for adaptive optics systems." *JOSA* 67.3 (1977): 390-393.

[156] Tyler, Glenn A. "Bandwidth considerations for tracking through turbulence." *JOSA A* 11.1 (1994): 358-367.

[157] Roddier, François, ed. *Adaptive optics in astronomy*. Cambridge university press, 1999.

[158] Vorontsov, M. A., et al. "Image quality criteria for an adaptive imaging system based on statistical analysis of the speckle field." *JOSA A* 13.7 (1996): 1456-1466.

[159] http://oe.ziti.uni-heidelberg.de/joomla/de/forschung/optische-messtechnik/21-shack-hartmann-wavefront-sensing.html

[160] Primot, J., G. Rousset, and J. C. Fontanella. "Deconvolution from wave-front sensing: a new technique for compensating turbulence-degraded images." *JOSA A* 7.9 (1990): 1598-1608.

[161] Roddier, Francçois. "Curvature sensing and compensation: a new concept in adaptive optics." *Applied Optics* 27.7 (1988): 1223-1225.

[162] Roddier, Francois, Malcolm Northcott, and J. Elon Graves. "A simple low-order adaptive optics system for near-infrared applications." *Publications of the Astronomical Society of the Pacific* (1991): 131-149.

[163] Dorn, Reinhold J., Barry E. Burke, and James W. Beletic. *A CCD-Based Curvature Wavefront Sensor for Adaptive Optics in Astronomy*. Springer Netherlands, 2004.

[164] Schwartz, C., E. Ribak, and S. G. Lipson. "Bimorph adaptive mirrors and curvature sensing." *JOSA A* 11.2 (1994): 895-902.

[165] O'meara, T. R. "The multidither principle in adaptive optics." *JOSA* 67.3 (1977): 306-314.

[166] Pearson, J. E., and S. Hansen. "Experimental studies of a deformable-mirror adaptive optical system." *JOSA* 67.3 (1977): 325-332.

[167] Vorontsov, Mikhail A., et al. "Adaptive optics based on analog parallel stochastic optimization: analysis and experimental demonstration." *JOSA A* 17.8 (2000): 1440-1453.

[168] Cao, Jingtai, et al. "Stochastic parallel gradient descent laser beam control algorithm for atmospheric compensation in free space optical communication." *Optik-International Journal for Light and Electron Optics* (2014).

[169] Ygouf, Marie, et al. "Wavefront sensorless multi-conjugate adaptive optics for imaging in deep atmospheric turbulence: preliminary numerical analysis." *Aerospace Conference, 2014 IEEE*. IEEE, 2014.

[170] Bo C., Xinyang L., Wenhan J. "Optimization of Stochastic Parallel Gradient Descent Algorithm for Adaptive Optics in Atmospheric Turbulence." *Chinese Journal of Lasers*, (2010), págs. 959-964. 37 (4).

[171] Naumov, A. F., et al. "Liquid-crystal adaptive lenses with modal control." *Optics Letters* 23.13 (1998): 992-994.

[172] Freeman, R. H., and James E. Pearson. "Deformable mirrors for all seasons and reasons." *25th Annual Technical Symposium*. International Society for Optics and Photonics, 1981.

[173] Sellin, I. A., D. J. Pegg, and R. Drouin. "Bimorph piezoelectric flexible mirror." *Phys. Rev. A* 17 (1978): 1966.

[174] Kokorowski, S. A. "Analysis of adaptive optical elements made from piezolectric bimorphs." *JOSA* 69.1 (1979): 181-187.

[175] M. L. Plett, "Adaptive Optics System for coupling a distorted Laser Beam into a Single Mode Optical Fiber", Master Thesis at University of Maryland,1999.

[176] Vdovin, Gleb, and P. M. Sarro. "Flexible mirror micromachined in silicon." *Applied optics* 34.16 (1995): 2968-2972.

[177] OKO Technologies http://www.okotech.com

[178] Boston Micromachines Corporation,. "The Wavefront Sensorless Adaptive Optics Demonstrator". *White Paper*. Cambridge : s.n., May, 2012.

[179] Farrell, Thomas, et al. "Task-based assessment of deformable mirrors." *Proc. SPIE*. Vol. 6467. 2007.

[180] Tholl, Hans Dieter. "Novel laser beam steering techniques." *Optics/Photonics in Security and Defence*. International Society for Optics and Photonics, 2006.

[181] Sweeney, Michael N., et al. "Design considerations for fast-steering mirrors (FSMs)." *International Symposium on Optical Science and Technology*. International Society for Optics and Photonics, 2002.

[182] Berta, Albert, et al. "Development of a commercial line of high-performance fast-steering mirrors." *SPIE's International Symposium on Optical Science, Engineering, and Instrumentation*. International Society for Optics and Photonics, 1999.

[183] Marshall, Gerald F. "Risley prism scan patterns." *SPIE's International Symposium on Optical Science, Engineering, and Instrumentation*. International Society for Optics and Photonics, 1999.

[184] Sánchez, Michael, and David Gutow. "Control laws for a three-element Risley prism optical beam pointer." *SPIE Optics+ Photonics*. International Society for Optics and Photonics, 2006.

[185] Sullivan, Mark T. "Synopsis of "Risley Prism Beam Pointe r"."

[186] (PI), Physik Instrumente. PZ 149E S-330 Tp/Tilt Platform. [White Paper]. Karlsruhe : s.n., 24 de July de 2007. pág. 24.

[187] (PI), Physiks Instrumente. E-616 Controller for Multi-Axis Piezo Tip/Tilt Mirrors and Platforms. [User Manual]. Karlsruhe : s.n., 2011. pág. 2.

[188] Boston Micromachines Corporation ., V.3.4.3 Rev C. *User Manual* . 2011. pág. 45.

[189] National Instruments Corporation. NI 622x Specifications. *M Series User Manual.* 2007.

[190] Chen, I. S. Reed and X. Boston "Error-Control Coding for Data Networks.", Kluwer Academic, 1999, The Kluwer International Series in Engineering and Computer Science, Vol. 508 .

[191] Liu, L. Hu, Q. Mu, Z. Cao, and L. Xuan. "Open-loop control of liquid-crystal spatial light modulators for vertical atmospheric turbulence wavefront correction*.", Applied Optics,* (2011) C50(1), págs. 82-89.

[192] Porter, Jason, et al. *Adaptive optics for vision science: Principles, practices, design and applications*. Vol. 171. John Wiley & Sons, 2006.

[193] Sodnik, Zoran, et al. "Adaptive optics and ESA's optical ground station." *SPIE Optical Engineering+ Applications*. International Society for Optics and Photonics, 2009.

[194] Berkefeld, Thomas, et al. "Adaptive optics for satellite-to-ground laser communication at the 1m Telescope of the ESA Optical Ground Station, Tenerife, Spain." *Proc. SPIE*. Vol. 7736. 2010.

[195] Sandalidis, Harilaos G., Theodoros A. Tsiftsis, and George K. Karagiannidis. "Optical wireless communications with heterodyne detection over turbulence channels with pointing errors." *Journal of lightwave technology* 27.20 (2009): 4440-4445.

[196] Belmonte, Aniceto. "Capacity of Coherent Laser Downlinks." *Journal of Lightwave Technology* 32.11 (2014): 2128-2132.

[197] Pawula, R_F, S. O. Rice, and J. Roberts. "Distribution of the phase angle between two vectors perturbed by Gaussian noise." *Communications, IEEE Transactions on* 30.8 (1982): 1828-1841.

[198] Goodman, Joseph W. *Speckle phenomena in optics: theory and applications*. Vol. 1. 2007.

[199] Belmonte, Aniceto, and Joseph M. Kahn. "Capacity of coherent free-space optical links using diversity-combining techniques." *Optics express* 17.15 (2009): 12601-12611.

[200] Belmonte, Aniceto, and Joseph M. Kahn. "Fundamental limits of diversity coherent reception on atmospheric optical channels." Signals, Systems and Computers, 2009 Conference Record of the Forty-Third Asilomar Conference on. IEEE, 2009.

[201] Belmonte, Aniceto, and Joseph M. Kahn. "Field conjugation adaptive arrays in atmospheric coherent optical links." GLOBECOM Workshops (GC Wkshps), 2010 IEEE. IEEE, 2010.

[202] Belmonte, Aniceto, and Joseph M. Kahn. "Efficiency of complex modulation methods in coherent free-space optical links." *Optics express* 18.4 (2010): 3928-3937.

[203] Vorontsov, Mikhail A., and Gary W. Carhart. "Adaptive wavefront control with asynchronous stochastic parallel gradient descent clusters." *JOSA A* 23.10 (2006): 2613-2622.

[204] Chen, Erhu, et al. "The Improvement of SPGD Algorithm Convergence in Satellite-to-Ground Laser Communication Links." *Procedia Engineering* 29 (2012): 409-414.

[205] Chen Bo, Li Xinyang and Jiang Wenhan. “Optimization of Stochastic Parallel Gradient Descent Algorithm for Adaptive Optics in Atmospheric Turbulence”. *Chinese Journal of Lasers*, 2010; 37(4): 959-964.